VRIJE UNIVERSITEIT

Frozen-Density Embedding

ACADEMISCH PROEFSCRIFT

ter verkrijging van de graad Doctor aan
de Vrije Universiteit Amsterdam,
op gezag van de rector magnificus
prof.dr. L.M. Bouter,
in het openbaar te verdedigen
ten overstaan van de promotiecommissie
van de faculteit der Exacte Wetenschappen
op donderdag 20 december 2007 om 15.45 uur
in de aula van de universiteit,
De Boelelaan 1105

door

Christoph Robert Jacob

geboren te Frankfurt am Main, Duitsland

promotor: prof.dr. E.J. Baerends
copromotor: dr. L. Visscher

Frozen-Density Embedding

Christoph R. Jacob

cover design by wrinkly pea   www.wrinklypea.com

Contents

Contents

Contents

Part I.

Introduction

1. Introduction

1.1. Embedding methods in theoretical chemistry

The subject of theoretical chemistry is the development of methods for the calculation of properties of molecules and their application to problems from different areas of chemistry.[1] Of particular interest are the calculation of the geometric structure of molecules, of the energetics of chemical reactions, and of molecular properties, such as electronic, vibrational or nuclear magnetic resonance (NMR) spectra. In many cases, such calculations are able to provide useful insight that cannot be obtained from experiment alone.

The most accurate and generally applicable methods in theoretical chemistry are those based on quantum mechanics, which solve the Schrödinger equation using different numerical schemes and approximations. Among these quantum chemical methods, one can distinguish wave function based *ab initio* methods and density-functional theory (DFT). The wave function based methods[2] form a well defined hierarchy, which offers a systematic way of approaching the exact solution of the Schrödinger equation. However, when more accurate wave function based methods are employed, the required computer time increases dramatically, so that such calculations quickly become infeasible.

DFT[3] is based on the solution of the Schrödinger equation as well, but it employs a different strategy by avoiding the calculation of the many-electron wave function. Due to its accuracy for a wide range of compounds and because the computational effort is in general lower than that of wave function based methods, DFT has become the method of choice for many practical applications. However, DFT relies on the use of an approximate functional for the exchange-correlation energy, and the accuracy of DFT calculations is limited by the quality of this approximate functional. Furthermore, in contrast to wave function based methods, there is no way of systematically improving the quality of DFT results. A more detailed discussion of quantum chemical methods, and in particular of DFT, can be found in Chapter 2.

Besides quantum chemical methods, there are the molecular mechanics (MM) methods, which are based on classical force fields obtained from fitting to experimental data or to the results of quantum chemical calculations. MM methods are computationally

inexpensive, and can be applied to very large systems. However, the applicability of the available force fields is usually limited to a rather restricted class of molecules for which the force field has been designed.

As this short overview shows, the methods available in theoretical chemistry differ significantly in their applicability, their accuracy and the computational effort that is required. As a rule of thumb, more accurate methods are in general computationally more expensive, and usually show a less favourable scaling of the computational effort with the size of the system. Therefore, calculations using the most accurate methods are often limited to small molecules in the gas phase, while calculations on larger systems are only feasible with less accurate methods.

One of the biggest challenges for theoretical chemistry is the realistic description of large systems such as biological systems (e.g., reactions catalyzed by enzymes) or of molecules in solution. Such a description requires not only the calculation of large systems, but also that the dynamics of the system at finite temperature is accounted for, i.e., long time scales have to be considered by performing calculations for a large number of different structures. Therefore, such calculations are often out of reach if one tries to apply accurate quantum chemical methods.

In many cases, however, one is only interested in a small part of the total system. For instance, in enzymes focus can be placed on the active center, where the reaction of interest takes place, while the protein environment is important for stabilizing this active center, but in general does not take part in the reaction itself. In the case of solvent effects, the main interest lies usually on properties of the solute molecule, while the surrounding solvent molecules are only important because of their effect on the solute.

Therefore, it is often not desirable to treat the whole system at the same level, but instead to apply methods in which different parts of the system are described using different approximation. Usually, one combines a high-level method for the important part of the system (the subsystem of interest) with a low-level method for the environment. This allows it to focus on the important parts, while not wasting computational effort on parts of the system were an accurate description is not essential.

There are a number of different embedding schemes available, that can be distinguished by the methods that are combined and by their treatment of the coupling between these different methods. In QM/MM methods,[4,5] a quantum chemical method (wave function based or DFT) is employed for the subsystem of interest, while a molecular mechanics description is used for the environment. In QM/QM embedding schemes,[6–8] different quantum chemical methods are employed for different part of the system. This can, for instance, be a highly accurate wave function based method for the subsystem of interest, which is combined with a DFT description of the environment. It is also possible that the same method is used for both parts of the system,

e.g., in a DFT-in-DFT embedding scheme. This can be advantageous if additional approximations are introduced for the description of the environment, or if the expensive calculation of molecular properties or spectra can be done for the subsystem of interest only.

In embedding methods, the total energy is expressed in terms of the energy of the subsystem of interest E_{I}, the energy of the environment E_{env}, and an interaction energy E_{int} as

$$E_{\mathrm{tot}} = E_{\mathrm{I}} + E_{\mathrm{env}} + E_{\mathrm{int}}. \tag{1.1}$$

Different embedding methods differ in the way in which the energies E_{I} and E_{env} are calculated and in the definition of the interaction energy E_{int}.

The simplest approach is that of the ONIOM family of embedding methods,[6,7] in which the energy of the system of interest is calculated for the isolated subsystem of interest (i.e., without including the environment) using a high-level method, whereas the energy of the environment is calculated for the isolated environment (i.e., in the absence of the subsystem of interest) using a low-level method. The interaction energy is calculated using the low-level method as,

$$E_{\mathrm{int}} = E_{\mathrm{tot}}^{\mathrm{low}} - E_{\mathrm{I}}^{\mathrm{low}} - E_{\mathrm{env}}^{\mathrm{low}}. \tag{1.2}$$

This results in the total energy expression

$$E_{\mathrm{tot}} = E_{\mathrm{I}}^{\mathrm{high}} - E_{\mathrm{I}}^{\mathrm{low}} + E_{\mathrm{tot}}^{\mathrm{low}}. \tag{1.3}$$

This ONIOM scheme allows the combination of any kind of methods and can be applied for both QM/QM and QM/MM embedding calculations. However, the coupling between the different parts of the system is only included in the energy expression. Therefore, no polarization of the subsystem of interest due to the environment is included and properties and spectra calculated for the subsystem of interest will not differ from those of the isolated subsystem (except for a change of the equilibrium geometry).

The description of the polarization of the subsystem of interest with respect to the environment requires that the calculation on the subsystem of interest is not done for the isolated subsystem, but that the interaction with the environment is included. The simplest possibility is the inclusion of an interaction potential that models the effect of the environment. In QM/MM schemes, this interaction potential is described using MM methods, by employing a suitable parametrization of this interaction potential.[4,9]

In QM/QM schemes employing wave function based methods, the inclusion of the polarization of the subsystem of interest due to the environment is not straightforward

and a suitable description is difficult to achieve. Such a description would require a partitioning of the wave function of the total system into wave functions of the subsystem of interest and of the environment, which requires either the introduction of additional approximations or leads to a scheme that is computationally very demanding (see, e.g., Refs. 10, 11).

However, within DFT the calculation of the wave function is avoided and it is, therefore, not necessary to partition the wave function. Instead, the electron density can be partitioned and it is possible to formulate a DFT-in-DFT embedding scheme in which the polarization of the subsystem of interest due to the environment is included by means of an effective embedding potential.[8] This embedding potential only depends on the (frozen) electron density of the environment, which makes it possible to introduce additional approximations for the environment. This DFT-in-DFT embedding method will be referred to as frozen-density embedding (FDE) in this thesis. In Chapter 3, a detailed introduction of the FDE scheme will be given.

The FDE scheme allows a both accurate and efficient description of the coupling between the subsystem of interest and the environment, that goes beyond the very simple coupling only at the level of the energy expression employed in the widely used ONIOM scheme. Furthermore, it has the advantage that it provides a formalism that is in principle exact and that, unlike QM/MM schemes, does not rely on an empirical parametrization. Therefore, FDE is a very promising scheme for tackling large systems, and this thesis will explore some of its possibilities.

1.2. This thesis

The topic of this thesis is the further development of the frozen-density embedding (FDE) method. It contributes to the theoretical development of by extending its applicability and by investigating and improving the involved approximations. Furthermore, by providing an efficient and flexible implementation, this thesis provides a tool for the application of FDE to challenging problems, such as the description of solvent effects.

This thesis is divided into four parts. In the first part, the theoretical framework is introduced. In Chapter 2, an introduction to density-functional theory is given, with a special focus on the treatment of the kinetic energy. The different possible treatments of the kinetic energy presented there provide the starting point for the FDE scheme, which is introduced in Chapter 3. Chapter 3 also reviews the previous theoretical work and applications related to FDE.

The second part is devoted to theoretical developments related to FDE. In Chapter 4, the FDE scheme is extended to the calculation of magnetic properties, in particular

of nuclear-magnetic resonance (NMR) shieldings. In Chapter 5, a contribution to the development of approximations for the nonadditive kinetic-energy, that are crucial for the FDE scheme, is given.

The third part presents an implementation of FDE. In Chapter 6, an efficient numerical integration scheme is developed, that makes FDE applicable for very large frozen environments (up to 1000 atoms). In Chapter 7, a flexible implementation of FDE is described that allows an arbitrary number of frozen fragments, and that further allows it to include the polarization of the environment is a very simple way.

Finally, the fourth part shows two applications of the FDE scheme. In Chapter 8, a study on van der Waals complexes is presented, which serves as a benchmark application to identify possible problems in the approximations made in FDE. In Chapter 9 a contribution to the application of FDE for modeling solvent effects on molecular properties is given, by providing a detailed comparison to the discrete reaction field solvent model.

1. Introduction

2. Density-functional theory and the kinetic energy

In this Chapter, an introduction to density-functional theory (DFT) is given, with a special focus on the kinetic energy. First, in Section 2.1 a brief introduction of the main concepts of quantum mechanics that are employed in theoretical chemistry is given. In Section 2.2, the foundations of DFT are explained. In particular, the Hohenberg–Kohn theorem is introduced, and the total energy functional and its components, especially the kinetic energy and the exchange-correlation energy, are discussed. Finally, in Section 2.3 different ways of handling the kinetic energy in DFT are explained. First, the conventional Kohn–Sham treatment of the kinetic energy is derived. This is followed by a discussion of orbital-free DFT and of approximate kinetic-energy functionals. Finally, a hybrid Kohn–Sham / orbital-free treatment of the kinetic energy is presented, which form the basis of the frozen-density embedding (FDE) scheme that is the topic of this thesis.

2.1. Quantum mechanics

Molecules consist of nuclei and electrons. The theory that describes such small particles is given by quantum mechanics[a] (for a good text book, see Ref. 14).

For the description of molecules, one usually applies the Born–Oppenheimer approximation and considers the position of the nuclei as fixed, while the electrons are treated quantum mechanically. Since the nuclei are much heavier than the electrons, their movement is usually slower than that of the electrons, and this approximation is, therefore, well justified. Hence, in the following, the nuclei will not be treated quantum mechanically and only systems of electrons, in the field of nuclei at fixed positions, will be considered.

According to quantum mechanics, all information about a given state of a system of electrons is contained in its wave function $\Psi(\boldsymbol{r}_1, s_1, \ldots, \boldsymbol{r}_N, s_N)$, which depends on

---

[a]In this thesis, only nonrelativistic quantum mechanics will be used. However, for systems containing heavy nuclei, one has to apply relativistic quantum mechanics. For details, see, e.g., Refs. 12, 13.

the spatial coordinates r_i and the spin coordinates s_i (for electrons, these can only take the values $+\frac{1}{2}$ and $-\frac{1}{2}$) of all N electrons. For reasons of simplicity, the wave function is usually chosen to be normalized, i.e.,

$$\langle \Psi | \Psi \rangle = |\Psi|^2 = \int \cdots \int \Psi^* \Psi \, d\boldsymbol{r_1} ds_1 \cdots d\boldsymbol{r}_N ds_N = 1. \tag{2.1}$$

Any wave function can be normalized by multiplication with the factor $1/\sqrt{|\Psi|^2}$.

For any measurable physical property of the system exists a corresponding Hermitian operator $\hat{O}$. In a measurement, only eigenvalues of this operator can be obtained, i.e., only values x_i for which there exists a wave function Ψ_i such that

$$\hat{O}\Psi_i = x_i \Psi_i. \tag{2.2}$$

Because of the hermiticity of $\hat{O}$, a given wave function Ψ can (in the case of a discrete spectrum[b]) be expressed as a linear combination of these (normalized) eigenfunctions Ψ_i, which form a complete and orthonormal set, as

$$\Psi = \sum_i c_i \Psi_i, \tag{2.3}$$

where the coefficients c_i can be obtained from $c_i = \langle \Psi | \Psi_i \rangle$. The probability that a measurement leads to the result x_i is then given by

$$|c_i|^2 = |\langle \Psi | \Psi_i \rangle|^2. \tag{2.4}$$

If the system is in the corresponding eigenstate Ψ_i of $\hat{O}$, this probability is 1 and any measurement will result in the value x_i.

For an arbitrary state described by the wave function Ψ, the expectation value of $\hat{O}$ is given by

$$\left\langle \hat{O} \right\rangle = \langle \Psi | \hat{O} | \Psi \rangle = \int \cdots \int \Psi^* \hat{O} \Psi \, d\boldsymbol{r_1} ds_1 \cdots d\boldsymbol{r}_N ds_N \tag{2.5}$$

It should be noted that this expectation value is the average value that would be obtained from a large number of measurements. If it is not an eigenvalue of $\hat{O}$, the expectation value itself will never be obtained in any measurement.

The position operator of the first electron is given by $\hat{\boldsymbol{r}}_1 = \boldsymbol{r}_1$. This operator has a continuous spectrum, i.e., any value of $\boldsymbol{r}_1$ is an eigenvalue, and the eigenfunctions are given by the Dirac delta functions $\delta(\boldsymbol{r}_1 - \boldsymbol{r'}_1)$. Therefore, the probability density for finding an electron at the position $\boldsymbol{r}$ (because the electrons are indistinguishable, this

---

[b]The generalization to operators with a continuous spectrum is straightforward, see Ref. 14.

is N-times the probability density for finding the first electron at this position, where N is the number of electrons) is

$$
\begin{aligned}
\rho(\boldsymbol{r}) &= N \mid \langle \Psi | \delta(\boldsymbol{r}_1 - \boldsymbol{r}) \rangle \mid^2 \\
&= N \left| \int \cdots \int \Psi^*(\boldsymbol{r_1}, s_1, \ldots, \boldsymbol{r}_N, s_N) \delta(\boldsymbol{r}_1 - \boldsymbol{r}) \, d\boldsymbol{r_1} ds_1 \cdots d\boldsymbol{r}_N ds_N \right|^2 \\
&= N \int \cdots \int |\Psi(\boldsymbol{r}, s_1, \ldots, \boldsymbol{r}_N, s_N)|^2 \, ds_1 \cdots d\boldsymbol{r}_N ds_N.
\end{aligned} \tag{2.6}
$$

This probability density of finding an electron at position $\boldsymbol{r}$ is usually referred to as "electron density". The probability P of finding an electron in the volume element $x \in [x_1, x_2], y \in [y_1, y_2], z \in [z_1, z_2]$ can be calculated as

$$
P = \int_{x_1}^{x_2} \int_{y_1}^{y_2} \int_{z_1}^{z_2} \rho(\boldsymbol{r}) \, dx dy dz. \tag{2.7}
$$

The momentum operator for the first electron is in atomic units[c] given by $\hat{p_1} = -i\nabla_1$, where the subscript 1 indicates that the derivative is only taken with respect to the coordinates $\boldsymbol{r}_1$ of the first electron. This operator also has a continuous spectrum, and its eigenfunctions are given by the plane waves $e^{-i\boldsymbol{p}\cdot\boldsymbol{r}}$. Therefore, the probability density for finding an electron with momentum $\boldsymbol{p}$ can be obtained from the Fourier transformation of the wave function.

All other operators can be obtained in terms of the position operator $\hat{\boldsymbol{r}} = \boldsymbol{r}$ and the momentum operator $\hat{p} = -i\nabla$. For instance, the kinetic energy operator is

$$
\hat{T} = \sum_{k=1}^{N} \frac{\hat{\boldsymbol{p}_k}^2}{2m_e} = -\sum_{k=1}^{N} \frac{\nabla_k^2}{2}, \tag{2.8}
$$

and, therefore, the expectation value of the kinetic energy is

$$
T = -\left\langle \Psi \left| \sum_{k=1}^{N} \frac{\nabla_k^2}{2} \right| \Psi \right\rangle = -\int \cdots \int \Psi^* \left(\sum_{k=1}^{N} \frac{\nabla_k^2}{2} \right) \Psi \, d\boldsymbol{r_1} ds_1 \cdots d\boldsymbol{r}_N ds_N. \tag{2.9}
$$

For molecules, one is usually interested in the stationary states, i.e., states with a constant energy. Of special interest is the stationary state with the lowest energy, the ground state of the system. These can be obtained by solving the time-independent Schrödinger equation

$$
\hat{H}\Psi_i = E_i\Psi_i, \tag{2.10}
$$

---

[c]In atomic units, the electron mass $m_e = 1$, the charge of the electron $e = 1$, $\hbar = 1$, and the Bohr length $a_0 = \frac{4\pi\epsilon_0 \ \hbar^2}{m_e e^2} = 1$. These atomic units will be used throughout this thesis.

where $\hat{H}$ is the Hamiltonian of the system, which is the operator corresponding to the total energy. The wave functions Ψ_i and the corresponding energies E_i of the stationary states are given by the eigenfunctions and eigenvalues, respectively, of this Schrödinger equation. The ground state is described by the wave function Ψ_0, which is the eigenfunction corresponding to the lowest eigenvalue E_0.

For a molecule in the absence of any external fields, the electronic Hamiltonian is

$$\hat{H} = -\sum_{k=1}^{N} \frac{\nabla_k^2}{2} - \sum_{k=1}^{N} \sum_{A=1}^{N_{nuc}} \frac{Z_A}{|\boldsymbol{r}_k - \boldsymbol{R}_A|} + \sum_{k=1}^{N} \sum_{l=k+1}^{N} \frac{1}{|\boldsymbol{r}_k - \boldsymbol{r}_l|}, \tag{2.11}$$

where $\boldsymbol{r}_i$ is the spatial coordinate of the ith electron, and $\boldsymbol{R}_A$ and Z_A are the coordinates and charges of the nuclei, respectively. The first term in the Hamiltonian is the kinetic energy operator, while the remaining two terms are the potential energy operator. The second term arises due to the attraction of the nuclei and the electrons, and the third term is due to the electron–electron repulsion.

To solve the Schrödinger equation for the ground-state wave function, the variational principle can be employed. It states that for any trial wave function $\tilde{\Psi}$,

$$\tilde{E}[\tilde{\Psi}] = \left\langle \tilde{\Psi} \middle| \hat{H} \middle| \tilde{\Psi} \right\rangle \geq E_0, \tag{2.12}$$

and that equality only holds for the exact ground-state wave function Ψ_0. Hence, the ground-state energy E_0 and wave function Ψ_0 can be obtained from the minimization

$$E_0 = \min_{\tilde{\Psi}} \tilde{E}[\tilde{\Psi}] = \min_{\tilde{\Psi}} \left\langle \tilde{\Psi} \middle| \hat{H} \middle| \tilde{\Psi} \right\rangle, \tag{2.13}$$

where the minimization runs over all allowed trial wave functions $\tilde{\Psi}$.

The space of "allowed wave functions" is defined by the Pauli principle, which states that for many-electron systems, the wave function has to be antisymmetric with respect to the exchange of two electrons, i.e.,

$$\Psi(\ldots, \boldsymbol{r}_i, s_i, \ldots, \boldsymbol{r}_j, s_j, \ldots) = -\Psi(\ldots, \boldsymbol{r}_j, s_j, \ldots, \boldsymbol{r}_i, s_i, \ldots). \tag{2.14}$$

The simplest ansatz for such an antisymmetric wave function is a Slater determinant, i.e., a wave function of the form

$$\Psi(\boldsymbol{r}_1, s_2, \ldots, \boldsymbol{r}_N, s_N) = \frac{1}{\sqrt{N!}} \begin{vmatrix} \phi_1(\boldsymbol{r}_1, s_1) & \phi_2(\boldsymbol{r}_1, s_1) & \ldots & \phi_N(\boldsymbol{r}_1, s_1) \\ \phi_1(\boldsymbol{r}_2, s_2) & \phi_2(\boldsymbol{r}_2, s_2) & \ldots & \phi_N(\boldsymbol{r}_2, s_2) \\ \vdots & \vdots & & \vdots \\ \phi_1(\boldsymbol{r}_N, s_N) & \phi_2(\boldsymbol{r}_N, s_N) & \ldots & \phi_N(\boldsymbol{r}_N, s_N) \end{vmatrix}, \tag{2.15}$$

where the $\{\phi_i\}$ are a set of orthonormal one-electron functions (orbitals). The chosen form of a determinant ensures the antisymmetry with respect to the exchange of two electrons.

If one performs the minimization of Eq. (2.13) only for wave functions that have the form of a single Slater determinant, this leads to the Hartee-Fock method (for details, see Refs. 15, 16). However, as this search space does not contain all possible wave functions, the Hartee-Fock method only provides an approximate ground-state energy, that is an upper bound to the correct ground-state energy, and an approximate wave function.

To obtain a better approximation, one has to use a linear combination of Slater determinants as ansatz for the trial wave function in Eq. (2.13). Performing this minimization for different expansions of the trial wave function in Slater determinants is the starting point of almost any post-Hartee-Fock wave function based method in quantum chemistry.

2.2. Density-functional theory

2.2.1. Hohenberg–Kohn theorem

The variational principle in combination of the expansion of the wave function in terms of Slater determinants offers a possible strategy for the determination of the ground-state wave function. However, this is still an extremely complicated problem. The wave function is a function of the $3N$ spatial coordinates of the electrons[d], and the space of allowed wave functions is—for systems with more than a few electrons—of an enormous size (the number of possible Slater determinants grows factorially with the number of considered orbitals).

In density-functional theory (for text books, see Refs. 3, 17), the complexity of this problem is reduced by considering the electron density

$$\rho(\boldsymbol{r}) = \int \cdots \int |\Psi(\boldsymbol{r}, \boldsymbol{r}_2, \ldots, \boldsymbol{r}_N)|^2 \; d\boldsymbol{r}_2 \cdots d\boldsymbol{r}_N \tag{2.16}$$

instead of the wave function $\Psi(\boldsymbol{r}_1, \ldots, \boldsymbol{r}_N)$. The electron density is a function of only three coordinates and is, therefore, a much simpler quantity than the wave function.

The theoretical justification for such a treatment is given by the Hohenberg–Kohn theorem.[18] Its first part states that there exists a one-to-one mapping between the

---

[d]For reasons of simplicity, in the following only the closed-shell case with N doubly occupied orbitals will be considered and the spin coordinate will, therefore, not be included.

Figure 2.1.: Illustration of the connection between the ground-state electron density and the total energy as given by the first part of the Hohenberg-Kohn theorem.

$$\rho(\boldsymbol{r}) \quad \overset{HK}{\longleftrightarrow} \quad v_{\text{ext}} \quad \longrightarrow \quad \hat{H} \quad \overset{SE}{\longrightarrow} \quad \Psi(\boldsymbol{r}_1, \ldots, \boldsymbol{r}_N) \quad \longrightarrow \quad E_0$$

external potential v_{ext} (in the case of molecules, the potential of the nuclei) and the ground-state electron density $\rho_0(\boldsymbol{r})$. This implies that from a given ground-state electron density $\rho_0(\boldsymbol{r})$, the corresponding external potential can be uniquely determined. With the knowledge of the external potential, the complete Hamiltonian of the system is known, and the wave function and with it all other properties of the system can—in principle—be determined. This connection between the ground-state electron density, the external potential, and the wave function is illustrated in Fig. 2.1.

Therefore, any property of a system of electrons can—in principle—be calculated from its ground-state electron density, since the ground-state wavefunction is given as a functional $\Psi_0[\rho]$ of the electron density. This establishes for a given external potential v_{ext} the existance of a density functional

$$E_v[\rho] = \left\langle \Psi_0[\rho] \left| \hat{T} + v_{\text{ext}} + \hat{V}_{\text{ee}} \right| \Psi_0[\rho] \right\rangle, \tag{2.17}$$

which provides an energy for any trial density in this external potential.

The second part of the Hohenberg–Kohn theorem provides a variational principle for the electron density. For any density ρ, the energy functional $E_v[\rho]$ will lead to an energy that is larger or equal to the ground-state energy, i.e.,

$$E_v[\rho] \geq E_0 \quad \forall \rho. \tag{2.18}$$

Equality only holds for the correct ground-state density ρ_0,

$$E_v[\rho] = E_0 \quad \text{only for} \quad \rho = \rho_0. \tag{2.19}$$

Therefore, the ground-state energy and the ground-state density ρ_0 can be calculated by minimizing the total-energy functional $E_v[\rho]$, i.e.,

$$E_0 = \min_\rho E_v[\rho], \tag{2.20}$$

where the search space includes all densities that correspond to an antisymmetric N-electron wave function. This search space is much smaller than that of all antisymmetric wave functions, thus simplifying the initial problem considerably.

2.2.2. The total energy functional

Even though the Hohenberg–Kohn theorem establishes the existence of a total-energy functional $E_v[\rho]$, the explicit form of this functional is unknown. In order to find suitable approximations, the total energy functional is usually decomposed into different contributions,

$$
\begin{aligned}
E_v[\rho] &= T[\rho] + V_{\mathrm{ne}}[\rho] + V_{\mathrm{ee}}[\rho] \\
&= T[\rho] + V_{\mathrm{ne}}[\rho] + J[\rho] + V_{ee}^{\mathrm{nonclassical}}[\rho].
\end{aligned}
\tag{2.21}
$$

In this expression, $T[\rho]$ is the (interacting) kinetic energy, $V_{\mathrm{ne}}[\rho]$ is the electrostatic attraction of the electrons and the nuclei, which is given by

$$
V_{ne}[\rho] = \int v_{\mathrm{nuc}}(\boldsymbol{r})\rho(\boldsymbol{r})d\boldsymbol{r},
\tag{2.22}
$$

and $V_{\mathrm{ee}}[\rho]$ is the electron-electron repulsion energy. The latter can be further decomposed into the classical Coulomb repulsion of the electron cloud, i.e.,

$$
J[\rho] = \int \frac{\rho(\boldsymbol{r})\rho(\boldsymbol{r}')}{|\boldsymbol{r} - \boldsymbol{r}'|}d\boldsymbol{r}d\boldsymbol{r}',
\tag{2.23}
$$

and the remaining nonclassical repulsion energy $V_{\mathrm{ee}}^{\mathrm{nonclassical}}[\rho]$.

While both the nuclear–electron attraction $V_{\mathrm{ne}}[\rho]$ and the Coulomb repulsion $J[\rho]$ can be calculated explicitly in terms of the electron density, the explicit form of the density functionals of the kinetic energy $T[\rho]$ and of the nonclassical electron–electron repulsion energy $V_{\mathrm{ee}}^{\mathrm{nonclassical}}[\rho]$ are not known. The (interacting) kinetic-energy functional is given by

$$
T[\rho] = -\frac{1}{2}\left\langle \Psi \left| \sum_{i=1}^{N} \nabla_i^2 \right| \Psi \right\rangle,
\tag{2.24}
$$

and the nonclassical electron–electron repulsion is given by

$$
V_{\mathrm{ee}}^{\mathrm{nonclassical}}[\rho] = \sum_{i=1}^{N}\sum_{j=i+1}^{N} \left\langle \Psi \left| \frac{1}{|\boldsymbol{r}_i - \boldsymbol{r}_j|} \right| \Psi \right\rangle - J[\rho]
\tag{2.25}
$$

where the wave function Ψ can be obtained from ρ according to the Hohenberg–Kohn theorem. However, in density-functional theory one tries to avoid this calculation of the wave function.

2.2.3. The noninteracting reference system

In order to simplify the calculation of the kinetic-energy functional, Kohn and Sham proposed to approximate the kinetic energy by introducing a reference system of noninteracting electrons.[19] The external potential v_s of this noninteracting reference system is chosen such that its electron density ρ is equal to the electron density of the original, interacting system. The Hamiltonian of this noninteracting reference system is given by

$$H = -\sum_{i=1}^{N} \frac{\nabla_i^2}{2} + \sum_{i=1}^{N} v_s(\boldsymbol{r}_i), \tag{2.26}$$

and the wave function solving the corresponding Schrödinger equation is given by a single Slater determinant consisting of the orbitals $\{\phi_i\}$, which are the solutions corresponding to the N lowest eigenvalues of the one-electron equations

$$\left[-\frac{\nabla^2}{2} + v_s(\boldsymbol{r}) \right] \phi_i(\boldsymbol{r}) = \epsilon_i \phi_i(\boldsymbol{r}) \quad i = 1, \dots, N. \tag{2.27}$$

The kinetic energy T_s of this noninteracting reference system[e] can be calculated easily from the orbitals ϕ_i as

$$T_s = -\frac{1}{2} \sum_{i=1}^{N} \int \phi_i^*(\boldsymbol{r}) \nabla^2 \phi_i(\boldsymbol{r}) \; d\boldsymbol{r}. \tag{2.28}$$

By introducing this noninteracting kinetic energy T_s, the total energy functional of Eq. (2.21) can be written as

$$\begin{aligned} E_v[\rho] &= T_s[\rho] + T_c[\rho] + V_{\text{ne}}[\rho] + J[\rho] + V_{ee}^{\text{nonclassical}}[\rho] \\ &= T_s[\rho] + V_{\text{ne}}[\rho] + J[\rho] + E_{xc}[\rho], \end{aligned} \tag{2.29}$$

where $T_c[\rho] = T[\rho] - T_s[\rho]$ is defined as the difference between the interacting and the noninteracting kinetic energy. This difference is usually included in the exchange-correlation energy,

$$E_{xc}[\rho] = V_{ee}^{\text{nonclassical}}[\rho] + T_c[\rho]. \tag{2.30}$$

It has to be stressed that the total energy functional given above is still an exact functional because even though the exact interacting kinetic energy has been replaced by the noninteracting kinetic energy, this difference has been included in $E_{xc}[\rho]$.

The introduction of the noninteracting reference system and its kinetic energy makes it possible to calculate T_s, the largest part of the kinetic energy, exactly so that only the much smaller exchange-correlation energy E_{xc} has to be approximated.

---

[e]The subscript s stands for "single-particle".

2.2.4. The exchange-correlation energy

The explicit form of the exchange-correlation energy functional is not know and, therefore, this functional has to be approximated. There is no generally applicable strategy for developing approximate exchange-correlation functionals, but a number of approximations are available. However, there is no systematic way of improving an existing approximation.

The simplest approximate exchange-correlation functional is the local density approximation (LDA). To derive the LDA, one considers a large number N of electrons in a cube of volume $V = l^3$, in which a positive charge is uniformly spread to compensate the negative charge of the electrons. If one takes the limit $N \to \infty$ and $V \to \infty$, while the density $\rho = N/V$ is kept finite, one obtains the model of the uniform electron gas.

The exchange-correlation energy density $\epsilon_{xc}^{\mathrm{uniform}} = E_{xc}^{\mathrm{uniform}}/V$ of the uniform electron gas with density ρ has been calculated accurately using quantum Monte-Carlo calculations by Ceperley and Alder.[20] Using these results, it is possible to obtain an expression for $\epsilon_{xc}^{\mathrm{uniform}}(\rho)$ in terms of the electron density. By applying this exchange-correlation energy density also for systems with a non-uniform electron density,

$$E_{xc}^{\mathrm{LDA}}[\rho] = \int \epsilon_{xc}^{\mathrm{uniform}}(\rho(\boldsymbol{r}))\rho(\boldsymbol{r})d\boldsymbol{r}, \tag{2.31}$$

one obtains the LDA exchange-correlation functional. Surprisingly, this LDA functional performs extremely well also for systems that are far from a uniform electron density distribution, such as atoms and molecules.

This local-density approximation can be improved by also considering the gradient of the density $\nabla\rho$. This leads to the generalized gradient approximation (GGA), in which—in the most general form—the exchange-correlation energy is approximated as

$$E_{xc}^{\mathrm{GGA}}[\rho, \nabla\rho] = E_{xc}^{\mathrm{LDA}}[\rho] + \int \rho(\boldsymbol{r})^{\frac{4}{3}} F(\rho(\boldsymbol{r}), \nabla\rho(\boldsymbol{r}))d\boldsymbol{r}, \tag{2.32}$$

where $F(\rho, \nabla\rho)$ is an enhancement factor depending on the density and its gradient. Usually, the exchange-correlation functional is split up into an exchange part E_x and a correlation part E_c, which are approximated separately. Popular exchange functionals include the functional of Becke[21] and of Perdew and Wang,[22] and for the correlation part, the functionals of Perdew,[23] and of Lee, Yang, and Parr[24] are widely used.

There are a number of more general approaches going beyond GGA functionals. In meta-GGA functionals, not only the density and its gradient, but also the kinetic-energy density τ, which depends on the second derivative of the density, is used as an additional variable.[25] Going even further, functionals that additionally addition

depend on the occupied or even on the virtual orbitals have been proposed (see, e.g., Refs. 26–28). Often, this is referred to as "Jacob's ladder", on which the exact exchange-correlation functional is reached by going to the next step on this ladder. However, in many cases the hierarchy of the different approximations is not that clear.

2.3. The kinetic energy in DFT

In Kohn–Sham DFT, the true, interacting kinetic energy $T[\rho] = \left\langle \Psi \left| \hat{T} \right| \Psi \right\rangle$ [cf. Eq. (2.24)], is approximated by the kinetic energy $T_s[\rho]$ of a noninteracting reference system with the same electron density, while the remainder $T_c[\rho]$ is included in the exchange-correlation energy. This leads to a decomposition of the total energy functional given in Eq. (2.29).

In this total-energy functional, the noninteracting kinetic-energy T_s has been expressed as a functional of the electron density ρ, even though it explicitly depends on the orbitals of the noninteracting reference system. This density functional has to be understood as follows: For a given electron density ρ, it is assumed that a noninteracting reference system with the same electron density ρ exists, i.e., that the density is v_s-representable. In this case the given density defines—according to the Hohenberg–Kohn theorem—the corresponding potential v_s. This potential defines the orbitals of the noninteracting reference system, from which the kinetic energy can be calculated. Thus, T_s is an implicit functional of the density ρ.

Another definition of T_s can be obtained within the Levy constrained-search formulation[17,29,30] of DFT, by defining

$$\tilde{T}_s[\rho] = \min_{\Psi \to \rho} \left\langle \Psi \left| \hat{T} \right| \Psi \right\rangle, \tag{2.33}$$

where the minimization is such that only antisymmetric wave functions yielding the electron density ρ are considered. This definition is more general than the definition given above, because it is not limited to v_s-representable densities, but it can be applied for any density that can be represented by an antisymmetric wave function.

It remains to be shown that for v_s-representable densities this definition is identical to the definition given above, i.e., that $\tilde{T}_s[\rho]$ is equal to the kinetic energy of the noninteracting reference system with density ρ. For this purpose, one considers the Schrödinger equation of this reference system, with the Hamiltonian given in Eq. (2.26). According to the variational principle, its ground-state energy E_s and wave function can be determined from

$$E_s = \min_{\Psi} \left\langle \Psi \left| \hat{T} + \sum_{i=1}^{N} v_s(\boldsymbol{r}_i) \right| \Psi \right\rangle. \tag{2.34}$$

Since the density ρ corresponding to the wave function is known, the minimization can be restricted to wave functions that yield this density, i.e.,

$$E_s[\rho] = \min_{\Psi \to \rho} \left\langle \Psi \left| \hat{T} \right| \Psi \right\rangle + \int v_s(\boldsymbol{r}) \rho(\boldsymbol{r}) d\boldsymbol{r}, \tag{2.35}$$

and therefore,

$$T_s[\rho] = E_s[\rho] - \int v_s(\boldsymbol{r}) \rho(\boldsymbol{r}) d\boldsymbol{r} = \min_{\Psi \to \rho} \left\langle \Psi \left| \hat{T} \right| \Psi \right\rangle \tag{2.36}$$

Since it is known that for the noninteracting reference system the ground-state wave function is a single Slater determinant, the search can be further constrained to single-determinant wave functions Ψ_D yielding the density ρ,

$$
\begin{aligned}
T_s[\rho] &= \min_{\Psi_D \to \rho} \left\langle \Psi \left| \hat{T} \right| \Psi \right\rangle \\
&= \min_{\sum_i |\phi_i|^2 = \rho} \sum_{i=1}^{N} \int \phi_i^*(\boldsymbol{r}) \left(\frac{-\nabla^2}{2} \right) \phi_i(\boldsymbol{r}) \; d\boldsymbol{r}.
\end{aligned}
\tag{2.37}
$$

For v_s-representable densities, this definition is equivalent to those given earlier, but it is also applicable for any N-representable density, i.e., for any density that can be expressed as a sum of the square of N orbitals.

However, even though the above definition is theoretically very useful, it does not make the practical evaluation of $T_s[\rho]$ any easier. Performing the constrained minimization of Eq. (2.37) using Lagrange minimization leads to the initial problem of determining the potential v_s yielding the density ρ (see Ref. 17, page 151). In the following, different strategies for handling the noninteracting kinetic energy T_s in practical calculations of the ground-state density will be discussed.

2.3.1. Kohn–Sham DFT

The ground-state density can be determined by minimizing the total-energy functional given above in Eq. (2.29). To ensure that only electron densities are considered that correspond to an antisymmetric N-electron wave function, one has to introduce the constraint that the electron density integrates to the correct number of electrons. In addition, it has to be made sure that the electron density is positive or zero at any point in space (i.e., $\rho(\boldsymbol{r}) \geq 0 \; \forall \boldsymbol{r}$). The following derivation of the KS equations is similar to the one given by van Leeuwen.[31]

The Lagrange minimization of the total-energy functional under the constraint that the number of electrons N is conserved (the positivity of the density will be ensured

2. DFT and the kinetic energy

at a later point) leads to the condition

$$0 = \frac{\delta}{\delta\rho}\left[E_v[\rho] - \mu\left(\int \rho(\boldsymbol{r})d\boldsymbol{r} - N\right)\right]$$
$$= \frac{\delta T_s[\rho]}{\delta\rho} + v_{\text{nuc}}(\boldsymbol{r}) + \int \frac{\rho(\boldsymbol{r'})}{|\boldsymbol{r} - \boldsymbol{r}|}d\boldsymbol{r'} + \frac{\delta E_{xc}[\rho]}{\delta\rho} - \mu. \tag{2.38}$$

However, the functional derivative of the kinetic-energy cannot be evaluated directly, since the evaluation of the kinetic-energy functional requires the knowledge of the orbitals of the corresponding noninteracting reference system.

According to the Hohenberg–Kohn theorem, the same density can alternatively be obtained by minimizing the total-energy functional of the noninteracting reference system,

$$E_s[\rho] = T_s[\rho] + \int \rho(\boldsymbol{r})v_s(\boldsymbol{r}) \ d\boldsymbol{r}, \tag{2.39}$$

under the constraint that the density contains the correct number of electrons. This minimization leads to the condition

$$0 = \frac{\delta}{\delta\rho}\left[E_s[\rho] - \mu\left(\int \rho(\boldsymbol{r})d\boldsymbol{r} - N\right)\right] = \frac{\delta T_s[\rho]}{\delta\rho} + v_s(\boldsymbol{r}) - \mu, \tag{2.40}$$

where the potential v_s, that leads to the correct density in the noninteracting reference system, is still unknown.

Comparing Eq. (2.38) with Eq. (2.40), one obtains for the ground-state density ρ_0,

$$v_s(\boldsymbol{r}) = v_{\text{nuc}}(\boldsymbol{r}) + \int \frac{\rho_0(\boldsymbol{r'})}{|\boldsymbol{r} - \boldsymbol{r}|}d\boldsymbol{r'} + \left.\frac{\partial E_{xc}[\rho]}{\partial\rho}\right|_{\rho=\rho_0}. \tag{2.41}$$

Therefore, the orbitals of the noninteracting reference system corresponding to the ground-state density can be obtained as solutions of the KS equations [cf. Eq. (2.27)]

$$\left[-\frac{\nabla^2}{2} + v_{\text{eff}}^{\text{KS}}[\rho](\boldsymbol{r})\right]\phi_i(\boldsymbol{r}) = \epsilon_i \ \phi_i(\boldsymbol{r}) \quad ; \quad i = 1, \ldots, N, \tag{2.42}$$

where the effective potential[f]

$$v_{\text{eff}}^{\text{KS}}[\rho] = v_{\text{nuc}}(\boldsymbol{r}) + \int \frac{\rho(\boldsymbol{r'})}{|\boldsymbol{r} - \boldsymbol{r}|}d\boldsymbol{r'} + \frac{\partial E_{xc}[\rho]}{\partial\rho} \tag{2.43}$$

---

[f]This effective potential, that is used during the self-consistent solution of the KS equations is labeled $v_{\text{eff}}^{\text{KS}}[\rho]$, to distinguish it from the potential $v_s[\rho]$ of the noninteracting reference system with a given density. Only for the ground-state density ρ_0, these two potentials are identical.

depends on the density $\rho = \sum_{i=1}^{N} |\phi_i|^2$ calculated from the KS orbitals ϕ_i. Hence, these equations have to be solved iteratively. Since the electron density is obtained as the sum of the squared KS orbitals, it is automatically ensured that it is larger or equal zero in all points in space.

An alternative derivation of the KS equations can be given by employing the Levy constrained-search definition of T_s. Using this definition, the minimization of the total-energy functional can be written as a two-step procedure,

$$E_0 = \min_{\rho} \left(\min_{\sum_i |\phi_i|^2 = \rho} \left[\sum_{i=1}^{N} \int \phi_i^*(\boldsymbol{r}) \left(\frac{-\nabla^2}{2} \right) \phi_i(\boldsymbol{r}) \ d\boldsymbol{r} \right] + V_{\text{ne}}[\rho] + J[\rho] + E_{xc}[\rho] \right),$$
(2.44)

where the outer minimization runs over all positive densities that integrate to the correct number of electrons, while the inner minimization exploits all single-determinant wave functions that yield a given density.

Since a search over all single-determinantal wave functions will automatically exploit all allowed electron densities, the minimization over ρ can be eliminated and one obtains,

$$E_0 = \min_{\phi_i} \left(\sum_{i=1}^{N} \int \phi_i^*(\boldsymbol{r}) \left(\frac{-\nabla^2}{2} \right) \phi_i(\boldsymbol{r}) \ d\boldsymbol{r} + V_{\text{ne}}[\rho] + J[\rho] + E_{xc}[\rho] \right)$$
$$= \min_{\phi_i} \left(T_s[\{\phi_i\}] + V_{\text{ne}}[\rho] + J[\rho] + E_{xc}[\rho] \right) = \min_{\phi_i} E[\{\phi_i\}].$$
(2.45)

This means that the total-energy density functional has been converted to a functional of the KS orbitals, and the determination of the electron density has been recast to a minimization with respect to these KS orbitals.

The minimization of $E[\{\phi_i\}]$ with respect to the KS orbitals under the constraint that these orbitals are orthonormal, leads to the condition,

$$0 = \frac{\delta}{\delta \phi_i^*} \left[E[\{\phi_i\}] - \sum_{j=1}^{N} \lambda_{ij} \left(\int \phi_i^*(\boldsymbol{r}) \phi_i(\boldsymbol{r}) d\boldsymbol{r} - \delta_{ij} \right) \right],$$
(2.46)

from which the KS equations can be obtained (for details, see the similar derivation of the Hartee–Fock equations in Ref. 16).

To solve the KS equations in practice, the KS orbitals are expanded in basis function,

$$\phi_i(\boldsymbol{r}) = \sum_{j=1}^{M} C_{ij} \chi_j(\boldsymbol{r}),$$
(2.47)

where χ_i are the basis functions, and the matrix $\boldsymbol{C}$ contains the expansion coefficients. For molecular systems, usually atom-centered Slater or Gaussian functions are used as basis functions, while for solid state and condensed phase systems under periodic boundary conditions, plane waves are employed.

With the overlap matrix $\boldsymbol{S}$,

$$S_{ij} = \int \chi_i^*(\boldsymbol{r})\chi_j(\boldsymbol{r})d\boldsymbol{r}, \tag{2.48}$$

and the Fock matrix $\boldsymbol{F}$

$$F_{ij} = \int \chi_i^*(\boldsymbol{r}) \left(\frac{-\nabla^2}{2} + v_{\text{eff}}^{\text{KS}}[\rho] \right) \chi_j(\boldsymbol{r})d\boldsymbol{r}, \tag{2.49}$$

the KS equations can, in the chosen basis set, be written as a generalized matrix eigenvalue problem,

$$\boldsymbol{FC} = \boldsymbol{SC\epsilon}, \tag{2.50}$$

where the diagonal matrix $\boldsymbol{\epsilon}$ contains the orbitals energies ϵ_i. By transforming this problem to an orthonormal basis, and then diagonalizing the transformed Fock matrix $\boldsymbol{F'}$, the expansion coefficients $\boldsymbol{C}$ can be calculated. Using these KS orbitals, a new Fock matrix is constructed, and this procedure is repeated iteratively until self-consistency is reached.

The Kohn–Sham formalism provides a practical scheme for DFT calculations. By introducing the orbitals of the noninteracting reference system, the noninteracting kinetic energy T_s can be treated exactly, while approximations are only introduced for the exchange-correlation energy, which has to be calculated using an approximate density functional. In combination with suitable exchange-correlation functionals, the KS-DFT scheme has been applied to a huge number of problems. Because of its good compromise between accuracy and efficiency—especially when compared to wave function based methods—it is one of the most successful methods in quantum chemistry.

However, the exact treatment of T_s comes at a price. While according to the Hohenberg–Kohn theorem, the wave function (a complicated function of $3N$ variables) can be replaced by the electron density (a function of only three variables), in the KS formalism a wave function is introduced. Even though in the KS case this wave function is of the simple form of a single Slater determinant, this requires the calculation of N orbitals (each a function of three variables), instead of only the electron density. In particular, the requirement that these orbitals are orthogonal, leads to the form of an eigenvalue problem, which requires a diagonalization step which is expensive for large systems.

2.3.2. Orbital-free DFT

In an orbital-free (OF) DFT scheme, the calculation of a wave function of the noninteracting reference system is completely avoided. This leads to a scheme that is much more efficient, since only the density itself has to be determined, but no orbitals have to be calculated and no diagonalization step is needed.

However, such a pure density-functional theory requires the knowledge of the kinetic-energy functional $T_s[\rho]$ in terms of the density only. Since the explicit form of this functional is not known, an approximate functional has to be used for $T_s[\rho]$. This means that not only the exchange-correlation energy is treated approximately, but that additional approximations have to be introduced for the kinetic energy. Different approximate orbital-free kinetic-energy functionals will be discussed in the following section.

In such an OF-DFT scheme, the density can be determined by minimizing the total-energy functional of Eq. (2.29) with respect to ρ, under the constraint that it integrates to the correct number of electrons and that the density is positive or zero at every point in space. This leads to the condition,

$$0 = \frac{\delta}{\delta\rho}\left[E[\rho] - \mu\left(\int \rho(\boldsymbol{r})d\boldsymbol{r} - N\right)\right] = \frac{\delta T_s[\rho]}{\delta\rho} + v_{\text{eff}}^{\text{KS}}[\rho] - \mu$$

$$\Rightarrow \mu = \frac{\delta T_s[\rho]}{\delta\rho} + v_{\text{eff}}^{\text{KS}}[\rho], \tag{2.51}$$

where the Lagrange multiplier μ can be identified with the orbital energy of the highest occupied KS orbital.[32] From the solution of this equation, the ground-state electron density can be obtained.

To ensure the positivity of the electron density, one can introduce a pseudo-orbital ϕ which is used as a new variational variable, and express the density as

$$\rho(\boldsymbol{r}) = \phi(\boldsymbol{r})^2. \tag{2.52}$$

By separating the kinetic-energy functional into a von Weizsäcker part (see below for details on this functional) and a remaining part,

$$T_s[\rho] = \frac{1}{8}\int \frac{|\nabla\rho(\boldsymbol{r})|^2}{\rho(\boldsymbol{r})}d\boldsymbol{r} + T_X[\rho] = \frac{1}{2}\int \nabla\phi(\boldsymbol{r})\nabla\phi(\boldsymbol{r})d\boldsymbol{r} + T_X[\rho] \tag{2.53}$$

one can obtain for the functional derivative of the kinetic-energy functional

$$\frac{\delta T_s[\rho]}{\delta\rho} = -\frac{1}{2}\frac{\nabla^2\phi}{\phi} + \frac{\delta T_X[\rho]}{\delta\rho}, \tag{2.54}$$

and this allows it to rewrite Eq. (2.51) as

$$\left(-\frac{1}{2}\nabla^2 + \left.\frac{\delta T_X[\rho]}{\delta \rho}\right|_{\rho=\phi(\boldsymbol{r})^2} + v_{\text{eff}}[\phi^2](\boldsymbol{r}) \right)\phi(\boldsymbol{r}) = \mu\phi(\boldsymbol{r}). \tag{2.55}$$

This equation has a similar form as the KS equation. However, it is only a single equation that has to be solved only for one pseudo-orbital and not for a set of orthogonal KS orbitals. This equation can be solved efficiently using different standard algorithms. Details can be found in section VI.1 of Ref. 33.

But the fact that this equation is similar to the KS equations also allows the simple implementation of OF-DFT in standard KS-DFT codes. By simply introducing the additional term $\frac{\delta T_X[\rho]}{\delta \rho}$ in the KS potential and by adjusting the occupation numbers in such a way that all electrons occupy the orbital with the lowest eigenvalue (which is then the pseudo-orbital of OF-DFT), one can perform OF-DFT calculations. However, even though such an implementation might be interesting for theoretical investigation, such a scheme will also not be more efficient than KS-DFT calculations unless one gets rid of the diagonalization step.

2.3.3. Orbital-free kinetic-energy functionals

For the OF-DFT scheme, an orbital-free kinetic-energy functional is needed, and suitable approximate functionals have to be found. For the exchange-correlation energy, very accurate approximate functionals exist, that can be applied to a wide range of different systems. However, approximating the kinetic energy is much more difficult. For this reason, Kohn and Sham introduced their exact treatment of the noninteracting kinetic energy, which made it for the first time possible to apply density-functional theory to molecules and turned DFT into an accurate and useful method. In the following, different approaches to the approximation of the kinetic-energy using an orbital-free functional will be discussed, and a brief overview of the performance of these functionals in OF-DFT calculations on solids and on molecules will be given.

As described above, one usually tries to approximate the noninteracting kinetic energy T_s using an approximate functional, not the true, interacting kinetic energy T. This has mainly two reasons. First, the difference between T_s and T is included in the exchange-correlation energy, and most approximate exchange-correlation functionals have been developed in such a way that they include this difference. Therefore, approximating T instead of T_s in OF-DFT calculations would also require the development of new exchange-correlation functionals. Second, the noninteracting kinetic-energy has a much simpler definition than the interacting kinetic energy. This makes it in several cases possible to use simpler arguments in the development of approximate functionals.

There are numerous different approaches to the development of approximate kinetic-energy functionals. In the following, a brief overview of the most important and widely used kinetic-energy functionals will be given. A more complete overview can be found in Ref. 33, and extensive information about the theoretical background, including many derivations, is given in Ref. 17.

Thomas-Fermi functional

As for the exchange-correlation energy, also for the kinetic energy the simplest possible approximation is the local-density approximation (LDA), which employs the kinetic-energy density calculated for the uniform electron gas already described in Sec. 2.2.4. As before, one considers a large number N of electrons in a cube of volume $V = l^3$ and takes the limit $N \to \infty$ and $V \to \infty$, while the density $\rho = N/V$ is kept finite. To calculate the noninteracting kinetic-energy T_s, one has to consider a uniform electron gas of noninteracting electrons.

The eigenfunctions (orbitals) of the noninteracting uniform electron gas are given by the plane waves that fit the dimensions of the considered cube,

$$\phi_{\boldsymbol{k}}(\boldsymbol{r}) = \frac{1}{\sqrt{V}} e^{i\boldsymbol{k}\cdot\boldsymbol{r}} \quad \text{with} \quad \boldsymbol{k} = \frac{2\pi}{l}\boldsymbol{n}, \quad n_x, n_y, n_z = 0, \pm 1, \pm 2, \dots, \tag{2.56}$$

with the orbital energies given by

$$E_{\boldsymbol{k}} = \frac{1}{8\pi^2}\boldsymbol{k}^2 \tag{2.57}$$

i.e., the orbital energies are proportional to the magnitude of the wave vector $\boldsymbol{k}$. For a given density ρ, all orbitals with $|\boldsymbol{k}| \leq k_F$ are occupied, where k_F is called the Fermi wave vector.

To calculate the electron density, one has to sum the densities of all occupied orbitals (the factor 2 accounts for the double occupation of the orbitals),

$$\rho(\boldsymbol{r}) = 2 \sum_{|\boldsymbol{k}| \leq k_F} |\phi_{\boldsymbol{k}}(\boldsymbol{r})|^2 = \frac{2}{V} \sum_{|\boldsymbol{k}| \leq k_F} e^{i\boldsymbol{k}\cdot\boldsymbol{r}} e^{-i\boldsymbol{k}\cdot\boldsymbol{r}} = \frac{2}{V} \sum_{|\boldsymbol{k}| \leq k_F} 1. \tag{2.58}$$

In the limit of the uniform electron gas, the sum can be replaced by an integral. In each volume element of volume $\frac{8\pi^3}{V}$, there is one orbital and, therefore, if $\boldsymbol{k}$ is used as integration variable, the integral has to be divided by this volume. One obtains (where it has been used that the integral is the volume of a ball with radius k_F),

$$\rho = \frac{2}{V}\frac{V}{8\pi^3} \int\limits_{|\boldsymbol{k}| \leq k_F} d\boldsymbol{k} = \frac{1}{4\pi^3} \int\limits_{|\boldsymbol{k}| \leq k_F} d\boldsymbol{k} = \frac{1}{4\pi^3}\frac{4\pi}{3}k_F^3 = \frac{1}{3\pi^2}k_F^3 \tag{2.59}$$

$$\Rightarrow \quad k_F = \left(3\pi^2\rho\right)^{1/3}. \tag{2.60}$$

2. DFT and the kinetic energy

The kinetic energy of one of the doubly occupied orbitals is given by

$$T_s(\boldsymbol{k}) = -\frac{1}{V} \int\limits_V e^{-i\boldsymbol{k}\cdot\boldsymbol{r}} \nabla^2 e^{i\boldsymbol{k}\cdot\boldsymbol{r}} d\boldsymbol{r} = -\frac{1}{V} \int\limits_V e^{-i\boldsymbol{k}\cdot\boldsymbol{r}} (-\boldsymbol{k}^2) e^{i\boldsymbol{k}\cdot\boldsymbol{r}} d\boldsymbol{r} = \boldsymbol{k}^2. \qquad (2.61)$$

and the total kinetic-energy density can be obtained by summing over the kinetic energies of all occupied orbitals and dividing by the volume of the considered cube,

$$t_s = \sum_{\boldsymbol{k} \ occ.} \frac{T_s(\boldsymbol{k})}{V} = \frac{1}{V} \sum_{\boldsymbol{k} \ occ.} \boldsymbol{k}^2. \qquad (2.62)$$

As above, in the limit of the electron gas this sum can be replaced by an integral (taking into account that in $\boldsymbol{k}$-space, there is one orbital in a volume of $\frac{8\pi^3}{V}$), and the integral is performed in spherical coordinates,

$$t_s = \frac{1}{V} \frac{V}{8\pi^3} \int\limits_{\boldsymbol{k} \ occ.} \boldsymbol{k}^2 d\boldsymbol{k} = \frac{1}{8\pi^3} \int_0^{k_F} \int_0^\pi \int_0^{2\pi} k^4 dk \sin\theta d\theta d\phi = \frac{1}{10\pi^2} k_F^5 \qquad (2.63)$$

By making use of the relationship between ρ and k_F obtained above, one obtains the kinetic-energy density t_s of the noninteracting electron gas in terms of the density,

$$t_s(\rho) = \frac{1}{10\pi^2} \left(3\pi^2\right)^{5/3} \rho^{5/3} = \frac{3}{10} \left(3\pi^2\right)^{2/3} \rho^{5/3} = C_{\text{TF}} \ \rho^{5/3}. \qquad (2.64)$$

By applying this noninteracting kinetic-energy density also for nonuniform systems, one obtains the Thomas–Fermi functional,[34,35]

$$T_s^{\text{TF}}[\rho] = C_{\text{TF}} \int \rho(\boldsymbol{r})^{5/3} \ d\boldsymbol{r}. \qquad (2.65)$$

However, in contrast to the LDA for the exchange-correlation energy, which is surprisingly accurate, the Thomas–Fermi functional performs poorly in most cases. If applied in OF-DFT, it does not lead to a correct description of atoms (in particular, no shell structure is obtained), and one can prove that it will not lead to any bound molecules (for details on this "non-binding theorem", see Sec. 6.3 in Ref. 17). Only for metals, which most closely resemble a uniform electron gas, the Thomas–Fermi functional leads to reasonable results.

von Weizsäcker functional

While the Thomas–Fermi functional describes the limiting case of a uniform electron gas, the von Weizsäcker functional[36] describes the limiting case of a one-orbital system, i.e., a one-electron system or a closed-shell two-electron system. This should

also be the correct limit in the asymptotic regions of molecules, where the density is dominated by the highest-occupied molecular orbital (HOMO), and near the nuclei, where the density is dominated by a $1s$-like orbital. In this limit, the Thomas–Fermi functional is completely wrong.

For a single-orbital system, the electron density is given by $\rho(\boldsymbol{r}) = \phi(\boldsymbol{r})^2$, where the orbital ϕ can be easily obtained from the density as

$$\phi(\boldsymbol{r}) = \pm\sqrt{\rho(\boldsymbol{r})}. \tag{2.66}$$

Using this orbital, the (noninteracting) kinetic energy can be calculated as

$$\begin{aligned} T_s^{\text{vW}}[\rho] &= -\frac{1}{2} \int \phi(\boldsymbol{r})\nabla^2\phi(\boldsymbol{r})d\boldsymbol{r} \\ &= -\frac{1}{2} \int \sqrt{\rho(\boldsymbol{r})}\nabla^2\sqrt{\rho(\boldsymbol{r})}d\boldsymbol{r}. \end{aligned} \tag{2.67}$$

Using integration by parts, one obtains the usual form of the von Weizsäcker functional

$$\begin{aligned} T_s^{\text{vW}}[\rho] &= \frac{1}{2} \int \left(\nabla\sqrt{\rho(\boldsymbol{r})}\right)\left(\nabla\sqrt{\rho(\boldsymbol{r})}\right)d\boldsymbol{r} \\ &= \frac{1}{8} \int \frac{|\nabla\rho(\boldsymbol{r})|^2}{\rho(\boldsymbol{r})}d\boldsymbol{r}, \end{aligned} \tag{2.68}$$

where in the last step the chain rule has been used in the derivative $\nabla\sqrt{\rho(\boldsymbol{r})} = \frac{\nabla\rho(\boldsymbol{r})}{2\sqrt{\rho(\boldsymbol{r})}}$.

This von Weizsäcker functional is the exact functional in the single-orbital case and in molecules, it provides the correct asymptotic limit and the correct behavior near the nuclei. However, in most other cases it is not accurate. In particular, for the uniform electron gas, where the gradient of the density vanishes, it gives a kinetic energy of zero, which is clearly wrong. Therefore, the von Weizsäcker functional is rarely used as a stand-alone functional, but instead it is often employed in combination with other approximations.

Conventional gradient expansion

One possible strategy of systematically improving the Thomas–Fermi functional is to introduce terms depending on the gradient of the density (such as the von Weizsäcker functional) and possibly even higher derivatives of the density in a series expansion. This leads to the conventional gradient expansion (CGE), in which the kinetic energy is expressed as

$$T_s^{\text{CGE}}[\rho] = \sum_{i=0}^{\infty} T_{2i}[\rho] = \sum_{i=0}^{\infty} \int t_{2i}(\rho(\boldsymbol{r}), \nabla\rho(\boldsymbol{r}), \dots)\, d\boldsymbol{r}. \tag{2.69}$$

There are different ways to derive the kinetic-energy densities t_{2i} in the above expansion, for details see Sec. 6.8 in Ref. 17. The zeroth order term is given by the Thomas–Fermi functional, while the second-order is given by $\frac{1}{9}$ times the von Weizsäcker functional. Therefore, the CGE up to second order is

$$T_s^{\text{CGE-2}}[\rho] = T_s^{\text{TF}} + \frac{1}{9}T_s^{\text{vW}}. \tag{2.70}$$

The forth and sixth-order terms are also available in the literature,[17,33] but for higher orders, no analytic expression exists.

Even though the strategy of a systematic series expansion is very appealing, there are two major problems with the CGE. First, for system with an inhomogeneous density the convergence is very slow and results obtained when only the leading terms of the expansion are included are usually poor. Second, in regions where the density decays exponentially, as it is the case in the asymptotic regions of atoms and molecules, T_{2i} diverges for the sixth and higher orders, and the associated functional derivative diverges for the forth and higher orders. Therefore, the CGE can not be used for constructing accurate orbital-free kinetic energy functionals.

Due to its simplicity, the second order expansion given above has been used in a number of cases. A slight modification is given by the so-called TFλvW functional,

$$T_s^{\text{TF}\lambda\text{vW}}[\rho] = T_s^{\text{TF}} + \lambda T_s^{\text{vW}}, \tag{2.71}$$

where λ is a constant. Different values of λ between 0 and 1 have been used, especially $\lambda = \frac{1}{5}$ has been found to be the optimal choice from numerical results for atoms. In contrast to the Thomas–Fermi functional, when the CGE or TFλvW functionals are applied in OF-DFT it is possible to obtain bound molecules. However, none of these approximations produces satisfactory results. In particular, for atoms no shell structure is obtained. A detailed study of the performance of TFλvW functionals for molecules can be found in Ref. 37.

GGA functionals

In analogy to the GGA for the exchange-correlation energy, the dependence on the gradient of the density can—instead of employing a series expansion—also be introduced by using an approximation of the form

$$T_s^{\text{GGA}}[\rho] = \int \rho^{5/3} F(\rho(\boldsymbol{r}), \nabla\rho(\boldsymbol{r})) \, d\boldsymbol{r}, \tag{2.72}$$

where $F(\rho, \nabla\rho)$ is an enhancement factor. Lee, Lee, and Parr suggested to use the same form of this enhancement factor as for the exchange-functional, i.e.,

$$T_s^{\text{GGA}}[\rho] = \int \rho^{5/3} F(s(\boldsymbol{r})) \, d\boldsymbol{r}, \tag{2.73}$$

where $s(\boldsymbol{r}) = \frac{1}{2(3\pi^2)^{1/3}} \frac{|\nabla\rho(\boldsymbol{r})|}{\rho(\boldsymbol{r})^{4/3}}$.

Using this strategy, a number of GGA kinetic-energy functionals has been suggested, either by using the unmodified enhancement factor of a given exchange functional, or by reparametrizing this enhancement factor. An overview and an numerical tests for kinetic energies of rare gas atoms can be found in Ref. 38.

One notable example of a GGA kinetic-energy functional is the functional developed by Karasiev *et al.*, who fitted the enhancement factor such that not, as usual, the densities or kinetic energies are reproduced, but that accurate gradients and equilibrium geometries are obtained.[39] This way, they obtain a functional that yields reasonable geometries for certain molecules not included in the fitting set.

However, also with GGA functionals, the densities calculated for atoms show no shell structure, and also for molecules and solids, the obtained results are usually poor. Nevertheless, GGA kinetic-energy functionals have been shown to be reasonably accurate if they are applied for a small part of the kinetic energy only[40] (as will be discussed below and in the next chapter).

Linear response functionals

Another approach to the construction of approximate kinetic-energy functionals is to consider the linear-response behavior of the uniform electron gas.[33,41] The change in the electron density caused by a change in the potential is for a translationally invariant system, to first order, given by

$$\delta\rho(\boldsymbol{r}) = \int \chi(\boldsymbol{r} - \boldsymbol{r}')\delta v(\boldsymbol{r}') \; d\boldsymbol{r}', \tag{2.74}$$

with the linear-response function

$$\chi(\boldsymbol{r} - \boldsymbol{r}') = \frac{\delta\rho(\boldsymbol{r})}{\delta v(\boldsymbol{r}')}. \tag{2.75}$$

By considering the inverse liner-response function and performing a Fourier transformation (denoted by the symbol $\hat{F}$), one obtains,

$$\frac{1}{\tilde{\chi}(\boldsymbol{q})} = \hat{F}\left(\frac{\delta v(\boldsymbol{r})}{\delta\rho(\boldsymbol{r}')}\right), \tag{2.76}$$

where $\tilde{\chi}(\boldsymbol{q})$ is the linear-response function in momentum space.

The linear-response function of the total KS potential can then be obtained from,

$$\frac{1}{\tilde{\chi}_s(\boldsymbol{q})} = \hat{F}\left(\frac{\delta v_{\text{eff}}^{\text{KS}}(\boldsymbol{r})}{\delta\rho(\boldsymbol{r}')}\right), \tag{2.77}$$

2. DFT and the kinetic energy

where the KS potential is according to Eq. (2.51) given by

$$v_{\text{eff}}^{\text{KS}}(\boldsymbol{r}) = -\frac{\delta T_s[\rho]}{\delta \rho(\boldsymbol{r})} + \mu, \tag{2.78}$$

and, therefore,

$$\frac{1}{\tilde{\chi}_s(\boldsymbol{q})} = -\hat{F}\left(\frac{\delta^2 T_s[\rho]}{\delta \rho(\boldsymbol{r})\delta \rho(\boldsymbol{r}')}\right). \tag{2.79}$$

For the uniform electron gas of density ρ_0, the the linear-response function is known, and its Fourier transformation is given by the Lindhard function,

$$\tilde{\chi}_{\text{Lind}}(\boldsymbol{q}) = -\frac{k_F}{\pi^2}\left(\frac{1}{2} + \frac{1-\eta^2}{4\eta}\ln\left|\frac{1+\eta}{1-\eta}\right|\right), \tag{2.80}$$

where $k_F = (3\pi^2 \rho_0)^{1/3}$, and $\eta = |\boldsymbol{q}|/(2k_F)$.

To construct kinetic-energy functionals that show the correct linear-response behavior for the uniform electron gas, one usually uses functionals of the form,

$$T_s^{\text{LR}}[\rho] = T_s^{\text{TF}}[\rho] + T_s^{\text{vW}}[\rho] + T_s^{\text{X}}[\rho], \tag{2.81}$$

where for T_s^{X} the simplest possible ansatz is

$$T_s^{\text{X}} = \int \rho(\boldsymbol{r})^\alpha K(|\boldsymbol{r} - \boldsymbol{r}'|)\rho(\boldsymbol{r}')^\alpha d\boldsymbol{r} d\boldsymbol{r}', \tag{2.82}$$

in which the parameter α has to be chosen appropriately.

The kernel $K(|\boldsymbol{r} - \boldsymbol{r}'|)$ is constructed such that the correct liner-response behavior is obtained for the uniform electron gas, i.e.,

$$\begin{aligned}
-\frac{1}{\tilde{\chi}_{\text{Lind}}(\boldsymbol{q})} &= \hat{F}\left(\frac{\delta^2 T_s^{\text{LR}}[\rho]}{\delta \rho(\boldsymbol{r})\delta \rho(\boldsymbol{r}')}\right) \\
&= \hat{F}\left(\frac{\delta^2 T_s^{\text{TF}}[\rho]}{\delta \rho(\boldsymbol{r})\delta \rho(\boldsymbol{r}')}\right) + \hat{F}\left(\frac{\delta^2 T_s^{\text{vW}}[\rho]}{\delta \rho(\boldsymbol{r})\delta \rho(\boldsymbol{r}')}\right) + \hat{F}\left(\frac{\delta^2 T_s^{\text{X}}[\rho]}{\delta \rho(\boldsymbol{r})\delta \rho(\boldsymbol{r}')}\right) \\
&= +\frac{\pi^2}{k_F} + \frac{3\pi^2\eta^2}{k_F} + \alpha^2 \rho_0^{2(\alpha-1)} K(\boldsymbol{q}),
\end{aligned} \tag{2.83}$$

where ρ_0 is the uniform density (for nonuniform systems, the average density is used) and the linear response functions of the Thomas–Fermi functional $\tilde{\chi}_{\text{TF}}(\boldsymbol{q}) = -\frac{k_F}{\pi^2}$ and of the von Weizsäcker functional $\tilde{\chi}_{\text{vW}}(\boldsymbol{q}) = -\frac{k_F}{3\pi^2\eta^2}$ have been used. Hence, one

obtains within this ansatz,

$$K(\boldsymbol{q}) = \frac{1}{\alpha^2 \rho_0^{2(\alpha-1)}} \left(\frac{1}{\tilde{\chi}_{\text{Lind}}(\boldsymbol{q})} - \frac{\pi^2}{k_F} - \frac{3\pi^2 \eta^2}{k_F} \right)$$

$$= -\frac{\pi^2}{k_F} \left[\left(\frac{1}{2} + \frac{1-\eta^2}{4\eta} \ln \left| \frac{1+\eta}{1-\eta} \right| \right)^{-1} + 1 + 3\eta^2 \right]. \tag{2.84}$$

For the choice of the parameter α, different parameters have been examined (for an overview, see Ref. [41]). In addition, a number of more complicated forms of $T_s^{\text{X}}[\rho]$ have been employed, by introducing different exponents α and β for the densities in Eq. [2.82] or by introducing a kernel that depends not only on $|\boldsymbol{r} - \boldsymbol{r}'|$ but also on the nonlocal two-body Fermi wave vector[42]

$$\xi_\gamma(\boldsymbol{r}, \boldsymbol{r}') = \left(\frac{k_F(\boldsymbol{r})^\gamma + k_F(\boldsymbol{r}')^\gamma}{2} \right)^{1/\gamma}, \tag{2.85}$$

where $k_F(\boldsymbol{r}) = (2\pi^2 \rho(\boldsymbol{r}))^{1/3}$. An overview of different such linear-response based kinetic-energy functionals can be found in Ref. [43].

The functional $T_s^{\text{X}}[\rho]$ can be evaluated in momentum space, which can be done efficiently in calculations employing periodic boundary conditions. Choly and Kaxiras have presented a way of evaluating this term in real space, which is based on numerical integration employing an evenly-space grid,[44] but this scheme is also taylored to the application in calculations with periodic-boundary conditions. Therefore, these linear-response based functionals have not been applied to the calculation of molecules so far.

Linear-response based kinetic-energy functionals have been shown to lead to accurate results for metals,[41] but also for non-metallic materials such as silicon.[43] These advanced functionals make it possible to employ OF-DFT for studying properties of simple materials. Carter *et al.* have applied a combination of OF-DFT with quasi-continuum mechanics to study the nanoindentation of fcc aluminum.[45] Furthermore, they have applied OF-DFT to study the diffusion and aggregation of vacancies in shocked aluminum.[46]

However, if one goes beyond the limited class of system for which OF-DFT in combination with a suitable functional is known to be reliable, the results are disappointing. Frankcombe *et al.* explored the ability of OF-DFT to describe the structures Al, NaH, AlH$_3$ and NaAlH$_4$, which are of interest in the context of hydrogen storage.[47] While they find that for the simple materials Al and NaH, the linear-response functionals described above lead to reasonable structures, they fail completely for the hydrides AlH$_3$ and NaAlH$_4$, where completely wrong structures are obtained. This shows that even though the performance of these functionals is good for a certain class of ma-

terials, one cannot expect a similar accuracy for even only slightly more complex materials.

2.3.4. A hybrid orbital-free / KS treatment of the kinetic-energy

Finally, not only the Kohn–Sham and the orbital-free treatment of the noninteracting kinetic energy are possible, but also a hybrid treatment can be employed. In this hybrid treatment, the electron density ρ is split up into two components $\rho = \rho_{\mathrm{I}} + \rho_{\mathrm{II}}$, and the noninteracting kinetic energy is written as,

$$T_s[\rho] = T_s[\rho_{\mathrm{I}}] + T_s[\rho_{\mathrm{II}}] + T_s^{\mathrm{nadd}}[\rho_{\mathrm{I}}, \rho_{\mathrm{II}}] \tag{2.86}$$

where the nonadditive kinetic energy is defined as

$$T_s^{\mathrm{nadd}}[\rho_{\mathrm{I}}, \rho_{\mathrm{II}}] = T_s[\rho_{\mathrm{I}} + \rho_{\mathrm{II}}] - T_s[\rho_{\mathrm{I}}] - T_s[\rho_{\mathrm{II}}]. \tag{2.87}$$

While the kinetic energies corresponding to the two components of the density ρ_{I} and ρ_{II} are treated using the corresponding KS orbitals, the nonadditive kinetic energy is calculated using an orbital-free density functional, i.e., the kinetic energy is calculated as

$$T_s[\{\phi_i^{(\mathrm{I})}\}, \{\phi_i^{(\mathrm{II})}\}] = \sum_{i=1}^{N} \int \phi_i^{(\mathrm{I})}(\boldsymbol{r})^* \left(\frac{-\nabla^2}{2} \right) \phi_i^{(\mathrm{I})}(\boldsymbol{r}) \ d\boldsymbol{r}$$
$$+ \sum_{i=1}^{N} \int \phi_i^{(\mathrm{II})}(\boldsymbol{r})^* \left(\frac{-\nabla^2}{2} \right) \phi_i^{(\mathrm{II})}(\boldsymbol{r}) \ d\boldsymbol{r} + \tilde{T}_s^{\mathrm{nadd}}[\rho_{\mathrm{I}}, \rho_{\mathrm{II}}]. \tag{2.88}$$

This way, the largest part of the kinetic energy is treated exactly using the KS orbitals, while only the smaller nonadditive kinetic energy has to be approximated using an orbital-free kinetic-energy functional.

It is important to note that the KS orbitals corresponding to the densities ρ_{I} and ρ_{II} form two orthogonal sets, but the orbitals in one of these sets are not necessarily orthogonal to orbitals in the other sets. In analogy to the second derivation of the KS equations given above in Sec. 2.3.1, the ground state can be determined by minimizing the total energy,

$$E_0 = \min_{\phi_i^{(\mathrm{I})}, \phi_i^{(\mathrm{II})}} \left(T_s[\{\phi_i^{(\mathrm{I})}\}, \{\phi_i^{(\mathrm{II})}\}] + V_{\mathrm{ne}}[\rho] + J[\rho] + E_{xc}[\rho] \right), \tag{2.89}$$

where the kinetic energy has been expressed as in Eq. (2.88). The above minimization has to be performed subject to the constraint that the sets of orbitals $\phi_i^{(\mathrm{I})}$ and $\phi_i^{(\mathrm{II})}$ are both orthogonal.

Even though this hybrid treatment might seem unnecessarily complicated, it provides a way of splitting up the total system into separate subsystems, which can be used as a starting point for efficient calculations of large systems. The frozen-density embedding scheme, which is the subject of this thesis, exploits this possibility. This scheme will be discussed in detail in the following chapter.

2. DFT and the kinetic energy

3. Frozen-density embedding

In this Chapter, an introduction into the frozen-density embedding (FDE) scheme and related methods is given. After the main idea, the partitioning of the electron density into subsystem densities, the general theory is presented. Afterwards, it is explained how this scheme can be used to model large environments, and how it can be used as an efficient alternative to conventional KS-DFT. This is followed by a discussion of the required approximations for the nonadditive kinetic energy. Furthermore, the extensions of FDE to time-dependent DFT and to wave-function theory (WFT) in DFT embedding are discussed. Finally, a review of previous applications of the FDE scheme and related methods is given.

3.1. Partitioning of the electron density

The FDE formalism[8,48] is based on a partitioning of the total electron density $\rho_{\text{tot}}(\boldsymbol{r})$ into the electron densities of two subsystems, i.e., it is represented as the sum of two components $\rho_{\text{I}}(\boldsymbol{r})$ and $\rho_{\text{II}}(\boldsymbol{r})$,

$$\rho_{\text{tot}}(\boldsymbol{r}) = \rho_{\text{I}}(\boldsymbol{r}) + \rho_{\text{II}}(\boldsymbol{r}). \tag{3.1}$$

Except for the requirement that both subsystem densities integrate to an integer number of electrons, they are not subject to any further conditions. In particular, the subsystem densities are allowed to overlap. In addition to the electron density, also the nuclear charges are partitioned accordingly. This partitioning of the density and of the nuclear charges defines two subsystems (subsystems I and II).

Given this partitioning of the electron density, the DFT total energy can (in the absence of any external fields) be expressed as a bifunctional of ρ_{I} and ρ_{II},

$$\begin{aligned}
E[\rho_{\text{I}}, \rho_{\text{II}}] = E_{\text{NN}} &+ \int \left(\rho_{\text{I}}(\boldsymbol{r}) + \rho_{\text{II}}(\boldsymbol{r})\right) \left(v_{\text{I}}^{\text{nuc}}(\boldsymbol{r}) + v_{\text{II}}^{\text{nuc}}(\boldsymbol{r})\right) \, d\boldsymbol{r} \\
&+ \frac{1}{2} \int \frac{(\rho_{\text{I}}(\boldsymbol{r}) + \rho_{\text{II}}(\boldsymbol{r}))(\rho_{\text{I}}(\boldsymbol{r}') + \rho_{\text{II}}(\boldsymbol{r}'))}{|\boldsymbol{r} - \boldsymbol{r}'|} \, d\boldsymbol{r} d\boldsymbol{r}' \\
&+ E_{xc}[\rho_{\text{I}} + \rho_{\text{II}}] + T_s[\rho_{\text{I}}] + T_s[\rho_{\text{II}}] + T_s^{\text{nadd}}[\rho_{\text{I}}, \rho_{\text{II}}],
\end{aligned} \tag{3.2}$$

where E_{NN} is the nuclear repulsion energy, $v_{\mathrm{I}}^{\mathrm{nuc}}$ and $v_{\mathrm{II}}^{\mathrm{nuc}}$ are the electrostatic potentials of the nuclei in subsystems I and II, respectively, E_{xc} is the exchange-correlation energy functional, $T_s[\rho]$ is the kinetic energy of the noninteracting reference system, and $T_s^{\mathrm{nadd}}[\rho_{\mathrm{I}}, \rho_{\mathrm{II}}]$ is the nonadditive kinetic energy, which is defined as

$$T_s^{\mathrm{nadd}}[\rho_{\mathrm{I}}, \rho_{\mathrm{II}}] = T_s[\rho_{\mathrm{I}} + \rho_{\mathrm{II}}] - T_s[\rho_{\mathrm{I}}] - T_s[\rho_{\mathrm{II}}]. \tag{3.3}$$

If the densities $\rho_{\mathrm{I}}(\boldsymbol{r})$ and $\rho_{\mathrm{II}}(\boldsymbol{r})$ are represented using the canonical Kohn-Sham (KS) orbitals[a] for the individual subsystems $\phi_i^{(n)}$ with $\rho_n(\boldsymbol{r}) = 2 \sum_{i=1}^{N_n/2} \phi_i^{(n)}(\boldsymbol{r})^* \phi_i^{(n)}(\boldsymbol{r})$ $(n = \mathrm{I}, \mathrm{II})$, it is possible to calculate the kinetic energy of the corresponding noninteracting reference system as

$$T_s[\rho_n] = -2 \sum_{i=1}^{N_n/2} \left\langle \phi_i^{(n)} \left| \frac{\nabla^2}{2} \right| \phi_i^{(n)} \right\rangle. \tag{3.4}$$

However, with the partitioning of the total electron density into $\rho_{\mathrm{I}}(\boldsymbol{r})$ and $\rho_{\mathrm{II}}(\boldsymbol{r})$ there is in general no representation of $\rho_{\mathrm{tot}}(\boldsymbol{r})$ in the canonical KS orbitals available, so that $T_s[\rho_{\mathrm{I}} + \rho_{\mathrm{II}}]$ cannot be calculated in this way. Therefore, in practical implementations $T_s^{\mathrm{nadd}}[\rho_{\mathrm{I}}, \rho_{\mathrm{II}}]$ has to be calculated using an approximated kinetic-energy functional.

The exchange-correlation energy in Eq. (3.2) can be split up in a similar way as the kinetic energy into

$$E_{xc}[\rho_{\mathrm{I}} + \rho_{\mathrm{II}}] = E_{xc}[\rho_{\mathrm{I}}] + E_{xc}[\rho_{\mathrm{II}}] + E_{xc}^{\mathrm{nadd}}[\rho_{\mathrm{I}}, \rho_{\mathrm{II}}], \tag{3.5}$$

where the nonadditive part of the exchange-correlation energy is defined as

$$E_{\mathrm{xc}}^{\mathrm{nadd}}[\rho_{\mathrm{I}}, \rho_{\mathrm{II}}] = E_{\mathrm{xc}}[\rho_{\mathrm{I}} + \rho_{\mathrm{II}}] - E_{\mathrm{xc}}[\rho_{\mathrm{I}}] - E_{\mathrm{xc}}[\rho_{\mathrm{II}}]. \tag{3.6}$$

This partitioning of the exchange-correlation energy functional is introduced here to make it possible to use different approximations for the exchange-correlation functionals in the two subsystems. This possibility will be further explored in Chapter 8.

3.2. The embedding potential

For a given frozen electron density $\rho_{\mathrm{II}}(\boldsymbol{r})$ in one of the subsystems (subsystem II) the electron density $\rho_{\mathrm{I}}(\boldsymbol{r})$ in the other subsystem (subsystem I) can be determined by minimizing the total energy bifunctional [Eq. (3.2)] with respect to ρ_{I}, while $\rho_{\mathrm{II}}(\boldsymbol{r})$ is kept frozen. If the complementary $\rho_{\mathrm{I}}(\boldsymbol{r})$ is positive, this will lead to the total density

---

[a] For reasons of simplicity, only the closed-shell case with $N/2$ doubly occupied orbitals will be considered. A generalization to open-shell systems is possible in a straightforward way

$\rho_{\text{tot}}(\boldsymbol{r}) = \rho_{\text{I}}(\boldsymbol{r}) + \rho_{\text{II}}(\boldsymbol{r})$ that minimizes the total energy functional. This total density is, therefore, the same density that could also be obtained from a conventional DFT calculation on the total system.

The minimization of the total energy $E[\rho_{\text{I}}, \rho_{\text{II}}]$ with respect to ρ_{I}, under the constraint that the number of electrons N_{I} in subsystem I is conserved, leads to the condition

$$
\begin{aligned}
0 &= \frac{\delta}{\delta\rho_{\text{I}}}\left[E[\rho_{\text{I}}, \rho_{\text{II}}] + \mu_{\text{I}}\left(\int \rho_{\text{I}}(r)dr - N_{\text{I}}\right)\right] \\
&= v_{\text{I}}^{\text{nuc}}(\boldsymbol{r}) + v_{\text{II}}^{\text{nuc}}(\boldsymbol{r}) + \int \frac{\rho_{\text{I}}(\boldsymbol{r}')}{|\boldsymbol{r} - \boldsymbol{r}'|}d\boldsymbol{r}' + \int \frac{\rho_{\text{II}}(\boldsymbol{r}')}{|\boldsymbol{r} - \boldsymbol{r}'|}d\boldsymbol{r}' \\
&\quad + \frac{\delta E_{\text{xc}}[\rho_{\text{I}} + \rho_{\text{II}}]}{\delta\rho_{\text{I}}} + \frac{\delta T_s[\rho_{\text{I}}]}{\delta\rho_{\text{I}}} + \frac{\delta T_s^{\text{nadd}}[\rho_{\text{I}}, \rho_{\text{II}}]}{\delta\rho_{\text{I}}} + \mu^{(\text{I})}.
\end{aligned}
\tag{3.7}
$$

If the electron density $\rho_{\text{I}}(\boldsymbol{r})$ determined from this minimization is v_s-representable,[17] it can be expressed as $\rho_{\text{I}}(\boldsymbol{r}) = 2\sum_i^{N_I/2}|\phi_i^{(\text{I})}(\boldsymbol{r})|^2$ in terms of the KS orbitals $\{\phi_i^{(\text{I})}(\boldsymbol{r})\}$ of subsystem I. These are determined by solving the Kohn–Sham equations with constraint electron density (KSCED equations),

$$
\left[-\frac{\nabla^2}{2} + v_{\text{eff}}^{\text{KSCED}}[\rho_{\text{I}}, \rho_{\text{II}}](\boldsymbol{r})\right]\phi_i^{(\text{I})}(\boldsymbol{r}) = \epsilon_i\,\phi_i^{(\text{I})}(\boldsymbol{r}); \quad i = 1, \ldots, N_{\text{I}}/2.
\tag{3.8}
$$

In these equations, the KSCED effective potential $v_{\text{eff}}^{\text{KSCED}}[\rho_{\text{I}}, \rho_{\text{II}}](\boldsymbol{r})$ is the yet unknown potential which, for a noninteracting system, leads to an electron density which is equal to the density obtained from minimizing the (interacting) total energy bifunctional of Eq. (3.2).

The electron density of this noninteracting reference system can be determined by minimizing the noninteracting energy functional

$$
E_s[\rho_{\text{I}}] = T_s[\rho_{\text{I}}] + \int \rho_{\text{I}}(\boldsymbol{r})v_{\text{eff}}^{\text{KSCED}}[\rho_{\text{I}}, \rho_{\text{II}}](\boldsymbol{r})d\boldsymbol{r},
\tag{3.9}
$$

with respect to ρ_{I}, under the constraint that the correct number of electrons N_{I} in subsystem I is conserved. This minimization leads to the condition

$$
\begin{aligned}
0 &= \frac{\delta}{\delta\rho_{\text{I}}}\left[E_s[\rho_{\text{I}}] + \mu_{\text{I}}\left(\int \rho_{\text{I}}(\boldsymbol{r})d\boldsymbol{r} - N_{\text{I}}\right)\right] \\
&= \frac{\delta T_s[\rho_{\text{I}}]}{\delta\rho_{\text{I}}} + v_{\text{eff}}^{\text{KSCED}}[\rho_{\text{I}}, \rho_{\text{II}}](\boldsymbol{r}) + \mu_{\text{I}}.
\end{aligned}
\tag{3.10}
$$

Comparing Eq. (3.7) and Eq. (3.10) one obtains

$$
v_{\text{eff}}^{\text{KSCED}}[\rho_{\text{I}}, \rho_{\text{II}}](\boldsymbol{r}) = v_{\text{eff}}^{\text{KS}}[\rho_{\text{tot}}](\boldsymbol{r}) + v_T[\rho_{\text{I}}, \rho_{\text{II}}](\boldsymbol{r}),
\tag{3.11}
$$

3. Frozen-density embedding

where $v_{\text{eff}}^{\text{KS}}[\rho_{\text{tot}}](\boldsymbol{r})$ is the KS effective potential for the total system. It contains the total nuclear potential, the Coulomb potential of the total electron density and the exchange-correlation potential of the total system,

$$v_{\text{eff}}^{\text{KS}}[\rho_{\text{tot}}](\boldsymbol{r}) = v_{\text{I}}^{\text{nuc}}(\boldsymbol{r}) + v_{\text{II}}^{\text{nuc}}(\boldsymbol{r}) + \int \frac{\rho_{\text{tot}}(\boldsymbol{r'})}{|\boldsymbol{r} - \boldsymbol{r'}|} d\boldsymbol{r'} + \left. \frac{\delta E_{\text{xc}}[\rho]}{\delta \rho} \right|_{\rho=\rho_{\text{tot}}(\boldsymbol{r})}. \qquad (3.12)$$

In addition, the KSCED effective potential contains a kinetic-energy component $v_T[\rho_{\text{I}}, \rho_{\text{II}}]$ which is given as the functional derivative of the nonadditive kinetic-energy bifunctional,

$$v_T[\rho_{\text{I}}, \rho_{\text{II}}](\boldsymbol{r}) = \frac{\delta T_s^{\text{nadd}}[\rho_{\text{I}}, \rho_{\text{II}}]}{\delta \rho_{\text{I}}} = \left. \frac{\delta T_s[\rho]}{\delta \rho} \right|_{\rho=\rho_{\text{tot}}(\boldsymbol{r})} - \left. \frac{\delta T_s[\rho]}{\delta \rho} \right|_{\rho=\rho_{\text{I}}(\boldsymbol{r})}. \qquad (3.13)$$

In practical applications of the FDE scheme, this kinetic-energy component v_T has to be modeled using an approximate kinetic-energy functional. It should be noted that in contrast to the bifunctional of the nonadditive kinetic energy of Eq. (3.3), v_T is not symmetric with respect to the exchange of the two electron densities, i.e., $v_T[\rho_{\text{I}}, \rho_{\text{II}}] \neq v_T[\rho_{\text{II}}, \rho_{\text{I}}]$.

To underline the effective embedding character of the FDE formalism, the KSCED effective potential is usually expressed in an alternative way than in Eq. (3.11), by separating terms that depend only on the electron density ρ_{I} and the positions of the nuclei of subsystem I and those that also depend on the frozen electron density ρ_{II} and the positions of the nuclei in the frozen subsystem. This leads to the expression

$$v_{\text{eff}}^{\text{KSCED}}[\rho_{\text{I}}, \rho_{\text{II}}](\boldsymbol{r}) = v_{\text{eff}}^{\text{KS}}[\rho_{\text{I}}](\boldsymbol{r}) + v_{\text{eff}}^{\text{emb}}[\rho_{\text{I}}, \rho_{\text{II}}](\boldsymbol{r}), \qquad (3.14)$$

where $v_{\text{eff}}^{\text{KS}}[\rho_{\text{I}}](\boldsymbol{r})$ is the KS effective potential of the isolated subsystem I containing the usual terms of the nuclear potential, the Coulomb potential of the electrons, and the exchange–correlation potential,

$$v_{\text{eff}}^{\text{KS}}[\rho_{\text{I}}](\boldsymbol{r}) = v_{\text{I}}^{\text{nuc}}(\boldsymbol{r}) + \int \frac{\rho_{\text{I}}(\boldsymbol{r'})}{|\boldsymbol{r} - \boldsymbol{r'}|} d\boldsymbol{r'} + \left. \frac{\delta E_{\text{xc}}[\rho]}{\delta \rho} \right|_{\rho=\rho_{\text{I}}(\boldsymbol{r})}. \qquad (3.15)$$

The effective embedding potential $v_{\text{eff}}^{\text{emb}}[\rho_{\text{I}}, \rho_{\text{II}}](\boldsymbol{r})$ describes the interaction of the subsystem I with the frozen density and nuclei of subsystem II and reads

$$v_{\text{eff}}^{\text{emb}}[\rho_{\text{I}}, \rho_{\text{II}}](\boldsymbol{r}) = v_{\text{II}}^{\text{nuc}}(\boldsymbol{r}) + \int \frac{\rho_{\text{II}}(\boldsymbol{r'})}{|\boldsymbol{r} - \boldsymbol{r'}|} d\boldsymbol{r'} + \frac{\delta E_{\text{xc}}^{\text{nadd}}[\rho_{\text{I}}, \rho_{\text{II}}]}{\delta \rho_{\text{I}}} + v_T[\rho_{\text{I}}, \rho_{\text{II}}](\boldsymbol{r}).$$
$$(3.16)$$

In addition to the electrostatic potential of the nuclei and the electrons in the frozen subsystem, this effective embedding potential also contains an exchange-correlation

component, which is given by the functional derivative of the nonadditive exchange-correlation energy [Eq. (3.6)] as,

$$\frac{\delta E_{\mathrm{xc}}^{\mathrm{nadd}}[\rho_{\mathrm{I}}, \rho_{\mathrm{II}}]}{\delta \rho_{\mathrm{I}}} = \left.\frac{\delta E_{\mathrm{xc}}[\rho]}{\delta \rho}\right|_{\rho=\rho_{\mathrm{I}}+\rho_{\mathrm{II}}} - \left.\frac{\delta E_{\mathrm{xc}}[\rho]}{\delta \rho}\right|_{\rho=\rho_{\mathrm{I}}} \tag{3.17}$$

and a kinetic-energy component as given in Eq. (3.13).

In summary, for a given frozen density $\rho_{\mathrm{II}}(\boldsymbol{r})$, the density of the nonfrozen subsystem $\rho_{\mathrm{I}}(\boldsymbol{r})$ can be obtained by solving KS-like equations

$$\left[-\frac{\nabla^2}{2} + v_{\mathrm{eff}}^{\mathrm{KS}}[\rho_{\mathrm{I}}](\boldsymbol{r}) + v_{\mathrm{eff}}^{\mathrm{emb}}[\rho_{\mathrm{I}}, \rho_{\mathrm{II}}](\boldsymbol{r})\right] \phi_i^{(\mathrm{I})}(\boldsymbol{r}) = \epsilon_i\ \phi_i^{(\mathrm{I})}(\boldsymbol{r}) \quad ; \quad i = 1, \ldots, N_{\mathrm{I}}/2,$$
$$\tag{3.18}$$

in which the effect of the environment is represented by the additional effective embedding potential $v_{\mathrm{eff}}^{\mathrm{emb}}$ as given in Eq. (3.16). If the initial assumption that the complementary ρ_{I} is positive and v_s-representable is fulfilled, the solution of these equations will directly yield the exact ground-state electron density of the total system.[48]

3.3. Approximate treatments of the environment

In typical applications of the FDE scheme, the nonfrozen subsystem I is a small system of interest, which is embedded in a much larger environment. Especially for the calculation of molecular properties (e.g., electronic excitation energies, or nuclear magnetic resonance shieldings), this will be a very efficient scheme, since the property calculation generally has to be performed for the nonfrozen subsystem only.

However, in these cases the construction of the electron density becomes a bottleneck if the standard approach is used and the frozen density is obtained using a DFT calculation of the full environment. Since Eq. (3.18) can be solved for any postulated electron density, $\rho_{\mathrm{II}}(\boldsymbol{r})$ may also be obtained from simpler considerations and this problem can be overcome by applying approximations in the constructions of the environment. Already in their initial papers, Wesolowski and Warshel proposed the use of such an approximate density to describe a water environment.[8,49]

In an initial study of solvent effects on excitation energies, Neugebauer *et al.* investigated the electronic absorption spectrum of acetone in water and tested different approximate descriptions of the frozen solvent environment. They found that compared to a full DFT calculation of the environment, the error introduced by using a superposition of gas-phase densities of isolated water molecules is less than 0.01 eV

for the $n \to \pi^*$ transition of interest. Subsequently, this strategy has been successfully applied in a number of studies of solvent effects on molecular properties.[CJ4,50] In some cases it was, however, necessary to include some solvent molecules in the nonfrozen system[CJ4] or to partially relax the frozen density with respect to the nonfrozen subsystem.[CJ5]

3.4. Subsystem density-functional theory

While the strategy to use approximate densities as described in the previous section can be applied for large environments, the FDE formalism can also be used to determine the electron densities of both subsystems. In particular, for most approximate environment densities, the requirements that the complementary ρ_I is v_s-representable and positive at any point in space will not be fulfilled. To correct for the errors introduced by these deficiencies of the approximate environment density, both the electron density in the nonfrozen subsystem and the environment density should be determined. This leads to the "subsystem DFT" formalism as it was initially proposed by Cortona,[51] which provides an efficient alternative to conventional KS-DFT.

The starting point for this subsystem DFT formulation is again the total energy bifunctional of Eq. (3.2), but now this total energy is not only minimized with respect to the electron density ρ_I in one of the subsystems while the density ρ_{II} in the other subsystem is kept frozen, but it is minimized with respect to the electron densities in both subsystems. This means that one determines a pair of electron densities $\{\rho_I, \rho_{II}\}$ such that these densities minimize the total energy, i.e., that the energy is stationary with respect to variations in both densities,

$$0 = dE = \left(\frac{\delta E}{\delta \rho_I}\right) \delta \rho_I + \left(\frac{\delta E}{\delta \rho_{II}}\right) \delta \rho_{II} \qquad \forall \delta \rho_I, \delta \rho_{II}, \tag{3.19}$$

where the functional derivatives with respect to ρ_I and ρ_{II} have to be understood as partial derivatives (the other density is kept constant) and where the variations $\delta \rho_I$ and $\delta \rho_{II}$ have to conserve the number of electrons N_I and N_{II} in the individual subsystems, respectively.

Obviously, if the total energy is stationary with respect to variations of both ρ_I and ρ_{II}, it will also be stationary with respect to variations of $\rho_{tot} = \rho_I + \rho_{II}$. However, it is important to note that the partitioning of the total density is not unique. As the total energy only depends on the total electron density ρ_{tot}, there will be many partitionings of the total electron density minimizing the total energy, even if the number of electrons in the subsystems are fixed.

The stationarity condition given in Eq. (3.19) leads to the conditions for the subsystem

densities

$$0 = \frac{\delta}{\delta\rho_{\mathrm{I}}} \left[E[\rho_{\mathrm{I}}, \rho_{\mathrm{II}}] + \mu_{\mathrm{I}} \left(\int \rho_{\mathrm{I}}(\boldsymbol{r}) d\boldsymbol{r} - N_{\mathrm{I}} \right) \right] \tag{3.20}$$

$$0 = \frac{\delta}{\delta\rho_{\mathrm{II}}} \left[E[\rho_{\mathrm{I}}, \rho_{\mathrm{II}}] + \mu_{\mathrm{II}} \left(\int \rho_{\mathrm{II}}(\boldsymbol{r}) d\boldsymbol{r} - N_{\mathrm{II}} \right) \right] \tag{3.21}$$

which—similar to what is explained above—lead to two coupled sets of KSCED equations,

$$\left[-\frac{\nabla^2}{2} + v_{\mathrm{eff}}^{\mathrm{KS}}[\rho_{\mathrm{I}}](\boldsymbol{r}) + v_{\mathrm{eff}}^{\mathrm{emb}}[\rho_{\mathrm{I}}, \rho_{\mathrm{II}}](\boldsymbol{r}) \right] \phi_i^{(I)}(\boldsymbol{r}) = \epsilon_i^{(I)} \ \phi_i^{(I)}(\boldsymbol{r}),$$
$$i = 1, \ldots, N_{\mathrm{I}}/2, \tag{3.22}$$

$$\left[-\frac{\nabla^2}{2} + v_{\mathrm{eff}}^{\mathrm{KS}}[\rho_{\mathrm{II}}](\boldsymbol{r}) + v_{\mathrm{eff}}^{\mathrm{emb}}[\rho_{\mathrm{II}}, \rho_{\mathrm{I}}](\boldsymbol{r}) \right] \phi_i^{(II)}(\boldsymbol{r}) = \epsilon_i^{(II)} \ \phi_i^{(II)}(\boldsymbol{r}),$$
$$i = 1, \ldots, N_{\mathrm{II}}/2, \tag{3.23}$$

where $v_{\mathrm{eff}}^{\mathrm{KS}}$ and $v_{\mathrm{eff}}^{\mathrm{KS}}$ are the KS potentials of the isolated subsystem I and II, respectively, and $v_{\mathrm{eff}}^{\mathrm{emb}}$ is the effective embedding potential as defined in Eq. (3.16).

As the effective embedding potential depends on the electron densities in both subsystems, these two equations are coupled and have to be solved iteratively. This can be done by applying so-called "freeze-and-thaw" cycles,[52] in which the roles of frozen and nonfrozen subsystem are interchanged until convergence is reached. Alternatively, the coupled KSCED equations can be solved simultaneously by updating both densities after each SCF cycle.[53,54]

The subsystem DFT scheme can be easily extended to an arbitrary number of subsystems by starting from the partitioning

$$\rho_{\mathrm{tot}}(\boldsymbol{r}) = \sum_{i=1}^{M} \rho_i(\boldsymbol{r}), \tag{3.24}$$

where M is the number of subsystems. This leads to a formulation similar to the one presented here, except that a set of M coupled KSCED equations is obtained, in which the frozen density in the effective embedding potential is replaced by the sum of the densities of all frozen subsystems.[51,53]

In Chapter 7, a flexible implementation of the FDE scheme will be presented, which allows both the FDE treatment using approximate environments and the subsystem DFT treatment with many subsystems as well as different intermediate schemes.

3.5. Approximating the nonadditive kinetic-energy

Both the total energy bifunctional and the effective embedding potential contain a nonadditive kinetic-energy component that usually cannot be calculated exactly. For the performance of the FDE scheme, the choice of the approximation which is used for this nonadditive kinetic-energy component is of great importance.

Usually, the nonadditive kinetic energy is approximated in the form

$$\tilde{T}_s^{\mathrm{nadd}}[\rho_{\mathrm{I}}, \rho_{\mathrm{II}}] = \tilde{T}_s[\rho_{\mathrm{I}} + \rho_{\mathrm{II}}] - \tilde{T}_s[\rho_{\mathrm{I}}] - \tilde{T}_s[\rho_{\mathrm{II}}], \tag{3.25}$$

and the kinetic-energy component v_T of the embedding potential is approximated as

$$\tilde{v}_T[\rho_{\mathrm{I}}, \rho_{\mathrm{II}}](\boldsymbol{r}) = \left. \frac{\delta \tilde{T}_s[\rho]}{\delta \rho} \right|_{\rho = \rho_{\mathrm{tot}}(\boldsymbol{r})} - \left. \frac{\delta \tilde{T}_s[\rho]}{\delta \rho} \right|_{\rho = \rho_{\mathrm{I}}(\boldsymbol{r})}, \tag{3.26}$$

where the tilde is used to label approximate quantities, and $\tilde{T}_s[\rho]$ refers to some approximate kinetic-energy functional.

An overview of different approximate kinetic-energy functionals has already been given in Chapter 2. Here, only a brief overview of the approximate functionals that are commonly used in combination with the FDE scheme is given. It should be noted that the requirements on the approximate kinetic-energy functionals for the use in FDE are quite different from those in orbital-free DFT. Since only a relatively small part of the kinetic energy has to be described by the approximate functional, even functionals that perform poorly in orbital-free DFT can provide reasonable results in FDE.

The simplest approximation for the kinetic-energy functional, corresponding to the local-density approximation for exchange and correlation, is the Thomas-Fermi functional,

$$\tilde{T}_s^{\mathrm{TF}}[\rho] = C_{TF} \int \rho^{5/3}(\boldsymbol{r}) d\boldsymbol{r}. \tag{3.27}$$

For the construction of GGA kinetic energy functionals, the suggestion of Lee, Lee and Parr[55] to use similar analytical forms for approximated kinetic-energy and exchange energy functionals can be applied, i.e.,

$$\tilde{E}_{\mathrm{x}}^{\mathrm{GGA}}[\rho] = -C_{\mathrm{x}} \int \rho^{4/3}(\boldsymbol{r}) F(s(\boldsymbol{r})) d\boldsymbol{r}, \tag{3.28}$$

and

$$\tilde{T}_s^{\mathrm{GGA}}[\rho] = C_{\mathrm{F}} \int \rho^{5/3}(\boldsymbol{r}) F(s(\boldsymbol{r})) d\boldsymbol{r}, \tag{3.29}$$

where $C_{\mathrm{x}} = \frac{3}{4}\left(\frac{3}{\pi}\right)^{1/3}$, $C_{TF} = \frac{3}{10}\left(\frac{3}{\pi^2}\right)^{2/3}$ and $s(\boldsymbol{r}) = \frac{1}{2(3\pi^2)^{1/3}}\frac{|\nabla\rho(\boldsymbol{r})|}{\rho(\boldsymbol{r})^{4/3}}$.

In a series of studies,[40,56,57] Wesolowski and co-workers compared the accuracy of different approximate kinetic-energy functionals, including the TF functional and several GGA functionals, for different hydrogen-bound complexes. In particular, they investigated FH$\cdots$NCH (Ref. [56]), HCN$\cdots$H$_2$ (Ref. [57]) and a test set consisting of $(H_2O)_2$, $(HF)_2$, $(HCl)_2$, and HF$\cdots$NCH (Ref. [40]).

By comparing results of freeze-and-thaw FDE calculations to supermolecular KS-DFT calculations it is found that the functional that yields the most accurate interacting energies for the investigated complexes is the GGA functional which has the same analytic form of the enhancement factor $F(s)$ as the exchange functional of Perdew and Wang[22] but should be reparametrized for the kinetic energy as described by Lembarki and Chermette.[58] This functional is commonly dubbed PW91k. The complete form of its enhancement factor reads,

$$F_{\mathrm{LC94}}(s) = \frac{1 + 0.093907s\,\mathrm{arcsinh}(76.32s) + \left(0.26608 - 0.0809615e^{-100s^2}\right)s^2}{1 + 0.093907s\,\mathrm{arcsinh}(76.32s) + 0.57767\times10^{-4}s^4}. \quad (3.30)$$

For the complexes that were considered, the interaction energies calculated using the PW91k functional agree very well with those from supermolecular KS-DFT calculations. However, when comparing dipole moments and electron densities, this agreement is not as good as for the interaction energies. In addition, it is found that approximate kinetic-energy functionals which are accurate for the energy are not necessarily as accurate for the electron density, i.e., for a given approximate kinetic energy functional $T_s[\rho]$ there is in general no link between the quality of $\tilde{T}_s^{\mathrm{nadd}}[\rho_{\mathrm{I}}, \rho_{\mathrm{II}}] = \tilde{T}_s[\rho_{\mathrm{I}} + \rho_{\mathrm{II}}] - \tilde{T}_s[\rho_{\mathrm{I}}] - \tilde{T}_s[\rho_{\mathrm{II}}]$ and $\tilde{v}_T[\rho_{\mathrm{I}}, \rho_{\mathrm{II}}](\boldsymbol{r}) = \left.\frac{\delta\tilde{T}_s[\rho]}{\delta\rho}\right|_{\rho=\rho_{\mathrm{tot}}(\boldsymbol{r})} - \left.\frac{\delta\tilde{T}_s[\rho]}{\delta\rho}\right|_{\rho=\rho_{\mathrm{I}}(\boldsymbol{r})}$. Nevertheless, the PW91k functional has been used in most applications of the FDE scheme and has also been used throughout this work (if not stated otherwise).

In Chapter 5, a new class of approximations to the kinetic-energy component v_T is introduced, which do not rely on Eq. (3.26) anymore. Instead, v_T is approximated directly by making use of its known exact behavior in a well-defined limit.

3.6. Extension to time-dependent DFT

A time-dependent linear-response generalization of the FDE scheme was derived by Casida and Wesolowski.[59] Under the assumption that the response to an external electromagnetic field in resonance with an electronic transition of the embedded molecule is localized at the nonfrozen subsystem, i.e., that the response of the frozen environ-

ment can be neglected, this leads—in addition to the kernel within the adiabatic local density approximation (ALDA) in conventional TDDFT—to an effective embedding kernel (see the supplementary material to Ref.[60]),

$$f_{\mathrm{xc}}^{\mathrm{emb}}(\boldsymbol{r}, \boldsymbol{r}') = \left.\frac{\delta^2 E_{\mathrm{xc}}[\rho]}{\delta\rho(\boldsymbol{r})\delta\rho(\boldsymbol{r}')}\right|_{\rho=\rho_{\mathrm{I}}+\rho_{\mathrm{II}}} - \left.\frac{\delta^2 E_{\mathrm{xc}}[\rho]}{\delta\rho(\boldsymbol{r})\delta\rho(\boldsymbol{r}')}\right|_{\rho=\rho_{\mathrm{I}}} + \frac{\delta^2 T_s^{\mathrm{nadd}}[\rho_{\mathrm{I}}, \rho_{\mathrm{II}}]}{\delta\rho_{\mathrm{I}}(\boldsymbol{r})\delta\rho_{\mathrm{I}}(\boldsymbol{r}')}, \quad (3.31)$$

which now also contains a contribution of the nonadditive kinetic energy. This contribution is, for consistency with the ALDA-kernel, approximated by using the (local density) Thomas–Fermi functional in Eq. (3.31). In this effective embedding kernel, the additional term depending on the solvent response function in the exact formulation in Ref. 59 is assumed to be negligible, and the exchange–correlation kernel in Eq. (3.31) is evaluated for the density ρ_{II} of the ground-state calculation. In an initial application, this TDDFT extension has been shown to be able to describe localized excitations in DNA base pairs accurately.[60]

Recently, Neugebauer derived a more general formulation by reformulating the formal TDDFT extension by Casida and Wesolowski in a finite basis set.[61] In this formulation, it is not necessary to neglect the response of the environment and it is possible to describe couplings between excitations in different subsystems. In addition to this exact formulation, he also suggests an approximate treatment, in which only a few couplings are included and demonstrates that this is sufficient to describe coupled excitations in a benzaldehyde dimer.

3.7. Extension to WFT-in-DFT embedding

Carter and co-workers have extended the FDE formalism to an WFT-in-DFT embedding scheme.[62,63] Starting from a partitioning of the total system into two subsystems, the total energy of the system can be expressed as

$$E_{\mathrm{tot}} = E_{\mathrm{I}} + E_{\mathrm{II}} + E_{\mathrm{int}}, \quad (3.32)$$

where the energy E_{I} of subsystem I will be described using wave-function based methods, the energy E_{II} of subsystem II will be described using DFT, and the interaction energy will also be treated using DFT. In DFT, this interaction energy between subsystem I (characterized by its electron density ρ_{I}) and subsystem II (characterized by its electron density ρ_{II}) is given by

$$E^{\mathrm{int}}[\rho_{\mathrm{I}}, \rho_{\mathrm{II}}] = E_{\mathrm{NN}}^{\mathrm{int}} + \int \rho_{\mathrm{I}}(\boldsymbol{r})v_{\mathrm{II}}^{\mathrm{nuc}}(\boldsymbol{r}) \, d\boldsymbol{r} + \int \rho_{\mathrm{II}}(\boldsymbol{r})v_{\mathrm{I}}^{\mathrm{nuc}}(\boldsymbol{r}) \, d\boldsymbol{r}$$
$$+ \int \frac{\rho_{\mathrm{I}}(\boldsymbol{r})\rho_{\mathrm{II}}(\boldsymbol{r}')}{|\boldsymbol{r} - \boldsymbol{r}'|} \, d\boldsymbol{r} d\boldsymbol{r}' + E_{xc}^{\mathrm{nadd}}[\rho_{\mathrm{I}}, \rho_{\mathrm{II}}] + T_s^{\mathrm{nadd}}[\rho_{\mathrm{I}}, \rho_{\mathrm{II}}], \quad (3.33)$$

where $E_{\text{NN}}^{\text{int}}$ is the interaction energy between the nuclei in the two subsystems, and E_{xc}^{nadd} and T_s^{nadd} are the nonadditive exchange-correlation and kinetic energies as defined in Eq. (3.3) and Eq. (3.6), respectively. As in the FDE scheme, the KS orbitals of the total system and the KS orbitals of subsystem I, which is treated using wave function based methods, are not available, so that an approximate kinetic-energy functional has to be used for the nonadditive kinetic energy.

The embedding potential for subsystem I due to the environment in subsystem II can now be obtained as functional derivative of the interaction energy E_{int} with respect to ρ_{I}, and one obtains the effective embedding potential

$$v_{\text{eff}}^{\text{emb}}[\rho_{\text{I}}, \rho_{\text{II}}](\boldsymbol{r}) = v_{\text{II}}^{\text{nuc}}(\boldsymbol{r}) + \int \frac{\rho_{\text{II}}(\boldsymbol{r'})}{|\boldsymbol{r} - \boldsymbol{r'}|}d\boldsymbol{r'} + \frac{\delta E_{\text{xc}}^{\text{nadd}}[\rho_{\text{I}}, \rho_{\text{II}}]}{\delta\rho_{\text{I}}} + \frac{\delta T_s^{\text{nadd}}[\rho_{\text{I}}, \rho_{\text{II}}]}{\delta\rho_{\text{I}}},$$

(3.34)

which is the same as the embedding potential of Eq. (3.16). All of the terms in this equation are evaluated using DFT, and this embedding potential is included in the one-electron part of the Fock matrix in the WFT treatment.

Carter and co-workers applied this WFT-in-DFT embedding scheme to investigate atoms and molecules adsorbed on metallic surfaces. While they use a periodic DFT description for the metal, the adsorbed molecule is treated more accurately using wave-function based methods. For the WFT part they applied different configuration interaction (CI) and complete active space SCF (CASSCF) methods. These allow an easy construction of the electron density, that is needed for the construction of the embedding potential.

In their initial setup,[63] the total electron density ρ_{tot} is obtained from a periodic DFT calculation on the total system. This total electron density is kept fixed in the following, and ρ_{I} (and implicitly also ρ_{II}) is determined from a wave-function calculation. Using a starting density for ρ_{I}, the embedding potential $v_{\text{eff}}^{\text{emb}}[\rho_{\text{I}}, \rho_{\text{tot}} - \rho_{\text{I}}]$ is constructed, and a new density ρ_{I} is obtained from a wave-function calculation employing this embedding potential. The new ρ_{I} is then used to update the embedding potential, and this procedure is repeated iteratively until convergence is reached.

In an improved setup,[64,65] the restriction that ρ_{tot} has to be kept fixed is relaxed. Instead, an initial density $\rho_{\text{I}}^{\text{bare}}$ of subsystem I is obtained from an isolated wave-function calculation, and the density $\rho_{\text{II}} = \rho_{\text{tot}} - \rho_{\text{I}}^{\text{bare}}$ is kept frozen in the following. As before, the embedding potential $v_{\text{eff}}^{\text{emb}}[\rho_{\text{I}}, \rho_{\text{II}}]$ is constructed, an updated ρ_{I} is obtained, and a new embedding potential is constructed. Again, this procedure is repeated until convergence is reached.

There is also work in progress using a slightly different scheme.[66] The embedding potential can also be obtained from a standard FDE calculation, either using an approximate environment density or "freeze-and-thaw" cycles. The effective embedding

potential from this FDE calculation can subsequently be used in a wave-function calculation on subsystem I. In contrast to the previous schemes, the embedding potential is constructed using the DFT density for subsystem I, instead of the density from the wave-function calculation. This scheme has the advantage that only a single wave-function calculation is required, and that it is not necessary to obtain the electron density from the wave-function calculation (which is rather demanding for many advanced methods). However, it will only be applicable if the density of subsystem I can be approximated rather accurately using DFT.

Carter and co-workers have applied their WFT-in-DFT embedding scheme to study the adsorption of CO on a Cu(111) surface[62,63] and to describe localized electronic excitations in a CO molecule adsorbed on a Pd(111) surface.[67,68] Furthermore, they have investigated the adsorption of a cobalt atom on a Cu(111) surface,[64] and they were able to obtain the experimentally observed spin-compensated ground-state, in contrast to the results of a conventional DFT treatment.

3.8. Review of applications of FDE

Since they were first proposed in 1991 and 1993, respectively, the subsystem formulation of DFT and the FDE scheme have been applied in a number of studies of small complexes, solid state systems, simulations of the condensed phase as well as investigations of biological systems. In this section, a brief overview of these applications will be given. However, this overview will probably not be complete. An extensive overview of the applications of the FDE scheme carried out by Wesolowski and co-workers is given in Ref. 48.

In their initial papers,[8,49] Wesolowski and Warshel investigated the solvation of a lithium ion in water and the solvation free energy of liquid water and methane. In these studies, the frozen solvent environments were constructed by using a superposition of the densities of isolated water or methane molecules, as described above.

Subsequently, Wesolowski and co-workers have performed a number of detailed studies[40,52,56,57] investigating the accuracy of different kinetic-energy functionals for hydrogen-bound complexes by comparing interaction energies obtained from "freeze-and-thaw" FDE calculations to those calculated in conventional KS-DFT calculation. This work has been followed up in studies on different sets of hydrogen-bound complexes, both for interaction energies[69] as well as for equilibrium structures.[70] However, these later studies focus on the comparison to high-level *ab initio* results, and in this case fortunate error cancellations might mask inaccuracies in the nonadditive kinetic-energy functionals used.

Similarly, it was found in studies on van der Waals complexes [of C_6H_6 and O_2, N_2,

CO (Ref. 71), of carbazole and Ne, Ar, CH_4, CO, N_2 (Ref. 72), and a large test set of complexes containing Ne, Ar, F_2, N_2, C_2H_2, C_2H_4, C_2H_6, C_3H_6, C_3H_8, C_6H_6, C_2F_6, (Ref. 73)], that interaction energies calculated in "freeze-and-thaw" FDE calculations agree better with *ab initio* benchmark data than conventional KS-DFT calculation. However, this better agreement is due to a fortunate error cancellation.

In contrast, in Chapter 8 (Ref. CJ3) a different type of study on $CO_2 \cdots X$ (X=He, Ne, Ar, Kr, Xe, Hg) van der Waals complexes is presented, that focuses on the identification of possible problem in the kinetic-energy functional by comparing the dipole moments calculated in "freeze-and-thaw" FDE calculations to those obtained in conventional KS-DFT calculations. The problems identified there were investigated in more detail in later works.[CJ7,74]

Besides these works that mainly focus on the theoretical aspects of the FDE scheme, it has also been applied to tackle problems from different areas of chemistry and physics. Most important, it has been used to determine various molecular properties of molecules in different environments. Wesolowski investigated the electron spin resonance (ESR) hyperfine coupling constants (hfcc's) of Mg^+ in Ne and Ar matrices, where the matrix environment was represented by a small cluster of rare gas atoms.[75] ESR hfcc's were also investigated by Neugebauer *et al.*, who studied H_2NO in water.[50] In both cases, a good agreement between the calculated hfcc's and the experimental values was found.

Solvent effects on different molecular properties have been looked at by Neugebauer and co-workers. In all these works, the solvent environment is approximated as a sum of the densities of isolated solvent molecules. To account for the dynamics of the solvent, the properties were calculated for a large number (several hundreds) of snapshots obtained from classical or Car-Parrinello molecular dynamics simulations, and the results were averaged. These very demanding calculations have been made possible by the efficiency of the FDE scheme, which allows the inclusion of solvent environments consisting of up to 1000 atoms.

Using this strategy, solvatochromic shifts, i.e., shifts in electronic excitation energies due to the solvent, have been investigated for acetone in water[76] and for the organic dye aminocoumarin C151 in *n*-hexane and in water.[CJ4] As mentioned above, solvent effects on ESR hfcc's have also been successfully calculated.[50] In Chapter 9 (Ref. CJ5) a systematic comparison of the FDE scheme to QM/MM methods for the description of solvent effects of different molecular properties will be presented.

Warshel and co-workers have applied the FDE scheme for calculations of free-energy surfaces of chemical reactions in solution and in biological environments. In combination with free energy perturbation (FEP) calculations using empirical valence bond (EVB) reference surfaces, they investigated the proton transfer reaction $F^- + HF \rightarrow FH + F^-$ in aqueous solution,[77] as well as the autodissociation of water in aqueous

solution.[78] They further studied the proton transfer between two water molecules in a $(Im)_3Zn^{2+}H_2O$ (Im = imidazole) complex, which is a model system for proton transfer reactions in zinc containing metalloenzymes.[79] Using similar techniques and by combining the FDE description of the active center of the protein to an MM treatment of the remaining parts of the protein, they were also able to calculate the redox potentials of the redox proteins plastocyanin and rusticyanin.[80]

More complex environments were also used in a study of the adsorption of CO in zeolites, in which the geometry and vibrational frequency of CO in different zeolite environments was investigated,[81] and in a theoretical investigation of the mechanism of the enzymatic reduction of nitrate, in which the frozen enzyme environment was modeled by four neighboring amino acids.[82]

The TDDFT extension of FDE,[59] initially benchmarked for DNA base pairs,[60] was employed in several different applications. It was used in the above mentioned studies of solvatochromic shifts[CJ4,CJ5,76] as well as for the calculation of polarizabilities.[CJ5] Furthermore, it has been used by Neugebauer *et al.* to describe induced circular dichroism (CD) in host–guest systems.[83] They studied the CD spectrum of a complex of 2-benzoylbenzoic acid with (−)-(R)-amphetamine and for a complex of L-leucine with an artificial amino acid receptor system. In both cases, a good agreement of the FDE results with supermolecular calculations was found. However, for a system consisting of phenole in a cyclodextrin cavity problems were found because FDE cannot describe couplings between excitations in the different subsystems. These deficiencies were solved by the subsystem TDDFT formalism introduced by Neugebauer in a later work.[61]

A number of questions from the area of solid state physics have been investigated using the FDE scheme, too. In an early study, Stefanovich and Troung investigated the adsorption of H_2O on a NaCl(001) surface.[84] They modeled the NaCl surface by using a frozen density, that was obtained as a sum of the (spherical) densities of the isolated Na^+ and Cl^- ions. Trail and Bird explored the ability of the FDE scheme to correctly describe the electron density in a unit cell of bulk aluminum.[85] The good agreement found in these applications is particularly interesting, since in these cases the interaction with the environment is rather strong. However, in the case of metals, this strong interaction can be accurately modeled by simple approximate kinetic-energy functionals, while this is not possible for molecular systems.

Choly *et al.* used the FDE scheme in molecular dynamics (MD) simulations to couple a DFT description of a small part of bulk aluminum with a more approximate treatment of the remaining bulk aluminum in the environment. The dynamics in this environment is described using classical potentials,[86] while for the smaller part of interest, an FDE-based description is employed. To model the electron density of the environment that is needed for the construction of the embedding potential, they

employed a superposition of the spherical densities of isolated aluminum atoms.

Properties of localized defects in solids have been investigated using FDE by García-Lastra *et al.*, who studied both crystal field splittings as well as changes in vibrational frequencies of MnF_6^{4-} subunits in Mn^{2+}-doped flouroperovskites.[87] Similarly, Zbiri *et al.* studied the crystal field splittings of lanthanide cations in chloroelpasolite crystals[88] and in elpasolite crystals.[89]

It has to be mentioned that also the subsystem DFT formulation has been used in several works on solid state systems. In the scheme initially proposed by Cortona,[51] the atoms of a crystal are treated as individual subsystems, and the electron density of each of these subsystems is optimized individually. However, in Cortona's scheme, the atomic densities are constraint to be spherical, and the potential is spherically averaged. This scheme has been applied to study several ionic crystals, such as alkali halides,[90] MgO and CaO,[91] alkali-earth sulfides,[92] alkali-earth oxides,[93] CaS, CaSe, and CaTe,[94] magnesium oxide,[95] as well as SrSe and SrTe.[96] Cortona's scheme has been extended by Boyer and Mehl,[97] who removed the constraint of spherical atomic densities and allowed deformations of the atomic densities. Using this method, which they called self-consistent atomic deformation (SCAD) method, alkali halides[98] and corundum (Al_2O_3)[99] have been studied.

Finally, the subsystem DFT formulation has been employed to perform molecular dynamics simulations of the condensed phase. Hutter and co-workers implemented an MD algorithm based on subsystem DFT in the CP2K package[100,101] and performed MD simulations of water at ambient conditions.[53] However, the pair distribution functions they obtained showed only an unstructured second solvation shell, and they attributed this wrong description to shortcomings of the approximate kinetic-energy functionals. Shimojo *et al.* developed another MD code based on subsystem DFT, using an efficient numerical integration scheme employing hierarchical real-space grids.[54] They have applied their implementation to MD simulations of aluminum nanoparticles and of nanoindentation of ceramics materials.[102]

3. Frozen-density embedding

Part II.

Theoretical Extensions

4. Calculation of nuclear magnetic resonance shieldings

Abstract

We have extended the frozen-density embedding (FDE) scheme within density-functional theory to include external magnetic fields and applied this extension to the nonrelativistic calculation of nuclear magnetic resonance (NMR) shieldings. This leads to a formulation in which the electron density and the induced current are calculated separately for the individual subsystems. If the current-dependence of the exchange-correlation functional and of the nonadditive kinetic-energy functional are neglected, the induced currents in the subsystems are not coupled and each of them can be determined without knowledge of the induced current in the other subsystem. This allows the calculation of the NMR shielding as a sum of contributions of the individual subsystems. As a test application, we have calculated the solvent shifts of the nitrogen shielding of acetonitrile for different solvents using small geometry-optimized clusters consisting of acetonitrile and one solvent molecule. By comparing to the solvent shifts obtained from supermolecular calculations we assess the accuracy of the solvent shifts obtained from FDE calculations. We find a good agreement between supermolecular and FDE calculations for different solvents. In most cases it is possible to neglect the contribution of the induced current in the solvent subsystem to the NMR shielding, but it has to be considered for aromatic solvents. We demonstrate that FDE can describe the effect of induced currents in the environment accurately.

4.1. Introduction

Nuclear magnetic resonance (NMR) spectroscopy is one of the most important and powerful tools in chemistry and biochemistry and quantum-chemical calculations of NMR parameters have developed into a routine task (for reviews, see Refs. [103] and [104]). Often these calculations assist in the assignment of NMR spectra and their interpretation (see, e.g., Refs. [105–109]). Due to its ease of application and computational efficiency, density-functional theory (DFT) is the standard method for the calculation of NMR parameters.

In the past years, there is an increasing interest in quantum-chemical calculations of NMR parameters for large systems (with a few hundred atoms), e.g., biological systems or molecules in solution or in other complex environments, and methods that show a linear scaling with the system size have been implemented for the Hartree-Fock and DFT calculations of NMR parameters.[110,111] However, even with linear scaling of the computational effort these methods still have high computational requirements for many systems of interest, since they require a full quantum-mechanical treatment of the whole system.

The NMR shielding describes the induced current near the NMR active nucleus, with the nuclear magnetic moment acting as a probe. Because the operator corresponding to this nuclear magnetic moment is relatively short ranged, scaling as r^{-2} with the distance r to the nucleus, the NMR shielding can be regarded as a rather "near-sighted" property. Therefore, it is often possible to focus on a subsystem that is close to the NMR active nucleus, avoiding the quantum-mechanical treatment of the full system. One possible way of exploiting this near-sightedness of the NMR shielding are methods that treat only a small part of the system containing the NMR active nuclei explicitly quantum mechanically, while a more approximate method is chosen to represent the environment. The most prominent example of methods following this strategy are combined quantum mechanics / molecular mechanics (QM/MM) methods.[4,112] However, the success of QM/MM methods relies on the careful parametrization of the force field used in the MM part.

For the special case that the environment is formed by a solvent, continuum solvation models, in which the solvent environment is described as a continuous medium characterized by its dielectric constant, can be employed for the calculation of NMR parameters.[113–115] While it is clear that continuum models are able to correctly describe unspecific solvent effects, i.e., dielectric medium effects, problems may appear in the description of specific effects such as hydrogen bonding. Especially for the calculation of NMR shieldings it has been found that it is necessary to combine the continuum description with the explicit inclusion of a number of solvent molecules.[116–118]

Frozen-density embedding (FDE), originally introduced by Wesolowski and Warshel,[8,48]

offers an appealing alternative for the DFT calculation of NMR shieldings in large systems. The FDE scheme is based on a partitioning into separate subsystems, which are each calculated separately, with the effect of the other (frozen) subsystems represented by an effective embedding potential which only depends on their charge density. Even though the construction of this embedding potential requires the use of an approximate kinetic-energy functional, the FDE scheme itself is in principle exact. It thus allows it to exploit the near-sightedness of the NMR shielding by focusing on the subsystem containing the NMR active nuclei while still keeping the quantum-mechanical treatment of the full system.

In this Chapter, we will extend the FDE formalism to the calculation of NMR shieldings and test the method for the calculation of solvent shifts of NMR shieldings, using small solute–solvent clusters.

This Chapter is organized as follows. First, we will present the theory of the calculation of NMR shieldings using frozen-density embedding in Sec. 4.2. After a brief review of nonrelativistic current density-functional theory in Sec. 4.2.1 and of the nonrelativistic DFT calculation of NMR shieldings in Sec 4.2.2, we present the theory of frozen-density embedding for systems in magnetic fields in Sec. 4.2.3. This theory is then applied to the calculation of NMR shieldings using FDE in Sec. 4.2.4. In Sec. 4.3 computational details are given, and in Sec. 4.4, the FDE formalism is applied to the calculation of the solvent shift of the nitrogen NMR shielding in acetonitrile. Concluding remarks follow in Sec. 4.5

4.2. Theory

4.2.1. Nonrelativistic current density-functional theory

The starting point for the nonrelativistic DFT calculation of NMR shieldings is the generalization of DFT to include magnetic fields, which is given by current density functional theory (CDFT) as it was first formulated for closed-shell systems by Vignale and Rasolt.[119] This requires to consider not only the electron density $\rho(\boldsymbol{r})$ as the basic variable, but also the current density $\boldsymbol{j}(\boldsymbol{r})$. They show that in order to prove an analog of the Hohenberg-Kohn theorem, it is necessary to use the electron density $\rho(\boldsymbol{r})$ and the paramagnetic current $\boldsymbol{j}_p(\boldsymbol{r}) = \boldsymbol{j}(\boldsymbol{r}) + \rho(\boldsymbol{r})\boldsymbol{A}(\boldsymbol{r})$ as basic variables, i.e., the (gauge-dependent) paramagnetic current $\boldsymbol{j}_p$ has to be used instead of the (gauge-invariant) total current $\boldsymbol{j}$.[119,120]

In the following, we will always consider a closed-shell system with N doubly occupied orbitals and with $2N$ electrons. For such a system in an external magnetic field the

4. Calculation of NMR shieldings

total energy functional is given by

$$E[\rho, \boldsymbol{j}_p] = T_s[\rho, \boldsymbol{j}_p] + \int v_{\text{nuc}}(\boldsymbol{r})\rho(\boldsymbol{r})\ d\boldsymbol{r}$$
$$- \int \boldsymbol{j}_p(\boldsymbol{r})\boldsymbol{A}(\boldsymbol{r})\ d\boldsymbol{r} + \frac{1}{2} \int \rho(\boldsymbol{r})A^2(\boldsymbol{r})\ d\boldsymbol{r}$$
$$+ \int \frac{\rho(\boldsymbol{r})\rho(\boldsymbol{r}')}{|\boldsymbol{r} - \boldsymbol{r}'|}\ d\boldsymbol{r} + E_{\text{xc}}[\rho, \boldsymbol{j}_p]. \tag{4.1}$$

We are using Hartree atomic units throughout this paper and have used the Coulomb gauge for the external vector potential ($\nabla \boldsymbol{A} = 0$). In the above expression, the external scalar potential v_{nuc} is the electrostatic potential of the nuclei and the external vector potential $\boldsymbol{A}(\boldsymbol{r})$ corresponds to the magnetic field. The total energy functional contains terms for the noninteracting kinetic energy, the electron–nuclei attraction, the interaction of the current and of the electron density with the external vector potential, the Coulomb repulsion of the electrons, and the exchange-correlation energy, which now also depends on the current.

The noninteracting kinetic energy $T_s[\rho, \boldsymbol{j}_p]$ is the kinetic energy of a reference system of noninteracting electrons having the same electron density ρ and paramagnetic current $\boldsymbol{j}_p$ as the interacting system. For such a system, the wave function is given by one single Slater determinant. The electron density is then given by

$$\rho(\boldsymbol{r}) = 2 \sum_{i=1}^{N} \phi_i^*(\boldsymbol{r})\phi_i(\boldsymbol{r}), \tag{4.2}$$

and the paramagnetic current is given by

$$\boldsymbol{j}_p(\boldsymbol{r}) = i \sum_{i=1}^{N} \{\phi_i^*(\boldsymbol{r})\nabla\phi_i(\boldsymbol{r}) - \phi_i(\boldsymbol{r})\nabla\phi_i^*(\boldsymbol{r})\}. \tag{4.3}$$

In this definition of the paramagnetic current the negative unit charge of the electron and the double occupation of the orbitals have been included.

Minimization of the total energy functional with respect to the Kohn–Sham (KS) orbitals $\{\phi_i\}$ of this noninteracting reference system under the constraint that the KS orbitals are orthonormal leads to KS equations for the determination of the KS orbitals $\{\phi_i\}$,

$$\left[\frac{1}{2}\left(-i\nabla + \boldsymbol{A}(\boldsymbol{r})\right)^2 + \frac{i}{2}\ \boldsymbol{A}_{\text{xc}}(\boldsymbol{r})\nabla + v_{\text{eff}}^{\text{KS}}[\rho](\boldsymbol{r})\right] \phi_i(\boldsymbol{r}) = \epsilon_i\ \phi_i(\boldsymbol{r}). \tag{4.4}$$

The KS effective potential $v_{\text{eff}}^{\text{KS}}[\rho]$ contains the usual terms of the nuclear potential, the Coulomb potential of the electrons and the exchange-correlation potential. In

addition, $\boldsymbol{A}_{\mathrm{xc}}(\boldsymbol{r}) = \frac{\delta E_{\mathrm{xc}}[\rho, \boldsymbol{j}_p]}{\delta \boldsymbol{j}_p(\boldsymbol{r})}$ enters these equations because of the current dependence of the exchange-correlation functional. It can be shown[119] that these one-electron equations are gauge invariant and that the total current $\boldsymbol{j}(\boldsymbol{r}) = \boldsymbol{j}_p(\boldsymbol{r}) - \rho(\boldsymbol{r})\boldsymbol{A}(\boldsymbol{r})$ obtained from it satisfies the continuity equation

$$\nabla \cdot \boldsymbol{j}(\boldsymbol{r}) + \frac{\partial \rho(\boldsymbol{r})}{\partial t} = 0. \tag{4.5}$$

For the calculation of NMR parameters, the current dependence of the exchange-correlation functional is usually neglected. This approximation is often referred to as "uncoupled DFT". In this case, the KS equations for systems in a magnetic field reduce to

$$\left[\frac{1}{2} \left(-i\nabla + \boldsymbol{A}(\boldsymbol{r})\right)^2 + v_{\mathrm{eff}}^{\mathrm{KS}}[\rho](\boldsymbol{r}) \right] \phi_i(\boldsymbol{r}) = \epsilon_i \; \phi_i(\boldsymbol{r}). \tag{4.6}$$

These equations can also be obtained from the usual KS equations by substitution of the momentum operator $\hat{p} = -i\nabla$ with $\hat{p} + \boldsymbol{A}(\boldsymbol{r})$.

4.2.2. Nonrelativistic DFT calculation of NMR shieldings

The NMR shielding tensor can be expressed in terms of the first-order current induced by a homogeneous external magnetic field, which is probed by the nuclear magnetic moment of the nucleus in question, as[121]

$$\sigma_{st} = -\frac{1}{c^2} \int \left[\frac{(\boldsymbol{r} - \boldsymbol{R}_{\mathrm{nuc}}) \times \boldsymbol{j}^{B_t}(\boldsymbol{r})}{|\boldsymbol{r} - \boldsymbol{R}_{\mathrm{nuc}}|^3} \right]_s d\boldsymbol{r}. \tag{4.7}$$

In this expression, the subscripts s and t refer to the individual Cartesian components, $\boldsymbol{R}_{\mathrm{nuc}}$ is the position of the NMR nucleus and the first-order induced current is given by $\boldsymbol{j}^{B_t}(\boldsymbol{r}) = \frac{\partial \boldsymbol{j}(\boldsymbol{r})}{\partial B_t}$, where the derivative is taken with respect to the Cartesian components of the external magnetic field $\boldsymbol{B}$.

As in the previous section, the induced current can be split up into a paramagnetic and a diamagnetic part,

$$\boldsymbol{j}^{B_t}(\boldsymbol{r}) = \boldsymbol{j}_p^{B_t}(\boldsymbol{r}) - \rho(\boldsymbol{r}) \frac{\partial \boldsymbol{A}(\boldsymbol{r})}{\partial B_t}. \tag{4.8}$$

With this decomposition, the shielding tensor can then also be written as a sum of a diamagnetic and a paramagnetic part,

$$\sigma_{st} = \sigma_{st}^D + \sigma_{st}^P. \tag{4.9}$$

4. Calculation of NMR shieldings

The diamagnetic part of the shielding tensor is given by

$$\sigma_{st}^{D} = \frac{1}{c^2} \int \left[\frac{(\boldsymbol{r} - \boldsymbol{R}_{\mathrm{nuc}}) \times \rho(\boldsymbol{r}) \frac{\partial \boldsymbol{A}(\boldsymbol{r})}{\partial B_t}}{|\boldsymbol{r} - \boldsymbol{R}_{\mathrm{nuc}}|^3} \right]_s dr = \int h_{st}^{11} \; \rho(\boldsymbol{r}) \; dr, \tag{4.10}$$

with the diamagnetic shielding operator

$$h_{st}^{11} = \frac{1}{2} \; \frac{\boldsymbol{r} \cdot (\boldsymbol{r} - \boldsymbol{R}_{\mathrm{nuc}}) \; \delta_{st} - r_s (r - R_{\mathrm{nuc}})_t}{|\boldsymbol{r} - \boldsymbol{R}_{\mathrm{nuc}}|^3}. \tag{4.11}$$

(We have followed the usual convention of specifying the order of the perturbation operator in the external magnetic field as superscripts.) The diamagnetic part only depends on the unperturbed electron density and does not require the knowledge of the perturbed orbitals.

The paramagnetic part of the shielding tensor is given by

$$\sigma_{st}^{P} = -\frac{1}{c^2} \int \left[\frac{(\boldsymbol{r} - \boldsymbol{R}_{\mathrm{nuc}}) \times \boldsymbol{j}_p^{B_t}(\boldsymbol{r})}{|\boldsymbol{r} - \boldsymbol{R}_{\mathrm{nuc}}|^3} \right]_s dr \tag{4.12}$$

and requires the knowledge of the first-order induced paramagnetic current $\boldsymbol{j}_p^{B_t}$, which can be determined from the response of the KS orbitals to a homogeneous external magnetic field. As described in the previous section, CDFT has to be used to describe systems in magnetic fields and in the approximation of uncoupled DFT, i.e., neglecting the current dependence of the exchange-correlation functional, the KS equations in the presence of a magnetic field are given by Eq. (4.6). To first order in the magnetic field strength, the perturbation that is introduced in these equations by a homogeneous external magnetic field is given by

$$\boldsymbol{h}^{10} = -\frac{i}{2} \; (\boldsymbol{r} \times \nabla). \tag{4.13}$$

This perturbation operator is purely imaginary, which implies that the first-order perturbed orbitals will also be purely imaginary and that the first-order change in the electron density vanishes.[122]

Choosing the unperturbed KS orbitals as real so that the first-order perturbed orbitals are purely imaginary, the first-order induced paramagnetic current can be expressed in terms of the KS orbitals as

$$\boldsymbol{j}_p^{B_t}(\boldsymbol{r}) = 2i \sum_{i=1}^{N} \left\{ \phi_i^{(0)}(\boldsymbol{r}) \nabla \phi_i^{B_t}(\boldsymbol{r}) \; - \; \phi_i^{B_t}(\boldsymbol{r}) \nabla \phi_i^{(0)}(\boldsymbol{r}) \right\}, \tag{4.14}$$

where the superscript (0) is used to refer to the KS orbitals of the unperturbed system and the first-order perturbed orbitals $\phi_i^{B_t}(\boldsymbol{r}) = \frac{\partial \phi_i(\boldsymbol{r})}{\partial B_t}$ describe the response of the KS orbitals to a homogeneous external magnetic field.

The first-order perturbed orbitals are usually determined by expanding them in terms of the canonical KS orbitals of the unperturbed system as

$$\phi_i^{B_t}(\boldsymbol{r}) = \sum_j u_{ij,t}\ \phi_j^{(0)}(\boldsymbol{r}), \tag{4.15}$$

where the coefficients u_{ij} can easily be determined from

$$u_{ij,t} = -\frac{\left\langle \phi_i^{(0)} \middle| h_t^{10} \middle| \phi_j^{(0)} \right\rangle}{\epsilon_i - \epsilon_j}. \tag{4.16}$$

In practical applications with atom-centered basis functions, it is necessary to ensure the gauge invariance of the above formulation. It is well known that fast basis set convergence can be achieved by employing gauge-including atomic orbitals (GIAOs),[123] i.e., by including a magnetic-field-dependent phase factor in the basis functions. This leads to additional terms in the expressions for both the diamagnetic and the paramagnetic shielding.[121] For reasons of simplicity, we will not mention these additional terms in the following, they are, however, included in the implementation that is used.

4.2.3. Frozen-density embedding for systems in external magnetic fields

In the frozen-density embedding (FDE) formalism within DFT[8,48] the total electron density $\rho_{\text{tot}}(\boldsymbol{r})$ is split up into two components $\rho^{(\text{I})}(\boldsymbol{r})$ and $\rho^{(\text{II})}(\boldsymbol{r})$, which add up to the total electron density,

$$\rho^{(\text{tot})}(\boldsymbol{r}) = \rho^{(\text{I})}(\boldsymbol{r}) + \rho^{(\text{II})}(\boldsymbol{r}). \tag{4.17}$$

Both $\rho^{(\text{I})}(\boldsymbol{r})$ and $\rho^{(\text{II})}(\boldsymbol{r})$ can then be determined separately from a set of one-electron equations in which the effect of the density in the other subsystem is represented in terms of an effective embedding potential.

To extend the FDE formalism to systems in magnetic fields, it is not sufficient to use only the electron density as a basic variable, since the energy is now also a functional of the paramagnetic current. Therefore, we make the same ansatz and split the paramagnetic current into contributions from the two separate subsystems,

$$\boldsymbol{j}_p^{(\text{tot})}(\boldsymbol{r}) = \boldsymbol{j}_p^{(\text{I})}(\boldsymbol{r}) + \boldsymbol{j}_p^{(\text{II})}(\boldsymbol{r}). \tag{4.18}$$

With these definitions, also the total current is given as the sum of the currents of the two subsystems, $\boldsymbol{j}^{(\text{tot})}(\boldsymbol{r}) = \boldsymbol{j}^{(\text{I})}(\boldsymbol{r}) + \boldsymbol{j}^{(\text{II})}(\boldsymbol{r})$. Furthermore, it has to be noticed

that if the continuity equation [Eq. (4.5)] is satisfied for each of the two subsystems individually, it is also satisfied for the total system and the above partitioning of the electron density and of the paramagnetic current are, therefore, justified in this case.

With this partitioning of the electron density and the paramagnetic current, the total energy functional for systems in magnetic fields of Eq. (4.1) can be formulated as a bifunctional in terms of the electron densities and paramagnetic currents of the two subsystems,

$$
\begin{aligned}
E[\rho^{(\mathrm{I})}, \boldsymbol{j}_p^{(\mathrm{I})}, & \rho^{(\mathrm{II})}, \boldsymbol{j}_p^{(\mathrm{II})}] = \\
& T_s[\rho^{(\mathrm{I})}, \boldsymbol{j}_p^{(\mathrm{I})}] + T_s[\rho^{(\mathrm{II})}, \boldsymbol{j}_p^{(\mathrm{II})}] + T_s^{\mathrm{nadd}}[\rho^{(\mathrm{I})}, \boldsymbol{j}_p^{(\mathrm{I})}, \rho^{(\mathrm{II})}, \boldsymbol{j}_p^{(\mathrm{II})}] \\
& + \int \left(\rho^{(\mathrm{I})}(\boldsymbol{r}) + \rho^{(\mathrm{II})}(\boldsymbol{r})\right) \left(v_{\mathrm{nuc}}^{(\mathrm{I})}(\boldsymbol{r}) + v_{\mathrm{nuc}}^{(\mathrm{II})}(\boldsymbol{r})\right) \, d\boldsymbol{r} \\
& + \int \frac{(\rho^{(\mathrm{I})}(\boldsymbol{r}) + \rho^{(\mathrm{II})}(\boldsymbol{r}))(\rho^{(\mathrm{I})}(\boldsymbol{r}') + \rho^{(\mathrm{II})}(\boldsymbol{r}'))}{|\boldsymbol{r} - \boldsymbol{r}'|} \, d\boldsymbol{r} d\boldsymbol{r}' \\
& - \int \left(\boldsymbol{j}_p^{(\mathrm{I})}(\boldsymbol{r}) + \boldsymbol{j}_p^{(\mathrm{II})}(\boldsymbol{r})\right) \boldsymbol{A}(\boldsymbol{r}) \, d\boldsymbol{r} \\
& + \frac{1}{2} \int \left(\rho^{(\mathrm{I})}(\boldsymbol{r}) + \rho^{(\mathrm{II})}(\boldsymbol{r})\right) A^2(\boldsymbol{r}) \, d\boldsymbol{r} \\
& + E_{\mathrm{xc}}[\rho^{(\mathrm{I})} + \rho^{(\mathrm{II})}, \boldsymbol{j}_p^{(\mathrm{I})} + \boldsymbol{j}_p^{(\mathrm{II})}],
\end{aligned}
\tag{4.19}
$$

where the nonadditive kinetic-energy functional T_s^{nadd} is defined as

$$
\begin{aligned}
T_s^{\mathrm{nadd}}[\rho^{(\mathrm{I})}, & \boldsymbol{j}_p^{(\mathrm{I})}, \rho^{(\mathrm{II})}, \boldsymbol{j}_p^{(\mathrm{II})}] \\
& = T_s[\rho^{(\mathrm{I})} + \rho^{(\mathrm{II})}, \boldsymbol{j}_p^{(\mathrm{I})} + \boldsymbol{j}_p^{(\mathrm{II})}] - T_s[\rho^{(\mathrm{I})}, \boldsymbol{j}_p^{(\mathrm{I})}] - T_s[\rho^{(\mathrm{II})}, \boldsymbol{j}_p^{(\mathrm{II})}].
\end{aligned}
\tag{4.20}
$$

If the densities and currents are represented using the KS orbitals of the individual subsystems, it is possible to calculate the noninteracting kinetic energy $T_s[\rho^{(\mathrm{I,II})}, \boldsymbol{j}_p^{(\mathrm{I,II})}]$ of the separate subsystems directly. However, with the partitioning of the electron density and current into the contributions of the two subsystems, the canonical KS orbitals of the total system are in general not available, so that the noninteracting kinetic energy $T_s[\rho^{(\mathrm{tot})}, \boldsymbol{j}_p^{(\mathrm{tot})}]$ of the total system cannot be calculated in this way. For this reason, in practical applications of the FDE scheme an appropriate orbital-independent approximation of T_s^{nadd} has to be applied.

The total energy bifunctional of Eq. (4.19) does not contain a current–current interaction between the currents in systems I and II. This magnetic interaction is not present in the nonrelativistic limit of electrodynamics,[122] where the electrons only interact via the Coulomb interaction, i.e., a magnetic electron–electron interaction is not included.

For a given electron density and paramagnetic current in subsystem II, the KS orbitals of subsystem I, $\{\phi_i^{(\mathrm{I})}\}$, can now be obtained by minimizing $E[\rho^{(\mathrm{I})}, \boldsymbol{j}_p^{(\mathrm{I})}, \rho^{(\mathrm{II})}, \boldsymbol{j}_p^{(\mathrm{II})}]$ with respect to the KS orbitals of subsystem I, under the constraint that these orbitals are orthonormal. This leads to a set of one-electron equations for the KS orbitals $\{\phi_i^{(\mathrm{I})}\}$,

$$
\begin{aligned}
&\left[\frac{1}{2} \left(-i\nabla + \boldsymbol{A}(\boldsymbol{r}) \right)^2 + v_{\mathrm{eff}}^{\mathrm{KSCED}}[\rho^{(\mathrm{I})}, \rho^{(\mathrm{II})}](\boldsymbol{r}) \right. \\
&\left. + i\, \frac{\delta T_s^{\mathrm{nadd}}[\rho^{(\mathrm{I})}, \boldsymbol{j}_p^{(\mathrm{I})}, \rho^{(\mathrm{II})}, \boldsymbol{j}_p^{(\mathrm{II})}]}{\delta \boldsymbol{j}_p^{(\mathrm{I})}(\boldsymbol{r})}\, \nabla + i\, \frac{\delta E_{\mathrm{xc}}[\rho^{(\mathrm{I})} + \rho^{(\mathrm{II})}, \boldsymbol{j}_p^{(\mathrm{I})} + \boldsymbol{j}_p^{(\mathrm{II})}]}{\delta \boldsymbol{j}_p^{(\mathrm{I})}(\boldsymbol{r})}\, \nabla \right] \phi_i^{(I)}(\boldsymbol{r}) \\
&= \epsilon_i \phi_i^{(I)}(\boldsymbol{r}).
\end{aligned}
\tag{4.21}
$$

These equations will, as in the case without magnetic fields, be referred to as Kohn–Sham equations with constrain electron density (KSCED). The KSCED effective potential in the above equations is given by

$$
v_{\mathrm{eff}}^{\mathrm{KSCED}}[\rho^{(\mathrm{I})}, \rho^{(\mathrm{II})}](\boldsymbol{r}) = v_{\mathrm{eff}}^{\mathrm{KS}}[\rho^{(\mathrm{I})}](\boldsymbol{r}) + v_{\mathrm{eff}}^{\mathrm{emb}}[\rho^{(\mathrm{I})}, \rho^{(\mathrm{II})}](\boldsymbol{r}),
\tag{4.22}
$$

where $v_{\mathrm{eff}}^{\mathrm{KS}}[\rho^{(\mathrm{I})}](\boldsymbol{r})$ is the KS effective potential of the isolated subsystem I containing the usual terms of the nuclear potential, Coulomb potential of the electrons, and the exchange–correlation potential. The effective embedding potential $v_{\mathrm{eff}}^{\mathrm{emb}}[\rho^{(\mathrm{I})}, \rho^{(\mathrm{II})}](\boldsymbol{r})$ describes the interaction of the subsystem I with the frozen density of subsystem II and reads

$$
\begin{aligned}
v_{\mathrm{eff}}^{\mathrm{emb}}[\rho^{(\mathrm{I})}, \rho^{(\mathrm{II})}](\boldsymbol{r}) = {}& v_{\mathrm{II}}^{\mathrm{nuc}}(\boldsymbol{r}) + \int \frac{\rho^{(\mathrm{II})}(\boldsymbol{r'})}{|\boldsymbol{r} - \boldsymbol{r'}|} d\boldsymbol{r'} \\
& + \left. \frac{\delta E_{\mathrm{xc}}[\rho]}{\delta \rho} \right|_{\rho = \rho^{(\mathrm{tot})}(\boldsymbol{r})} - \left. \frac{\delta E_{\mathrm{xc}}[\rho]}{\delta \rho} \right|_{\rho = \rho^{(\mathrm{I})}(\boldsymbol{r})} \\
& + \frac{\delta T_s^{\mathrm{nadd}}[\rho^{(\mathrm{I})}, \rho^{(\mathrm{II})}]}{\delta \rho^{(\mathrm{I})}(\boldsymbol{r})}.
\end{aligned}
\tag{4.23}
$$

The KS orbitals of subsystem I can then be obtained by solving the KSCED equations self-consistently.

If the assumption that $\rho^{(\mathrm{tot})} - \rho^{(\mathrm{II})}$ is positive and v_s-representable[17] and that $\boldsymbol{j}_p^{(\mathrm{tot})} - \boldsymbol{j}_p^{(\mathrm{II})}$ is v_s-representable is fulfilled, the solution of Eq. (4.21) will—in the case that the exact nonadditive kinetic-energy functional would be used—yield the same total electron density and total current as the solution of Eq. (4.4), i.e., as the corresponding supermolecular KS-DFT calculation (using the same approximation for the exchange-correlation functional). If the initial assumptions are not satisfied, Eq. (4.21) can be solved in "freeze-and-thaw" cycles by exchanging the role of the frozen and nonfrozen

system, i.e., by solving two coupled sets of KSCED equations for subsystems I and II.

Usually in the calculation of NMR parameters the current dependence of the exchange-correlation functional is neglected. In this case, the corresponding term drops out of the KSCED equations. However, in the case that the exact nonadditive kinetic-energy functional would be used, the solution of the KSCED equations will still yield the same solution as the supermolecular KS-DFT calculation in which the same approximation is made.

In practical applications of the FDE formalism, approximations have to be used for the nonadditive kinetic-energy functional. The approximations that are available for the nonadditive kinetic-energy functional[40] do not include a current dependence. For the calculation of NMR parameters it will, therefore, be the first choice to apply these approximations and to neglect the current dependence. It can be expected that for weakly interacting systems, where the available approximations are applicable, the error introduced by the neglect of the current dependence is smaller than the intrinsic error of the approximate functionals. However, the validity of this assumption has to be assessed in test calculations of NMR parameters.

If the current dependence both of the nonadditive kinetic-energy functional and of the exchange-correlation functional is neglected, the KSCED equations reduce to

$$\left[\frac{1}{2} \left(-i\nabla + \boldsymbol{A}(\boldsymbol{r})\right)^2 + v_{\text{eff}}^{\text{KSCED}}[\rho^{(\text{I})}, \rho^{(\text{II})}](\boldsymbol{r}) \right] \phi_i^{(I)}(\boldsymbol{r}) = \epsilon_i \phi_i^{(I)}(\boldsymbol{r}) \qquad (4.24)$$

The absence of a magnetic interaction between the currents in the two subsystems and the neglect of the current dependence of T_s^{nadd} and of E_{xc} have the consequence that the KSCED equations for subsystems I and II are not coupled via the current. This means that calculations on the nonfrozen subsystem can be carried out without knowledge of the induced current in the frozen subsystem.

Finally, it is important to note that the electron density and current that are given by the KS orbitals obtained from the KSCED equations will satisfy the continuity equation [Eq. (4.5)], because the KSCED equations are of the same form as the KS equations of CDFT.

4.2.4. Calculation of NMR Shieldings with frozen-density embedding

The FDE formalism described in the previous section is now applied to the calculation of NMR shielding tensors by decomposing the first-order current induced by an external homogeneous magnetic field into the contributions of the two individual

subsystems,

$$\boldsymbol{j}^{B_t} = \boldsymbol{j}^{(I)B_t} + \boldsymbol{j}^{(II)B_t}. \tag{4.25}$$

With this decomposition, also the shielding tensor [Eq. (4.7)] separates into contributions of the two subsystems,

$$\sigma_{st} = \sigma_{st}^{(I)} + \sigma_{st}^{(II)}, \tag{4.26}$$

where

$$\sigma_{st}^{(n)} = -\frac{1}{c^2} \int \left[\frac{(\boldsymbol{r} - \boldsymbol{R}_{\mathrm{nuc}}) \times \boldsymbol{j}^{(n)B_t}(\boldsymbol{r})}{|\boldsymbol{r} - \boldsymbol{R}_{\mathrm{nuc}}|^3} \right]_s \, d\boldsymbol{r} \qquad (n = I, II). \tag{4.27}$$

As before, these can again be split up into diamagnetic and paramagnetic contributions.

These contributions to the shielding tensor are determined separately for the individual subsystems. The starting point is the determination of the ground-state electron density of the two subsystems by solving the KSCED equations for both fragments in freeze-and-thaw cycles. The diamagnetic shielding can then be evaluated directly, since it only depends on the unperturbed electron densities,

$$\sigma_{st}^D = \sigma_{st}^{D,(I)} + \sigma_{st}^{D,(II)}, \tag{4.28}$$

with

$$\sigma_{st}^{D,(n)} = \int h_{st}^{11} \, \rho^{(n)}(\boldsymbol{r}) \, d\boldsymbol{r} \qquad (n = I, II). \tag{4.29}$$

The calculation of the paramagnetic shielding requires the determination of the first-order current that is induced by a homogeneous external magnetic field in each subsystem. For the evaluation of the induced current in one of the subsystems, the induced current in the frozen system is not needed because there is no dependence on the current in the frozen subsystem in Eq. (4.24) and because the homogeneous external magnetic field does not induce a first-order change in the electron density (see Section 4.2.2), i.e., the external magnetic field does not induce any coupling between the two subsystems. Therefore, the first-order perturbed orbitals and thus the induced paramagnetic current can be determined separately for the subsystems by using Eq. (4.16) and it is not necessary to determine the induced current in freeze-and-thaw cycles. Within the FDE formalism, the paramagnetic shielding can thus simply be calculated by adding the contributions of the individual subsystems,

$$\sigma_{st}^P = \sigma_{st}^{P,(I)} + \sigma_{st}^{P,(II)}, \tag{4.30}$$

with

$$\sigma_{st}^{P,(n)} = -\frac{1}{c^2} \int \left[\frac{(\boldsymbol{r} - \boldsymbol{R}_{\text{nuc}}) \times \boldsymbol{j}_p^{(n)B_t}(\boldsymbol{r})}{|\boldsymbol{r} - \boldsymbol{R}_{\text{nuc}}|^3} \right]_s d\boldsymbol{r} \qquad (n = \text{I}, \text{II}). \qquad (4.31)$$

In the calculation of the NMR shielding of one subsystem, no additional contributions arise due to the other subsystem, i.e., all the effects of the other (frozen) subsystem are included already in the effective embedding potential that is used in the determination of the ground-state electron density and KS orbitals.

Two approximations are made in the theory presented above. First, the approximation of uncoupled DFT is employed, i.e., the current dependence of the exchange-correlation functional is neglected. This approximation is consistently made both in supermolecular DFT calculations and in FDE calculations of NMR shieldings. Second, the current dependence of the nonadditive kinetic-energy functional is also neglected. It can be expected that this approximation is only valid if the interaction between the two subsystems is sufficiently weak and that in the case of stronger interactions, such as chemical bonds, between the subsystems, it will not be possible to neglect the current-dependence of the nonadditive kinetic-energy functional anymore. The validity of this approximations will therefore depend on choosing an appropriate partitioning into subsystems. However, the same restrictions apply for the available approximate functionals for the nonadditive kinetic energy.

In the calculation of NMR shieldings, the induced current is only probed by the nuclear spin of the NMR nucleus in question [see Eq. (4.7)], so that the most important contributions to the shielding tensor are due to the induced current in the vicinity of the NMR nucleus. The subsystem-based formulation of the calculation of NMR shieldings presented above has the advantage that it makes it possible to exploit this near-sightedness of the NMR shielding very easily. The main contribution to the NMR shielding and to chemical shifts is the contribution of the subsystem that contains the NMR nucleus. In many cases, it will be possible to neglect the contribution of the other subsystem to the NMR shielding, i.e., the effect of the other subsystem is only included in the calculation of the ground-state density and KS orbitals. It is also possible to construct the electron density of an environment using further approximations, for instance by using a sum-of-fragments density, or by applying freeze-and-thaw cycles only for parts of the system that are close to the subsystem of interest.[CJ5,76]

4.3. Computational details

All density functional calculations were performed using the Amsterdam Density Functional (ADF) package.[124,125] The FDE scheme of Wesolowski and Warshel[8] has

been implemented in the most recent version of ADF using an efficient numerical integration scheme.[CJ4] For the nonadditive kinetic-energy component of the embedding potential we chose to employ, based on previous results of Wesolowski *et al.*,[40,56,71] the PW91k kinetic-energy functional.[58]

The calculations of NMR shieldings were performed using the NMR program of Schreckenbach and Ziegler that is part of the ADF package,[126] which calculates the shielding tensor using GIAOs.[123] The calculation of NMR shieldings using the FDE scheme does not require major modifications of the program that is used for the calculation of the shielding. It only has to be ensured that the electron density and KS orbitals obtained from an FDE calculation can be used and that the effective embedding potential is included in the total KS potential that is needed in the NMR calculation. In addition, the calculation of the contribution of the frozen subsystem to the shielding requires the possibility to calculate the shielding tensor at an arbitrary position [nucleus-independent chemical shifts (NICSs)], which we implemented in the NMR program of ADF for this work.

We have used two different approximations for the exchange-correlation potential, the generalized-gradient approximation (GGA) functional BP86, consisting of the exchange functional by Becke[21] and the correlation functional by Perdew,[23] and the "statistical averaging of molecular orbital potentials" (SAOP),[26,127,128] which has been shown to improve the description of NMR chemical shifts significantly with respect to GGA functionals.[129] In the FDE calculations using the orbital-dependent SAOP potential, the exchange–correlation component of the effective embedding potential was approximated using the Becke–Perdew–Wang (BPW91) exchange-correlation functional.[21,130]

We have used the TZ2P basis set from the ADF basis set library, which is of triple-ζ quality and contains two sets of polarization functions, and the ZORA-QZ4P basis set, which is of quadruple-ζ quality and contains four sets of polarization functions.

4.4. Results and discussion

To assess the quality of chemical shifts calculated using the FDE formalism we have performed test calculations on small systems. The accuracy of the FDE calculations can be tested by comparing them to supermolecular KS-DFT calculations using the same approximation for the exchange-correlation functional.[CJ3] In the limit that the exact (current-dependent) nonadditive kinetic-energy functional is used, both methods should yield identical results.

As a test application, we investigate the effect of different solvents on the nitrogen shielding in acetonitrile, CH_3CN. The nitrogen shielding is known to be very sensitive

to environment effects, and the nitrogen shielding in acetonitrile has been used as a model system for studying environment effects on NMR chemical shifts in earlier studies.[116,131]

As model systems for these solvent effects, we have used small clusters consisting of acetonitrile and one solvent molecule. As solvents we have investigated water, chloroform, cyclohexane, and benzene. This simple cluster model will certainly not be able to give a realistic description of all solvent effects on the nitrogen chemical shifts. A more realistic description would require the inclusion of a much larger number of solvent molecules and would also require the inclusion of the dynamics in solution. However, this is not the purpose of this study, as we only want to assess the accuracy of the FDE calculation by comparing to supermolecular KS-DFT calculations.

There are different approximations involved in the FDE scheme that can lead to differences with respect to supermolecular KS-DFT calculations. First, approximations have to be used for the nonadditive kinetic-energy functional, and for the calculation of NMR chemical shifts the current dependence of the nonadditive kinetic energy is neglected. Second, in calculations using orbital-dependent approximations to the exchange-correlation potential such as SAOP, one furthermore encounters the complication that the supermolecular exchange-correlation potential is constructed in terms of a set of supermolecular orbitals. This potential cannot be reconstructed in a KSCED calculation since only the subsystem orbitals are available. This makes it necessary to choose a non-orbital-dependent form for the nonadditive exchange-correlation contribution to the effective embedding potential, introducing an additional inconsistency relative to the supermolecular calculation.[CJ3] This is not the case with a GGA potential such as BP86, because then the same approximation can be used for the exchange-correlation potential in the subsystems and for the nonadditive exchange-correlation contribution to the embedding potential.

A third origin of differences with respect to the supermolecular calculation is the finite basis set that is used.[40] The most obvious choice for the basis set in the FDE calculations is to use only basis functions that are centered on the atoms in the considered subsystem to expand the corresponding density. Calculations using this monomolecular basis set expansion will be labeled FDE(m). However, this choice of the basis functions introduces an additional source of differences to the supermolecular calculation. In the expansion of the total electron density the products of basis functions centered at atoms in different subsystems are neglected. Furthermore, since the total number of electrons in both subsystems is fixed, a charge transfer between the two subsystems is not possible. These problems are both removed if the full supermolecular basis set is used to expand the density of both subsystems. Calculations using this supermolecular basis set expansion will be labeled FDE(s).

In addition, further approximations can be applied in the construction of the electron

density of the solvent. Instead of obtaining the electron density of the two subsystems using freeze-and-thaw cycles, the electron density of the solvent can be obtained from a gas-phase calculation (i.e, the electron density of the isolated solvent molecule is used). Such a gas-phase density can be improved by applying one single freeze-and-thaw cycle (i.e., the gas-phase density is polarized). In the following, we will indicate the number of freeze-and-thaw cycles that have been applied. Calculations using the frozen gas-phase density of the solvent will be labeled FDE(x,0), calculations in which one single freeze-and-thaw cycle was applied will be labeled FDE(x,1), and calculations in which freeze-and-thaw cycles were applied until the NMR shielding was converged will be labeled FDE(x,∞), where $x=s,m$ indicate the basis set expansion that was used.

Finally, in the FDE calculation of NMR shieldings the contribution of the induced current in the solvent subsystem to the shielding has to be included to be consistent with the supermolecular KS-DFT calculation. As we will see, it is possible to neglect this additional contribution in many cases.

The structures of the acetonitrile–solvent clusters that were used in the calculations are shown in Figure 4.1. These structures have been obtained from geometry optimizations using the BP86 exchange-correlation functional in combination with a TZ2P basis set. They have been confirmed to represent local minima on the potential energy surface, but they do not represent global minima.

In the following we will investigate the solvent shifts on the isotropic shielding of the nitrogen nucleus in acetonitrile, which are defined as

$$\Delta\sigma = \sigma_{\text{cluster}} - \sigma_{\text{acetonitrile}}, \tag{4.32}$$

where σ_{cluster} denotes the isotropic shielding as calculated for the acetonitrile–solvent cluster (either using a supermolecular KS-DFT calculation or an FDE calculation) and $\sigma_{\text{acetonitrile}}$ denotes the isotropic shielding calculated for the isolated acetonitrile molecule. For the calculations on the isolated acetonitrile molecule, the same geometry as in the acetonitrile–solvent cluster is used, i.e., the change of the acetonitrile geometry due to the presence of the solvent molecule is not included in the solvent shift. This geometric effect is the same for both supermolecular KS-DFT calculations and for the FDE calculations, since the same geometries are used in both calculations.

For each acetonitrile–solvent cluster considered, the solvent shifts for calculations using the same exchange-correlation functional and basis set are reported with respect to the same isolated acetonitrile calculation, i.e., all differences between supermolecular KS-DFT calculations and FDE calculations, as well as differences between FDE calculations employing different additional approximations, are visible in the reported solvent shifts.

Figure 4.1.: Structures of the acetonitrile–solvent clusters used in the calculations: (a) acetonitrile–water, (b) acetonitrile–chloroform, (c) acetonitrile–cyclohexane, and (d) acetonitrile–benzene
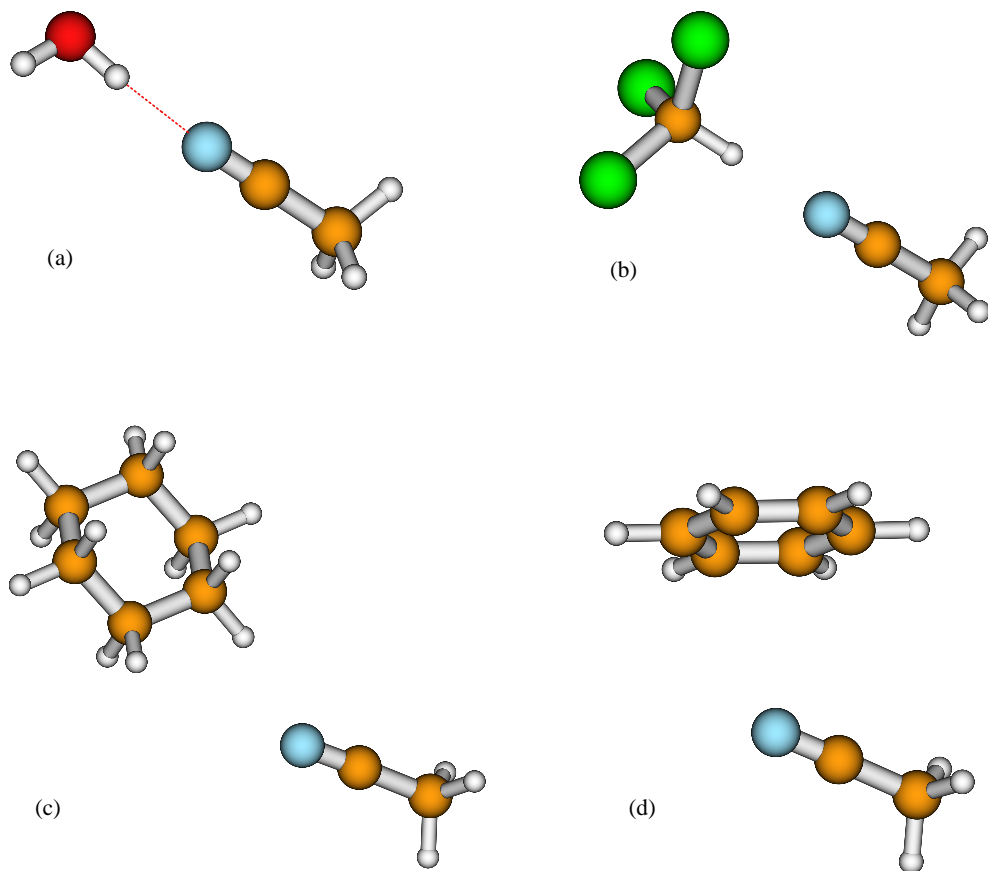

(a)

(b)

(c)

(d)

Table 4.1.: Solvent shift of the nitrogen NMR shielding in the acetonitrile–water cluster relative to isolated acetonitrile, calculated using supermolecular KS-DFT calculations and FDE calculations. See text for details.

	BP86		SAOP	
	TZ2P	QZ4P	TZ2P	QZ4P
Supermolecule	15.89	15.05	17.73	16.99
FDE(m,0)	12.57	12.04	12.18	11.89
FDE(m,1)	16.49	16.41	15.58	15.63
FDE(m,∞)	16.64	16.64	15.70	15.79
FDE(s,∞)	17.16	16.44	15.82	15.40

4.4.1. Acetonitrile–water

First, we investigate the acetonitrile–water cluster as a model for the effects of a water solution on the nitrogen chemical shift in acetonitrile. Due to the formation of a hydrogen bond between the solvent water molecule and the nitrogen atom of the acetonitrile, which is also the NMR nucleus under investigation, a large solvent shift can be expected. The results obtained for the acetonitrile–water cluster are summarized in Table 4.1.

As expected, the supermolecular KS-DFT calculations show a large solvent shift on the nitrogen shielding in acetonitrile of 15.05 ppm using the GGA functional BP86 and of 16.99 ppm using the SAOP potential. With both functionals, the change in the solvent shift when going from the TZ2P to the larger QZ4P basis set is smaller than 1 ppm, so that with respect to the basis set the solvent shifts can be considered as converged within this accuracy. It should be noted that this is not the case for the absolute shieldings, which still show a strong basis set dependence due to the addition of more tight basis functions. In the calculations using the BP86 functional, the absolute nitrogen shielding in acetonitrile changes from -24.71 to -31.19 ppm when going from the TZ2P to the QZ4P basis set, in the calculations using SAOP it changes from -17.76 to -22.17 ppm.

Already using the most simple embedding method, labeled FDE(m,0) in the table, in which the frozen electron density is taken from an isolated water molecule, the largest part of the solvent shift is recovered, and the solvent shift calculated for the supermolecule is underestimated by only approximately 3 ppm for the BP86 calculations and approximately 5 ppm for the SAOP calculations. If the frozen density is polarized in one single freeze-and-thaw cycle [FDE(m,1)], the solvent shifts agree

very well with the supermolecular calculation. With the BP86 functional, the differences are for both basis sets smaller than 1.4 ppm. In the calculations using SAOP, where an additional approximation has to be made in the nonadditive kinetic-energy functional, the differences are slightly larger, but still for both basis sets smaller than 2.3 ppm. These differences are small compared to the range of the nitrogen shielding scale of about 600 ppm for organic molecules.

Applying freeze-and-thaw cycles until the NMR shieldings are converged to the accuracy reported here does not change the solvent shifts significantly. In all cases, convergence is achieved after at most three full freeze-and-thaw cycles. The inclusion of basis functions located on the frozen subsystem does not change the solvent shifts significantly either.

One interesting finding is that the difference between the results obtained with the different basis sets is much smaller in the FDE(m,∞) calculations than in the FDE(s,∞) and in the supermolecular calculations. This can be explained by the absence of basis set superposition error (BSSE) in the case of the FDE(m) calculations. In these calculations BSSE is explicitly excluded because no basis functions on the frozen fragment are included. However, the FDE(s,∞) calculations and not the BSSE-free FDE(m,∞) calculations have to be compared to the supermolecular calculations, since both will consistently include a BSSE of approximately the same size. Even though the basis set convergence in the BSSE-free FDE(m,∞) calculations is faster, the small differences between the FDE(m,∞) and the FDE(s,∞) results, as well as the small differences between the results using the different basis sets show that the BSSE is sufficiently small compared to other sources of errors.

The contribution of the induced current in the frozen water molecule to the shielding is in all FDE calculations smaller than 0.2 ppm and thus negligible and has not been included in the solvent shifts given in the table.

4.4.2. Acetonitrile–chloroform

As another example of a polar solvent we have looked at chloroform. The solvent shifts calculated for the acetonitrile–chloroform cluster are summarized in Table 4.2.

The supermolecular KS-DFT calculations show a large solvent shift of the nitrogen shielding, but the shifts calculated with the QZ4P basis set of 12.91 and 13.97 ppm with BP86 and SAOP, respectively, are smaller than for the acetonitrile–water cluster because of the smaller polarity of the solvent molecule. As for water, the FDE$(m,0)$ calculations are able to recover the largest part of this solvent shift, underestimating the shift calculated in the supermolecule. If the frozen density is allowed to be polarized, differences between FDE and the supermolecular calculation are reduced. In the

Table 4.2.: Solvent shift of the nitrogen NMR shielding in the acetonitrile–chloroform cluster relative to isolated acetonitrile, calculated using supermolecular KS-DFT calculations and FDE calculations. See text for details.

	BP86		SAOP	
	TZ2P	QZ4P	TZ2P	QZ4P
Supermolecule	12.91	12.24	14.11	13.97
FDE(m,0)	10.35	9.87	9.04	8.52
FDE(m,1)	14.76	14.81	13.07	12.97
FDE(m,∞)	14.96	15.09	13.23	13.23
FDE(s,∞)	15.22	14.82	13.04	12.86

calculations using the BP86 functional, the agreement is with both basis sets better than 2.6 ppm, with SAOP the differences are even below 1 ppm. However, as there is an additional approximation involved in the case of the SAOP calculations, this better agreement is probably due to a fortunate error cancellation between the nonadditive kinetic-energy functional and the nonadditive exchange-correlation functional.

As for the acetonitrile–water cluster, using additional freeze-and-thaw cycles and including basis functions on the frozen system does not change the solvent shifts significantly. Again the contribution of the induced current in the (frozen) chloroform molecule is smaller than 0.2 ppm.

4.4.3. Acetonitrile–cyclohexane

As an example of a nonpolar solvent we have investigated cyclohexane and the solvent shifts obtained for the acetonitrile–cyclohexane cluster are summarized in Table 4.3.

As expected for the weak interaction between acetonitrile and the nonpolar cyclohexane, the solvent shift is very small. The calculations using the QZ4P basis set predict with the BP86 functional a solvent shift of 0.32 ppm and with SAOP a solvent shift of 2.45 ppm. In the FDE(m,0) calculations the solvent shift is almost zero (smaller than 0.3 ppm) with both functionals. However, if one freeze-and-thaw cycle is applied for the solvent molecule the solvent shift increases by about 2 ppm. In the case of the BP86 functional, this leads to an overestimation of the supermolecular shift by ca. 2.5 ppm. With SAOP, the agreement with the supermolecular result is very good, but again this is probably due to a fortunate error cancellation.

Table 4.3.: Solvent shift of the nitrogen NMR shielding in the acetonitrile–cyclohexane cluster relative to isolated acetonitrile, calculated using supermolecular KS-DFT calculations and FDE calculations. See text for details.

	BP86		SAOP	
	TZ2P	QZ4P	TZ2P	QZ4P
Supermolecule	0.39	0.32	2.88	2.45
FDE(m,0)	0.07	0.29	−0.24	−0.06
FDE(m,1)	2.21	2.77	1.70	2.13
FDE(m,∞)	2.27	2.85	1.74	2.19
FDE(s,∞)	2.50	2.51	1.63	1.71

Even though the absolute error is of the same size in the case of water and of chloroform, the relative error is unacceptably large if one is interested in accurate results for nonpolar solvents. As it is believed that the PW91k kinetic energy functional that is used for the kinetic energy component in the embedding potential is rather accurate for weakly interacting systems, this is quite surprising. It could be that the larger error in the calculation of NMR parameters is caused by the neglect of the current dependency of the nonadditive kinetic-energy functional. However, even with these large relative errors, the solvent shifts predicted by FDE are qualitatively correct and the absolute error is comparable to the differences between different approximations for the exchange-correlation functional.

Also for the acetonitrile–cyclohexane cluster, neither additional freeze-and-thaw cycles nor the inclusion of the basis functions of the frozen system changes the solvent shifts significantly. As expected the contribution of the induced current of the environment is below 0.2 ppm and is therefore neglected.

4.4.4. Acetonitrile–benzene

Finally, we have considered benzene as the prototypical nonpolar, aromatic solvent. For aromatic solvents, the contributions of the induced current in the solvent are expected to be significant, because there are large currents induced in the aromatic solvent.[132,133] These effects have also been explored experimentally and are known as aromatic solvent induced shifts (ASISs).[134] The solvent shifts calculated for the acetonitrile–benzene cluster are summarized in Table 4.4.

Table 4.4.: Solvent shift of the nitrogen NMR shielding in the acetonitrile–benzene cluster relative to isolated acetonitrile, calculated using supermolecular KS-DFT calculations and FDE calculations. The environment contribution of the induced current in the benzene molecule to the shielding is labeled "env". See text for details.

	BP86		SAOP	
	TZ2P	QZ4P	TZ2P	QZ4P
Supermolecule	−2.74	−0.29	0.69	2.42
FDE(m,0)	−4.60	−2.53	−3.88	−2.10
FDE(m,1)	−3.47	−1.20	−2.87	−0.95
FDE(m,∞)	−3.46	−1.18	−2.86	−0.97
FDE(s,∞)	−3.39	−1.04	−3.06	−1.10
env(m,∞)	+1.34	+1.37	+1.32	+1.39
FDE+env(m,∞)	−2.12	0.19	−1.54	0.42
FDE+env(s,∞)	−2.07	0.31	−1.76	0.24

The supermolecular calculations using the BP86 functional predict a small negative solvent shift of −0.29 ppm with the QZ4P basis set for the acetonitrile–benzene cluster considered here. In contrast to that, the shift of 2.42 ppm predicted by the supermolecular calculations using the SAOP potential and the QZ4P basis set is also small, but positive. In addition, the results obtained using the TZ2P and the QZ4P basis set differ in both cases by about 2.0–2.5 ppm. This worse basis set convergence compared to the systems considered earlier can be attributed to the importance of diffuse basis functions in this weakly interacting system. Even though the supermolecular calculations do not provide a clear picture, it is still possible to compare the results obtained to the FDE calculations using the same functional and basis set.

As for the other systems, only one single freeze-and-thaw cycle is sufficient to converge the solvent shift to the required accuracy and also the inclusion of the basis functions of the frozen system is not important. When using the BP86 functional, the FDE(m,1) calculations predict a solvent shift that is with the TZ2P basis set 0.73 ppm smaller and for the QZ4P basis set 0.91 ppm smaller than the solvent shift obtained from the supermolecular calculation. In the calculations using SAOP, the difference amounts to 3.56 ppm with the TZ2P basis set and 3.37 ppm with the QZ4P basis set. These differences found in the calculations using SAOP are larger than those found for the other systems.

The picture changes when the contribution of the induced current in the benzene molecule is included. This environment contribution, which can be calculated from a calculation of the NICS at the position of the nitrogen nucleus for the benzene molecule (using the electron density and KS orbitals obtained in the embedding calculation), is given in Table 4.4 in the row labeled env(m,∞). It amounts to approximately 1.4 ppm and can therefore certainly not be neglected. If this contribution is included, the agreement between the FDE(m) calculations and the supermolecular calculations improves significantly. In the calculations using BP86, the differences are for both basis sets smaller than 0.7 ppm, for the calculations using SAOP they are smaller than 2.3 ppm.

4.5. Conclusions

In this paper, we have presented an extension of the frozen-density embedding (FDE) formalism to the calculation of NMR chemical shifts. This leads to a formulation of the nonrelativistic DFT calculation of NMR shieldings that is based on the partitioning of the system into several fragments, which are treated separately. For each fragment the ground-state density as well as the first-order current induced by a homogeneous external magnetic field are calculated separately and the effect of the other (frozen) fragments is included via an effective embedding potential. If the current dependence of the exchange-correlation functional and of the nonadditive kinetic-energy functional are neglected, this embedding potential does not depend on the induced current in the frozen fragment. This absence of a coupling via the current makes it possible to simply calculate the contributions of the individual fragments to the NMR shielding from their ground-state electron densities and KS orbitals.

The formalism presented is very well suited to exploit the near-sightedness of the NMR shielding by applying additional approximations, e.g., by neglecting the induced current in fragments that are far away from the NMR nucleus and by using simplified ways of constructing the electron density of the fragments that do not contain the NMR nucleus.

Our test applications to small clusters of acetonitrile with different solvents show that the FDE scheme is able to reproduce the solvent shifts calculated in supermolecular KS-DFT calculations. The error of the FDE calculations with respect to the supermolecular calculations is about 2 ppm for the nitrogen shielding investigated here, which is about as large as the error of the currently available approximate exchange-correlation functionals. If the SAOP potential is used, the errors with respect to the supermolecular calculation are in most cases smaller, which is probably due to error cancellation.

Whereas absolute errors as large as 2 ppm are acceptable in the case of water and chloroform, where the frozen solvent molecule is very close to the NMR nucleus and even forms direct hydrogen bonds to the NMR nucleus, an error of this size is quite large in the case of weaker interactions, where the solvent shift is smaller. For these systems, improvements in the approximations to the nonadditive kinetic-energy functional might be needed to achieve more reliable results. If in future applications to larger systems a higher accuracy is required, it is possible to circumvent this problem by simply extending the nonfrozen fragment. This strategy has already been followed in earlier works.[CJ4]

The test calculations further show that for the systems studied here it is not necessary to include basis functions that are centered on the frozen fragments, making it possible to employ the computationally simpler FDE(m) scheme. However, it is in most cases required to include the polarization of the frozen solvent density by one single freeze-and-thaw cycle, especially if hydrogen bonds are present between solvent and solute. This is similar to what was found in earlier studies, where the FDE formalism was applied to modeling solvent effects on different other molecular properties.[CJ5]

In most cases it is possible to neglect the contribution of the induced current in the solvent molecule to the shielding, only for an aromatic solvent, where these induced currents are large, is this additional contribution significant, but even in this case it is possible to retain the separation of the total system into separate fragments. For a realistic modeling of the effects of an aromatic solvent on the NMR shielding of solute molecules, the contributions will become even more important, because these contributions of the currents induced in neighboring solvent molecules will add up to a large contribution of the aromatic environment.[132,134]

For an application of the FDE scheme to a realistic modeling of solvent shift in NMR shieldings it will be necessary to use much larger solvent environments than in the test systems studied here, requiring also a proper sampling of a large number of solvent structures. This is feasible using the FDE scheme, as has been shown in earlier studies of solvent effects on different properties by Neugebauer and coworkers.[CJ4,50,76] Its extension to the calculation of NMR chemical shifts presented in this paper and the good agreement between the FDE calculations and supermolecular DFT calculations we found for a number test systems, make this kind of applications to large systems attractive. Furthermore, the possibility to describe the induced currents in the environment allows the applications of the FDE scheme to the calculation of NMR chemical shifts for systems in environments where these play an important role, such as aromatic solvents or biological systems, and that are difficult to tackle with other environment models, such as continuum solvation or QM/MM models.

4. Calculation of NMR shieldings

5. Exact functional derivative of the nonadditive kinetic-energy bifunctional in the long-distance limit

Abstract

We have investigated the functional derivative of the nonadditive kinetic-energy bifunctional, which appears in the embedding potential that is used in the frozen-density embedding (FDE) formalism, in the limit that the separation of the subsystems is large. We have derived an exact expression for this kinetic-energy component of the embedding potential and have applied this expression to deduce its exact form in this limit. Comparing to the approximations currently in use, we find that while these approximations are correct at the nonfrozen subsystem, they fail completely at the frozen subsystem. Using test calculations on two model systems, an $H_2O \cdots Li^+$ complex and a cluster of aminocoumarin C151 surrounded by 30 water molecules, it is shown that this failure leads to a wrong description of unoccupied orbitals, which can lead to convergence problems caused by too low-lying unoccupied orbitals and which can further have serious consequences for the calculation of response properties. Based on these results, a simple correction is proposed and it is shown that this correction is able to fix the observed problems for the model systems studied.

5.1. Introduction

The frozen-density embedding (FDE) formalism within density-functional theory (DFT)[8,48] offers an efficient scheme for the quantum chemical description of large systems by splitting the total system into an active subsystem and a frozen environment. It is based on a partitioning of the electron density of the total system ρ_{tot} into the electron densities ρ_{I} and ρ_{II} of two appropriately chosen subsystems. These electron densities of the subsystems are each calculated separately, with the effect of the other subsystem represented by an effective embedding potential which only depends on its charge density. This embedding potential contains a component v_T that is given by the functional derivative of the nonadditive kinetic-energy bifunctional,

$$v_T[\rho_{\text{I}}, \rho_{\text{II}}](\boldsymbol{r}) = \frac{\delta T_s^{\text{nadd}}[\rho_{\text{I}}, \rho_{\text{II}}]}{\delta \rho_{\text{I}}} = \left. \frac{\delta T_s[\rho]}{\delta \rho} \right|_{\rho = \rho_{\text{tot}}(\boldsymbol{r})} - \left. \frac{\delta T_s[\rho]}{\delta \rho} \right|_{\rho = \rho_{\text{I}}(\boldsymbol{r})}, \qquad (5.1)$$

where the nonadditive kinetic energy T_s^{nadd} is defined as

$$T_s^{\text{nadd}}[\rho_{\text{I}}, \rho_{\text{II}}] = T_s[\rho_{\text{I}} + \rho_{\text{II}}] - T_s[\rho_{\text{I}}] - T_s[\rho_{\text{II}}]. \qquad (5.2)$$

In the above expressions, $T_s[\rho]$ is the kinetic energy of the noninteracting reference system, as it is defined within Kohn–Sham (KS) DFT, which is usually calculated using the KS orbitals.

However, with the given partitioning into subsystems, the KS orbitals are only available for the subsystems and not for the full system and $T_s[\rho_{\text{I}} + \rho_{\text{II}}]$ can therefore not be calculated directly. For this reason, in practical applications approximations have to be introduced in the construction of the kinetic-energy component $v_T[\rho_{\text{I}}, \rho_{\text{II}}]$ of the embedding potential. Up to now, only approximations of the form

$$\tilde{v}_T[\rho_{\text{I}}, \rho_{\text{II}}](\boldsymbol{r}) = \left. \frac{\delta \tilde{T}_s[\rho]}{\delta \rho} \right|_{\rho = \rho_{\text{tot}}(\boldsymbol{r})} - \left. \frac{\delta \tilde{T}_s[\rho]}{\delta \rho} \right|_{\rho = \rho_{\text{I}}(\boldsymbol{r})} \qquad (5.3)$$

have been applied, where the tilde is used to label approximate quantities, and $\tilde{T}_s[\rho]$ refers to some approximate kinetic-energy functional. The simplest approximation for the kinetic-energy functional, corresponding to the local-density approximation (LDA), is the well-known Thomas-Fermi functional, and a large number of more advanced approximate kinetic-energy functionals are available (for an overview see, e.g., Refs. 33 and 38).

For their application in calculations using the FDE scheme, different generalized-gradient approximation (GGA) kinetic-energy functionals have been tested and compared for a number of weakly interacting systems.[40,56,71] Based on these results, a large number of studies employing the FDE scheme have been conducted using the

PW91k kinetic-energy functional, which is a GGA functional using the same analytic form of the enhancement factor as the exchange functional of Perdew and Wang,[22] but that has been reparametrized for the kinetic energy by Lembarki and Chermette.[58]

The approximation of $v_T[\rho_I, \rho_{II}]$ using Eq. (5.3) in combination with the PW91k kinetic-energy functional has been shown to yield reliable results in FDE calculations in a number of studies. In particular, it has been found to be accurate in studies of weakly interacting complexes[CJ3,60,72,73] and of solvent effects on different molecular properties.[CJ4,CJ5,CJ6,76] However, the applicability of the currently available kinetic-energy functional is limited to systems where the interaction between the two subsystems is not too strong. While accurate results can be obtained for van der Waals complexes as well as for hydrogen-bound systems, a description of stronger interactions such as chemical bonds is not possible. It thus remains a challenge to develop approximations to $v_T[\rho_I, \rho_{II}]$ that are applicable also in the case of stronger interactions.

Also, in the case of weaker interactions the currently available kinetic-energy functionals need improvements for certain applications. Iannuzzi *et al.* have made use of FDE for molecular dynamics simulations in the condensed phase,[53] but have found that with the available LDA and GGA kinetic-energy functionals, they were not able to describe water at ambient conditions correctly. The pair distribution functions they obtained showed only an unstructured second solvation shell, and they attributed this wrong description to shortcomings of the approximate kinetic-energy functional.

Furthermore, for weakly interacting complexes an "electron-leak" problem in FDE calculations has been discussed. Near the nuclei in the frozen subsystem, the attractive nuclear potential is very large and, when using LDA or GGA kinetic-energy functionals, the kinetic-energy component of the embedding potential is not able to completely compensate this attraction. This might then lead to electrons of the non-frozen system leaking to the nuclei of the frozen subsystem, causing an artificial charge transfer between the subsystems. This problem has first been discussed for a complex of a fluorine anion and a water molecule at short distances by Stefanovich and Truong,[84] who proposed the use of a pseudopotential representing the core orbitals to overcome this problem. However, Dulak and Wesolowski reinvestigated this electron-leak problem for $F^- \cdots H_2O$ and $Li^+ \cdots OH_2$ and found that at short distances it is of no importance for the calculation of the ground-state density and interaction energies.[74] On the other hand, in calculations on $CO_2 \cdots X$ (X = He, Ne, Ar, Kr, Xe, and Hg) van der Waals complexes, it was found that for the complexes containing the heavier rare gases or mercury the dipole moment is overestimated if basis functions on the frozen system are included. This has also been attributed to the fact that close to the nuclei the PW91k kinetic-energy functional is not able to compensate the large nuclear attraction.[CJ3]

In order to devise more accurate approximations of the kinetic-energy component v_T of the embedding potential, we will in this work investigate v_T in the limit of large separation of the two subsystems. In the quest for more accurate approximate functionals, both for the exchange-correlation energy as well as for the kinetic energy, it is a widely followed and successfully applied strategy to use exact physical boundary conditions and/or the known behavior in simple limiting cases. These can be used as guidance in the construction of approximate functionals by requiring that the approximations obey these physical limits.

Following this strategy, several approximate exchange-correlation functionals have been constructed, e.g., the GGA functional PBE[135] and the meta-GGA functional TPSS.[25] Furthermore, exchange-correlation potentials have been constructed that have the correct asymptotic behavior far from the nuclei, which is particularly important for describing response properties.[26,136] Also, for the construction of approximate kinetic-energy functionals, this strategy has been applied. One example is a class of functionals by Carter and co-workers that are constructed to yield exact results for the linear response of the uniform electron gas.[41–43]

Instead of looking at the kinetic-energy functional itself, in this work we will focus on the quantity of interest directly, which is, in the case of the FDE scheme, the kinetic-energy component v_T of the embedding potential. As we will show, in the limit of large separation of the two subsystems, the two terms on the right-hand side of Eq. (5.1) do behave very differently in regions where either ρ_{I} or ρ_{II} are large, which can be used to deduce the exact v_T in this limit. It turns out that for regions where ρ_{II} is large, the available LDA or GGA kinetic-energy functionals do not obey this limit.

This Chapter is organized as follows. First, we derive an expression for the exact nonadditive kinetic-energy potential in Sec. 5.2. This is then used in Sec. 5.3 to investigate the exact embedding potential at large separation of the two subsystems. After giving the computational details in Sec. 5.4, we show in Sec. 5.5 for model systems that the approximations currently in use for the kinetic-energy potential are not able to describe this long-distance limit correctly and investigate the consequences of this failure. In Sec. 5.6, a correction is proposed that enforces the correct embedding potential in the considered limit before we summarize and conclude in Sec. 5.7.

5.2. The exact nonadditive kinetic-energy potential

The calculation of the kinetic-energy component $v_T[\rho_{\mathrm{I}}, \rho_{\mathrm{II}}](\boldsymbol{r})$ of the KSCED effective potential requires the evaluation of the functional derivative $\frac{\delta T_s[\rho]}{\delta \rho}$ for two different electron densities—for the density of the nonfrozen subsystem I and for the total

electron density. In this section we will first describe a general procedure for the evaluation of $\frac{\delta T_s[\rho]}{\delta \rho}$ for an arbitrary v_s-representable electron density.

The functional derivative of the nonadditive kinetic-energy bifunctional with respect to the electron density cannot be evaluated directly since the noninteracting kinetic energy does not depend directly on the density, but it requires the knowledge of the KS orbitals. The KS orbitals are an implicit functional of the electron density because the electron density uniquely defines a corresponding KS potential $v_s[\rho]$, which, in turn, determines the KS orbitals. The usual method for the evaluation of the functional derivative of orbital-dependent functionals is the optimized effective potential (OEP) method.[137]

However, in the case of the kinetic energy an alternative route is possible for the evaluation of $\frac{\delta T_s[\rho]}{\delta \rho}$. For an arbitrary v_s-representable electron density $\rho(\boldsymbol{r})$ there exists the corresponding KS potential $v_s[\rho](\boldsymbol{r})$, i.e., the potential that will yield the density $\rho(\boldsymbol{r})$. The existence of this one-to-one mapping between the electron density and the KS potential is given by the first Hohenberg–Kohn theorem.[17,18] Throughout this paper, we use $v_s[\rho]$ to refer to this KS potential, yielding the density $\rho(\boldsymbol{r})$. This is to be distinguished from the KS effective potential $v_{\text{eff}}^{\text{KS}}[\rho]$ that can be calculated from the electron density ρ according to Eq. 3.15. Only for the ground-state electron density $\rho_0(\boldsymbol{r})$, which can be obtained from the self-consistent solution of the KS equations, $v_s[\rho_0]$ and $v_{\text{eff}}^{\text{KS}}[\rho_0]$ are identical. For the practical evaluation of $v_s[\rho]$ from a given density $\rho(\boldsymbol{r})$, there are different numerical schemes available.[136,138,139]

To evaluate the functional derivative $\frac{\delta T_s[\rho]}{\delta \rho}$, we will consider this KS potential $v_s^\rho(\boldsymbol{r})$ as fixed by the given input density; i.e., the functional dependence on $\rho(\boldsymbol{r})$ is replaced by a parametrical dependence. For this fixed potential $v_s^\rho(\boldsymbol{r})$, the electron density $\rho(\boldsymbol{r})$ is the density which minimizes the total-energy functional

$$E_{v_s^\rho}[\rho] = T_s[\rho] + \int v_s^\rho(\boldsymbol{r})\rho(\boldsymbol{r}) \; d\boldsymbol{r} \tag{5.4}$$

of a system of noninteracting electrons with $v_s^\rho(\boldsymbol{r})$ as the external potential under the constraint that the electron density integrates to the correct number of electrons. Therefore, the electron density $\rho(\boldsymbol{r})$ is the solution of the Lagrange minimization problem[17]

$$\delta \left\{ E_{v_s^\rho}[\rho] - \mu^\rho \left(\int \rho(\boldsymbol{r})d\boldsymbol{r} - N \right) \right\} = 0, \tag{5.5}$$

which is equivalent to the Euler-Lagrange equation

$$\mu^\rho = \frac{\delta E_{v_s^\rho}[\rho]}{\delta \rho(\boldsymbol{r})} = \frac{\delta T_s[\rho]}{\delta \rho(\boldsymbol{r})} + v_s^\rho(\boldsymbol{r}), \tag{5.6}$$

where μ^ρ is a constant that depends on the input electron density and that can be identified to equal the orbital energy of the highest occupied molecular orbital (HOMO) in the exact functional limit.[32]

This Euler-Lagrange equation with the potential $v_s^\rho(\boldsymbol{r})$ holds for the given electron density $\rho(\boldsymbol{r})$, and it can be employed to evaluate the functional derivative of the noninteracting kinetic energy $\frac{\delta T_s[\rho]}{\delta \rho}$ from

$$\frac{\delta T_s[\rho]}{\delta \rho(\boldsymbol{r})} = -v_s^\rho(\boldsymbol{r}) + \mu^\rho. \tag{5.7}$$

When solving the KSCED equations, the above functional derivative is needed for two different electron densities, for the electron density of the nonfrozen subsystem $\rho_{\mathrm{I}}(\boldsymbol{r})$ and for the total electron density $\rho_{\mathrm{tot}}(\boldsymbol{r})$. Using the obtained expression for $\frac{\delta T_s[\rho]}{\delta \rho}$, the kinetic-energy component of the KSCED effective potential [Eq. (5.1)] can be written as

$$v_T[\rho_{\mathrm{I}}, \rho_{\mathrm{II}}](\boldsymbol{r}) = \frac{\delta T_s^{\mathrm{nadd}}[\rho_{\mathrm{I}}, \rho_{\mathrm{II}}]}{\delta \rho_{\mathrm{I}}} = v_s[\rho_{\mathrm{I}}](\boldsymbol{r}) - v_s[\rho_{\mathrm{tot}}](\boldsymbol{r}) + \Delta \mu. \tag{5.8}$$

In this expression $\Delta \mu = \mu^{\rho_{\mathrm{I}}} - \mu^{\rho_{\mathrm{tot}}}$ is a constant shift of the potential that leads to a constant shift in the orbital energies but that will effect neither the obtained orbitals nor the orbital energy differences. Therefore, the shift $\Delta \mu$ can be ignored in the following.

The above expression for $v_T[\rho_{\mathrm{I}}, \rho_{\mathrm{II}}]$ can be employed for arbitrary pairs of v_s-representable electron densities ρ_{I} and ρ_{tot} and can, in principle, be used to evaluate the exact contribution of the nonadditive kinetic energy to the effective embedding potential during the solution of the KSCED equations. However, it requires the knowledge of the KS potentials corresponding to ρ_{I} and to ρ_{tot}, respectively. Those are, in general, not easy to obtain in practical calculations. The application of Eq. 5.8 for the calculation of the exact embedding potential will be the subject of our future work. In the present work, we will employ it to investigate $v_T[\rho_{\mathrm{I}}, \rho_{\mathrm{II}}]$ in the long-distance limit without actually reconstructing KS potentials from the electron density.

5.3. Exact effective embedding potential in the long-distance limit

In the following, the effective embedding potential will be investigated in the limit of a large separation of the two subsystems. This limit will be referred to as the

"long-distance limit". In this considered limit, the overlap of the electron densities of the two subsystems will be very small and at every point in space $\boldsymbol{r}$,

$$\rho_{\text{tot}}(\boldsymbol{r}) \approx \rho_{\text{I}}(\boldsymbol{r}) \quad \vee \quad \rho_{\text{tot}}(\boldsymbol{r}) \approx \rho_{\text{II}}(\boldsymbol{r}). \tag{5.9}$$

This implies that also the corresponding KS potentials do not "overlap", that is, at every point in space $\boldsymbol{r}$,

$$v_s[\rho_{\text{tot}}](\boldsymbol{r}) \approx v_s[\rho_{\text{I}}](\boldsymbol{r}) \quad \vee \quad v_s[\rho_{\text{tot}}](\boldsymbol{r}) \approx v_s[\rho_{\text{II}}](\boldsymbol{r}), \tag{5.10}$$

where we assumed that both $v_s[\rho_{\text{I}}](\boldsymbol{r})$ and $v_s[\rho_{\text{II}}](\boldsymbol{r})$, and therefore also $v_s[\rho_{\text{tot}}](\boldsymbol{r})$, have been chosen such that they go to 0 at infinity, i.e., where the corresponding density approaches 0.

In addition, we will assume that the electron density ρ_{II} of the frozen subsystem in the environment is close to the correct total density, i.e., that the chosen partitioning of the electron density is such that the subsystem densities are equal to the ground-state densities of the separated subsystems. This restriction rules out the case where there is a charge transfer between the subsystems. Even though this is a quite severe restriction, this is the most common use of the FDE scheme. In most practical applications, an approximate $\rho_{\text{II}}(\boldsymbol{r})$ is used, which is chosen such that it can be considered a good approximation to the correct electron density in the environment.

It should be noted that in the following "exact" effective embedding potential refers to the embedding potential that is constructed using the exact kinetic-energy component v_T. This does not require that also the exact exchange-correlation potential is used, but approximate exchange-correlation potentials can be employed. However, when using the exact embedding potential, the results of a fully variational FDE calculation (in which the electron density of both subsystems is updated in freeze-and-thaw cycles), will be equal to the electron density calculated from a supermolecular KS-DFT calculation using the same approximate exchange-correlation potential. In the following, we will restrict ourselves to approximate exchange-correlation potentials that only depend on the electron density locally, i.e., to LDA and GGA functionals.

Under these assumptions, the KS potential that yields the correct total electron density can, in the long-distance limit, be decomposed as

$$v_s[\rho_{\text{tot}}](\boldsymbol{r}) \approx v_s[\rho_{\text{I}}](\boldsymbol{r}) + v_s[\rho_{\text{II}}](\boldsymbol{r}); \tag{5.11}$$

i.e., it can be written as the sum of the KS potentials that correspond to the individual electron densities of the subsystems. It should be pointed out that this decomposition is only exact if approximate exchange-correlation potentials that only depend locally on the electron-density are employed. It is not valid if the exact KS potentials are considered.

5.3.1. Embedding potential at the nonfrozen subsystem

In the region of the nonfrozen subsystem I, where ρ_{II} is negligibly small $[\rho_{\text{II}}(\boldsymbol{r}) \approx 0]$, the total density equals the density of the nonfrozen subsystem I, i.e., $\rho_{\text{I}}(\boldsymbol{r}) \approx \rho_{\text{tot}}(\boldsymbol{r})$. This implies, under the assumptions made above, that

$$v_s[\rho_{\text{tot}}](\boldsymbol{r}) \approx v_s[\rho_{\text{I}}](\boldsymbol{r}), \tag{5.12}$$

and it follows from Eq. (5.8) that

$$v_T[\rho_{\text{I}}, \rho_{\text{II}}](\boldsymbol{r}) \approx 0 \quad \text{for} \quad \rho_{\text{II}}(\boldsymbol{r}) \approx 0; \tag{5.13}$$

i.e., the kinetic-energy component of the effective embedding potential disappears.

If a local approximation (LDA or GGA) to the exchange-correlation potential is used, also the exchange-correlation component of the effective embedding potential in Eq. (3.16) cancels, and the effective embedding potential reduces to the purely electrostatic embedding potential,

$$v_{\text{eff}}^{\text{emb}}[\rho_{\text{I}}, \rho_{\text{II}}](\boldsymbol{r}) = v_{\text{II}}^{\text{nuc}}(\boldsymbol{r}) + \int \frac{\rho_{\text{II}}(\boldsymbol{r}')}{|\boldsymbol{r} - \boldsymbol{r}'|} d\boldsymbol{r}' \quad \text{for} \quad \rho_{\text{II}}(\boldsymbol{r}) \approx 0. \tag{5.14}$$

5.3.2. Embedding potential at the frozen subsystem

In the region of the frozen subsystem II, where ρ_{I} is negligibly small $[\rho_{\text{I}}(\boldsymbol{r}) \approx 0]$, the total density equals the density of the frozen subsystem II, i.e., $\rho_{\text{II}}(\boldsymbol{r}) \approx \rho_{\text{tot}}(\boldsymbol{r})$. This implies, under the assumptions made above,

$$v_s[\rho_{\text{tot}}](\boldsymbol{r}) \approx v_s[\rho_{\text{II}}](\boldsymbol{r}) \tag{5.15}$$

and

$$v_s[\rho_{\text{I}}](\boldsymbol{r}) \approx 0, \tag{5.16}$$

and it follows from Eq. (5.8) that

$$v_T[\rho_{\text{I}}, \rho_{\text{II}}](\boldsymbol{r}) \approx -v_s[\rho_{\text{II}}](\boldsymbol{r}) \quad \text{for} \quad \rho_{\text{I}}(\boldsymbol{r}) \approx 0. \tag{5.17}$$

As the frozen density $\rho_{\text{II}}(\boldsymbol{r})$ has usually been obtained from the self-consistent solution of the KS equations in an earlier step, the corresponding KS potential $v_s[\rho_{\text{II}}](\boldsymbol{r})$ is known and is given by the effective potential that was used to obtain $\rho_{\text{II}}(\boldsymbol{r})$. In the simplest case, ρ_{II} has been obtained from an isolated KS-DFT calculation. In this case, the KS potential corresponding to $\rho_{\text{II}}(\boldsymbol{r})$ is given by

$$v_s[\rho_{\text{II}}](\boldsymbol{r}) = v_{\text{eff}}^{\text{KS}}[\rho_{\text{II}}](\boldsymbol{r}) = v_{\text{II}}^{\text{nuc}}(\boldsymbol{r}) + \int \frac{\rho_{\text{II}}(\boldsymbol{r}')}{|\boldsymbol{r} - \boldsymbol{r}'|} d\boldsymbol{r}' + \left. \frac{\delta E_{\text{xc}}[\rho]}{\delta \rho} \right|_{\rho = \rho_{\text{II}}(\boldsymbol{r})}, \tag{5.18}$$

and, therefore,

$$v_T[\rho_I, \rho_{II}](\boldsymbol{r}) \approx -v_{II}^{nuc}(\boldsymbol{r}) - \int \frac{\rho_{II}(\boldsymbol{r}')}{|\boldsymbol{r} - \boldsymbol{r}'|} d\boldsymbol{r}' - \frac{\delta E_{xc}[\rho]}{\delta \rho}\Bigg|_{\rho=\rho_{II}(\boldsymbol{r})} \quad \text{for} \quad \rho_I(\boldsymbol{r}) \approx 0. \quad (5.19)$$

The nuclear potential and the electrostatic potential of the electrons exactly cancel the corresponding terms in the effective embedding potential [Eq. (3.16)] and in the case of a local approximation (LDA or GGA) for the exchange-correlation potential, the exchange-correlation component cancels, too. Therefore, the kinetic-energy component cancels all the other terms of v_{eff}^{emb}, and one obtains

$$v_{eff}^{emb}[\rho_I, \rho_{II}](\boldsymbol{r}) = 0 \quad \text{for} \quad \rho_I(\boldsymbol{r}) \approx 0. \quad (5.20)$$

If the frozen density ρ_{II} has not been obtained from an isolated molecule calculation, but from a FDE calculation itself, as it is done when performing freeze-and-thaw cycles, the KS potential corresponding to $\rho_{II}(\boldsymbol{r})$ also contains the effective embedding potential, i.e.,

$$v_s[\rho_{II}](\boldsymbol{r}) = v_{eff}^{KS}[\rho_{II}](\boldsymbol{r}) + v_{eff}^{emb}[\rho_{II}, \rho_I](\boldsymbol{r}), \quad (5.21)$$

where $v_{eff}^{emb}[\rho_{II}, \rho_I](\boldsymbol{r})$ is the embedding potential that appears when ρ_{II} is calculated in a FDE calculation in the presence of the (frozen) ρ_I density, i.e., when the roles of ρ_I and ρ_{II} are interchanged in a freeze-and-thaw calculation.

Since the distance between the two subsystems is large, the effective embedding potential in the calculation of ρ_{II} is, as described above in Sec. 5.3.1, in the regions of interest given by the electrostatic potential only. Therefore,

$$v_T[\rho_I, \rho_{II}](\boldsymbol{r}) \approx -v_{eff}^{KS}[\rho_{II}](\boldsymbol{r}) - v_I^{nuc}(\boldsymbol{r}) - \int \frac{\rho_I(\boldsymbol{r}')}{|\boldsymbol{r} - \boldsymbol{r}'|} d\boldsymbol{r}' \quad \text{for} \quad \rho_I(\boldsymbol{r}) \approx 0. \quad (5.22)$$

The effective embedding potential at the frozen system is then given by

$$v_{eff}^{emb}[\rho_I, \rho_{II}](\boldsymbol{r}) = -v_I^{nuc}(\boldsymbol{r}) - \int \frac{\rho_I(\boldsymbol{r}')}{|\boldsymbol{r} - \boldsymbol{r}'|} d\boldsymbol{r}' \quad \text{for} \quad \rho_I(\boldsymbol{r}) \approx 0. \quad (5.23)$$

This effective embedding potential cancels the corresponding terms in the KS effective potential of the embedded subsystem $v_{eff}^{KS}[\rho_I]$, so that the total effective potential used in the calculation of the embedded subsystem is zero at the frozen subsystem,

$$v_{eff}^{KSCED}[\rho_I](\boldsymbol{r}) \approx 0 \quad \text{for} \quad \rho_I(\boldsymbol{r}) \approx 0. \quad (5.24)$$

5.4. Computational details

All density functional calculations have been performed using the Amsterdam density functional (ADF) package.[124,125] The FDE scheme of Wesolowski and Warshel[8] has been implemented in the most recent version of ADF using an efficient numerical integration scheme.[CJ4] The PW91 exchange-correlation functional[22,130] in combination with the TZ2P basis set from the ADF basis set library[124] has been employed in all calculations. If not stated otherwise, in the FDE calculations the PW91k kinetic-energy functional[58] has been used to approximate the kinetic-energy component of the embedding potential according to Eq. (5.3). The calculations on $H_2O \cdots Li^+$ presented below have been independently verified using the implementation of the FDE scheme in the DEMON2K program package.[140]

In the FDE calculations, there are two possibilities for the choice of the basis functions which are used to expand the density of the nonfrozen subsystems.[CJ3,40] The most obvious choice is to use only basis functions that are centered on the atoms in the considered subsystem to expand the corresponding density. Calculations using this monomolecular basis set expansion will be labeled as FDE(m). However, in this case an inconsistency with respect to the supermolecular calculation is introduced since the products of basis functions of different subsystems cannot be used for expanding the electron density. Therefore, it is more accurate to include all basis functions, also those of the frozen subsystem, in FDE the calculation. Calculations using this supermolecular basis set expansion will be labeled as FDE(s).

5.5. The failure of the available approximate kinetic-energy potentials in the long-distance limit

The currently available approximations to the kinetic-energy component v_T of the embedding potential, which are of the form

$$\tilde{v}_T[\rho_{\mathrm{I}}, \rho_{\mathrm{II}}](\boldsymbol{r}) = \left.\frac{\delta \tilde{T}_s[\rho]}{\delta \rho}\right|_{\rho=\rho_{\mathrm{tot}}(\boldsymbol{r})} - \left.\frac{\delta \tilde{T}_s[\rho]}{\delta \rho}\right|_{\rho=\rho_{\mathrm{I}}(\boldsymbol{r})}, \tag{5.25}$$

only partly satisfy the exact long-distance limit that was derived in the previous section. At the nonfrozen subsystem, $\rho_{\mathrm{I}}(\boldsymbol{r}) \approx \rho_{\mathrm{tot}}(\boldsymbol{r})$ and, therefore, the two terms in Eq. (5.25) will cancel, such that the correct long-distance limit given by Eq. (5.13) is obtained.

In contrast, at the frozen subsystem Eq. (5.25) reduces to

$$\tilde{v}_T[\rho_{\mathrm{I}}, \rho_{\mathrm{II}}](\boldsymbol{r}) = \left.\frac{\delta \tilde{T}_s[\rho]}{\delta \rho}\right|_{\rho=\rho_{\mathrm{II}}(\boldsymbol{r})} \qquad \text{for} \quad \rho_{\mathrm{I}}(\boldsymbol{r}) \approx 0 \qquad (5.26)$$

and it is not evident that the available kinetic-energy functionals fulfill the exact limit given by Eq. (5.17), i.e., that the kinetic-energy component cancels the electrostatic and exchange-correlation components of the effective embedding potential.

This wrong description of the long-distance limit can be considered a serious shortcoming of the approximate kinetic-energy functionals that are currently in use in practical applications of the FDE scheme. At the frozen system, the available approximate kinetic-energy functionals, used in Eq. (5.3) to approximate the kinetic-energy component v_T of the effective embedding potential, are in general not able to compensate the electrostatic parts of the embedding potential, as they should in the exact long-distance limit. We will investigate the consequences of this wrong description in the following.

To illustrate the behavior of the embedding potential in the different regions, we investigated a $H_2O\cdots Li^+$ complex as a simple model system. This complex has already been used in earlier studies of the possible charge-leak problem in FDE calculations.[74,84] The structure of this complex, as it was used in the calculations, is shown in Fig. 5.1. As a starting point, we use the optimized geometry of $H_2O\cdots Li^+$, which assumes a planar structure with C_{2v} symmetry and $d(\text{O–H}) = 0.97$Å, $\angle(\text{H–O–H}) = 105.1°$ and $d(\text{O–Li}) = 1.8$Å. To investigate the limit of large separations of the two subsystems, the O–Li distance is varied.

In the FDE calculations, the positively charged Li^+ ion is used as the frozen subsystem (ρ_{II}). The electron density of the Li^+ subsystem is calculated for the isolated ion in the gas phase. The H_2O molecule constitutes the nonfrozen subsystem (ρ_{I}), and its electron density is calculated in a FDE calculation in the presence of the frozen Li^+ electron density. At large separations, the effect of the H_2O subsystem on the Li^+ ion can be expected to be very small; i.e., the frozen Li^+ density will be very close to the correct total density, so that the assumptions made in Sec. 5.3 are fulfilled. On the other hand, the effect of the frozen Li^+ subsystem can be expected to be significant even when the overlap of the electron densities is negligible since its positive charge gives rise to a long-range electrostatic interaction.

As a reference, we first performed supermolecular KS-DFT calculations. The orbital energies obtained in this supermolecular calculation as a function of the O–Li distance are shown in Fig. 5.2, and pictures of the relevant orbitals are shown in Fig. 5.3.

The HOMO in the supermolecular calculation is a lone-pair p orbital on the water molecule. When the distance between the two fragments is increased, its orbital

Figure 5.1.: Structure of the employed model system $H_2O \cdots Li^+$. In the calculations the O–Li distance is varied; the picture is for d(O–Li) = 5.8 Å. An isosurface plot of the electron density is also shown to illustrate the partitioning into subsystems. Graphics: ADF-VIEW [141]
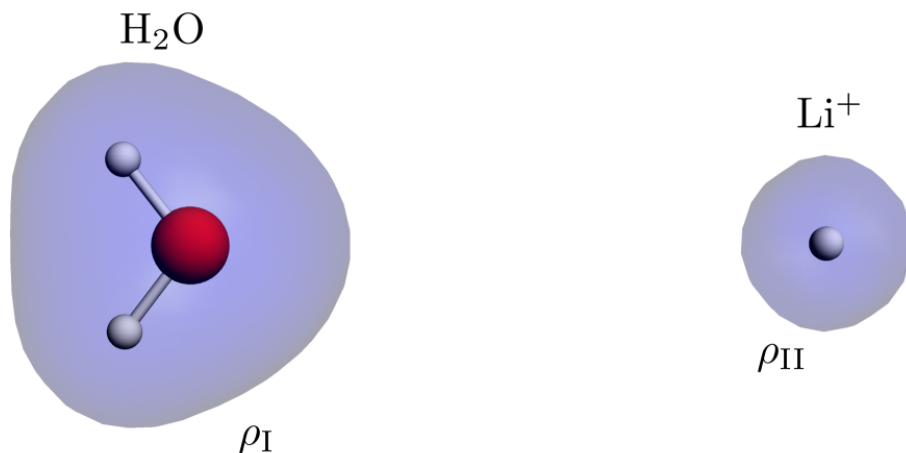
Figure 5.2.: Orbital energies calculated in a supermolecular KS-DFT calculation as a function of the O–Li distance. See text for details.
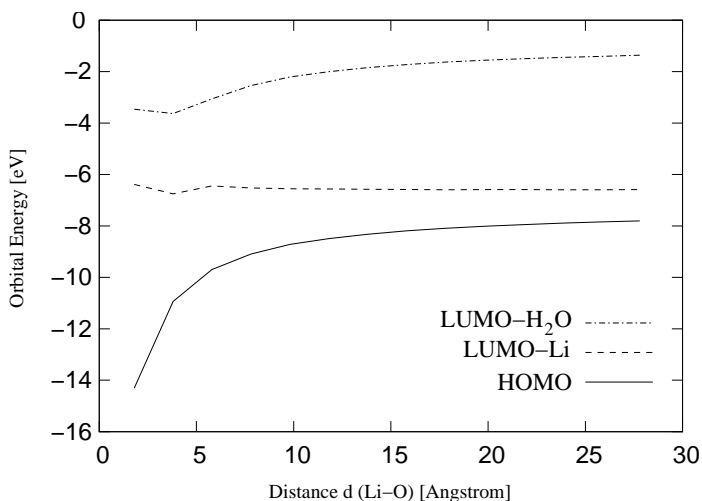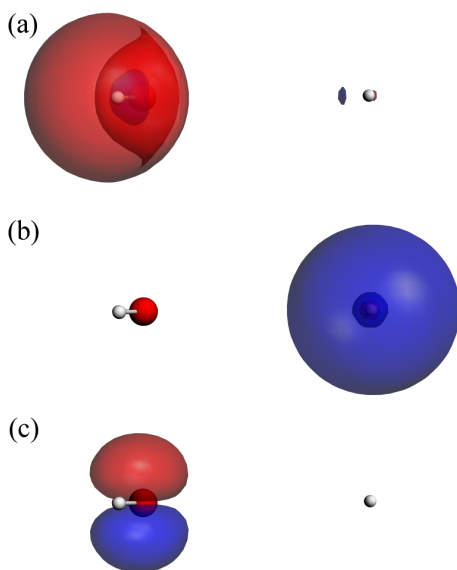
Figure 5.3.: Isosurface plots of the orbitals calculated in a supermolecular KS-DFT calculation for d(O–Li) = 5.8Å. Shown are (a) the lowest unoccupied H_2O orbital (LUMO-H_2O), (b) the lowest unoccupied Li^+ orbital (LUMO-Li), and (c) the highest occupied H_2O orbital (HOMO-H_2O). See text for details. Graphics: ADF-VIEW [141].

(a)

(b)

(c)

energy increases. This is due to the Coulomb potential of the charged Li^+ ion that is felt at the water molecule. The lowest unoccupied molecular orbital (LUMO) is the rather diffuse $2s$ orbital on the Li^+ ion (labeled LUMO-Li). Its orbital energy is almost constant with increasing distance between the fragments since at larger distances there is no interaction of this orbital with the H_2O molecule. Only close to the equilibrium distance there is some overlap of the LUMO-Li with H_2O orbitals. In addition, the figures also include the lowest unoccupied H_2O orbital, labeled LUMO-H_2O, i.e., the lowest unoccupied orbital that is mainly located at the H_2O molecule. This is a diffuse s-like orbital. As it is localized at the water molecule, its orbital energy shows the same Coulombic behavior as that of the HOMO when the distance between the fragments is increased.

The orbital energies of the HOMO and the LUMO in FDE calculations on the H_2O subsystem in the presence of the frozen Li^+ density, using both the monomolecular and the supermolecular expansion, are shown in Fig. 5.4. Pictures of the orbitals obtained with FDE(m) are shown in Fig. 5.5, and the orbitals calculated in the FDE(s) calculations are shown in Fig. 5.6.

Both in the FDE(m) and in the FDE(s) calculations the HOMO of the H_2O subsystem is the same orbital as the HOMO in the supermolecular calculation, and the orbital energy is identical to the orbital energy calculated in the supermolecular calculation. Since this orbital is localized at the H_2O subsystem, at larger separations of the two subsystems it is exposed to the embedding potential at the nonfrozen system only. As shown above, in these regions the embedding potential should reduce to the purely electrostatic embedding potential. With the approximate kinetic-energy functionals in use this limit is reproduced correctly.

In the FDE(m) calculation the LUMO of the H_2O subsystem is at larger separations of the two subsystems similar to the LUMO-H_2O in the supermolecular calculation. It is a diffuse s-like orbital localized at the water subsystem. Therefore, it does not correspond to the LUMO of the supermolecule, but to the lowest unoccupied orbital of the subsystem in question. The orbital energy of the LUMO equals at larger distances the orbital energy of the LUMO-H_2O in the supermolecular calculation.

In the FDE(s) calculation, where the basis functions centered at the Li subsystem are included, a completely different orbital is found as the LUMO. In contrast to the FDE(m) calculation, where the LUMO was localized at the H_2O subsystem, a rather diffuse, nodeless s orbital localized at the Li^+ ion is obtained. The orbital energy of this orbital is at larger distances -8.6 eV, which is approximately 2.0 eV lower than the orbital energy of the LUMO-Li obtained in the supermolecular calculation. Since the orbital is localized at the Li^+ subsystem its orbital energy is almost constant when the distance between the subsystems is increased. At O–Li distances larger than approximately 12 Å, the energy of the HOMO becomes larger than the orbital

Figure 5.4.: Orbital energies calculated in FDE calculations on the H_2O subsystem in the presence of the frozen Li^+ subsystem as a function of the O–Li distance. Both results using the supermolecular basis set expansion [FDE(s)] and the monomolecular basis set expansion [FDE(m)] are shown. For comparison, also the corresponding supermolecular orbitals are included.
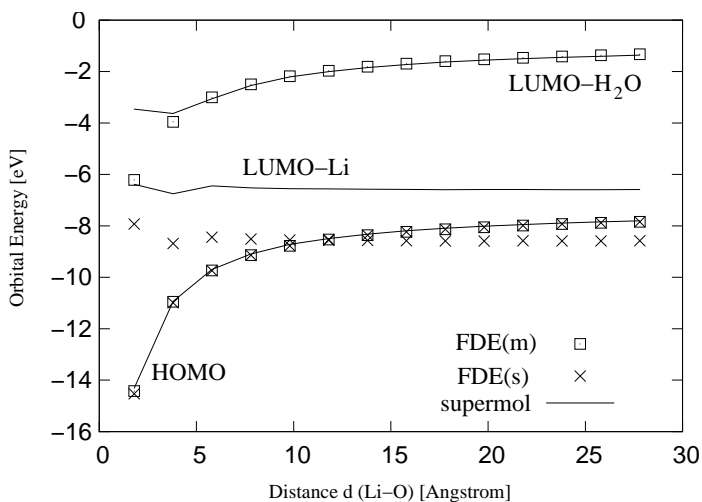
Figure 5.5.: Isosurface plots of the H_2O orbitals calculated in a FDE(m) calcula-
tion in the presence of the frozen Li^+ subsystem for d(O–Li) $= 5.8$Å.
Only basis functions of the H_2O subsystem are included (monomolecu-
lar expansion). Shown are (a) the lowest unoccupied molecular orbital
and (b) the highest occupied molecular orbital. See text for details.
Graphics: ADF-VIEW [141].

(a)

(b)
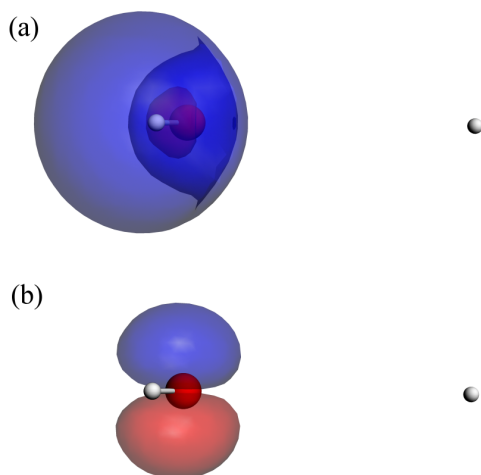
Figure 5.6.: Isosurface plots of the H_2O orbitals calculated in a FDE(s) calculation in the presence of the frozen Li^+ subsystem for d(O–Li) $= 5.8$Å. Basis functions of both subsystems are used in the FDE calculation (supermolecular expansion). Shown are (a) the lowest unoccupied molecular orbital and (b) the highest occupied molecular orbital. See text for details. Graphics: ADF-VIEW [141].

(a)

(b)
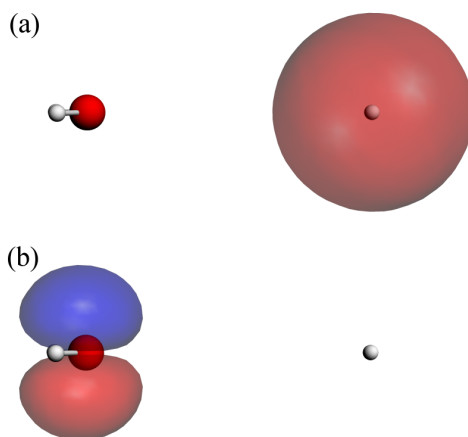
energy of the LUMO. In these cases the calculation has to be forced to converge to a nonaufbau solution.

The fact that a bound unoccupied orbital appears at the frozen subsystem is a consequence of the wrong limit of the kinetic-energy component of the embedding potential for the approximate kinetic-energy functional PW91k applied here. If the kinetic-energy component of the embedding potential shows the correct long-distance limit derived in Sec 5.3.2 at the frozen system, the (repulsive) kinetic-energy component should cancel the attractive electrostatic potential. In this case, there should not be any bound orbitals localized at the frozen subsystem. The low-lying unoccupied orbital localized at the Li^+ subsystem is thus an artifact introduced by the use of an approximate kinetic-energy functional. The PW91k kinetic-energy functional is not able to compensate the attractive electrostatic parts of the embedding potential, which leads to an artificially too low-lying virtual orbital localized at the frozen subsystem. This wrong description is similar to the problems that arise if purely electrostatic models (e.g., point charges) are used to describe an environment, where additional measures, such as the introduction of pseudopotentials or a damping factor for the nuclear attraction, have to be taken to avoid the localization of charge on the environment.[142]

It should be noted that the limiting case for the embedding potential is quite different from the behavior that appears if a pseudopotential approach is used for representing the frozen subsystem, like it is, for instance, done in the effective group potential method.[143,144] In this case, only the occupied orbitals of the frozen subsystem are projected out of the variational space used for the nonfrozen system, so that all virtual orbitals present in the supermolecular calculation, including those localized at the frozen subsystem, will appear in the calculation on the nonfrozen subsystem. The partitioning of the electron density into the electron densities of subsystems that is the starting point for the FDE scheme leads to a partitioning not only of the occupied orbitals, but also implies a partitioning of the virtual orbital space. This is a consequence of the use of a local embedding potential that does not contain any projection operators, unlike in pseudopotential approaches.

To investigate the influence of the approximate kinetic-energy functional, we also performed calculations using the Thomas–Fermi (TF) functional to approximate the kinetic-energy component of the embedding potential. In this case, the general picture is identical to that obtained using PW91k, only that in the FDE(s) calculation the LUMO, which is also localized at the Li subsystem, has an even lower orbital energy. At larger distances, its orbital energy is approximately -8.7 eV, i.e., 2.1 eV lower than that of the LUMO-Li in the supermolecular calculation. Therefore, also when using the TF functional, the orbital energy of the artificially too low-lying LUMO is below the orbital energy of the HOMO, and a nonaufbau solution is obtained.

We did not investigate approximate GGA kinetic-energy functionals other than PW91k since only the TF functional and PW91k have been widely applied in practical applications of FDE. However, none of them ensures the correct long-distance limit. It can therefore be expected that any GGA kinetic-energy functional will behave similar to PW91k and show this shortcoming if applied for approximating the kinetic-energy component of the embedding potential.

Even though the failure of the kinetic-energy component of the embedding potential in the long-distance limit leads to artificially too low-lying unoccupied orbitals, it does not change the occupied orbitals, since in the region of the nonfrozen subsystem the embedding potential is correct. Therefore, the calculated electron density will not be affected, as long as no orbital localized at the frozen subsystem is occupied and as long as there is no electron density leaking into the regions of the frozen system. However, the artificially too low-lying virtual orbitals will lead to a number of problems in practical applications of FDE.

First, as it was shown here in the case of $H_2O \cdots Li$, their orbital energies can be of similar size as the orbital energy of the HOMO of the nonfrozen system, or even drop below the orbital energy of the HOMO. This will lead to serious convergence problems since the self-consistent field procedure has to be forced to converge to a nonaufbau solution. Second, the accurate description of virtual orbitals is crucial for the correct description of response properties such as excitation energies, which is a very important application of the FDE scheme.[CJ4,76,83] In the calculation of response properties, the artificially too low-lying virtual orbitals will introduce spurious excitations to these orbitals. Even though they will, in general, have a low oscillator strength, they might mix with other excitations and thus influence the calculated absorption spectra.

In the FDE(m) calculations, the problem of artificially too low-lying virtual orbitals does not occur because there are no basis functions present that probe the regions of the frozen system, where the embedding potential is wrong. This might be a practical way of avoiding the problems discussed above. However, it does not solve them. Since FDE should be exact in the exact-functional limit, it should also be applicable when larger basis sets are used. In many cases, it might be necessary to include basis functions on the frozen system, at least for a few atoms involved in (hydrogen) bonds with the nonfrozen subsystem because these basis functions are important to model the charge density in the bonding region.[40,69] Furthermore, the calculation of response properties of the nonfrozen subsystem often requires the use of basis sets containing very diffuse functions.[CJ5] In calculations on weakly interacting systems such as van der Waals complexes the inclusion of diffuse functions is in many cases required.[CJ3] These diffuse basis functions on the nonfrozen system will also probe the embedding potential at the frozen subsystem, thus possibly leading to artificially too low-lying virtual orbitals, even in FDE(m) calculations. In the examples presented here, the

use of basis functions of the frozen subsystem would normally not be necessary, but they have been included to identify problems that will appear with sufficiently diffuse basis sets more clearly.

To demonstrate that the wrong long-distance limit of the kinetic-energy component v_T of the embedding potential does not only have consequences in rather artificial model systems, but also in cases that are of importance in practical applications, we have also investigated the system studied in Ref. CJ4, where solvent effects on the absorption spectrum of the organic dye aminocoumarin C151 have been studied. For our test calculations, we employed a cluster consisting of the aminocoumarin C151 molecule and the 30 closest solvent water molecules, using the coordinates of one arbitrary snapshot from the molecular dynamics simulation performed in Ref. CJ4. The structure of this cluster is shown in Fig. 5.7.

In the FDE calculations, the frozen subsystem is formed by the solvent environment, and a sum of the electron densities calculated for the isolated water molecules is used to approximate the frozen density ρ_{II}. For studying solvent effects it has been shown[76] that this is usually a good approximation to the true electron density of the solvent. It can, therefore, be assumed that this approximated density in the regions of the frozen density—at least in the regions where the overlap with the density of the nonfrozen subsystem is small—is close to the exact total density and that in these regions the assumptions made in Sec. 5.3 are fulfilled.

The orbital energies of the four highest occupied MOs and of the unoccupied orbitals with orbital energies lower than -0.3 eV calculated for this test system are shown in Fig. 5.8. As a starting point, the orbitals calculated for the isolated aminocoumarin C151 are given. In this case, the virtual orbitals ($59a$ – $62a$) are antibonding orbitals of the aminocoumarin C151. In the FDE(m) calculation, the orbital energies change significantly with respect to the isolated molecule calculation, which is due to the influence of the solvent environment. However, for both the occupied and the unoccupied orbitals in the energy range of interest, the main character of the orbitals does not change.

In the FDE(s) calculations, the orbital energies of the orbitals 55a to 61a are all slightly lower than in the FDE(m) calculation but do not change significantly. This can be attributed to the larger basis set available in the FDE(s) calculation. However, additional virtual orbitals ($62a$ – $65a$) show up in the energy range of interest that were not present in the FDE(m) calculation. Isosurface plots of these unoccupied orbitals are shown in Fig. 5.7.

It can be seen that all four of these unoccupied orbitals are mainly localized at the water environment. As discussed above, these orbitals should not be present in the calculation of the aminocoumarin C151 subsystem. They are thus artificially too low-lying orbitals introduced by the wrong long-distance limit of the approximations used

Figure 5.7.: Structure of an aminocoumarin C151 molecule surrounded by 30 water solvent molecules and isosurface plots (contour value: 0.03) of the spurious unoccupied orbitals obtained in the FDE(s) calculation. See text for details. Graphics: VMD [145].

(a) 62a

(b) 63a

(c) 64a

(d) 65a
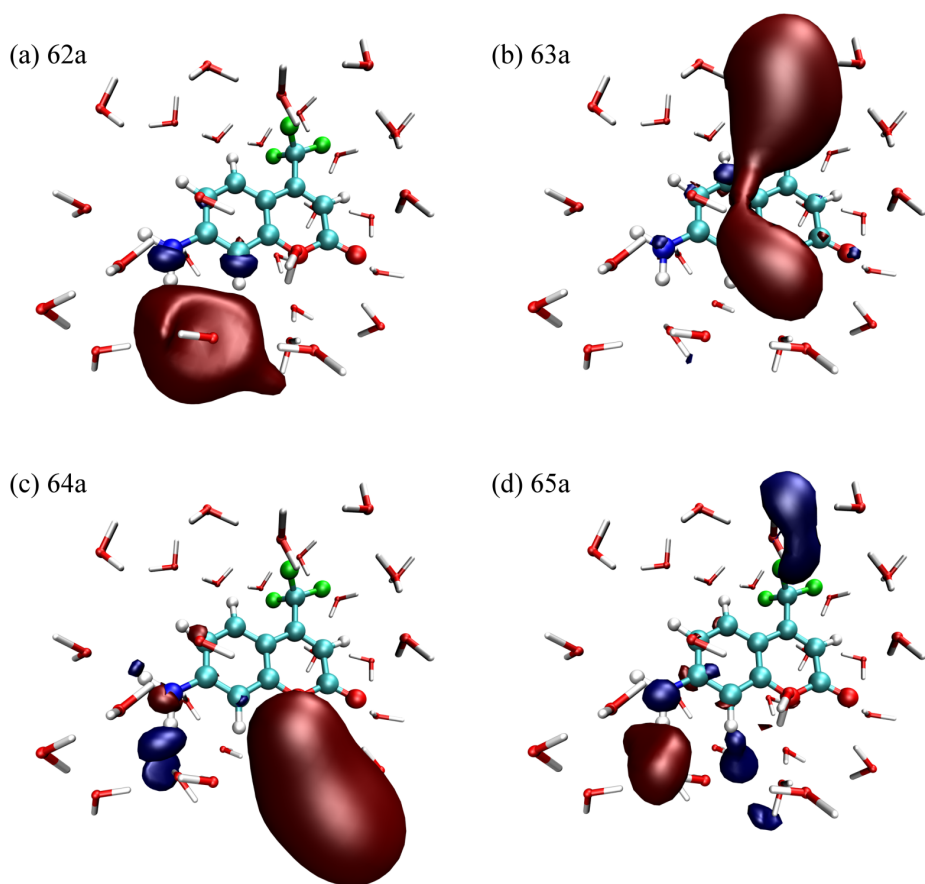
Figure 5.8.: Orbital energies (in eV) of the relevant orbitals calculated for aminocoumarin C151 surrounded by 30 water molecules. Only orbitals with energies lower than −0.3 eV have been included. As reference, the orbital energies calculated for the isolated aminocoumarin C151 are shown first, together with those calculated both using FDE(m) and FDE(s). Finally, the orbital energies calculated in a FDE(s) calculation using the long-distance corrected approximation to v_T are given [labeled FDE(s)-corr]. See text for details.
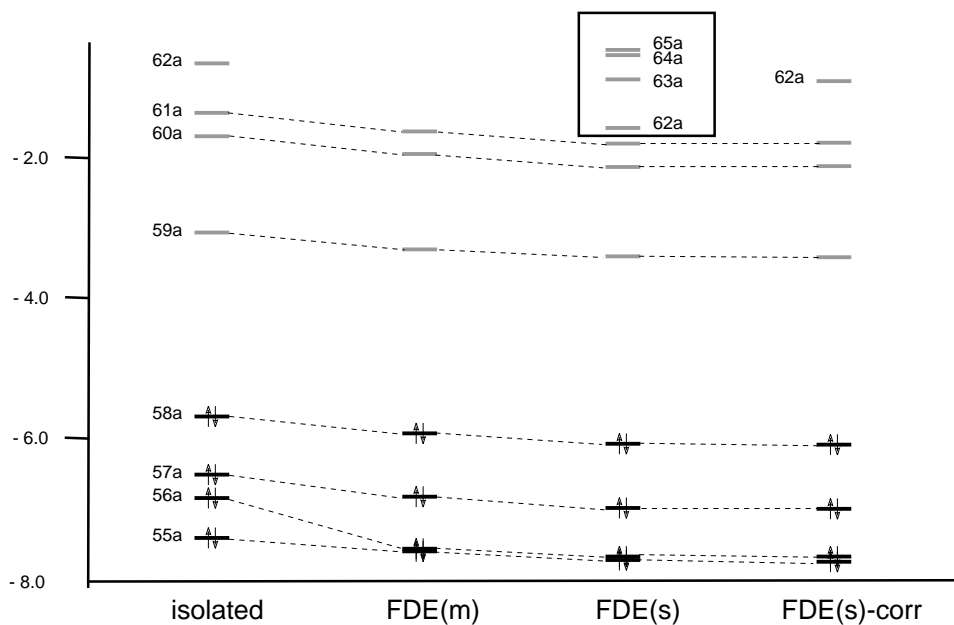
for the kinetic-energy component of the embedding potential. This shows that this wrong limit does also have consequences in realistic systems that have been studied using the FDE scheme, if basis functions that can probe the regions of the frozen subsystem are present.

The artificially too low-lying virtual orbitals also show up in the calculation of the absorption spectrum by introducing spurious excitations. In the spectrum calculated using time-dependent DFT (TDDFT), the seventh excitation has a contribution of 28.1% of an excitation from orbital 58a to orbital 63a, i.e., of an excitation to one of the spurious virtual orbitals, and the eighth excitation has a contribution of 69.4% of such an excitation. The excitation energies of both of these excitations appear in the energy range of interest and show a significant oscillator strength. In the FDE(m) calculation, no similar excitations are found.

5.6. A long-distance corrected approximation to v_T

To compensate for the wrong long-distance limit of the kinetic-energy component of the embedding potential, we can improve the currently available approximations, which employ Eq. (5.3) in combination with an approximate LDA or GGA kinetic-energy functional, by enforcing the correct long-distance limit. The strategy followed is similar to that applied in Refs. 146 and 147 to enforce the correct description of charge-transfer excitations in TDDFT.

To achieve the correct long-distance limit, we augment the approximate kinetic-energy component $\tilde{v}_T$ of the embedding potential with a correction term v_T^{corr}, i.e.,

$$\tilde{v}_T[\rho_{\mathrm{I}}, \rho_{\mathrm{II}}](\boldsymbol{r}) = \left.\frac{\delta \tilde{T}_s[\rho]}{\delta \rho}\right|_{\rho=\rho_{\mathrm{tot}}(\boldsymbol{r})} - \left.\frac{\delta \tilde{T}_s[\rho]}{\delta \rho}\right|_{\rho=\rho_{\mathrm{I}}(\boldsymbol{r})} + v_T^{\mathrm{corr}}[\rho_{\mathrm{I}}, \rho_{\mathrm{II}}](\boldsymbol{r}). \qquad (5.27)$$

This correction term should enforce the correct long-distance limit at the frozen system. In all other cases, it should leave the approximate $\tilde{v}_T$ unchanged because it is expected to be a rather good approximation in those cases and currently there are no better approximations available.

5. Exact long-distance limit

For this correction term, we therefore chose the form

$$v_T^{\text{corr}}[\rho_{\text{I}}, \rho_{\text{II}}](\boldsymbol{r}) = - \exp\left[-\left(\frac{\rho_{\text{I}}(\boldsymbol{r})}{\alpha\,\rho_{\text{II}}(\boldsymbol{r})}\right)^2\right] \quad \left(v_{\text{II}}^{\text{nuc}}(\boldsymbol{r}) + \int \frac{\rho_{\text{II}}(\boldsymbol{r}')}{|\boldsymbol{r} - \boldsymbol{r}'|}d\boldsymbol{r}'\right.$$

$$+ \left.\frac{\delta E_{\text{xc}}[\rho]}{\delta\rho}\right|_{\rho=\rho_{\text{tot}}(\boldsymbol{r})} - \left.\frac{\delta E_{\text{xc}}[\rho]}{\delta\rho}\right|_{\rho=\rho_{\text{I}}(\boldsymbol{r})}$$

$$+ \left.\frac{\delta\tilde{T}_s[\rho]}{\delta\rho}\right|_{\rho=\rho_{\text{tot}}(\boldsymbol{r})} - \left.\frac{\delta\tilde{T}_s[\rho]}{\delta\rho}\right|_{\rho=\rho_{\text{I}}(\boldsymbol{r})}\bigg). \tag{5.28}$$

In this expression, the first factor serves as a switching function that turns on the correction when needed, but that is zero otherwise. When the correction is switched on, i.e., the exponential in the above expression equals 1, the term in parentheses, which equals the approximate effective embedding potential, is subtracted, thus leading to the total effective embedding potential being zero and enforcing the correct long-distance limit at the frozen subsystem. To decide when this correction is switched on, we used the ratio of $\rho_{\text{I}}(\boldsymbol{r})$ and $\rho_{\text{II}}(\boldsymbol{r})$ in the switching function; i.e., when $\rho_{\text{II}}(\boldsymbol{r})$ is sufficiently large compared to $\rho_{\text{I}}(\boldsymbol{r})$, the correction is switched on. Based on numerical tests, we chose a value of 0.1 for the parameter α, which means that the correction is applied when $\rho_{\text{II}}(\boldsymbol{r})$ is ten times as large as $\rho_{\text{I}}(\boldsymbol{r})$.

It should be noted that this proposed correction can only be applied if the initial assumptions given in Sec. 5.3 are fulfilled, i.e., if the partitioning of the total electron density is such that the electron densities of the subsystems equal the ground-state densities of the separated subsystems. This is not the case if there is charge transfer between the subsystems. In such cases, the correction given above will enforce a long-distance limit that is not correct.

The orbital energies calculated using this long-distance correction in combination with the PW91k kinetic-energy functional for the $H_2O\cdots Li$ complex studied above are shown in Fig. 5.9. It can be seen that, while the orbital energy of the HOMO still agrees with the supermolecular HOMO, the spurious LUMO-Li found in the FDE(s) calculation does not appear anymore. Instead, the LUMO is given by an orbital localized at the H_2O subsystem, and its orbital energy agrees with the orbital energy of the LUMO-H_2O found in the supermolecular calculation.

Finally, we applied the correction in the calculation of aminocoumarin C151 surrounded by water. The orbital energies calculated in the FDE(s) calculation using the long-distance correction are included in Fig. 5.8. It can be seen that while the orbital energies of the other orbitals do not change significantly, the spurious virtual orbitals 62a to 65a found in the uncorrected FDE(s) calculation, which were mainly localized at the water environment, do not appear anymore. Instead, there is only one virtual orbital 62a that was not present in the FDE(m) calculation.

Figure 5.9.: Orbital energies calculated in FDE calculations on the H_2O subsystem in the presence of the frozen Li^+ subsystem using the PW91k kinetic-energy functional in combination with the long-distance correction as a function of the O–Li distance. As reference, the results of the super-molecular DFT calculation are also shown. See text for details.
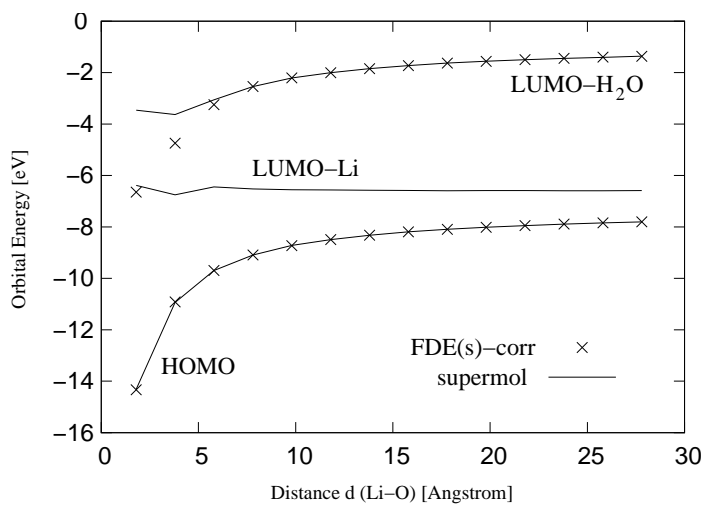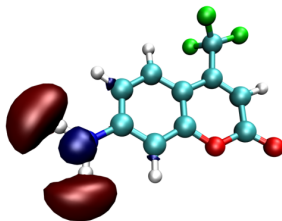
Figure 5.10.: Isosurface plots (contour value: 0.05) of the unoccupied orbital $62a$ calculated for (a) aminocoumarin C151 surrounded by 30 water molecules using the long-distance corrected approximation to v_T in a FDE(s) calculation and (b) the isolated aminocoumarin C151. See text for details. Graphics: VMD [145].

(a) FDE(s)-corr
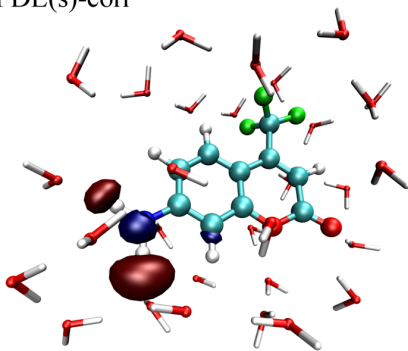
(b) isolated

An isosurface plot of this orbital is shown in Fig. 5.10. This virtual orbital is not localized at the water environment, but it is a N–H antibonding orbital of the amino group. A similar orbital is also present in the isolated molecule calculation (also shown in Fig. 5.10 for comparison). A closer inspection of the orbitals in the FDE(s) calculation shows that, actually, the virtual orbitals $62a$, $64a$ and $65a$ do also have a contribution from such an N–H antibonding orbital. The long-distance correction is thus able to remove the spurious contributions localized at the environment while keeping the contributions corresponding to virtual orbitals localized at the nonfrozen subsystem.

However, in the FDE(m) calculation such a N–H antibonding orbital appears only with a positive orbital energy. The long-distance correction not only compensates the attractive potential in the environment, but also the repulsive parts of the embedding potential. As the $62a$ orbital reaches out into regions of the environment where the embedding potential is mainly repulsive, this leads to a lowering of its orbital energy. If the long-distance correction is also applied in the FDE(m) calculation, a virtual orbital $62a$ similar to that in the FDE(s) calculation is found at an orbital energy of -0.26 eV, which is still significantly higher than in the FDE(s) calculation. This remaining difference is due to the larger flexibility of the basis set in the FDE(s) calculation.

5.7. Conclusions

We have derived an exact expression for the kinetic-energy component v_T of the embedding potential that is used in the FDE scheme. By relating the functional derivative of the noninteracting kinetic-energy $T_s[\rho]$ to the KS potential $v_s[\rho]$ corresponding to this density, we obtain a way of calculating v_T exactly for an arbitrary pair of v_s-representable densities. In future work, this could be applied for performing FDE calculations using the exact kinetic-energy potential that could serve as a reference for developing improved approximations to v_T.

In this paper, we have applied the obtained expression to investigate v_T in the long-distance limit. We have shown that—under the assumption that the frozen electron density is close to the exact total electron density at the frozen subsystem—for large separations of the two subsystems the embedding potential at the nonfrozen subsystem should reduce to the purely electrostatic embedding potential, while at the frozen subsystem it should be zero.

One consequence of this exact limit is that for well-separated subsystems, not only the electron density and thus the occupied orbitals, but also the virtual orbitals are divided between the two subsystems; i.e., in the FDE calculation on one of the

subsystems no virtual orbitals of the other subsystems should appear. This is a fundamental difference to pseudopotential approaches, in which only the occupied orbitals are projected out.

We have shown that while in the long-distance limit the approximations currently in use for v_T are correct at the nonfrozen subsystem, they fail at the frozen system, where the available GGA kinetic-energy functionals are not able to cancel the electrostatic and exchange-correlation components of the embedding potential. As our calculations on model systems have shown, this, in general, does not influence the calculated electron density and the calculated occupied orbitals, but it leads to artificially too low-lying virtual orbitals. These are problematic in two respects. First, as shown for $H_2O \cdots Li$, their orbital energy can drop below that of the HOMO, leading to nonaufbau solutions. Second, these spurious virtual orbitals will influence the calculation of response properties, for which a good description of virtual orbitals is crucial.

While it is in many cases possible to avoid these problems by not including basis functions on the frozen subsystem in the calculation of the nonfrozen subsystem [FDE(m)], these basis functions might be necessary to accurately describe hydrogen bonds between the subsystems or diffuse basis functions on the nonfrozen subsystem might be able to probe the regions in which the embedding potential is wrong. In these cases, we recommend the use of the long-distance correction proposed in this work.

However, while the proposed long-distance correction is able to remove the spurious virtual orbitals in the model systems studied here, its applicability is rather limited. First, it can only be used if the partitioning is such that the subsystem densities are close to the ground-state densities of the well-separated subsystems and it will, therefore, not work if there is a (partial) charge transfer from the nonfrozen to the frozen subsystem. It might be possible to devise more advanced corrections that detect such cases, e.g., by monitoring the orbital energies of both subsystems. Second, the proposed correction does only work in combination with approximate kinetic-energy functionals that are wrong in the long-distance limit. If it is used with the exact kinetic-energy functional, the correction of Eq. (5.28) will still give nonzero contributions. And third, the kinetic-energy component of the embedding potential obtained with this correction cannot be expressed as the functional derivative of an energy functional. For these reasons, this correction can only be viewed as a first step toward more advanced approximations that ensure the correct long-distance limit.

Furthermore, the fact that the available approximations to v_T fail completely at the frozen subsystem makes it very likely that they can be considerably improved in the regions where the densities of the two subsystems overlap. The correction proposed in this work can be seen as a first step towards a new generation of approximations, which do not employ Eq. (5.3), i.e., which make use of an approximate kinetic-energy

functional but that approximate v_T directly and which are constructed such that they obey the exact limits derived here. This might possibly be a promising route on the way to approximations that will also be applicable in the case of stronger interactions and thus remove some of the limitations the FDE scheme currently still has.

5. Exact long-distance limit

Part III.

Implementation

6. Improved efficiency for frozen-density embedding calculations

Abstract

An improved implementation of frozen-density embedding (FDE) is presented. Due to an efficient numerical integration scheme, this implementation makes it possible to apply FDE to large solvent shells (up to more than 1000 atoms in the present example). For sufficiently large environments, the size of the grid used in the numerical integration does not increase with the size of the environment, and therefore the computer time required for the most expensive steps of the calculation (such as the SCF iterations or the solution of the TDDFT eigenvalue problem) is constant.

6.1. Introduction

A great advantage of the frozen-density embedding scheme in comparison to super-molecule calculations is the restriction to the orbital space of the embedded system. As a consequence, the dimension of the Fock matrix and of the TDDFT eigenvalue problem (see, e.g., Refs. 148–150), are independent of the system size.

The bottleneck in frozen-density calculations for large solvation shells is the generation

of the solvent density, which in principle requires a converged SCF for the system to be frozen in the embedding calculation. In Ref. 76 it was shown that this can be avoided without significant loss of accuracy in the excitation energies by using a superposition of molecular densities for the solvent. This approach made it possible to apply the embedding scheme to excitations of systems solvated by several hundreds of solvent molecules. For ground-state properties, similar construction methods of approximate environmental densities have been employed.[49,77,79,86]

However, the first implementation used in Ref. 76 still showed a rather strong increase of the CPU time with increasing system size. Calculations with up to 300 water molecules could be carried out, but statistical analyses with solvent shells of this size were out of reach.

We now implemented a version of the frozen-density embedding which is improved in three respects: (i) The generation of the sum-of-fragment density has been made more efficient, (ii) the cost of the numerical integration has been significantly decreased by using a reduced integration grid, and (iii) linear scaling techniques are employed.

6.2. Efficient numerical integration scheme

ADF uses a numerical integration scheme for evaluating the the matrix elements of the Coulomb and exchange-correlation potential.[125] As many steps scale linearly with the number of grid points, the generation of an efficient integration grid is of great importance to speed up the calculations.

Besides the integrals that are needed in the calculation of the isolated system I, also the matrix elements of the embedding potential are necessary in KSCED calculations. These matrix elements are given by

$$\langle \chi_i | v_{\text{eff}}^{\text{emb}} | \chi_j \rangle = \int \chi_i^*(\boldsymbol{r}) v_{\text{eff}}^{\text{emb}}(\boldsymbol{r}) \chi_j(\boldsymbol{r}) \; d\boldsymbol{r} \qquad (6.1)$$

where $v_{\text{eff}}^{\text{emb}}$ is the embedding potential,

$$v_{\text{eff}}^{\text{emb}}[\rho_{\text{I}}, \rho_{\text{II}}](\boldsymbol{r}) = v_{\text{II}}^{\text{nuc}}(\boldsymbol{r}) + \int \frac{\rho_{\text{II}}(\boldsymbol{r'})}{|\boldsymbol{r} - \boldsymbol{r'}|} d\boldsymbol{r'} + \frac{\delta E_{\text{xc}}^{\text{nadd}}[\rho_{\text{I}}, \rho_{\text{II}}]}{\delta \rho_{\text{I}}} + v_T[\rho_{\text{I}}, \rho_{\text{II}}](\boldsymbol{r}), \; (6.2)$$

and χ_i are the STO-basis functions that are used in the calculation of the non-frozen system and that are usually centered only on the atoms in the non-frozen system. The integration grid should be constructed in such a way that only the region in space where the integrand is not negligible is covered.

Among the different components of the embedding potential, the integration of the Coulomb potential for the frozen system puts the most severe requirements on the

integration grid, since the singularities of the Coulomb potential at the nuclei of the frozen system need to be integrated accurately. We therefore concentrate in the following on this contribution to the embedding potential. The previous implementation of the FDE scheme in ADF used the same integration grid that would be employed in a full super-molecular calculation to avoid problems in this step. However, this integration grid is much larger than necessary, especially in calculations where the frozen environment becomes very large.

The numerical integration used in ADF[124,125] is based on a partitioning of space into atomic polyhedra that are constructed as Voronoi cells around the atoms and the remaining "outer region". Inside the atomic polyhedra a dense spherical grid around the atom ensures an accurate integration of the Coulomb singularity of the nucleus, while in the outer region only few integration points are needed. Details of this grid generation are explained in Ref. 151.

In the improved FDE implementation, atomic polyhedra are only constructed for atoms that are within a certain distance from atoms in the non-frozen system (4.0 Å in the present example). All other atoms in the frozen part are considered part of the outer region. This ensures sufficiently many grid points for an accurate integration where the integrand in Eq. (6.1) is non-negligible, while only few integration points are created in in those regions where the integrand vanishes because the basis functions $\chi_{i,j}$ of the non-frozen system are small. With the integration grid generated in this way, the number of grid points for larger environments does no longer increase with the size of the frozen environment.

It is important to note that numerical integration over basis or fit functions of the frozen system is completely avoided. The (electronic) Coulomb part of the embedding potential,

$$v_{\text{Coulomb}}^{\text{emb}}(\boldsymbol{r}) = \int \frac{\rho_{\text{II}}(\boldsymbol{r}')}{|\boldsymbol{r} - \boldsymbol{r}'|} d\boldsymbol{r}' \tag{6.3}$$

is calculated using density fitting, i.e., the electron density of the frozen environment $\rho_{\text{II}}(\mathbf{r})$ expressed as a linear combination of STO fit functions χ^{fit}:

$$\rho_{\text{II}}(\boldsymbol{r}) \approx \sum_i c_i \chi_i^{\text{fit}}(\boldsymbol{r}) \tag{6.4}$$

These fit functions are centered on the atoms of the frozen environment. Integrals over these functions—as needed for $v_{\text{Coulomb}}^{\text{emb}}(\boldsymbol{r})$—can easily be calculated analytically.[125] The Coulomb potential has to be evaluated only on the integration grid in the non-frozen system.

A further speed-up of the calculations is achieved by the use of linear scaling techniques[152] to skip complete blocks of integration points for basis functions that are small on these parts of the grid.

Figure 6.1.: Structure of the organic dye aminocoumarin C151, and of five water molecules that are closest in the MD snapshot employed for the test calculations. See text for details.
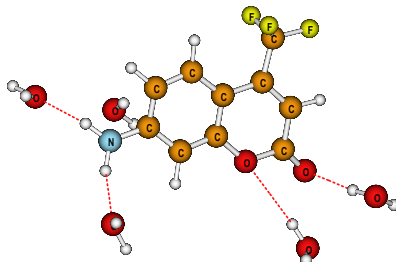

With this improved implementation, for most parts of the calculation the CPU time needed does not depend on the size of the frozen environment anymore. For large environments, the number of grid points is constant, even if the size of the frozen system is further increased. Therefore the time needed for one SCF cycle and the time spent for the TDDFT calculation are also independent of the size of the frozen system.

There are two steps that still do scale roughly linear with the size of the environment: the construction and fitting of the environment density and the calculation of the frozen density and its Coulomb potential in the grid points. Since the density of the environment is frozen during the SCF, these steps are only performed once at the beginning of the calculation. The frozen density and the corresponding Coulomb potential are then stored for further use.

6.3. Results

To demonstrate the efficiency of this improved implementation, we have performed test calculations on the organic dye molecule aminocoumarin C151, which is shown in Fig. 6.1. For these tests, an arbitrary snapshot from a classical MD simulation was employed, and up to 500 solvent water molecules have been included in the frozen environment. For the preparation of the frozen-density, the innermost 50 water molecules were treated as flexible fragments with the geometries they have in the snapshot, while a uniform rigid structure (optimized in vacuo) was assumed for the outer water molecules (cf. Ref. 76). The structure of aminocoumarin surrounded by 300 water molecules is shown in Fig 6.2

Figure 6.2.: Structure of aminocoumarin C151, surrounded by 300 solvent water molecules. Graphics: VMD [145].
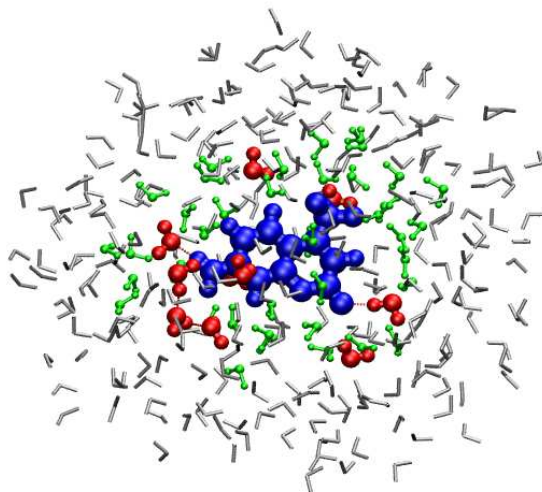
Due to the efficient numerical integration scheme, a large speed-up of the embedding calculations could be achieved. Figure 6.3 shows the CPU times for calculations (on one processor of an SGI Altix 3700) of the 5 lowest excitations of aminocoumarin C151 solvated by 0 to 500 water molecules.

The frozen-density preparation step is reduced to a very small amount of the total CPU time, and typically takes less than 10 minutes even for the largest systems considered here. The calculation of the frozen density and its Coulomb potential in the grid points still shows an approximately linear increase in computer time with the size of the frozen system, while the time needed for one SCF cycle is constant (about 8 min in the present example). The effort for the TDDFT part is approximately 55 min for all embedded calculations for this snapshot, independently of the size of the solvent shell. The deviations between excitation energies calculated with the reduced grid and with a full integration grid are negligible (typically not larger than ≈ 0.0001 eV).

While the CPU time only increases slightly with the size of the solvent shell, the inclusion of additional solvent molecules has a large influence on the calculated excitation energies. In Fig. 6.4, excitation energy is show as a function of the size of the solvent shell. For the first 50 water molecules, the behavior of the excitation

Figure 6.3.: Total CPU times for calculations of the 5 lowest excitations of aminocoumarin C151 on one processor of an SGI Altix 3700 as a function of the number of frozen water molecules considered. The CPU times include the frozen-density preparation, embedded SCF, and embedded TDDFT steps. Additionally, a linear fit to the wall clock times of the embedding calculations is shown.
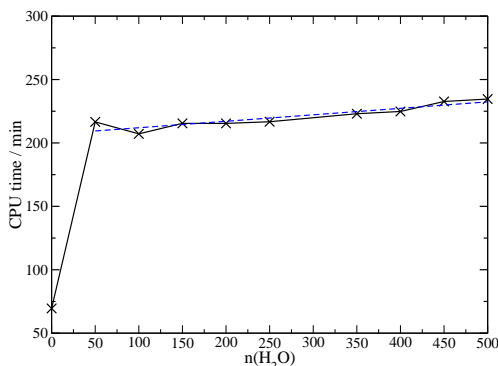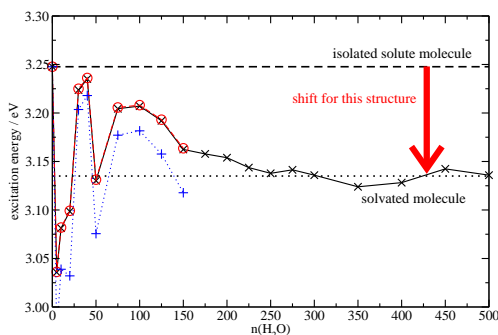

Figure 6.4.: Excitation energy of aminocoumarin C151 as a function of the size of the (water) solvent shell considered in the frozen-density calculation for an arbitrary snapshot from an MD simulation. Three different basis sets have been used for the frozen density: (i) DZ (dotted line/symbol:"+"), (ii) DZP (solid line/symbol: cross), (iii) TZP (dashed line/symbol: circle).

energies is rather irregular, while adding additional water molecules the excitation energy converges more regularly. It can be seen that a solvent shell of approximately 300 water molecules is needed to obtain converged excitation energies.

6.4. Conclusion

Due to an optimized grid generation scheme and the combination of linear-scaling techniques with the frozen-density embedding as well as the efficient generation of solvent densities by a sum-of-fragments approach, the size of the explicitly modeled environment could be extended to solvent shells including more than 1000 atoms.

Since such calculations are easily possible even on single CPUs of a modern PC, modeling general solvent effects by an evaluation of several hundreds of snapshots including large solvation shells becomes feasible. Explicit solvent models for systems of this size were, up to now, restricted to (semi-)empirical models, whereas frozen-density embedding does not require any empirical information - apart from the usual parametrization in the density functionals.

The improved implementation described in this Chapter has been applied in a more extensive study[CJ4] of the solvent effect on the excitation energies of aminocoumarin C151, where the spectrum in water and in n-hexane was simulated by averaging over 400 snapshots obtained from a classical MD simulation. For each snapshot, a solvent shells consisting of 900 atoms was employed. The solvent shift between the polar solvent water and the nonpolar solvent n-hexane calculated in this way agreed very well with the experimental results.

6. *Improved efficiency for FDE calculations*

7. A flexible implementation of frozen-density embedding for use in multilevel simulations

Abstract

A new implementation of frozen-density embedding (FDE) in the Amsterdam Density Functional (ADF) program package is presented. FDE is based on a subsystem formulation of density-functional theory (DFT), in which a large system is assembled from an arbitrary number of subsystems, which are coupled by an effective embedding potential. The new implementation allows both an optimization of all subsystems as a linear-scaling alternative to a conventional DFT treatment, the calculation of one active fragment in the presence of a frozen environment, and intermediate setups, in which individual subsystems are fully optimized, partially optimized, or completely frozen. It is shown how this flexible setup can facilitate the application of FDE in multilevel simulations.

7.1. Introduction

Applications of quantum chemical methods for studying biological systems often require the use of multilevel methods, i.e., methods that treat different parts of the total system using different approximations (for recent examples, see, e.g., Refs. 80,

153–155). In particular, QM/QM methods[6] (i.e., multilevel methods that apply different quantum mechanical (QM) methods in different regions), and QM/MM methods[5,156,157] (i.e., methods that combine a QM treatment with a molecular mechanics (MM) treatment) are widely used.

Different multilevel methods can be classified according to the way in which the interaction between the different levels is described.[9] Many methods, in particular QM/QM methods, only employ what is usually referred to as mechanical coupling, i.e., the coupling between the different regions is only described at the level of the total energy.[6,7,158,159] In these methods, no effect of the other region is included in the potential, so that only an indirect effect on molecular properties due to changes in the equilibrium structure can be described. In contrast, most standard QM/MM methods[4,5,142] include the electrostatic potential of the MM environment in the QM calculation (electronic coupling), thus allowing a more adequate description of molecular properties. An even more accurate description of the coupling can be obtained by also considering the polarization of the MM environment due to the QM part, as it is done in some advanced QM/MM schemes that employ polarizable force fields.[160–162]

However, QM/MM methods rely on a careful parametrization of the MM part, and even though there are accurate force fields available for many classes of compounds, these often cannot be applied for non-standard system, such as compounds containing transition metal atoms. On the other hand, common QM/QM methods do not suffer from these restrictions, but they are limited to describing the interaction between the different regions at the level of mechanical coupling only.

One promising multilevel method is the frozen-density embedding (FDE) scheme within density-functional theory first developed by Wesolowski and Warshel.[8,48] It describes the full system on a quantum mechanical basis and at the same time includes the electronic coupling between different regions. Even though the FDE scheme relies on the use of an approximate kinetic-energy functional, it offers a treatment that is in principle exact. It has been successfully applied in a number of studies, e.g., of solvent effects on absorption spectra,[CJ4,CJ5,76] electron spin resonance (ESR) parameters[50] and nuclear magnetic resonance (NMR) chemical shifts.[CJ6] It has further been employed for describing induced circular dichroism in host–guest systems[83] and for free-energy calculations in protein environments.[78,80]

In the subsystem formulation of DFT,[51] which forms the starting point for FDE, the total system is partitioned into N subsystems, and the total electron density $\rho_{\text{tot}}(\boldsymbol{r})$ is represented as the sum of the electron densities of these fragments $\rho_i(\boldsymbol{r})$ $(i = 1, \ldots, N)$. Given this partitioning of the electron density, the DFT total energy

can be expressed as a functional of the subsystem densities.

$$E[\rho_1, \ldots, \rho_N] = \int \rho_{\text{tot}}(\boldsymbol{r}) \left(\sum_{i=1}^{N} v_i^{\text{nuc}}(\boldsymbol{r}) \right) \, d\boldsymbol{r} + \frac{1}{2} \int \frac{\rho_{\text{tot}}(\boldsymbol{r})\rho_{\text{tot}}(\boldsymbol{r'})}{|\boldsymbol{r} - \boldsymbol{r'}|} \, d\boldsymbol{r} d\boldsymbol{r'}$$
$$+ E_{xc}[\rho_{\text{tot}}] + \sum_{i=1}^{N} T_s[\rho_i] + T_s^{\text{nadd}}[\rho_1, \ldots, \rho_N], \tag{7.1}$$

where $\rho_{\text{tot}} = \sum_{i=1}^{N} \rho_i$ is the total electron density, v_i^{nuc} is the electrostatic potential of the nuclei in subsystem i, E_{xc} is the exchange-correlation functional, and $T_s^{\text{nadd}}[\rho_1, \ldots, \rho_i]$ is the nonadditive kinetic-energy functional, which is defined as

$$T_s^{\text{nadd}}[\rho_1, \ldots, \rho_N] = T_s[\rho_{\text{tot}}] - \sum_{i=1}^{N} T_s[\rho_i]. \tag{7.2}$$

In the above expressions, $T_s[\rho]$ is the kinetic energy of the noninteracting reference system, as it is defined within Kohn–Sham (KS) DFT, which is usually calculated using the KS orbitals. However, with the given partitioning into subsystems, KS orbitals are only available for the subsystems and not for the full system and $T_s[\rho_{\text{tot}}]$ can therefore not be calculated directly. For this reason, in practical applications an approximate kinetic energy functional has to be used to evaluate T_s^{nadd}. Most previous applications employ either the Thomas–Fermi (TF) kinetic energy functional or the GGA functional PW91k,[58] which have been shown to yield accurate results for weakly interacting and hydrogen-bound systems.[CJ3,40] However, the applicability of these functionals is limited to cases in which the interaction between the subsystems is not too large, and the description of covalent bonds between subsystems is currently not possible. The development of improved approximate kinetic-energy functionals for the application in the FDE scheme is, therefore, an active area of research.[CJ7,48]

The electron densities of the individual subsystem ρ_i can be determined by minimizing the above total energy functional with respect to the density of this subsystem, while keeping the densities of the other subsystems frozen. This leads to a set of coupled KS-like equations,

$$\left[-\frac{\nabla^2}{2} + v_{\text{eff}}^{\text{KS}}[\rho_i](\boldsymbol{r}) + v_{\text{emb}}^{(i)}[\rho_1, \ldots, \rho_N](\boldsymbol{r}) \right] \phi_k^{(i)}(\boldsymbol{r}) = \epsilon_k^{(i)} \, \phi_k^{(i)}(\boldsymbol{r}) \tag{7.3}$$

from which the KS orbitals $\{\phi_k^{(i)}\}$ and the associated electron density ρ_i of the subsystem can be obtained. In this equation, $v_{\text{eff}}^{\text{KS}}[\rho_i]$ is the KS effective potential of the isolated subsystem i containing the usual terms of the nuclear potential, the Coulomb potential of the electron, and the exchange–correlation potential. The effective embedding potential $v_{\text{emb}}^{(i)}[\rho_1, \ldots, \rho_N]$ contains the effect of the other subsystems

on subsystem i and is given by

$$
\begin{aligned}
v_{\mathrm{emb}}^{(\mathrm{i})}[\rho_1,\ldots,\rho_N] = {} & \sum_{j\neq i} v_j^{\mathrm{nuc}}(\boldsymbol{r}) + \sum_{j\neq i} \int \frac{\rho_j(\boldsymbol{r}')}{|\boldsymbol{r}-\boldsymbol{r}'|} d\boldsymbol{r}' \\
& + \frac{\delta E_{\mathrm{xc}}[\rho]}{\delta\rho}\bigg|_{\rho=\rho_{\mathrm{tot}}(\boldsymbol{r})} - \frac{\delta E_{\mathrm{xc}}[\rho]}{\delta\rho}\bigg|_{\rho=\rho_i(\boldsymbol{r})} + \frac{\delta T_s^{\mathrm{nadd}}[\rho_1,\ldots,\rho_N]}{\delta\rho_i(\boldsymbol{r})}.
\end{aligned}
\tag{7.4}
$$

It contains the potential of the environment, the Coulomb potential of the electrons in the environment, a nonadditive exchange-correlation component, and a kinetic-energy component.

However, since the density of all the other subsystems appears in the embedding potential for one of the subsystems, the subsystem densities have to be determined iteratively.[51] One possibility of doing this is to employ "freeze-and-thaw" cycles,[52] i.e., to determine the electron density of one active subsystem, which is then frozen while the density of the next subsystem is determined. This procedure can be repeated multiple times for each subsystem, until the densities of all subsystems are converged. Alternatively, the orbitals of all subsystems can be determined simultaneously by constructing a block-diagonal Fock-matrix (consisting of one block for each subsystem) in each SCF iteration, i.e., in each SCF iteration the electron densities of all subsystems are updated.

This fully variational approach, in which the densities of all subsystems are optimized, can be used as an alternative to conventional KS-DFT calculation for large systems. By construction, it scales linearly with the number of subsystems. Initially, it has been applied by Cortona and co-workers for calculations on simple ionic crystals (e.g., alkali halides,[90] alkali-earth oxides,[93] and alkali-earth sulfides[92]), by determining the densities of the ions individually. While in the implementation of Cortona, these densities are constraint to be spherical, an extended scheme has been implemented by Mehl and co-workers. They allow deformations of the atomic densities, and studied alkali halides[98] and corundum.[99]

Recently, the fully variational subsystem DFT approach has been implemented by Iannuzzi *et al.* in the CP2K (Refs. 100, 101) program package.[53] With their implementation molecular dynamics simulations can be performed, in which the individual molecules are treated as subsystems. In this scheme all subsystems are treated on the same footing and the implementation is most efficient in the case of subsystems of the same kind, e.g., the molecules in a homogeneous liquid phase. Another implementation has been presented by Shimojo *et al.* who also implemented this subsystem DFT scheme in combination with a numerical integration scheme employing hierarchical real-space grids as an efficient alternative to standard KS-DFT calculations.[54] They have applied their implementation to MD simulations of aluminum nanoparticles and of nanoindentation of ceramics materials.[102]

The presented subsystem formulation of DFT can also be employed as a method to model the effect of an environment by only optimizing the electron density of one active subsystem in the presence of a frozen environment density and by introducing additional approximations in the construction of this frozen density.[8,49] This strategy, usually referred to as frozen-density embedding (FDE), has been applied in a number of studies of solvent effects on different molecular properties, in which the solvent was constructed as a superposition of the gas phase densities of the individual solvent molecules.[CJ4,CJ5,50,76]

It is particularly suited for studying molecular properties, which are often rather local and can be described well in terms of an active system (of which some property is calculated) and an environment. The theory presented above has been generalized to the calculation of a number of properties, like the calculation of electronic absorption spectra using time-dependent DFT (TDDFT)[59,61] and of NMR shieldings.[CJ6] In these cases also the property calculation is sped up significantly compared to the treatment of the full system, because it only has to be performed for the much smaller active subsystem (which has been influenced by the environment).

The FDE scheme as described above was implemented by Wesolowski and co-workers both in deMon and in deMon2k[163–165] as well as in the Amsterdam Density-Functional (ADF) program package.[CJ4,124,125] Both implementations are limited to two subsystems, of which one is optimized while the other subsystem is kept frozen. In ADF, this frozen density can also be composed from the density of several fragments to obtain approximate environment densities. In both implementations, it is also possible to perform fully variational subsystem DFT calculations by exchanging the role of the frozen and the nonfrozen subsystem in freeze-and-thaw cycles, but this requires several runs of the program and is in general limited to two subsystems.

The implementation in ADF uses an efficient numerical integration scheme that makes it applicable also in the case of rather large (up to more than 1000 atoms) environments (see, e.g., Ref. CJ4). Furthermore, ADF supports the generalization of FDE to TDDFT[59,60] and to the calculation of NMR parameters[CJ6] and can therefore be applied for calculating a wide range of molecular properties (see, e.g., Refs. CJ5, 50, 83).

In this paper, we present a new, improved implementation of FDE in the ADF program package, based on the previous implementation of Wesolowski and coworkers. This new implementation is an intermediate between the two approaches described above, i.e., the fully variational subsystem DFT treatment and the frozen-density embedding approach using an approximate environment. In our implementation the total system is composed of an arbitrary number of fragments that can each be treated using different levels of accuracy, while the interaction between the fragments is described by the embedding potential of Eq. (7.4). On the one hand, the density of

all subsystems can be fully optimized, leading to a subsystem DFT implementation similar to that of Hutter and coworkers.[53] On the other hand, it is also possible to optimize only the density of one active subsystem, while all other subsystems form a frozen environment, leading to the FDE scheme previously implemented in ADF. Furthermore, our implementation also allows all kinds of intermediate setup, e.g., a number of subsystems is fully optimized, while for other subsystems the gas-phase density is only polarized in one freeze-and-thaw cycle and while for the remaining subsystems the frozen density of the isolated molecule is used. In addition, a number of additional options can be specified for each fragment.

7.2. Implementation

Our implementation of FDE in the ADF program package makes use of the concept of fragments, that is central to many aspects of the ADF package.[125] In ADF, any system is build from fragments, which are either atoms or larger parts of the system under study. A lot of quantities calculated, in particular the bonding energy, are then expressed relative to these fragments, and a number of the analysis tools of ADF, like the energy decomposition analysis,[166] rely on the decomposition of the total system into the initial fragments.

This fragments setup has been extended by introducing frozen fragments as a new type of fragments. Similar to the usual nonfrozen fragments, for each frozen fragment the results of a previous ADF calculation have to be provided. In the simplest possible setup, only one frozen fragment is used. In this case, the nonfrozen subsystem will be build from all nonfrozen fragments, as it is normally done in ADF. The frozen fragment will be used as frozen density, and an embedding potential according to Eq. (7.4) will be included in the calculation of the nonfrozen subsystem. This simple setup with only one frozen fragment is similar to the FDE implementation that was previously available in ADF.

In addition, our new implementation also allows the use of more than one frozen fragment. In this case, the frozen densities of all these frozen fragments are added when the embedding potential is constructed. This allows the use of frozen densities that are given by the sum of the densities of isolated molecules, as they are used in studies of solvent effects,[CJ4,76] in a very simple way. If the frozen environment is composed of identical molecules and if the same geometry is used for these molecules, the density of the isolated molecules only has to be calculated once, and this density will be automatically rotated and translated so that it can be used for multiple frozen fragments.

For each fragment, a number of additional options can be specified. It is possible

to choose whether the exact density (calculated using the molecular orbital coefficients) or the fitted density, which can be calculated more efficiently, should be used for the construction of the frozen density. Furthermore, it can be specified whether the basis functions of a frozen fragment are included in the calculation of the non-frozen subsystem. This way it is easily possible to perform calculations using the so-called supermolecular basis set expansion, which is useful for benchmarking calculations.[CJ3,52]

Our new implementation allows the efficient treatment of very large environments. In particular, it employs the numerical integration scheme described in Ref. [CJ4], which uses an integration grid that is centered on the nonfrozen subsystem and which does not increase in size for sufficiently large environments. Therefore, the computational effort for most parts of the calculation, like the self-consistent field (SCF) iterations or property calculations does not increase if the size of the environment is increased. Only the computational effort for the construction of the electrostatic part of the embedding potential and of the frozen electron density, which are both only done once at the beginning of the calculation, scales linearly with the size of the environment. Furthermore, the implementation is efficiently parallelized by applying ADF's parallelization techniques, in particular by distributing the grid points used for the numerical integration among the available nodes.

One of the major new features of our implementation is the ability to relax the electron density of individual frozen subsystems. For each frozen fragment, it is possible to specify whether its density should be relaxed. In this case, the electron density of this fragment will be calculated in a "freeze-and-thaw" cycle, i.e., the fragment is thawed, while all other fragments are frozen. This will be repeated for all frozen fragments for which the density should be relaxed. These relaxation steps are performed several times, until all densities are converged, or until a user-specified maximum number of freeze-and-thaw cycles has been reached. The computational efficiency of the implementation in the case of freeze-and-thaw cycles is ensured by constructing different numerical integration grids as described in Ref. [CJ4] for each of the fragments that are relaxed.

By relaxing the density of all frozen subsystems, fully variational subsystem DFT calculations can be performed. However, the main advantage of our flexible setup is the possibility to relax the density only for certain frozen subsystems. This allows the combination of the subsystem DFT approach as an efficient alternative to conventional KS-DFT calculations with the approximate frozen density treatment of large environments.

In Figure 7.1, an schematic overview of the different types of fragments that are possible and of the options that can be specified for each fragment is given. The implementation contains a number of approximate kinetic-energy functionals for the

Figure 7.1.: Schematic overview of the fragment-based implementation. The implementation support nonfrozen fragments, normal frozen fragments, and frozen fragments for which the density is relaxed in freeze-and-thaw cycles. In addition, a number of options are available for each fragment.
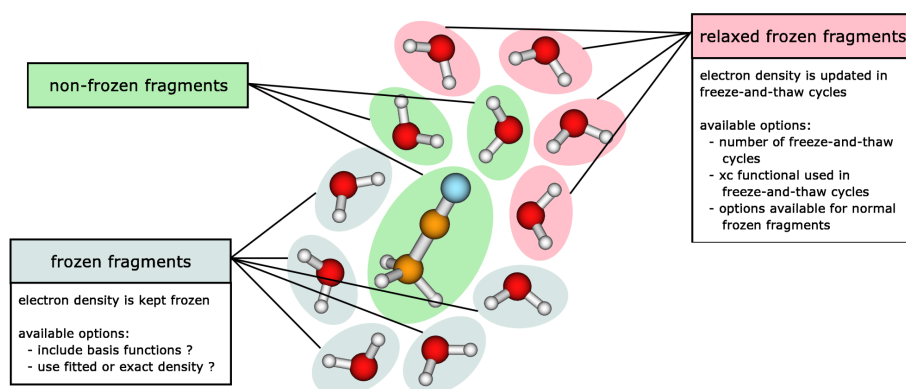

use in the FDE embedding potential, including the Thomas-Fermi functional and the widely used PW91k functional. The code for the evaluation of these functionals has been retained from the previous implementation of Wesolowski, as it was already suitable for the new setup.

For its flexible setup, our implementation makes use of modern object-oriented programming techniques. The code is written in Fortran90, and introduces abstract data types (ADTs) to represent fragments and their properties (like geometry, symmetry information, basis and fit function sets, molecular orbital coefficients, and fit coefficients). The use of these ADTs is not restricted to the FDE code, but they are now used throughout large parts of ADF. This restructured setup also facilitates the implementation of several extensions of the FDE formalism, such as the recently developed scheme for general subsystem TDDFT calculations on an arbitrary number of subsystems[61] that is based on the TDDFT generalization of FDE.[59]

7.3. Example of Application

To illustrate the capabilities of our new implementation, we present some test calculations from an ongoing project,[167] the description of the solvent effect on the nitrogen NMR chemical shift for acetonitrile in water. We have performed calculations on

Figure 7.2.: Structures of the acetonitrile–water clusters used in the test calcula-
tions. (a) acetonitrile surrounded by 15 water molecules, (b) acetoni-
trile surrounded by 25 water molecules, (c) acetonitrile surrounded by
40 water molecules. Graphics: VMD (Ref. [145])

(a)   (b)   (c)
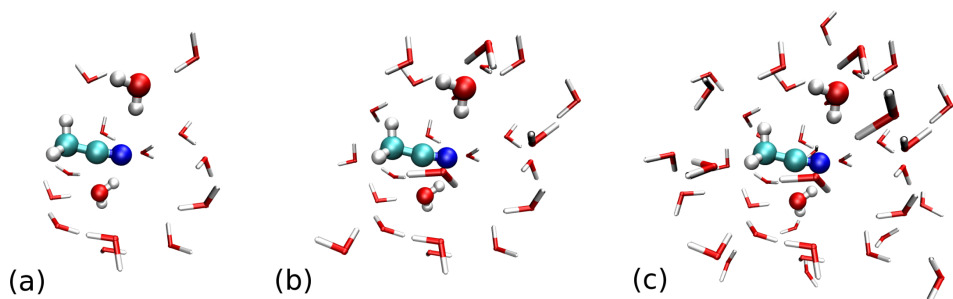
small clusters consisting of acetonitrile and 15, 25, and 40 water molecules, respec-
tively. The structures have been taken from an arbitrary snapshot of a classical MD
simulation. This simulation was performed with the NAMD high performance paral-
lel molecular dynamics package[168] using a box of 30 Å in diameter, and the system was
described using CHARMM force field,[169] with standard TIP3P water molecules.[170]
The water molecules included in the cluster are those nearest to the nitrogen atom of
the acetonitrile. The studied clusters are shown in Figure 7.2.

In the calculations presented in the following, the NMR shieldings have been calcu-
lated using the extension of FDE to the calculation of magnetic properties,[CJ6] and
based on the tests performed in Ref. [CJ6] the contributions of the induced current in
the environment have been neglected. In all calculations, the TZ2P basis set from
the ADF basis set library[124] has been used for acetonitrile as well as for water, and
the exchange-correlation functional BP86, consisting of the exchange functional by
Becke[21] and the correlation functional by Perdew,[23] has been employed throughout.
The kinetic-energy functional PW91k[58] has been used to approximate the nonadditive
kinetic-energy component of the FDE embedding potential.

In the FDE embedding calculations, the nonfrozen subsystem is formed by the ace-
tonitrile molecule and the two closest water molecules. These are included in the
nonfrozen subsystem in order to describe the hydrogen bonds to the nitrogen atom
of acetonitrile accurately. The remaining water molecules are included in the calcu-
lation as frozen fragments, for which the density of the isolated molecule is used as
initial frozen density. Since all solvent water molecules share the same geometry, this
initial density only has to be calculated once and can then be used for all frozen water

molecules.

The solvent shifts of the nitrogen NMR shielding calculated for the different clusters are given in Table 7.1. In all cases, the solvent shifts, i.e., the shift relative to the isolated acetonitrile molecule, are given.

For the cluster of acetonitrile and 15 water molecules, already the FDE calculation using the simplest sum-of-fragments (SumFrag) approximation for the frozen density, in which the frozen densities of the isolated molecules are used for all frozen fragments, leads to a solvent shift of 12.6 ppm. This is rather accurate compared to 14.0 ppm calculated in the conventional, supermolecular KS-DFT calculation. To improve this first approximation of the frozen density, our new implementation makes it possible to relax the electron densities of selected frozen fragments. In Table 7.1, the effect of relaxing the densities of some of the solvent water molecules is shown. In all cases, the densities were only relaxed in one freeze-in-thaw cycle, since we found that additional freeze-and-thaw cycles only have a minor effect on the calculated NMR shielding.

For the closest three water molecules, relaxing the density leads to an increase in the solvent shift of in total 1.2 ppm. For the water molecules that are further away, this effect is smaller. Relaxing the densities of five additional water molecules leads to an increase of only 0.9 ppm, and of the next five water molecules of only 0.7 ppm, i.e., the effect of relaxation decreases for water molecules that are further away from the nitrogen atom. However, as can be seen from Figure 7.2 also some of the water molecules at a larger distance from the nitrogen atom can be rather close to other parts of the acetonitrile molecule, so that it is not surprising that the relaxation of their density has an effect on the solvent shift that is rather large.

If the densities of all 13 frozen water molecules are relaxed, a solvent shift of 15.3 ppm is obtained, which is 1.3 ppm higher than the reference value from the supermolecular calculation. This remaining difference is due to the approximations introduced by the subsystem DFT treatment, in particular inaccuracies of the approximate kinetic-energy functional, differences in the basis set expansion,[52] and in the case of the calculation of NMR parameters also the neglect of the current dependence of the nonadditive kinetic energy and of the induced current in the frozen fragments.[CJ6] By including more water molecules in the nonfrozen subsystem this error can be reduced, but this will also lead to an increase of the computational cost. The fact that the solvent shift calculated using the simple SumFrag approximation is nearly as close to the supermolecular reference value as in the case where all frozen densities are relaxed is due to an error cancellation between the error introduced by the approximate frozen density and the errors of the FDE treatment mentioned above.

When considering the large clusters containing 25 and 40 water molecules, respectively, the same trends as for the small cluster can be observed. While relaxing the densities of the water molecules close to the nitrogen atom has a larger effect, the ef-

Table 7.1.: Solvent shifts $\Delta\sigma$ of the nitrogen NMR shielding in acetonitrile–water clusters with 15, 25, and 40 water molecules, respectively. In the FDE calculations, the closest two water molecules have been included in the nonfrozen subsystem, for the remaining frozen fragments different approximations have been employed. For comparison, also the results of a conventional, supermolecular calculation are given. See text for details.

	15 H_2O		25 H_2O		40 H_2O	
	$\Delta\sigma$ / ppm		$\Delta\sigma$ / ppm		$\Delta\sigma$ / ppm	
isolated	0.0		0.0		0.0	
SumFrag	12.6		11.9		11.8	
1 H_2O relaxed	12.9	+0.3	12.3	+0.4	11.9	+0.1
2 H_2O relaxed	13.3	+0.4	12.7	+0.4	12.4	+0.5
3 H_2O relaxed	13.7	+0.4	13.3	+0.6	13.1	+0.7
8 H_2O relaxed	14.6	+0.9	13.9	+0.6	14.0	+0.9
13 H_2O relaxed	15.3	+0.7	14.7	+0.8	14.7	+0.7
23 H_2O relaxed			15.2	+0.5	14.6	−0.1
38 H_2O relaxed					14.6	0.0
supermolecule	14.0		13.1		12.5	

fect of relaxing ten additional water molecules is only +0.5 ppm and −0.1 ppm in the clusters containing 25 and 40 water molecules, respectively. While for the relaxation of the water molecules closer to the acetonitrile, the effect of relaxation is roughly the same for all cluster sizes, for the relaxation of these ten water molecules this is not the case. This is because in the cluster containing 25 water molecules they are only polarized by the inner water molecules, while in the large cluster containing 40 water molecules, another layer of water molecules has been added that also polarizes the ten water molecules in question. The effect of this outer layer is largest for the water molecules closest to it, i.e., further away from the acetonitrile, while its effect on the inner water molecules is rather small. In the cluster containing 40 water molecules, the effect of relaxing the densities of the additional outer layer of 25 water molecules is negligible.

For both clusters, the difference between the supermolecular reference value and the solvent shift calculated when the densities of all frozen water molecules are relaxed are approximately 2 ppm. It should be noted that this error is of similar size as other errors that appear in the conventional KS-DFT calculation of NMR shieldings, such as basis set effects and inaccuracies in the exchange-correlation functional. As mentioned above, in the case that fewer frozen water molecules are relaxed, the error introduced by the FDE treatment, in particular the use of an approximate kinetic-energy functional, are (partly) canceled by the error caused by the use of a more approximate frozen density.

In Table 7.2, the wall clock time required for the calculations discussed above on 8 dual processor nodes of an Intel Xeon 3.4 GHz cluster are given. These timings show for the three clusters a slight increase in the required computer time when a larger number of frozen fragments are relaxed. This is due to the additional freeze-and-thaw cycles needed in this case. Going to a larger cluster, the required time increases approximately linear with the number of water molecules included, which is due to the increased size of the numerical integration grid as well as the additional effort for constructing the larger frozen density. Because of this linear scaling, the FDE calculations are significantly more efficient compared to the supermolecular calculation of the NMR shielding, especially for larger clusters. A large part of this difference is caused by the fact that in the FDE case, the calculation of the NMR shielding can be performed for the much smaller nonfrozen system only, while including the effect of the frozen environment in the FDE embedding potential.

The test calculation presented above demonstrate how the approximate frozen density can be improved by relaxing the densities of frozen fragments. Especially for solvent molecules close to the nonfrozen subsystem, this will be important to obtain accurate results.[CJ4,CJ5] However, for solvent molecules that are further away from the nonfrozen subsystem the effect of relaxation is rather small. Therefore, it is possible to restrict the number of frozen fragments that are relaxed and to avoid the increased

Table 7.2.: Wall clock time (in minutes) required for the calculation of the nitrogen
NMR shielding in acetonitrile–water clusters with 15, 25, and 40 water
molecules, respectively, on 8 dual processor nodes of an Intel Xeon 3.4
GHz cluster, using different approximations for the frozen density. See
text for details.

	15 H_2O	25 H_2O	40 H_2O
isolated	0.4	0.4	0.4
SumFrag	1.7	2.1	2.9
1 H_2O relaxed	2.6	3.1	4.3
2 H_2O relaxed	2.8	3.6	5.0
3 H_2O relaxed	3.0	3.8	5.0
8 H_2O relaxed	3.6	5.2	6.2
13 H_2O relaxed	4.0	5.3	7.2
23 H_2O relaxed		7.1	9.4
38 H_2O relaxed			12.8
supermolecule	8.5	29.8	103.5

computational effort caused by relaxing the densities of all frozen fragments. This
will be particularly useful in practical applications requiring calculations for hundreds
of snapshots and the inclusion of a large number of solvent molecules. Based on our
tests, we chose to relax the densities of 13 solvent water molecules, in addition to
the two water molecules that are included in the nonfrozen subsystem. However,
the accurate description of the nitrogen NMR chemical shift of acetonitrile in water
will require calculations on a large number for snapshots from MD simulations. This
requires more thorough tests than those presented here, and a detailed study will be
presented elsewhere.[167]

The solvent shifts of the nitrogen NMR shielding calculated in FDE calculations
using this setup (i.e., two water molecules are nonfrozen, and the densities of 13
additional water molecules are relaxed) including up to 250 water molecules are shown
in Figure 7.3. It can be seen that up to approximately 100 water molecules, the solvent
shift shows a rather irregular behavior, while adding further water molecules leads
to a smooth increase of the solvent shift. The observation that the water molecules
50 to 75 lead to a larger change of the solvent shifts than water molecules 25 to
50 is due to the geometries of the investigated clusters. Since the water molecules
are chosen according to their distance from the nitrogen atom of the acetonitrile
molecule, the water molecules 50 to 75 include several water molecules close to methyl
group of acetonitrile, which influence its electronic structure significantly. Only after
approximately 100 solvent water molecules have been included, the acetonitrile is

Figure 7.3.: Solvent shift on the nitrogen NMR shielding of acetonitrile in water (solid line), calculated including solvent shells of different size. The results of the FDE calculations (squares/diamonds) and for small solvent shells of supermolecule calculations (triangles) are given. In addition, also the wall clock time (dashed line) required on 8 dual processor nodes of an Intel Xeon 3.4 GHz cluster are shown. See text for details.
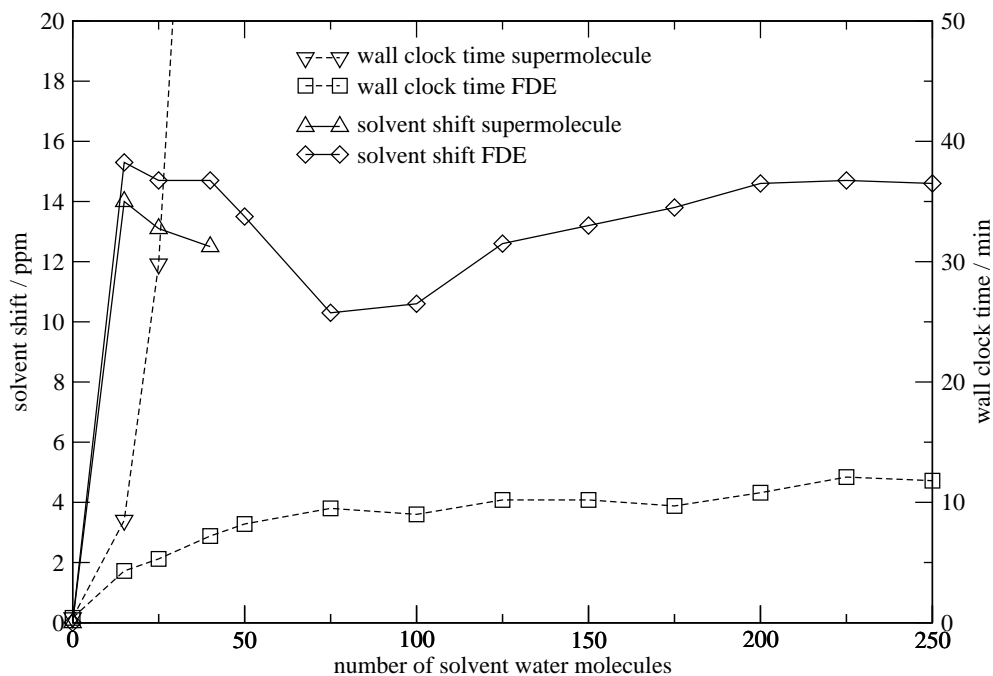
completely surrounded by solvent molecules and the effect of the addition of further solvent molecules becomes more regular.

As can be seen from Figure 7.3, approximately 200 solvent water molecules have to be included to obtain a solvent shift that is converged with respect to the size of the solvent shell. The required wall clock times that are included in Figure 7.3 show that this is easily possible in the FDE calculations. While for solvent shells up to 50 atoms the computer time increases approximately linearly, for larger solvent shells the time required for the FDE calculation is almost constant. In contrast, due to their unfavorable scaling, the conventional supermolecular KS-DFT calculations become infeasible already for rather small solvent shells.

7.4. Conclusions

We have presented a new implementation of the FDE scheme, which allows both a frozen density treatment using an approximate environment density as well as a subsystem DFT treatment, in which the densities of all subsystems are determined. In addition, intermediate treatments are possible, in which only the densities of a few subsystems are relaxed, in the presence of a larger frozen environment.

This flexible scheme offers several new possibilities for the multilevel description of environment effects. The partial relaxation of the electron density of the environment makes it possible to include not only the electronic coupling of the environment with the nonfrozen subsystem, but to include the polarization of the environment due to the nonfrozen subsystem as well. This results in a very accurate description of the coupling between different regions described at the QM level, in contrast to other popular QM/QM methods[6,7,158,159] that only include a mechanical coupling between the different regions.

As we show for the NMR chemical shift of acetonitrile in water, this flexible FDE scheme can be employed to improve the FDE treatment using an approximate environment density. By relaxing the electron densities of some solvent molecules that are close to the subsystem of interest, it is possible to adjust the accuracy of the description of the environment to the degree needed. At the same time, the total time of the computation only increases moderately. In particular, the time needed for the calculation of the NMR chemical shift does not increase, since it can be performed for the nonfrozen subsystem only.

Because of the numerical integration scheme used, our FDE implementation is very efficient, in particular for large frozen environments. It allows the treatment of environments consisting of hundreds of atoms, which makes it an attractive method for modeling large systems such as solvent environments or biological systems.

7. A flexible implementation of FDE for use in multilevel simulations

The FDE implementation described here is included in the 2007 release of the ADF program package. The FDE scheme can be combined with the calculation of several molecular properties that are available in ADF. Currently, properties that depend directly on the electron density (such as dipole and quadrupole moments), electronic excitation energies and polarizabilities can be calculated, as well as NMR shieldings and ESR hyperfine coupling constants. The extension to other properties, such as energy gradients, vibrational frequencies, and NMR spin–spin coupling constants is currently in progress. The FDE scheme can be further be combined with additional, more approximate descriptions of environments that are present in ADF, like continuum solvation models or different QM/MM schemes.

The user's guide describing in details all the features and options in detail can be found in Appendix A of this thesis. A detailed documentation of the technical aspects of the implementation can be found in Appendix B

Our flexible setup will make several extensions of our implementation possible. An extension of the implementation to the calculation of excited states, that uses the recently proposed protocol for subsystem-TDDFT calculations with an arbitrary number of subsystems,[61] is currently being integrated into the new FDE implementation and will be included in a future release. First test applications of this methods have already shown that it will be very useful for the description of excitonic couplings between different subsystem.

In addition, we are working on an extension to molecular dynamics and on coupling our implementation to *ab initio* codes to allow the treatment of individual subsystems using wave function based methods, similar to the *ab initio*-in-DFT embedding scheme by Carter and co-workers.[63,64,67]

Part IV.

Applications

8. Calculation of induced dipole moments in $CO_2 \cdots X$ (X = He, Ne, Ar, Kr, Xe, Hg) van-der-Waals complexes

Abstract

The frozen-density embedding scheme within density-functional theory is applied to the calculation of induced dipole moments of the van der Waals complexes $CO_2 \cdots X$ (X = He, Ne, Ar, Kr, Xe, Hg). The accuracy of the embedding scheme is investigated by comparing to the results of supermolecule Kohn-Sham density-functional theory calculations. The influence of the basis set and the consequences of using orbital dependent approximations to the exchange-correlation potential in embedding calculations are examined. It is found that in supermolecular Kohn-Sham density-functional calculations, different common approximations to the exchange-correlation potential are not able to describe the induced dipole moments correctly and the reasons for this failure are analyzed. It is shown that the orbital-free embedding scheme is a useful tool for applying different approximations to the exchange-correlation potential in different subsystems and that a physically guided choice of approximations for the different subsystems improves the calculated dipole moments significantly.

8.1. Introduction

The frozen-density embedding (FDE) scheme within density-functional theory (DFT) by Wesolowski and Warshel[8,48] is a promising approach to the efficient calculation of large scale molecular systems because it allows to split up the calculation using a "divide-and-conquer" strategy. However, even though the FDE scheme has been applied successfully to a number of different systems (see, e.g., Refs. 40, 76, 77), there remain a number of open questions related to the quality of the approximations to the nonadditive kinetic-energy functional. For the development of improved approximations it is of great importance to identify and analyze the possible problems of the currently used approximations.

The accuracy of the FDE scheme can be assesed be by comparing the results of FDE calculations in which the electron densities of both subsystems are fully relaxed in freeze-and-thaw cycles as explained in Chapter 3 to results obtained from supermolecular Kohn–Sham (KS) DFT calculations. In this chapter, the accuracy of the FDE scheme is invesigated for weakly interacting $CO_2 \cdots X$ (X = He, Ne, Ar, Kr, Xe, Hg) van der Waals complexes.

We note that in the FDE scheme an approximated nonadditive kinetic-energy functional is used for two different purposes: First, its functional derivative is used in the construction of the embedding potential [Eqs. (3.16) and (3.13)] which is used to calculate the electron density and second, the functional itself is needed to calculate the total energy [Eqs. (3.2) and (3.3)]. Since the induced dipole moments depend directly on the density we only need to consider the functional derivative of the approximate nonadditive kinetic-energy functional and not the nonadditive kinetic-energy functional itself. This reduces the chances of encountering error cancellations which could mask possible problems with the method.

Furthermore, the ability to apply different approximations for the exchange-correlation potential for different subsystems in a straightforward way is another application of the FDE scheme not exploited previously which will be examined in this chapter. This is particularly useful since the approximate exchange-correlation potentials which are applied in practical calculations do not lead to exact results. In this chapter, we show that a physically guided choice of approximations to the exchange-correlation potential for different subsystems can lead to results which are superior to those obtained from using a single KS-DFT calculation. This approach follows ideas similar to those of Carter and co-workers,[62,67] in which instead of selecting the most appropriate approximation to the exchange-correlation potential for a given subsystem, as we do in the current work, they replaced the DFT description for one of the subsystems by a wave-function-based *ab initio* one.

The induced dipole moments in the weakly interacting $CO_2 \cdots X$ (X = He, Ne, Ar,

Kr, Xe, Hg) van der Waals complexes are ideally suited to investigate the performance of the FDE scheme and the quality of the approximation to the nonadditive kinetic-energy functional in detail. The interaction in these van der Waals complexes is weak and the overlap between the densities of the CO_2 molecule and the rare-gas or mercury atom is small. The FDE scheme has been applied to other van der Waals complexes before[71–73] and the approximated nonadditive kinetic-energy functional used there has been shown to be the most accurate, both for the energy and for the potential, among a large family of gradient-dependent approximations. In particular, it gives accurate interaction energies for weakly overlapping densities.

The induced dipole moments in these complexes should be mainly determined by the electrostatic interaction and the Pauli repulsion between the CO_2 molecule and the rare-gas or mercury atom. KS-DFT and the FDE scheme are believed to be able to describe both effects accurately. Dispersion interactions, which cannot be described correctly within KS-DFT, would be important for the calculation of interaction energies and of geometries, but they should only have a small influence on the induced dipole moment. However, the accurate calculation of the induced dipole moments in the van der Waals complexes investigated here is still a challenging task. The calculated dipole moments will be very sensitive to small changes in the electron density and can, therefore, be used as a good measure for the quality of the electron density which results from FDE calculations.

van der Waals complexes of CO_2 and a rare-gas atom have been subject to a number of experimental and theoretical studies because they are a prototype system for the weak interaction of nonpolar constituents. For all CO_2 – rare-gas complexes, infrared[171,172] and microwave spectra[173–175] have been measured. All experiments have found that the complexes have a T-shaped geometry. Except for $CO_2 \cdots He$, the dipole moments of the complexes have been determined from measurements of the Stark effect on the rotational transitions. In our study, we also include the $CO_2 \cdots Hg$ complex, which can be viewed as an analog of the CO_2 – rare-gas complexes. This complex has also been investigated experimentally by microwave spectroscopy where a T-shaped structure has been found from the rotational spectrum and the dipole moment has been determined from the Stark effect splitting.[176]

A number of theoretical works deal with CO_2–rare-gas complexes. For $CO_2 \cdots He$, $CO_2 \cdots Ne$, and $CO_2 \cdots Ar$, the potential energy surfaces have been calculated using Møller-Plesset perturbation theory.[177–180] All these calculations confirm that the T-shaped structure is the global minimum on the potential-energy surface and that the linear structure is a local minimum at significantly higher energy. Maroulis and Haskopoulos[181] have studied the induced dipole moments and polarizabilities in the CO_2 – rare-gas complexes using second order Møller-Plesset perturbation theory (MP2). For the He and Ne complexes, they also performed CCSD(T) calculations, which are in good agreement with the MP2 results.

This Chapter is organized as follows. After a brief outline of the methodology and the computational details in Sec. 8.2, the results of the calculations are discussed in Sec. 8.3: In Sec. 8.3.1, a simple electrostatic interaction model for the description of the induced dipole moments in the considered complexes is presented. In Sec. 8.3.2, we present the results of supermolecular KS-DFT calculations of $CO_2 \cdots X$. These calculations show that different exchange-correlation potentials fail to reproduce the experimentally observed induced dipole moments and we investigate the reasons for this failure. In Sec. 8.3.3, we investigate the performance of the FDE scheme by comparing the results of embedding calculations to the supermolecular KS-DFT results and it is demonstrated how the FDE scheme can be used to get around the problems we have found when comparing the supermolecular KS-DFT calculations to experiment in Sec. 8.3.4. Concluding remarks are collected in Sec. 8.4.

8.2. Methodology and computational details

All calculations were performed using the Amsterdam Density-Functional (ADF) package.[124,125]

In all FDE calculations, the electron densities of both subsystems have been fully relaxed, i.e., the set of the two coupled KSCED equations,

$$
\left[-\frac{\nabla^2}{2} + v_{\text{eff}}^{\text{KS}}[\boldsymbol{r}; \rho_{\text{I}}] + v_{\text{eff}}^{\text{emb}}[\boldsymbol{r}; \rho_{\text{I}}, \rho_{\text{II}}] \right] \phi_i^{(I)}(\boldsymbol{r}) = \epsilon_i^{(I)} \, \phi_i^{(I)}(\boldsymbol{r}), \quad i = 1, \ldots, N_{\text{I}},
$$

(8.1)

$$
\left[-\frac{\nabla^2}{2} + v_{\text{eff}}^{\text{KS}}[\boldsymbol{r}; \rho_{\text{II}}] + v_{\text{eff}}^{\text{emb}}[\boldsymbol{r}; \rho_{\text{II}}, \rho_{\text{I}}] \right] \phi_i^{(II)}(\boldsymbol{r}) = \epsilon_i^{(II)} \, \phi_i^{(II)}(\boldsymbol{r}), \quad i = 1, \ldots, N_{\text{II}},
$$

(8.2)

has been solved iteratively. In these equations, $v_{\text{eff}}^{\text{KS}}[\boldsymbol{r}; \rho_{\text{I}}]$ and $v_{\text{eff}}^{\text{KS}}[\boldsymbol{r}; \rho_{\text{II}}]$ are the KS potentials of the isolated subsystem I or II, respectively, and $v_{\text{eff}}^{\text{emb}}$ is the KSCED effective embedding potential as defined in Eq. (3.16). As explained in Chapter 3 this procedure is equivalent to minimizing the total energy bifunctional given in Eq. (3.2).

The kinetic-energy component of the effective embedding potential has been approximated using the PW91k kinetic-energy functional,[58] because this functional has been found be the most accurate among different GGA functionals for a test set of weakly interacting systems.[40]

In the supermolecular KS-DFT calculations two different approximations were employed for the exchange-correlation potential: The Perdew-Wang 91 functional,

dubbed PW91,[22,130] which is a typical example of the generalized gradient approxima-
tion (GGA) and the "statistical averaging of (model) orbital potentials"
(SAOP),[26,127,128] which is a more advanced approximation to the KS potential and
shows the correct Coulombic decay of the potential at long distances.

In practical applications of the FDE scheme, not only the nonadditive kinetic-energy
component of the effective embedding potential has to be approximated, but also
the exchange-correlation potential, which enters these equations at different points:
First, it appears as part of the KS potentials $v_{\text{eff}}^{\text{KS}}$ of subsystems I and II. Since the
electron densities of the two subsystems are determined separately, it is possible to use
different approximations for the different subsystems. Furthermore, it is also possible
to use orbital-dependent approximations to the exchange-correlation potential of the
isolated subsystems I and II. The benefits of these possibilities, not investigated in
detail so far, will be demonstrated in this work. Second, an approximation to the
exchange-correlation potential is also needed in the effective embedding potential,
where the nonadditive exchange-correlation component of Eq. (3.17) appears. For
this component it is in general not possible to use orbital-dependent approximations
because there is no representation of $\rho_{\text{tot}}(\boldsymbol{r})$ in the canonical KS orbitals available.

In the calculations presented here, different combinations of the two approximations
PW91 and SAOP were used in these calculations. First, calculations were performed
using PW91 both in the KS potential of the isolated subsystems and in the effective
embedding potential. These calculations will be referred to as FDE/PW91. Second,
the SAOP potential was used to approximate the exchange-correlation potential in
the KS potentials of the isolated subsystems $[v_{\text{eff}}^{\text{KS}}[\boldsymbol{r}; \rho_{I,II}]$ in Eqs. (8.1) and (8.2)].
Because the SAOP potential is orbital dependent it does not provide an expression
for the nonadditive exchange-correlation potential and therefore, cannot be used in
the effective embedding potential. We chose to use the PW91 functional for the
nonadditive exchange-correlation contributions to the effective embedding potential
$[v_{\text{eff}}^{\text{emb}}$ in Eqs. (8.1) and (8.2)] in these calculations, which introduces an inconsistency
compared to the supermolecular KS-DFT calculations using SAOP. This inconsis-
tency relative to supermolecular calculations will be further discussed in Sec. 8.3.3.
Calculations using this combination of approximations to the exchange-correlation
potential will be labeled FDE/SAOP.

Finally, we will present FDE calculations where different approximations to the
exchange-correlation potential in the KS potential of the isolated subsystems I and
II were chosen based on the physical knowledge about the investigated system and
the available approximations. In these calculations, which will be referred to as
FDE/combi, PW91 was used to approximate the exchange-correlation potential in
the KS potential of the isolated subsystem I $V_{\text{eff}}^{\text{KS}}[\boldsymbol{r}; \rho_{\text{I}}]$ in Eq. (8.1) and SAOP was
used in the KS potential of the isolated subsystem II $[V_{\text{eff}}^{\text{KS}}[\boldsymbol{r}; \rho_{\text{II}}]$ in Eq. (8.2)]. For the
complexes investigated in this work fragment I was chosen to be the CO_2 molecule

and fragment II was chosen to be the attached rare-gas or mercury atom. For the nonadditive exchange-correlation contribution to the effective embedding potential [$V_{\text{eff}}^{\text{emb}}$ in Eqs. (8.1) and (8.2)], PW91 was used.

To include the effects of relativity for the complexes containing the heavier elements Xe or Hg, the scalar zeroth order regular approximation (ZORA)[182–184] was used. The calculations of dipole polarizabilities were done using TDDFT as implemented in ADF.[149,185] For numerical integration we used a grid that was denser than the default settings of ADF to get the dipole moments with the required accuracy. In the FDE calculations, the same integration grid as in the corresponding supermolecular KS-DFT calculations was used. The use of a grid which is larger than the one in KS-DFT calculations for the isolated subsystems is needed because of the embedding potential extends over the environment.

By default, the ADF package uses the fitted electron density for the evaluation of the exchange-correlation potential. We found that for the evaluation of the nonadditive kinetic-energy and exchange-correlation contributions to the embedding potential in weakly interacting systems this fitted density is not accurate enough, especially when gradient-dependent functionals are used. This can be related to the differences between the fitted and the exact electron density in the outer regions, that are usually not important for the evaluation of the exchange-correlation potential, but that are significant for the contributions of the nonadditive kinetic energy to the embedding potential in FDE calculations. Therefore, we modified the ADF implementation of the FDE scheme[164] to use the exact electron density of both subsystems (ρ_{I} and ρ_{II}) in the evaluation of the nonadditive kinetic-energy and exchange-correlation contributions to the embedding potential.

For the accurate calculation of the induced dipole moments in the $CO_2 \cdots X$ complexes, large basis sets with a sufficient number of diffuse functions are needed.[181] We used a series of basis sets of increasing size to examine the influence of the basis set on the calculated dipole moments. First, we used the quadruple-ζ basis set with four sets of polarization functions (QZ4P) from the ADF basis set library.[124] In addition, we used the even-tempered ET-pVQZ basis set,[186] which was augmented with field-induced polarization functions (aug-ET-pVQZ).[187,188] This augmented basis set is smaller than the QZ4P basis set, but it was shown to be of similar quality for the calculation of various molecular properties.[186] Finally, we used the largest basis set available in the ADF basis set library, the even-tempered ET-QZ3P-3DIFFUSE basis set, which is of quadruple-ζ quality and contains three sets of diffuse functions. Unfortunately, the large even-tempered basis sets ET-pVQZ and ET-QZ3P-3DIFFUSE are only available for the elements up to Kr. Therefore, we have extended the standard QZ4P basis sets for Xe and Hg with additional diffuse functions, using the scheme described in Refs. 187 and 188, yielding the basis set labeled aug-QZ4P in this work. The convergence of the induced dipole moments with the size of the basis set will be

Table 8.1.: Intermolecular distances R used in this work (in a.u.). R denotes the distance between the carbon atom and the rare-gas or mercury atom in the T-shaped geometry of $CO_2 \cdots X$.

X	R
He	6.019
Ne	6.206
Ar	6.605
Kr	6.846
Xe	7.332
Hg	6.983

discussed in the following section.

All calculations were performed for the same T-shaped geometries, which were used in Ref. 181, at which the C-O bond length in the CO_2 molecule is kept fixed at the experimental value of 2.192 a.u. (Ref. 189). The C–Rg (Rg= He, Ne, Ar, Kr, Xe) distances obtained from MP2 calculations taken from Ref. 181 were used. These values are in excellent agreement with the experimental geometries. For $CO_2 \cdots Hg$, the experimental C–Hg distance[176] was used. Table 8.1 collects the used distances.

8.3. Results and discussion

8.3.1. Simple electrostatic interaction model

In a simple electrostatic model, the interaction of the CO_2 molecule and the attached rare-gas or mercury atom can be described in the following picture: The electric field of the CO_2 molecule, which can be approximated by the electric field of a quadrupole, distorts the charge distribution around the rare-gas or mercury atom and induces a dipole moment which is given by

$$\mu_{\text{ind}} = \frac{3 \, Q_{xx} \, \alpha_X}{R^4}, \tag{8.3}$$

where Q_{xx} is the xx component of the traceless quadrupole moment of CO_2 (the z axis being along the CO_2 molecule), α_X is the static dipole polarizability of the attached atom X, and R is the C–X distance.

In Table 8.2, the induced dipole moments calculated using the model of Eq. (8.3) are

Table 8.2.: Induced dipole moments (in debye) of $CO_2 \cdots X$ complexes, calculated from the simple electrostatic interaction model as described in the text.

	He	Ne	Ar	Kr	Xe	Hg
electrostatic model	0.0128	0.0219	0.0708	0.0928	0.1148	0.1734
Experiment[a]		0.0244	0.0679	0.0829	0.1029	0.1070

[a]References 175 and 176.

given. The experimental values for the polarizabilities of the rare-gas atoms[190] and mercury,[191] which are also given in Table 8.4, were used. For the quadrupole moment of CO_2 the experimental value of $Q_{xx} = 1.595$ a.u. (Ref. 192) was used.

The results obtained within this simple model already account for the largest part of the experimentally observed induced dipole moments. It is — if experimental values are used as an input — able to reproduce the increase in the induced dipole moments along this series of complexes qualitatively and is able to give numerical values which are in reasonable agreement with the experimental dipole moments.

This simple electrostatic interaction model neglects the effects of higher multipole moments of the CO_2 molecule and of the finite size of the attached atom, which are expected to become more important if the size of the attached atom increases. The electrostatic interaction model could be further refined to take these effects into account, but it would still neglect the effects of Pauli repulsion and orbital interactions, which can only be described using quantum chemical methods.

Comparing the results which are obtained from the electrostatic interaction model with the experimental induced dipole moments shows that the effects which are neglected in the simple model become more important when going to the heavier attached atoms. Especially for the mercury complex the electrostatic interaction model overestimates the induced dipole moment significantly.

Still, the fact that the main part of the induced dipole moment originates from the interaction of the quadrupole moment of the CO_2 molecule with the polarizable electron cloud of the attached atom shows that it is important to ensure that the methods used in more advanced calculations are capable of describing the CO_2 quadrupole moment and the polarizability of the attached atom accurately.

8.3.2. Supermolecular KS-DFT calculations

To provide a reference for the discussion of the results of the FDE calculations, we first performed supermolecular KS-DFT calculations. These calculations will also be used to investigate the influence of the basis set and the approximated exchange-correlation potential on the induced dipole moments. Table 8.3 shows the results for supermolecular KS-DFT calculations using PW91 and different basis sets. They are compared to the experimentally observed dipole moments and the results of the CCSD(T) and MP2 calculations.[181] The calculated dipole moments are — unlike the values given by Maroulis and Haskopoulos in Ref. 181 — not corrected for basis set superposition errors (BSSE) to make comparisons with the results of the FDE calculations in the next sections easier. Nevertheless, we calculated the effect of the BSSE on the dipole moments using the counterpoise correction method and found these corrections to be small in all cases. In the calculations using the largest basis set the BSSE correction is smaller than 0.001 D for all complexes.

The results with different basis sets show that inclusion of diffuse functions is of great importance for the calculation of the induced dipole moments. The inclusion of diffuse functions when going from ET-pVQZ to aug-ET-pVQZ and when going from QZ4P to ET-QZ3P-3DIFFUSE/aug-QZ4P results in a large increase in the induced dipole moments. For the basis sets which do already include diffuse functions, the difference in the induced dipole moments when going from the aug-ET-pVQZ basis set to the largest basis set used (ET-QZ3P-3DIFFUSE) is significantly smaller. The negligibly small BSSE correction gives another indication that the results obtained with the largest basis set are close to the basis set limit. All calculations presented in the following section use these large basis sets, e.g., ET-QZ3P-3DIFFUSE for the elements up to Kr and aug-QZ4P for Xe and Hg.

Comparing the results of the PW91 calculations to the experimental values, one notices that, except for $CO_2 \cdots He$, the induced dipole moments are overestimated in all cases. For $CO_2 \cdots He$, where no experimental value is available, the calculated dipole moment is slightly below the CCSD(T) calculation by Maroulis *et al.*.

In the previous section, it was pointed out that to be able to describe the the induced dipole moments correctly, it is important to describe the polarizability of the attached atom accurately. GGA potentials like PW91 are known to overestimate polarizabilities[26] because they do not give the correct asymptotic behavior of the KS potential.[136] Therefore, we also use the SAOP potential, which does have the correct asymptotic behavior and which is known to perform well in the calculation of polarizabilities.[26] In Table 8.4, the calculated induced dipole moments and static dipole polarizabilities calculated using PW91 and SAOP are given together with the experimental values.

We notice that PW91 overestimates indeed the polarizabilities of the rare-gases and

Table 8.3.: Induced dipole moments (in debye) of $CO_2 \cdots X$ complexes calculated from supermolecule KS-DFT calculations with the PW91 functional using different basis sets. For comparison, the experimental values and the results of the previous MP2 and CCSD(T) calculations are also given.

		He	Ne	Ar	Kr	Xe	Hg
KS-DFT	ET-pVQZ	0.0123	0.0228	0.0611	0.0890		
	aug-ET-pVQZ	0.0132	0.0229	0.0743	0.0995		
	QZ4P	0.0102	0.0211	0.0712	0.0916	0.1132	0.1385
	ET-QZ3P-3DIFFUSE[a]	0.0134	0.0253	0.0736	0.0943	0.1194	0.1464
MP2[b]		0.0160	0.0274	0.0714	0.0877	0.0976	
CCSD(T)[c]		0.0158	0.0267				
Experiment[d]			0.0244	0.0679	0.0829	0.1029	0.1070

[a] Basis set aug-QZ4P was used for Xe and Hg.
[b] Reference 181.
[c] Reference 181.
[d] References 175 and 176.

Table 8.4.: Dipole moments μ (in debye) of $X \cdots CO_2$ complexes and static dipole polarizabilities α (in a.u.) of X calculated from supermolecular KS-DFT calculations using both PW91 and SAOP. In all calculations, the largest basis set available (aug-QZ4P for Xe and Hg and ET-QZ3P-3DIFFUSE for all other elements) have been used. For comparison, the experimental values and the results of the previous MP2 and CCSD(T) calculations are also given.

		He	Ne	Ar	Kr	Xe	Hg
Dipole moment μ	KS-DFT (PW91)	0.0134	0.0253	0.0736	0.0943	0.1194	0.1494
	KS-DFT (SAOP)	0.0190	0.0286	0.0831	0.1112	0.1375	0.1651
	MP2[a]	0.0160	0.0274	0.0714	0.0877	0.0976	
	CCSD(T)[b]	0.0158	0.0267				
	Experiment[c]		0.0244	0.0679	0.0829	0.1029	0.1070
Polarizability α	KS-DFT (PW91)	1.59	3.13	12.10	18.09	29.11	35.14
	KS-DFT (SAOP)	1.42	2.57	11.56	17.30	28.28	30.02
	Experiment[d]	1.38	2.67	11.07	16.77	27.29	33.91

[a]Reference 181.
[b]Reference 181.
[c]References 175 and 176.
[d]References 190 and 191.

Table 8.5.: Quadrupole moment Q_{xx} (in atomic units) of CO_2 calculated using KS-DFT with the ET-QZ3P-3DIFFUSE basis set.

	Q_{xx}
PW91	1.55
SAOP	1.85
Experiment[a]	1.595

[a]Reference 192.

mercury while the SAOP potential gives polarizabilities which are in good agreement with the experiment. But even though SAOP gives better polarizabilities, for the induced dipole moments the agreement with experiment calculated is much worse than for PW91. These surprising findings are explained by looking at quadrupole moments of CO_2 calculated with KS-DFT using PW91 and SAOP, which are given in Table 8.5. While the quadrupole moment calculated using PW91 is in good agreement with the experimental value, the SAOP potential overestimates the CO_2 quadrupole moment by 15%.

Summarizing the results of the supermolecular KS-DFT calculations, we can conclude that both PW91 and SAOP fail to reproduce the induced dipole moments of the investigated $CO_2 \cdots X$ complexes, but for quite different reasons. PW91 overestimates the dipole polarizability of the rare-gases, a consequence of the wrong asymptotic behavior of GGA potentials. On the other hand SAOP does describe the polarizabilities of the rare-gases correctly, due to its correct asymptotic behavior, but it gives a poor description of the quadrupole moment of CO_2.

8.3.3. Frozen-density embedding calculations

To assess the performance of the FDE scheme we compared the induced dipole moments calculated using this scheme to the results of the supermolecular KS-DFT calculations presented in the previous section. This comparison was done for the two approximations to the exchange-correlation potential considered in the previous section: PW91 and SAOP.

We applied the FDE scheme in freeze-and-thaw iterations as described above. In all the calculations done here the dipole moment was converged to an accuracy of 0.0001 D after only two or three freeze-and-thaw iterations. The dipole moments calculated for the two subsystems were added to yield the total induced dipole moment.

Following the formalism presented in Chapter 3, applying the FDE scheme in freeze-

and-thaw iterations should result in the same electron density and thus the same total dipole moment as the supermolecular KS-DFT calculation. However, there are some approximations involved, which can lead to differences between the FDE results and the results of supermolecular KS-DFT calculations.

First, in all FDE calculation, the approximated nonadditive kinetic-energy functional is not exact and its functional derivative, which is used in the construction of the embedding potential, is not exact either. Second, in calculations using orbital-dependent approximations to the exchange-correlation potential like SAOP, one furthermore encounters the complication that the supermolecular exchange-correlation potential is constructed in terms of a set of supermolecular orbitals. This potential cannot be reconstructed in a FDE calculation since only the subsystem orbitals are available. This makes it necessary to choose a non-orbital-dependent form for the nonadditive exchange-correlation contribution, introducing an additional inconsistency relative to the supermolecular calculation. This is not the case with a GGA potential like PW91, because then the same approximation can be used for the exchange-correlation potential in the subsystems and for the nonadditive exchange-correlation contribution to the embedding potential. Therefore, the treatment of the exchange-correlation potential in KS-DFT and FDE calculations is consistent.

With regard to possible basis set errors, there are two possibilities for the choice of the basis functions which are used to expand the densities of the two subsystems.[40] The most obvious choice is to use only basis functions that are centered on the atoms in the considered subsystem to expand the corresponding density. This choice is in line with the "divide-and-conquer" strategy mentioned earlier since the size of the KS-Fock matrix is reduced in the separate calculations of $\rho_I(\boldsymbol{r})$ and $\rho_{II}(\boldsymbol{r})$. Calculations using this monomolecular basis set expansion will be labeled FDE(m) following the convention of Ref. 40. However, this choice of the basis functions introduces an additional source of differences to the the supermolecular calculation. In the expansion of the total electron density the products of basis functions centered at atoms in different subsystems are neglected. Furthermore, since the total number of electrons in both subsystems is fixed, a charge transfer between the two subsystems is not possible.

These problems are both removed in the FDE(s) scheme which uses the full supermolecular basis set to expand the density of both subsystems. In this scheme, the advantage of the computational efficiency is lost. However, it is interesting from a theoretical point of view because the only sources of differences between FDE(s) and supermolecular KS-DFT calculations are the approximation to the nonadditive kinetic-energy functional which is used when constructing the embedding potential and, in SAOP calculations, the approximations in the nonadditive exchange-correlation component of the embedding potential. It was, however, noticed in earlier works[40,57] that in the FDE(s) scheme the results are more sensitive to problems in the kinetic-energy

Table 8.6.: Induced dipole moments (in debye) in $CO_2 \cdots X$ complexes calculated using the FDE scheme with different approximations for the exchange-correlation potential (FDE/PW91, FDE/SAOP, and FDE/combi; see text for details). In all calculations, the largest basis set available (aug-QZ4P for Xe and Hg and ET-QZ3P-3DIFFUSE for all other elements) have been used. For comparison, the results of the corresponding super-molecule KS-DFT calculations are also given, as well as the experimental values and the results of the previous MP2 and CCSD(T) calculations.

		He	Ne	Ar	Kr	Xe	Hg
FDE/PW91	FDE(m)	0.0136	0.0261	0.0747	0.0949	0.1136	0.1529
	FDE(s)	0.0121	0.0258	0.0761	0.1028	0.1231	0.1771
PW91	KS-DFT	0.0134	0.0253	0.0736	0.0943	0.1194	0.1464
FDE/SAOP	FDE(m)	0.0128	0.0225	0.0775	0.0999	0.1204	0.1467
	FDE(s)	0.0116	0.0220	0.0780	0.1042	0.1273	0.1606
SAOP	KS-DFT	0.0190	0.0286	0.0831	0.1112	0.1375	0.1651
FDE/combi	FDE(m)	0.0103	0.0200	0.0668	0.0859	0.1017	0.1249
MP2[a]		0.0160	0.0274	0.0714	0.0877	0.0976	
CCSD(T)[b]		0.0158	0.0267				
Experiment[c]			0.0244	0.0679	0.0829	0.1029	0.1070

[a]Reference 181.
[b]Reference 181.
[c]References 175 and 176.

potential because the electron density is more flexible. Furthermore it should be noted that the differences between the FDE(s) and FDE(m) schemes should become smaller for larger basis sets as they approach the basis set limit.[48]

In Table 8.6, the induced dipole moments calculated with the FDE scheme using different approximations to the exchange-correlation potential are presented and compared to the results of the corresponding supermolecule KS-DFT calculations and to the experimental dipole moments.

In the FDE/PW91 calculations the induced dipole moments calculated using the FDE(m) scheme are in excellent agreement with the results of the corresponding supermolecular KS-DFT calculations. For all considered complexes these differences are below 5%. Opposite to what would be expected, the agreement with the supermolecular KS-DFT calculations is worse for FDE(s). For the Ar, Kr, Xe, and Hg

complexes, the dipole moment calculated within the FDE(s) scheme overestimates the dipole moments by up to 20%, with the differences becoming larger when moving to the heavier attached atoms. While for the Ne complex the FDE(s) result is in good agreement with both the FDE(m) and the supermolecular KS-DFT result, for the He complex the FDE(s) dipole moment underestimates the supermolecular result by 10%.

The increase in the dipole moment which is observed for the complexes with the heavier attached atoms when going from FDE(m) to FDE(s) corresponds to electron density of the rare-gas or mercury atom being moved in the direction of the CO_2 molecule and the decrease for the $CO_2 \cdots He$ complex corresponds to electron density of the CO_2 molecule which is moved in the direction of the He atom. We think that these artificial differences between FDE(m) and FDE(s) are mainly caused by problems of the embedding potential in the region close to the nuclei of the frozen subsystem. Near these nuclei the embedding potential has to compensate the large attractive Coulomb potential of the nuclear charge. The observed differences indicate that this is not achieved completely: In the calculation of a rare-gas or mercury atom next to a frozen CO_2 fragment there is a small amount of electron density that is pulled to the C and O nuclei, leading to an artificial increase of the dipole moment. This effect shows up the most for the fragment which is more polarizable, e.g., the rare-gas or mercury in the complexes with the heavier attached atoms. In the $CO_2 \cdots He$ complex the effect is the other way around. In the calculation of the He fragment, a small amount of the more polarizable CO_2 electron density is attracted by the He nucleus. This kind of charge transfer can only occur if the basis set used is flexible enough near these nuclei in the frozen fragment, which is only the case in the FDE(s) scheme. In the FDE(m) calculations, the basis functions centered on the nuclei of the frozen subsystem are not available so that the amount of spurious charge transfer is smaller or not existent. It is important to note that the dipole moment, which is investigated here, is very sensitive to this kind of charge transfer so that small problems in the embedding potential have already a significant effect.

For the FDE(m)/SAOP calculations, the agreement with the corresponding supermolecular KS-DFT calculations is not as good as in the FDE/PW91 calculations. This is not surprising because of the contribution of the nonadditive exchange-correlation potential to the effective embedding potential an additional inconsistency is introduced. For the Ar, Kr, Xe, and Hg complexes the differences are rather small (below 13%), but for the He and Ne complexes the differences are larger (up to 32% for He). A reason for this behavior can be found in the way the SAOP potential is constructed. SAOP uses a statistical averaging over orbital potentials, in which the difference between the orbital energy and the orbital energy of the highest occupied molecular orbital (HOMO) is used to interpolate between two functional forms of the exchange-correlation potential: one that is optimal for the core region and one that is optimal for the valence region. For the He and Ne complexes, the highest occupied

rare-gas orbitals, which are most important for the induced dipole moments, are more than 5 eV lower in energy than the HOMO and give rise to a "core" contribution to the exchange-correlation potential. In the FDE calculations, the two subsystems are calculated separately, however, so that the rare-gas HOMO is then considered a valence orbital with corresponding contribution to the exchange-correlation potential. In the Kr, Xe, and Hg complexes, the rare-gas HOMO is also the HOMO in the supermolecular calculation, while for the Ar complex it is only about 1 eV below the HOMO of the supermolecule, so that these differences between the supermolecular KS-DFT calculation and the FDE calculation are then much smaller.

Comparing the FDE(s)/SAOP calculations to the FDE(m)/SAOP ones shows the same differences that were observed with FDE/PW91. Even with the large basis sets used here, the FDE(s) results differ significantly from the FDE(m) results. As with FDE/PW91, for the Kr, Xe, and Hg complexes, the dipole moments calculated using FDE(s) are larger than the the FDE(m) values, with the difference increasing when going to the heavier elements. For the Ne and Ar complexes, the differences between FDE(m) and FDE(s) are not significant, while for the He complex the FDE(s) dipole moment is smaller than the FDE(s) one. These differences can be explained in the same way as it was done above for the FDE/PW91 results. The fact that the FDE(s) results are actually closer to the supermolecular KS-DFT results than the FDE(m) results seems only to be a fortunate error cancellation between the nonadditive exchange-correlation and kinetic-energy contributions to the embedding potential.

8.3.4. Embedding with a combination of different exchange-correlation approximations

The supermolecular KS-DFT calculations in Sec. 8.3.2 showed that both GGA potentials like PW91 as well as the asymptotically correct SAOP potential are not able to reproduce the experimental dipole moments of the investigated $CO_2 \cdots X$ complexes correctly, because none of them is able to accurately describe the quadrupole moment of CO_2 and the polarizability of the attached atom at the same time.

One advantage of the FDE scheme presented here is that it allows one to use different approximations for the exchange-correlation potential in the two subsystems in a straightforward way. Therefore, we performed FDE calculations (FDE/combi) using PW91 to approximate the exchange-correlation potential in the KS potential of the CO_2 fragment (because it reproduces the quadrupole moment of CO_2 correctly) and SAOP in the KS potential of the rare-gas or mercury fragment (because it is able to describe the polarizability of the attached atom correctly). We would like to note that the use of this combination of different approximations is not just an arbitrary choice but one that is based on both physical knowledge about the systems under investi-

gation (see the simple electrostatic interaction model presented in Sec. 8.3.1) and on knowledge about the ability of different approximations to describe the polarizabilities and molecular multipole moments correctly.

In the previous section, we have demonstrated that the FDE scheme works well for the considered complexes both with PW91 and with SAOP. Therefore, we are confident that the embedding scheme will also work when these different approximations are combined by using them for the two subsystems. We can expect that the errors introduced by the use of the embedding scheme will be similar to the errors observed in the previous section. To get around the problems with the nonadditive kinetic-energy potential which were found in the previous section, we only applied the $FDE(m)$ scheme here, that is less affected by these problems.

The results of these calculations are shown in Table 8.6. For the Ar, Kr, Xe and Hg complexes the embedding calculations using a combination of different approximations significantly improve the results of the simple electrostatic interaction model of Sec. 8.3.1, while giving dipole moments of comparable quality for the He and Ne complexes.

The results obtained in the FDE/combi calculations are, for the Ar, Kr, and, Xe complexes, in perfect agreement with the experimental values, with the differences being smaller than 5%. For $CO_2 \cdots Ne$, the experimental dipole moment is underestimated by about 20% and an underestimation is also observed for $CO_2 \cdots He$, where we have to compare to CCSD(T) calculations because no experimental value is available. For $CO_2 \cdots Hg$, the experimental value is overestimated by about 20%. These differences are of about the same size as the differences between the $FDE(m)/SAOP$ calculations and the corresponding supermolecular KS-DFT calculations in the previous section, so that these differences can be mainly attributed to the approximation which has to be made in the nonadditive exchange-correlation potential and the nonadditive kinetic-energy functional.

8.4. Conclusions

In this study, we have for the first time applied the FDE scheme to the calculation of induced dipole moments in van der Waals complexes. We have shown that the embedding calculations are able to reproduce the results of supermolecular KS-DFT calculations, if only basis functions centered on atoms of the nonfrozen subsystem are included [$FDE(m)$]. The agreement is much better with a GGA potential like PW91 than for calculations using the orbital dependent SAOP potential, which can be explained by the additional approximations in the exchange-correlation part of the embedding potential that have to be made in this case.

Including the basis functions of the frozen subsystem in the embedding calculations [FDE(s)] lead to a spurious change transfer. We attribute this to the approximation used for the nonadditive kinetic-energy part of the embedding potential. These problems are most important if there are larger differences between the nuclear charges in the two subsystems, like in the $CO_2 \cdots X$ complexes where X is a heavier rare-gas or a mercury atom.

For the van der Waals complexes investigated here, it is possible to circumvent these problems by using the FDE(m) scheme that does not probe the embedding potential in the region around the nuclei of the frozen subsystem as much as the FDE(s) scheme does. However, this will not be possible in systems with a stronger interaction or where a charge transfer between the subsystems occurs indeed, because for these systems the inclusion of the additional basis functions in the FDE(s) is very important. Therefore, it will be interesting for future work to analyze these problems in more detail and to develop more advanced approximations to the nonadditive kinetic-energy functional [a].

Furthermore, we have demonstrated that the FDE scheme is a useful tool for combining different approximated exchange-correlation potentials by applying different approximations in the different subsystems. In this study, we have made use of this feature for the calculation of induced dipole moments, where both the GGA potential PW91 and the asymptotically correct SAOP potential fail to give a correct overall description. The FDE scheme made it possible to use in both subsystems an approximation to the exchange-correlation potential that is able to describe those properties of the fragments correctly that are important for the induced dipole moment of the complex: the polarizability for the rare-gas or mercury atom and the quadrupole moment for the CO_2 molecule. This strategy makes it possible to get induced dipole moments for the $CO_2 \cdots X$ van der Waals complexes that are in good agreement with the experiment, whereas KS-DFT calculations fail to achive this. We mention here that a similar scheme was recently, mainly for reasons of computational efficiency, also used in studies on solvatochromism.[CJ4,76] While the SAOP potential was used to get accurate excitation energies for the solute, the local-density approximation (LDA) was used to describe the solvent molecules.

---

[a]This observation was the starting point for the work on improved approximations to the kinetic-energy component of the effective embedding potential in Chapter 5 (Ref. CJ7)

9. Comparison of frozen-density embedding and discrete reaction field solvent models for molecular properties

Abstract

We investigate the performance of two explicit solvent models in connection with density-functional theory (DFT) for the calculation of molecular properties. In our comparison we include the discrete reaction field (DRF) model, a combined quantum mechanics and molecular mechanics (QM/MM) model using a polarizable force field, and the frozen-density embedding (FDE) scheme. We employ these solvent models for ground-state properties (dipole and quadrupole moments) and response properties (electronic excitation energies and frequency-dependent polarizabilities) of a water molecule in the liquid phase. It is found that both solvent models agree for ground-state properties, while there are significant differences in the description of response properties. The origin of these differences is analyzed in detail and it is found that they are mainly caused by a different description of the ground-state molecular orbitals of the solute. In addition, for the calculation of the polarizabilities, the inclusion of the response of the solvent to the polarization of the solute becomes important. This effect is included in the DRF model, but is missing in the FDE scheme. A way of including it in FDE calculations of the polarizabilities using finite field calculations is demonstrated.

9.1. Introduction

Since properties and reactions of molecules are usually studied in solution, and since the solvent might not be innocent in experimental studies, there has been a growing interest in including solvent effects in theoretical investigations (for reviews, see, e.g., Refs. 113, 193). Many solvent models used in quantum chemical studies are developed and well-tested for reproducing solvation energies or reaction energies in solution.[1,194,195] In some solvent models, only an (interaction) energy term is added so that effects on molecular properties cannot be described, apart from changes in the equilibrium structure. But modeling solvent effects on molecular properties has also attracted considerable attention during the past years, and several models for the inclusion of solvent effects on a more fundamental level have been proposed and tested (see, e.g., Refs. 76, 114, 161, 162, 196–207).

The models for the description of solvation effects can be divided into two groups. In continuum solvation models[113,193,208] the solvent is described as a continuous medium that is characterized by its dielectric constant, with the solute molecule residing inside a cavity in this medium. The solute molecule can then be treated with different quantum mechanical (QM) methods. Since the atomistic structure of the solvent is not explicitly included in these continuum models, the averaging over different solvent configurations is implicitly included in the continuum description that is parameterized to include all the degrees of freedom of the solvent. While it is clear that continuum models are able to correctly describe non-specific solvation effects, i.e., dielectric medium effects, their ability to describe specific interactions like hydrogen bonding is less obvious. Although progress in this direction has been made, a description of specific interactions within continuum models apparently requires a very careful parameterization of the size and shape of the cavity in which the solute molecule is placed.[195]

A physically more appealing approach to the description of specific solvent effects is given by discrete solvent models in which the geometrical structure of the solvent is explicitly included. This offers a more straightforward way to take specific interactions into account. However, to provide a complete description of all solvation effects in discrete models it is necessary to average over the degrees of freedom of the solvent. This can be achieved by sampling over a large number of snapshots from classical[209] or Car–Parinello molecular dynamics (CPMD)[210,211] simulations. For all these solvent structures, the molecular properties of interest are then calculated using quantum mechanical methods, taking the (discrete) solvent into account in a cluster model.[198,200] This can, for instance, be done using density-functional theory (DFT)[17] for ground-state properties or time-dependent DFT (TDDFT)[148,212] for response properties. Finally, the calculated property is averaged over the ensemble of solvent structures. This approach is denoted as "sequential molecular dynamics

followed by quantum mechanics calculations" (S-MD/QM) following the terminology of Canuto *et al.*.[200] It usually requires the inclusion of a large number of solvent molecules in the solvent structures, which makes it necessary to use very efficient methods for the calculation of molecular properties.

The most accurate approach would be the calculation of the properties of interest from supermolecular calculations by using a sufficiently large cluster (if no periodic boundary conditions can be used) in the quantum chemical calculation. However, this approach is usually very demanding, since a large number of solvent molecules has to be included, which quickly becomes infeasible for large solutes. In addition, the supermolecular approach does not directly yield molecular properties of the solute. Analysis of the results requires some partitioning of the wave function that is usually not unique so the calculated molecular properties will strongly depend on the partitioning scheme used.[213]

More efficient, though more approximate approaches are combined quantum mechanics and molecular mechanics (QM/MM) models[4,156,157,214,215] in which only the solute is treated using QM methods, while molecular mechanics methods (MM) are used to describe the solvent as well as the interactions between solute and solvent. The restriction of the QM treatment to the solute system makes the calculation of molecular properties for a large number of structures feasible. However, the force field used in the MM part has to be parameterized carefully to describe the solute–solvent interactions accurately. In addition, quantum mechanical effects to these interactions, which are important in the inner solvent shell, can only be modeled indirectly in an empirical way, even though there are studies that claim that carefully parameterized QM/MM models can yield results that are more reliable than DFT calculations.[216] For the calculation of response properties, it has been noted that it is necessary to use a polarizable molecular mechanics model in which the solute can respond to charge redistribution in the solute.[160] One example of such a polarizable QM/MM scheme is the discrete reaction field (DRF) model,[161,197,217] which has been implemented within DFT for ground-state[161] and response properties.[162] The DRF model has been previously applied to the calculation of molecular (hyper-)polarizabilities and of nonlinear optical (NLO) properties in solution.[218–220]

Frozen-density embedding (FDE)[8,48] within DFT can be regarded as a compromise between explicit QM models based on supermolecular cluster calculations and solvent treatments based on effective solvent–solute interaction potentials as used in DRF. In the FDE scheme, the (frozen) electron density of the solute is used to construct an embedding potential that enters in the calculation of the solute properties. The whole system (solute and solvent) is treated at a QM level, but the electron density of the solute and the solvent subsystems are determined separately. The calculation of orbitals for the supersystem is thus avoided. Even though FDE is in principle exact, further approximations—in addition to those present in conventional Kohn–

Sham (KS) DFT—have to be introduced. For modeling solvation effects, FDE is usually combined with a simplified method for constructing the electron density of the solvent, e.g., a sum-of-molecular-fragments approach.[76] Since the calculation of molecular (response) properties is done within a limited orbital space of the solute only, FDE is very efficient, especially in the case of response properties.

Both DRF and FDE are promising approaches for the calculation of molecular (response) properties in solution, mainly because their efficiency allows the calculation of molecular properties for a large number of solvent structures. In addition, both DRF and FDE introduce a "natural partitioning" of the supermolecular system into a solute and a solvent system, which makes it possible to uniquely define molecular properties in solution.

Even though both methods have been applied to the calculation of ground-state and response properties in solution in a number of earlier studies, there are several open questions. The DRF model relies on fitted parameters for atomic charges and polarizabilities and it is unclear if this parameterization is generally applicable. In the FDE scheme, an approximate nonadditive kinetic-energy functional has to be used.[48] Furthermore, in the calculation of response properties the response of the (frozen) solvent is neglected. The approximations that are made in the two methods are quite different and their importance for the calculation of different molecular properties is not fully tested.

In this paper we present a detailed comparison of the DRF model and the FDE scheme for calculating different molecular properties in solution. For this comparison, we use a simple test system, a water molecule inside a solvation shell consisting of 127 water molecules. This system is a well-established benchmark for the assessment of discrete solvent models.[161,162,197,217,221] Since we are only interested in a comparison of the two different solvent models for the calculation of molecular properties, we did not average over a large number of snapshots, but only use one solvent structure instead. This allows us to focus on the differences in the description of the solvent effects.

This Chapter is organized as follows. In Sec. 9.2, a brief introduction into the theoretical background of DRF is given. In Sec. 9.3, we present a detailed comparison of these two solvent models for a water molecule solvated in water. First, in Sec. 9.3.1, the solvent models are compared for ground-state properties, namely the dipole and the quadrupole moment. This is followed by a comparison of the performance of DRF and FDE for response properties. In Sec. 9.3.2, they are compared for the calculation of electronic excitation energies and in Sec. 9.3.3 for the calculation of static and frequency-dependent polarizabilities. Concluding remarks follow in Sec. 9.4.

9.2. Methodology

9.2.1. The discrete reaction field model

The DRF model is a polarizable quantum mechanics/molecular mechanics (QM/MM) model. The solvent is represented by atomic charges q_s and polarizabilities α_s that are placed at positions $\boldsymbol{R}_s$. Although the DRF model can describe a frequency-dependent atomic polarizability,[222,223] we will assume that the atomic polarizabilities are independent of the frequency. This is expected to be a reasonable assumption due to the small dispersion of the polarizability in the frequency range that lies well below any electronic excitation. In the DRF model the QM/MM operator at a point $\boldsymbol{r}$ is given as an extra term in the effective potential in the KS equations,[161]

$$\left[-\frac{\nabla^2}{2} + V_{\text{eff}}^{\text{KS}}[\rho](\boldsymbol{r}) + V^{\text{DRF}}[\rho](\boldsymbol{r}) \right] \phi_i(\boldsymbol{r}) = \epsilon_i \; \phi_i(\boldsymbol{r}), \quad i = 1, \dots, N. \tag{9.1}$$

where the DRF potential is given by

$$\begin{aligned} V^{\text{DRF}}[\rho](\boldsymbol{r}) &= V^{\text{el}}(\boldsymbol{r}) + V^{\text{pol}}[\rho](\boldsymbol{r}) \\ &= \sum_s \frac{q_s}{|\boldsymbol{r} - \boldsymbol{R}_s|} + \sum_s \boldsymbol{\mu}_s^{\text{ind}} \cdot \frac{(\boldsymbol{r} - \boldsymbol{R}_s)}{|\boldsymbol{r} - \boldsymbol{R}_s|^3}. \end{aligned} \tag{9.2}$$

The first term, V^{el}, describes the Coulomb interaction between the QM system (the solute) and the permanent charge distribution of the solvent molecules. The second term, V^{pol}, describes the many-body polarization of the solvent molecules.

The induced atomic dipole at a site s is given by

$$\boldsymbol{\mu}_s^{\text{ind}} = \alpha_s \left[\boldsymbol{F}_s^{\text{init}} + \sum_{t, t \neq s} \boldsymbol{T}_{st}^{(2)} \boldsymbol{\mu}_t^{\text{ind}} \right], \tag{9.3}$$

where $\boldsymbol{T}_{st}^{(2)}$ is the screened dipole interaction tensor[161,224,225] for the interaction between sites s and t. The induced dipole arises from the field $\boldsymbol{F}_s^{\text{init}}$ at site s that is due to the electronic charge distribution of the QM part, the field from the QM nuclei, and the field from the point charges at the solvent molecules as well as the field from all other induced dipoles. The induced dipole moments are therefore calculated self-consistently in every iteration of the KS procedure.

The combination of the DRF model with TDDFT linear response theory was presented in Ref. 162. It introduces an additional contribution in the TDDFT kernel that describes the change in the DRF potential of Eq. (9.2) due to a perturbation in

the electron density of the QM system, i.e., the response of the atomic polarizabilities. This additional contribution is given by

$$f^{DRF}(\boldsymbol{r}, \boldsymbol{r}') = \frac{\delta V^{DRF}[\rho](\boldsymbol{r})}{\delta \rho(\boldsymbol{r}')}$$
$$= \sum_s \sum_t \frac{(\boldsymbol{r}' - \boldsymbol{R}_t)}{|\boldsymbol{r}' - \boldsymbol{R}_t|^3} \cdot \boldsymbol{B}_{st} \frac{(\boldsymbol{R}_s - \boldsymbol{r})}{|\boldsymbol{R}_s - \boldsymbol{r}|^3}. \tag{9.4}$$

In this equation $\boldsymbol{B}_{st}$ is the relay matrix that relates the induced dipole moment at site s to the electric field at site t and that is defined by

$$\boldsymbol{\mu}_s^{\mathrm{ind}} = \sum_t \boldsymbol{B}_{st} \boldsymbol{F}_t. \tag{9.5}$$

This relay matrix is never calculated explicitly, but the induced dipole moments due to the first-order change in the electron density are calculated iteratively by solving Eq. (9.3) in the linear-response calculation. Details can be found in Ref. 162.

9.2.2. Computational details

All density functional calculations were performed using the Amsterdam Density Functional (ADF) package.[124,125] The "statistical averaging of molecular orbital potentials" (SAOP) potential[26,127,128] was used to approximate the exchange–correlation potential, since it is well suited for the calculation of response properties. To provide a consistent comparison we also employed the SAOP potential for ground-state properties, even though it has been found that SAOP is less reliable in this case.[CJ3]

All calculations were done using the VDiff basis set from the ADF basis set library, which is a triple-ζ-quality Slater basis set containing additional diffuse functions. Previous studies[161,162] showed that this basis set is sufficiently large for the accurate calculation of both ground-state and response properties investigated here. This was confirmed in the present work by test calculations using the large even-tempered ET-QZ3P-3DIFFUSE Slater basis set, in which the results did not change significantly.

In the FDE calculations, the initial solvent density was constructed as a sum of the electron densities of molecular fragments calculated using the local-density approximation (LDA) and a DZP basis set. In the FDE calculations using the orbital-dependent SAOP potential, the exchange–correlation component of the effective embedding potential was approximated using the Becke–Perdew–Wang (BPW91) exchange–correlation functional.[21,130]

The parameters needed for the solvent molecules in the DRF model, i.e., point charges and atomic polarizabilities, were adopted from Ref. 161. The point charges are $q_H =$

0.3345 a.u. and $q_O = -0.6690$ a.u. which generate a molecular dipole moment of 1.88 Debye. The atomic polarizabilities are $\alpha_H = 0.0690$ a.u. and $\alpha_O = 9.3005$ a.u. which reproduced the molecular polarizability tensor with a mean polarizability of 9.62 a.u. and a polarizability anisotropy of 0.52 a.u. The screening parameter, $a = 2.1304$, used in Eq. 9.3, was taken from Ref. 225.

The calculations of excitation energies and of polarizabilities were done using the TDDFT implementation of ADF.[149,185] The finite field calculations of the polarizabilities in Sec. 9.3.3 were performed using an electric field of of 0.001 a.u.. To obtain the static mean polarizability, six separate calculations were performed in which an electric field was applied in x, y, and z direction. The individual components of the polarizability tensor were then obtained by numerical differentiation of the dipole moment.

9.3. Results and discussion

The comparison of the DRF and the FDE solvent models is carried out for the system investigated in Refs. 161 and 162, where a water molecule in the "liquid phase" was studied. It is a fixed structure of 128 rigid water molecules. The structure was obtained from a molecular dynamics simulation using a polarizable force field in an earlier work.[221] One of the 128 water molecules is considered as the solute, while the remaining 127 form the solvent shell. The structure of the water molecule inside the solvent shell is shown in Fig. 9.1 and the coordinates are given in the Supplementary Material.

We note that by using only one solvent structure any effects of the dynamics of the solvent are neglected, i.e., the fluctuations in the geometrical structure of both the solute and the solvent molecules are not taken into account and replaced by a static picture. For correctly describing all solvent effects it would be necessary to include a large number of solvent structures instead of just one average configuration.[CJ4,76] It will, therefore, be difficult to directly compare the obtained results to experimental values. However, the error that results from neglecting the dynamical effects will be made consistently in all calculations. As the purpose of this study is to provide a comparison of different solvent models, this consistent error is not relevant for the conclusions drawn here. Furthermore, the restriction to only one structure enables us to do a very detailed analysis of the results and greatly simplifies their interpretation.

Figure 9.1.: Structure of a water molecule inside a solvent shell of 127 water molecules. The "solvated" water molecule is the one that is highlighted, the other two water molecules are considered to belong to the solvent shell. Coordinates are given in the Supplementary Material.

Table 9.1.: Dipole moments μ (in debye), solvation shifts in dipole moments $\Delta^{\mathrm{solv}}\mu$ (in debye) relative to the isolated molecule, and traceless quadrupole moments Q (in a.u.) for an isolated water molecule in the gas phase and inside a solvation shell of 127 water molecules modeled using DRF as well as FDE. For FDE results are given with an unrelaxed sum-of-molecular-fragments electron density for the solvent (SumFrag) and with a solvent density in which the density of the ten innermost water molecules is relaxed with respect to the solute (relaxed).

	xc-functional	μ	$\Delta^{\mathrm{solv}}\mu$	Q_{xx}	Q_{yy}	Q_{zz}
isolated	BP86	1.80		1.79	-1.86	0.07
	SAOP	1.95		1.76	-1.84	0.08
DRF	BP86	2.66	$+0.86$	2.05	-2.15	0.11
	SAOP	2.68	$+0.73$	1.99	-2.09	0.11
FDE(SumFrag)	BP86	2.45	$+0.65$	2.04	-2.12	0.09
	SAOP	2.52	$+0.57$	1.98	-2.07	0.08
FDE(relaxed)	BP86	2.71	$+0.91$	2.09	-2.17	0.08
	SAOP	2.75	$+0.80$	2.03	-2.11	0.08

9.3.1. Dipole and quadrupole moments

First, we compare the performance of DRF and FDE for dipole and quadrupole moments. These are both ground-state properties that depend directly on the electron density. They are a sensitive measure for the distribution of the electron density obtained within the different solvent models.

Table 9.1 gives the dipole and quadrupole moments that were calculated for the isolated water molecule and for the water molecule in the "liquid phase", i.e., inside a solvation shell of 127 water molecules. The calculations were done using both the SAOP potential, that will also be used in the calculations of response properties in the following sections, and the BP86 functional. We included BP86 in this comparison because it was noticed that while SAOP is performing very well for response properties, it sometimes fails for dipole and quadruple moments.[CJ3]

For the isolated water molecule, the dipole moment calculated using BP86 is in good agreement with the experimental value[190] of 1.854 D, while SAOP overestimates the dipole moment. However, BP86 and SAOP are in excellent agreement for the quadrupole moment.

For the water molecule in solution, DRF predicts a shift in the dipole moment of 0.86 D with BP86 and a smaller shift of 0.73 D with SAOP, resulting in dipole moments that

are in good agreement for BP86 and SAOP. The results obtained here differ slightly from the results of Ref. 161 because of the slightly different basis sets. The increase of the dipole moment of water in the liquid phase relative to the gas phase has been discussed in detail in Ref. 161. Although for the dipole moment of water in the liquid phase no direct comparison with experiment is possible, there are a number of studies that deduce dipole moments of liquid water from various experiments. An overview is given in Ref. 161 where it is argued that 3.1 D can be used as an upper limit, while the lower limit is given by 2.5 D. The dipole moments calculated using DRF lie within these boundaries. In addition, in Ref. 161 the results of the DRF calculations were found to be in good agreement with CCSD calculations[221] using a solvent model similar to DRF and the same water structure that predict a dipole moment of 2.71 D.

The FDE calculations using a sum-of-molecular-fragments electron density for the solvent [labeled FDE(SumFrag)] predict a shift in the dipole moment that is significantly smaller than that predicted by DRF. The situation changes when relaxation of the solvent electron density is included into the FDE calculations [labeled FDE(relaxed)]. In this case, the calculated dipole moments, using BP86 as well as SAOP, are in good agreement with the dipole moment calculated using DRF. This shows that the effect of polarization of the solvent density is of great importance for the correct description of the dipole moment in the system considered here. It was already noticed in earlier works[CJ4,60] that the inclusion of relaxation has strong influence in systems with direct hydrogen bonds between the solvated molecule and the solvent. Since relaxation is needed mainly for the correct description of hydrogen bonds it is sufficient to relax the solvent molecules that are close to the solvated molecule whereas relaxation of the outer solvent shells can safely be neglected.[CJ4]

In FDE the effect of relaxation of the solvent density, i.e., of changes in the solvent electron density due to the solvated molecule, has to be included explicitly using freeze-and-thaw cycles. In DRF calculations a discrete model of the same effect is used, where the polarization of the solvent electron density is modeled using distributed atomic polarizabilities that can be obtained from gas-phase calculations. While this strategy of modeling the change of the solvent density is computationally more efficient than the full treatment in FDE, the FDE description should be more accurate, especially at short distances where the discretization of the charge distribution gives larger errors.

For the quadrupole moments, the shift from the gas phase to the liquid phase is smaller than for the dipole moment. The quadrupole moments calculated using DRF and FDE are in good agreement. While the effect of relaxation in the FDE calculations is large for the dipole moment, this is not the case for the quadrupole moment.

Summarizing these results, we find that for the dipole moment and the quadrupole moment DRF and FDE give results that are very similar if relaxation of the inner-

most solvent molecules is included in FDE. Since both the dipole and the quadrupole moment only depend on the calculated electron density, these results give a good indication that the electron densities calculated within the different solvent models are not very different.

9.3.2. Excitation energies

After comparing DRF and FDE for ground-state properties, we investigate the performance of the different solvent models for properties depending on the density response, starting with the electronic excitation energies. Table 9.2 gives the excitation energies of the three lowest excitations of an isolated water molecule and of the corresponding excitations for the system described in the previous section, a water molecule inside a solvation shell consisting of 127 water molecules. Additionally, the solvation shifts of the excitation energies and the oscillator strengths of the corresponding transitions are reported.

The excitation spectra of water in the gas-phase and in the condensed phase are known experimentally[226–228] and have been discussed in detail before (see, e.g., Ref. 229). The gas-phase spectrum shows two very diffuse bands with absorption maxima at 7.4 eV and at 9.7 eV, which are assigned to the the $1^1A_1 \rightarrow 1^1B_1$ and to the $1^1A_1 \rightarrow 2^1A_1$ transition, respectively. Qualitatively, both excitations have significant Rydberg character. The $1^1A_1 \rightarrow 1^1A_2$ transition, which is the second excitation in the calculations, is dipole forbidden in the gas phase. The excitation spectrum of liquid water shows two very broad overlapping bands. The first band has a maximum at 8.2 eV (corresponding to a solvent shift of approximately 0.8 eV), while the maximum of the second band is at 9.9 eV (corresponding to a much smaller solvent shift of 0.2 eV).

The Rydberg character of the excitations requires the use of a large number of diffuse functions in the basis set and of an asymptotically correct exchange–correlation potential like SAOP.[230,231] If this is taken care of, the results for the isolated molecule in the gas phase are in good agreement with the experimental values. For the water molecule in the "liquid phase", DRF predicts solvent shifts of approximately 0.7 eV for the lowest three transitions. These results have already been discussed in Ref. 162. The predicted solvent shifts are of similar size for the first and the third excitation. For the first excitation, the calculated solvent shift is in fair agreement with experiment, but there is a significant overestimation of the solvent shift for the third excitation.

FDE using a sum-of-molecular-fragments solvent density predicts significantly larger solvent shifts than DRF. The shifts increase even further to roughly 1.2 eV if relaxation of the solvent density is included. In this case, FDE predicts solvent shifts that are larger than the shifts predicted by DRF by 0.47, 0.31, and 0.61 eV for the first, second,

Table 9.2.: Excitation energies E_{ex} (in eV) of the three lowest excitation for an isolated water molecule in the gas phase and of the corresponding excitation energies for a water molecule inside a solvation shell of 127 water molecules modeled using DRF and FDE. The solvation shifts of the excitation energies $\Delta^{solv} E_{ex}$ (in eV) and the oscillator strength f (in a.u.) are also given.

	$1^1A_1 \to 1^1B_1$			$1^1A_1 \to 1^1A_2$			$1^1A_1 \to 2^1A_1$		
	E_{ex}	$\Delta^{solv} E_{ex}$	f	E_{ex}	$\Delta^{solv} E_{ex}$	f	E_{ex}	$\Delta^{solv} E_{ex}$	f
isolated	7.76		0.05	9.61		0.00	9.72		0.09
DRF	8.41	+0.65	0.08	10.38	+0.77	0.011	10.40	+0.68	0.11
FDE(SumFrag)	8.71	+0.95	0.07	10.43	+0.82	0.0023	10.70	+0.98	0.04
FDE(relaxed)	8.88	+1.12	0.07	10.69	+1.08	0.0011	11.01	+1.29	0.06

Table 9.3.: Excitation energies E_{ex} and solvation shifts in excitation energies $\Delta^{\mathrm{solv}} E_{\mathrm{ex}}$ (both in eV) of the lowest excitation of a water molecule in the gas phase and in a cluster with two solvent water molecules, modeled using DRF and FDE. In addition, the results of a supermolecular KS-DFT calculation of the same cluster are given, see text for details.

	E_{ex}	$\Delta^{\mathrm{solv}} E_{\mathrm{ex}}$
isolated	7.76	
DRF	8.08	+0.32
FDE(relaxed)	8.30	+0.54
supermolecule	8.43	+0.67

and third transition, respectively. Like DRF, also FDE predicts similar solvent shifts for the first and the third transition. The shifts predicted by FDE are larger than those obtained with DRF, but for the lowest excitation there is still a fair agreement with the experimentally observed shift. However, also FDE does not describe the lower solvent shift for the third transition correctly. As mentioned earlier, it is difficult to directly compare the obtained solvent shifts to experiment, because we only considered one average solvent structure.

The accuracy of the two different solvent models for the electronic excitations investigated here can be assessed by a comparison to the results of a supermolecular DFT calculation. Such a supermolecular calculation contains all interactions that are modeled in DRF and FDE explicitly, so that it can provide information about the quality of the approximations made in the two models. Obtaining the excitation energies of interest from a supermolecular calculation is problematic, because the charge-transfer excitation problem in TDDFT leads to a large number of artificially too low excitations in the energy range of interest.[76] In addition, for the system investigated here, where also the solvent is water, the lowest excitation energies of the solvent molecules will also perturb the analysis.

To minimize these problems, the comparison with a supermolecular calculation is done for a small cluster consisting only of the water molecule in question and of the two closest solvent water molecules. The structure is a substructure of the larger cluster containing 127 solvent molecules and is shown in Fig. 9.2. In this structure, the "solvated" water molecule is involved in two hydrogen bonds.

Even though in this small cluster the solvent shift of the excitation energies will be much smaller than for the larger water cluster considered earlier, the main cause of the differences between DRF and FDE is expected to originate form the innermost solvent molecules. This small cluster will therefore already provide useful information.

Figure 9.2.: Structure of the cluster containing a water molecule and the two closest solvent water molecules. The "solvated" water molecule is the one that is highlighted, the other two water molecules are considered to belong to the solvent shell.
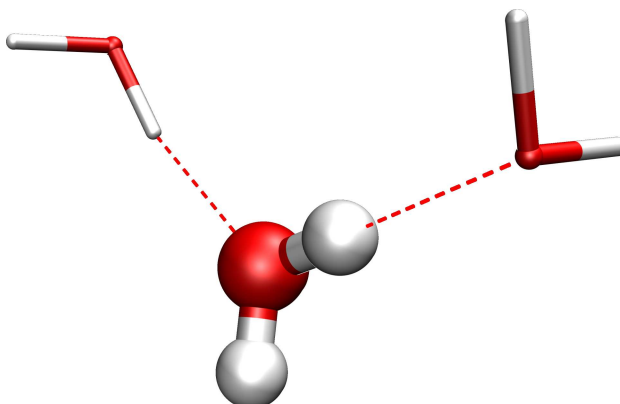
The lowest excitation energy of the "solvated" water molecule calculated using DRF and FDE as well as a supermolecular calculation are given in Table 9.3. In the supermolecular calculation, the DZP basis set was used for the two solvent molecules for consistency with the FDE calculation. As in all previous calculations, the VDiff basis set is used for the solute molecule. The transition corresponding to the lowest excitation of the isolated water molecule is identified using the transition density overlap criterion introduced in Ref. 76. The excitation that is found to have the largest overlap with the lowest transition of the isolated water molecule is the seventh excitation in the supermolecular calculation.

The solvent shift obtained using FDE is in reasonable agreement with the result of the supermolecular calculation, with FDE slightly underestimating the supermolecular result by 0.13 eV. In contrast to this, DRF yields a value that significantly underestimates the solvent shift by 0.35 eV. This indicates that for the calculation of excitation energies the FDE scheme provides an approximation that is closer to the full description of the solvent effects than the DRF model. In the following we will analyze the reasons for the differences in the excitation energies obtained with DRF and FDE and try to identify the problems and shortcomings of the different solvent models. For this analysis we will focus on the lowest excitation only.

For this analysis we split up the calculated excitation energies into different compo-

Table 9.4.: Analysis of the excitation energies calculated for an isolated water molecule and for a water molecule inside a solvent shell of 127 water molecules using DRF and FDE to model the solvent shell. The HOMO–LUMO gap $\Delta\epsilon$ as calculated for the ground-state is given as a first order approximation to the excitation energy. $\Delta_{\text{vac}}^{\text{resp}}E_{\text{ex}}$ refers to the correction to this gap as calculated using TDDFT without including any contributions of the environment. The additional contributions of the environment to the excitation energies are given as $\Delta_{\text{env}}^{\text{resp}}E_{\text{ex}}$. (All values in eV)

	$\Delta\epsilon$	$\Delta_{\text{vac}}^{\text{resp}}E_{\text{ex}}$	$\Delta_{\text{env}}^{\text{resp}}E_{\text{ex}}$	E_{ex}
isolated	7.59	+0.17	−	7.76
DRF	8.29	+0.15	−0.03	8.41
FDE(relaxed)	8.67	+0.14	+0.07	8.88

nents into

$$E_{\text{ex}} = \Delta\epsilon + \Delta_{\text{vac}}^{\text{resp}}E_{\text{ex}} + \Delta_{\text{env}}^{\text{resp}}E_{\text{ex}}. \tag{9.6}$$

In this equation, $\Delta\epsilon$ is the orbital energy difference, i.e., for the excitation studied here the difference between the orbital energies of the highest occupied molecular orbital (HOMO) and the lowest unoccupied molecular orbital (LUMO). The "vacuum" response contribution $\Delta_{\text{vac}}^{\text{resp}}E_{\text{ex}}$ is the correction that TDDFT applies to the HOMO–LUMO gap if the effects of the environment are only included in the KS step but not in the TDDFT part of the calculation. It is calculated by subtracting the HOMO–LUMO gap, obtained for the solvated water molecule, from the excitation energy that is calculated from the embedded orbitals without including any additional contributions of the solvent model in the exchange–correlation kernel. It is important to note that for the calculations using solvent models, both the HOMO–LUMO gap $\Delta\epsilon$ as well as the "vacuum" contribution $\Delta_{\text{vac}}^{\text{resp}}E_{\text{ex}}$ include the effect of the solvent model on the ground-state orbitals and orbitals energies.

In addition to this effect on the ground-state orbitals, both solvent models employed here introduce an additional term in the exchange–correlation kernel that give rise to the environment contribution $\Delta_{\text{env}}^{\text{resp}}E_{\text{ex}}$. For DRF, this additional contribution is given by Eq. (9.4) and describes the response of the induced dipoles on the solvent to the change in electronic density upon excitation. For FDE, the additional contribution is given by the effective embedding kernel of Eq. (3.31) that arises from the contribution of the nonadditive kinetic energy and the nonadditivity of the exchange–correlation functional and its derivatives.

The results of the decomposition of the excitation energies according to Eq. (9.6) for

the isolated water molecule and for the solvated water molecule described using either DRF or FDE are given in Table 9.4. The differences in the calculated excitation energies are mainly explained by the effects that the solvent models have on the HOMO-LUMO gap, which amounts to 0.70 eV for DRF and to 1.08 eV for FDE. The "vacuum" response correction $\Delta_{\mathrm{vac}}^{\mathrm{resp}} E_{\mathrm{ex}}$ is of similar size for both the isolated molecule calculation and the calculations in solution (DRF and FDE). The difference is only approximately -0.03 eV, which is negligible compared to the large change in the HOMO–LUMO gap that is induced by the solvation shell.

The additional environment correction $\Delta_{\mathrm{env}}^{\mathrm{resp}} E_{\mathrm{ex}}$ is also small compared to the change in the HOMO–LUMO gap caused by the solvation shell. However, these corrections are responsible for a part of the differences that are observed between DRF and FDE. In DRF the environment correction is negative, i.e., it lowers the calculated excitation energy, because the response of the solvent stabilizes the excited state. In FDE, the environment contribution is positive and therefore increases the excitation energy. This is because the effective embedding kernel in FDE contains the effects of the Pauli repulsion of the solvent molecules, that will destabilize the excited state. These environmental contributions in DRF and FDE are largely complementary, i.e., each of them is describing an effect that is missing in the other model. In total, the different description of the solvent effects in TDDFT causes a difference in the excitation energies of 0.10 eV. This is a small part of the total difference between DRF and FDE of 0.47 eV.

The differences in the HOMO–LUMO gap are mainly caused by two effects that are included in FDE but that are absent in the DRF model. First, the effects of hydrogen bonding are only partly included in the purely electrostatic DRF model. For the solvated water molecule considered here, the HOMO is stabilized by hydrogen bonding, while the LUMO is destabilized. Hydrogen bonding thus leads to an increase of the HOMO–LUMO gap. This chemical bonding part of the hydrogen bonding should be described correctly by FDE, while DRF only contains the electrostatic part. As a second effect, FDE also includes the Pauli repulsion of the solvent. The unoccupied orbitals partly extend into regions that are occupied by solvent molecules and experience the Pauli repulsion of their electrons. This leads to a further increase of the orbital energies of the diffuse unoccupied orbitals and therefore to an increase of the HOMO–LUMO gap. This is especially important in the system investigated here, since the lowest excitation is quite diffuse.

9.3.3. Polarizabilities

Finally, we compare the performance of DRF and FDE for modeling solvent effects on polarizabilities, again using the same solvent structure. In Table 9.5 for both the isolated molecule and the water molecule in the solvent cage the calcu-

Table 9.5.: Static and frequency-dependent polarizabilities calculated for an isolated water molecule in the gas phase and inside a solvation shell of 127 water molecules modeled using DRF and FDE. The mean polarizabilities $\bar{\alpha}$ and the polarizability anisotropy γ are given. Frequencies ω and polarizabilities are given in atomic units.

	ω	$\bar{\alpha}$	γ
isolated	0.0000	9.40	0.91
	0.0428	9.47	0.89
	0.0570	9.51	0.88
	0.0856	9.65	0.82
DRF	0.0000	9.62	0.72
	0.0428	9.68	0.71
	0.0570	9.73	0.71
	0.0856	9.87	0.70
FDE(SumFrag)	0.0000	8.77	0.47
	0.0428	8.82	0.47
	0.0570	8.86	0.46
	0.0856	8.98	0.46
FDE(relaxed)	0.0000	8.67	0.50
	0.0428	8.72	0.50
	0.0570	8.76	0.50
	0.0856	8.87	0.50

lated mean polarizabilities and the polarizability anisotropies γ are given. Both the static polarizabilities and the frequency-dependent polarizabilities at the frequencies $\omega = 0.0428, 0.0570, 0.0856$ a.u. ($\lambda = 1064, 800, 532$ nm, respectively) are given.

The static mean polarizability of 9.40 a.u. calculated for the isolated molecule is in good agreement with both the results of previous CCSD(T) calculations[232] (9.62 a.u.) and with the experimental value of 9.83 a.u. taken from Ref. [233]. For the frequency-dependent polarizabilities our DFT results are in good agreement with previous CCSD calculations[217] that obtained mean polarizabilities of 9.52 a.u., 9.57 a.u., and 9.71 a.u. calculated at frequencies of 0.0428 a.u., 0.0570 a.u., and 0.0856 a.u., respectively.

For the water molecule inside the solvation shell of 127 water molecules, DRF predicts a slight increase of the mean polarizability of approximately 0.2 a.u., both for the static and for the frequency-dependent polarizabilities. For the polarizability anisotropy, DRF predicts a slight decrease, in agreement with the previous results of Ref. [162]. With FDE, the mean polarizability decreases in solution by approximately 0.7 a.u. compared to the isolated molecule, which is in contrast to the increase in polarizability

Table 9.6.: Analysis of the static mean polarizabilities calculated for an isolated water molecule and for a water molecule inside a solvent shell of 127 water molecules using DRF and FDE to model the solvent shell. First,the mean polarizability calculated without including any effects of the environment in the TDDFT calculation is given as $\bar{\alpha}_{\text{noenv}}$. The additional contributions of the environment to the polarizabilities are given as $\Delta_{\text{env}}^{\text{resp}}\alpha$. The resulting mean polarizability is given as $\bar{\alpha}_{\text{tot}}$. All polarizabilities are given in atomic units.

	$\bar{\alpha}_{\text{noenv}}$	$\Delta_{\text{env}}^{\text{resp}}\alpha$	$\bar{\alpha}_{\text{tot}}$
isolated	9.40	−	9.40
DRF	9.22	+0.40	9.62
FDE(relaxed)	8.78	−0.11	8.67

that was found with DRF. The polarizability anisotropies calculated using FDE are in qualitative agreement with the DRF calculations, but FDE predicts a lowering about twice as large as predicted by DRF. We further note that for the calculation of the polarizabilities the relaxation of the solvent density in the FDE approach is much less important than for dipole moments and excitation energies.

The most striking finding of this comparison is the qualitative difference between DRF and FDE for the mean polarizabilities. With DRF the mean polarizability increases in solution, whereas it decreases with FDE. To analyze the qualitative differences between DRF and FDE, we performed an analysis similar to that in Sec. 9.3.2 for the excitation energies. We decomposed the calculated shifts of the mean polarizability in solution into contributions due to changes in the (ground-state) molecular orbitals and solvent contributions in the linear response calculation. To simplify this analysis, we focus on the static mean polarizabilities.

The static mean polarizabilities calculated using the different solvent models are decomposed according to

$$\bar{\alpha}_{\text{tot}} = \bar{\alpha}_{\text{noenv}} + \Delta_{\text{env}}^{\text{resp}}\alpha, \tag{9.7}$$

where $\bar{\alpha}_{\text{noenv}}$ is the static mean polarizability calculated from the embedded orbitals without including the additional environmental contributions in the linear response calculation. The results of this analysis are given in Table 9.6.

The mean polarizabilities $\bar{\alpha}_{\text{noenv}}$ follow the trend that is given by the solvent shifts of the excitation energies, since larger excitation energies should qualitatively correspond to smaller mean polarizabilities. In the case of a larger solvent shift of the excitation energies, the mean polarizability without the environment contribution should

also decrease. For DRF, the mean polarizability in solution decreases by 0.18 a.u. compared to the isolated molecule, which is in agreement with the larger excitation energies. For FDE, where the solvent shift of the excitation energies is even larger than in DRF, the mean polarizability in solution decreases by 0.62 a.u. compared to the isolated molecule.

The qualitative differences between DRF and FDE are caused by the environmental corrections to the mean polarizabilities $\Delta_{\text{env}}^{\text{resp}}\alpha$ that appear when the contributions of the environment are also included in the TDDFT part of the calculation. In the case of the DRF calculation, this correction contains the effect of the response of the solvent to the polarization of the solvated molecule. This response stabilizes the polarized molecule and therefore leads to an increase of the polarizability. This correction to the mean polarizability of +0.40 a.u. is larger than the change in the polarizability due to the changed molecular orbitals in solution of −0.18 a.u. and leads to an overall increase of the mean polarizability in solution. For the FDE calculation, where the response of the solvent is neglected, the environmental correction is much smaller than the corresponding DRF correction and is of opposite sign, i.e., the environment destabilizes the polarized molecule and thus leads to a lower polarizability. The FDE correction does therefore not change the lowering of the mean polarizability in solution that could be estimated from the increase of the excitation energies.

This analysis shows that for the calculation of polarizabilities the inclusion of the solvent response is apparently very important. For the system considered here, it changes the sign of the solvent effect on the static mean polarizability in the DRF calculation. On the other hand, even though the response of the solvent is included, the ground-state orbital energies obtained from DRF are worse than the ones obtained from FDE, because the effects of hydrogen bonding and of Pauli repulsion are only partly accounted for.

In the FDE calculation, where the response of the solvent is missing in the current TDDFT extension, it is possible to include the response of the solvent in the FDE calculations by calculating the static polarizabilities from the change in the dipole moment due to a finite electric field. In these calculations one can allow the solvent density to adapt to the polarization of the solute water molecule due to an applied electric field so that the response of the solvent is included. To estimate the effect of the environmental response in the FDE case, we calculate the difference between the static mean polarizabilities obtained from two different series of finite-field calculations. In the first calculations, the solvent density is relaxed with respect to the nonpolarized solute molecule, whereas it was relaxed with respect to the solute molecule polarized by the applied electric field in the second series of calculations to include the response of the solvent.

The first calculations were performed by converging the electron densities of the sol-

vent and the solute in two freeze-and-thaw FDE iterations. As in all earlier calculations, in theses freeze-and-thaw iterations only the ten solvent molecules that are closest to the solute are allowed to relax, while for all other solvent molecules the frozen gas-phase density is used. The relaxed solvent density was then used as the frozen density in an FDE calculation of the solute water molecule. From the numerical differentiation of the dipole moment obtained in this calculation with respect to the applied electric field, the polarizability tensor was obtained. These calculations yield a static mean polarizability of 7.79 a.u. In these finite-field calculations the solvent density cannot respond to the polarization of the solute. The corresponding TDDFT calculation that is labeled as FDE(relaxed) in Table 9.5 resulted in a mean polarizability of 8.67 a.u. The difference between these values arise because in the TDDFT calculations the ALDA approximation is used for the exchange–correlation kernel in combination with the SAOP potential. Therefore, the polarizabilities obtained from finite-field SAOP calculations do not agree with the TDDFT results. However, since the SAOP potential was designed to be used together with the ALDA kernel, the TDDFT calculations using ALDA should be more accurate than the finite-field calculation (that correspond to a TDDFT calculation using the "true" SAOP kernel).[26]

To obtain the polarizability from finite-field FDE calculations that take the response of the solvent into account, the electron densities of the solute and the solvent were calculated from freeze-and-thaw FDE calculations in which a finite electric field was applied in the calculation of the solute water molecule. The finite electric field was not applied in the calculations of the solvent electron density since we are only interested in the calculation of the local solute polarizability. Including the finite electric field also in the solvent calculations would introduce a screening of the macroscopic field at the solute molecule, leading to the so-called effective polarizability.[218] By applying the finite electric field in all calculations of the solute during the freeze-and-thaw cycles, the converged solvent density is relaxed with respect to the polarized solute molecule. The polarizabilities obtained from numerical differentiation of the dipole moments thus include the response of the solvent with respect to the solute polarization. From these calculations, a static mean polarizability of 8.09 a.u. is obtained. The difference between these two sets of finite-field FDE calculations, which is our estimate for the effect of the solvent response on the mean polarizability, amounts to +0.30 a.u.. This is comparable to the solvent response correction of +0.40 a.u. in the DRF case.

Adding this correction to the static mean polarizability from the TDDFT calculations using FDE to model the solvent leads to an estimated total static mean polarizability of 8.97 a.u.. I.e., even when the (positive) correction due to the response of the solvent is taken into account, the FDE calculations still predict a decrease in the static mean polarizability in solution compared to the isolated molecule. The DRF model predicts an increase, because the response of the solvent—modeled by atomic polarizabilities—is the largest solvent effect. In contrast to this, the major solvent effect in the FDE calculation arises from the increased HOMO–LUMO gap and, thus,

leads to a smaller mean polarizability.

9.4. Conclusions

In this work we performed a detailed comparison of the two discrete solvent models DRF and FDE for a number of molecular properties. For the dipole and quadrupole moment as ground-state properties both solvent models lead to similar results. To be able to account for the polarization of the solvent in FDE, it is necessary to relax the solvent density with respect to the solute in freeze-and-thaw cycles. The same effect is included in DRF in a computationally more efficient, though more approximate way by using distributed atomic polarizabilities.

For response properties, there are significant differences between the two solvent models. In the case of the excitation energies of the water system studied here, FDE predicts a larger solvent solvent shift than the DRF model. Our analysis showed that this difference mainly originates from a different description of the ground-state molecular orbitals of the solute molecule. The embedded orbitals obtained from the FDE calculation show a larger HOMO–LUMO gap than those obtained in the DRF calculation.

We attribute this difference in the HOMO–LUMO gap to a different description of short-range effects, the most important effects being direct hydrogen bonding between the solute and the solvent as well as the additional Pauli repulsion of the solvent on the diffuse excited states. Since the FDE scheme is in principle exact, it should be able to describe these effects more accurately than the DRF model, where both effects can only be modeled by the parameterization of the atomic point charges and polarizabilities. This was confirmed by a comparison to a supermolecular calculation on a smaller system that agreed well with the excitation energy calculated using FDE, while DRF yields an excitation energy that is too low. The small contribution of the response of the solvent to the excitation energies shows that the approximation of a response localized on the solute in the FDE calculation of excitation energies is obviously fulfilled.

For the polarizabilities, the effect of the response of the solvent to the polarization of the solute becomes nearly as important as the effect of the solvent on the ground-state orbitals, whereas it was negligible for the calculation of excitation energies. The solvent response is modeled in DRF by means of distributed atomic polarizabilities, but it is missing in the TDDFT extension of the FDE scheme. Since it can apparently not be neglected for the calculation of molecular polarizabilities in solution, DRF performs better for this kind of response properties. It can be expected that the effect of the solvent response will become even more important when going to

hyperpolarizabilities and other nonlinear optical properties.

The inclusion of the environmental response in DRF does not overcome the problems that are caused by the inaccurate description of the ground-state orbitals of the solute. The finite-field calculations that were done to get an estimate of the polarizability calculated using FDE including the response of the environment still yield a static mean polarizability that significantly differs from the results of the DRF calculation. In particular, the two models predict a different sign of the solvent shift in the mean polarizability. It would, therefore, be interesting to extend the FDE scheme to explicitly include the response of the solvent, since the finite-field approach employed here can only be applied for static polarizabilities. This would make the FDE scheme more generally applicable, e.g., to the calculation of other nonlinear optical properties in solution.

Summary

The frozen-density embedding (FDE) scheme within density-functional theory (DFT) provides a very powerful tool for the quantum chemical treatment of large systems. It is based on a partitioning of the electron density into the density of an active subsystem and a frozen environment. In the calculation of the density of the active subsystem, the effect of the frozen environment is represented by an effective embedding potential, that contains the electrostatic potential of the environment, an exchange-correlation component and a kinetic-energy component. In contrast to most other embedding schemes used in theoretical chemistry, the FDE scheme provides a formulation that is in principle exact.

This thesis deals with various aspects of the FDE scheme. An introduction of the methods of theoretical chemistry, in particular of DFT, and of the FDE scheme is given in Part I of this thesis.

Part II of this thesis provides theoretical extensions and improvements of the FDE scheme. In Chapter 4 it is shown how the FDE scheme can be applied to the calculation of nuclear-magnetic resonance (NMR) shieldings. Since the description of magnetic properties within DFT requires the use of the current density as a basic variable—in addition to the electron density—this makes a generalization of the FDE formalism necessary. By starting from nonrelativistic current DFT and by partitioning not only the electron density, but also the current density, such a generalized FDE formalism is given. It is shown that this introduces a formal dependence of the nonadditive kinetic-energy functional, which appears in the effective embedding potential, on the current densities in the subsystems.

If the usual approximations are introduced and the current dependence of the exchange-correlation potential of the nonadditive kinetic-energy functional are neglected, one arrives at a formulation in which the currents in the two subsystems that are induced by an external magnetic field are not coupled, and the NMR shielding can be calculated as a sum of contributions calculated for the individual subsystem. Since the NMR shielding only depends on the induced current in the vicinity of the NMR active nucleus, the contribution arising from the induced current in the subsystem containing this nucleus is dominant and the contribution due to the induced current in the other subsystem can usually be neglected. Altogether, this extension of the FDE scheme provides a simple and efficient scheme for calculating NMR shieldings

in large systems.

Even though the FDE scheme is in principle exact, a kinetic-energy component v_T appears in the embedding potential that is given by the functional derivative of the nonadditive kinetic-energy functional. To calculate v_T, an approximate kinetic-energy functional is needed and the applicability of the FDE scheme is limited by the accuracy of the available approximate functionals. Chapter 5 is devoted to improving the available approximations for the kinetic-energy component v_T of the embedding potential.

One strategy for developing approximate functionals is to investigate physical limits that are known exactly. In the present case, the form of v_T is investigated in the exact long-distance limit, i.e., in the limit of an infinite separation of the two subsystems. It can be shown that with the available approximate kinetic-energy functionals a wrong form of v_T is obtained in the regions of the frozen subsystem. The kinetic-energy component should cancel the electrostatic and exchange-correlation components, but the available approximate kinetic-energy functionals are not able to compensate the large nuclear attraction.

For two test systems, a $H_2O\cdots Li^+$ complex and an organic dye molecule surrounded by 30 water molecules, it is shown that this wrong behaviour of v_T leads to too low-lying virtual orbitals, that can lead to serious problems by causing convergence problems and by introducing spurious excitations in calculations of response properties. Based on the knowledge of the exact form of v_T in the long-distance limit, a correction can be proposed that enforces the correct form in this limit and removes the observed problems.

In Part III of this thesis (Chapters 6 and 7) an implementation of the FDE scheme is described. This implementation uses a very flexible setup, in which the total system is composed from an arbitrary number of fragments. For each frozen fragment, it can be chosen whether its density is kept completely frozen or if it is updated in freeze-and-thaw cycles. This allows a number of different setups. By employing a number of frozen fragments it is possible to use an approximate environment density, that is obtained as a sum of the densities of isolated molecules. On the other hand, it is also possible to relax the densities of all fragments in freeze-and-thaw cycles, which provides an efficient alternative to conventional DFT calculations. In addition, intermediate setups can be employed, in which the densities of a few frozen fragments are relaxed. This makes it possible to describe the polarization of the environment with respect to the nonfrozen subsystem.

The implementation employs an efficient numerical integration scheme with an integration grid that is mainly centered on the nonfrozen subsystem, and makes use of linear scaling techniques for the evaluation of the electrostatic potential and the electron density of the frozen subsystems. For large environments, the size of the in-

tegration grid does not increase and, therefore, the required computer time is almost constant when the size of the environment increases. This makes it possible to treat very large environments, for instance in studies of solvent effects, and the efficient implementation described here has already been used in a number of applications.

Part IV of this thesis includes two applications of the FDE scheme. In Chapter 8, the accuracy of FDE is investigated for weakly interacting $CO_2 \cdots X$ (X = He, Ne, Ar, Kr, Xe, Hg) van der Waals complexes. By comparing the results of fully converged freeze-and-thaw FDE calculations in which the densities of both subsystems are optimized to conventional supermolecular DFT calculations, it is possible to investigate possible problems in the approximate functionals used for the kinetic-energy component of the embedding potential. It is found that while the agreement is very good if no basis functions centered on the frozen system are included, problems arise when these basis functions are included. This is attributed to the problems in the available approximate kinetic-energy functionals that are investigated in Chapter 5.

As a second result, Chapter 8 shows how the FDE scheme can be used to apply different approximations to the exchange-correlation potential is different regions. In the case of the investigated $CO_2 \cdots X$ complexes, no common exchange-correlation approximation leads to a good agreement of the induced dipole moment calculated in a supermolecular DFT calculation with the experimental data. The induced dipole moment is mainly due to the polarization of the rare gas atom due to the quadrupole moment of the CO_2 molecule. It turns out that no approximation is able to describe both the polarizability of the rare gas atom and the quadrupole moment of CO_2 correctly. While a conventional GGA functional such as PW91 yields an accurate quadrupole moment for CO_2, it overestimates—because of its wrong asymptotic behaviour—the polarizability of the rare gas atom. On the other hand, the asymptotically correct SAOP potential results in polarizabilities that agree very well with experiment, but it yields an inaccurate quadrupole moment for CO_2. The FDE scheme provides a way to circumvent these problems by combining the PW91 functional for CO_2 with SAOP for the rare gas atom. This combination leads to induced dipole moments that are in good agreement with experiment.

An important field of application of the FDE scheme is the description of solvent effects on molecular properties. A realistic description of such solvent effects requires the inclusion of a large number of solvent molecules to account for the large solvent environment as well as calculations for a large number of solvent structures to account for the dynamics of the solvent. Therefore, an efficient method such as FDE is required for the calculation of the molecular properties.

In Chapter 9, a comparison of FDE with another solvent model, the discrete reaction field (DRF) model, a QM/MM scheme employing a polarizable force field, is given. The performance of FDE and DRF is compared for dipole and quadrupole

moments, excitation energies, and polarizabilities. These tests have been performed for a water molecules surrounded by a solvent shell of 127 water molecules, and only one representative structure has been used.

It is found that the two solvent models agree well for the ground-state properties (dipole and quadrupole moments). This shows that the electron density and the occupied orbitals calculated with FDE and DRF are very similar. However, there are significant differences for the response properties (excitation energies and polarizabilities). The analysis shows that this is due to two main reasons. First, the description of the virtual orbitals differs between the two solvent models. In FDE, the kinetic-energy component of the embedding potential provides a more accurate description of the effects of Pauli repulsion than the purely electrostatic model employed in DRF. Second, DRF includes the response of the environment, whereas this term is missing in FDE. While it is found that this environment response can be neglected in the case of excitation energies, it becomes important when calculating polarizabilities.

Several projects are already ongoing that build upon the results included in this thesis. The extension of FDE to the calculation of NMR shieldings is currently being applied to the calculation of the solvent shifts of the nitrogen shielding of acetonitrile in different solvents.[a] Furthermore, the extension of FDE to other magnetic properties, such as spin–spin couplings is underway.

A very promising extension of FDE is the application of its embedding potential to couple wave-function based *ab initio* methods to DFT. Currently, we are working on the application of such an *ab initio*-in-DFT embedding scheme to calculate electronic excitation energies of molecules in solution.[b]

One of the main challenges remains the extension of the applicability of FDE to systems in which there are covalent bonds between the active subsystem and the environment. This will require the development of improved approximate kinetic-energy functionals. One promising approach might be the application of the ideas that were used in Chapter 5 to derive the exact long-distance limit in a self-consistent scheme for the calculation of the exact embedding potential.[c]

---

[a] R. E. Bulo, Ch. R. Jacob, and L. Visscher, "NMR Solvent Shifts of Acetonitrile from Frozen-Density Embedding Calculations", to be submitted (2007).

[b] A. Severo Pereira Gomes, Ch. R. Jacob, and L. Visscher, in preparation (2007).

[c] Ch. R. Jacob and L. Visscher, in preparation (2007).

Samenvatting

De "bevroren dichtheid"-inbeddingsmethode

De "bevroren dichtheid"-inbeddingsmethode (frozen-embedding density, FDE), die
op de dichtheidsfunktionaaltheorie (DFT) gebaseerd is, levert een zeer krachtig hulp-
middel voor de kwantumchemische behandeling van grote systemen. Zij is gebaseerd
op het opdelen van de elektronendichtheid in de dichtheid van een actief subsysteem
en die van een bevroren omgeving. In de berekening van de dichtheid van het actieve
subsysteem wordt het effect van de bevroren omgeving meegenomen door middel van
een effectieve inbeddingspotentiaal, die bestaat uit de elektrostatische potentiaal van
de omgeving, een bijdrage van de exchange-correlatie potentiaal en een deel van de
kinetische energie. In tegenstelling tot de meeste andere inbeddingsmethodes die in
de theoretische chemie worden gebruikt, is de FDE-inbeddingsmethode in principe
exact.

Dit proefschrift behandelt diverse aspecten van de FDE-inbeddingsmethode. Een
inleiding in de methodes van theoretische chemie, in het bijzonder van DFT, en de
FDE-inbeddingsmethode wordt gegeven in deel I van dit proefschrift.

Deel II van dit proefschrift behandelt theoretische uitbreidingen en verbeteringen van
de FDE-inbeddingsmethode. In hoofdstuk 4 wordt daarom aangetoond hoe de FDE-
inbeddingsmethode op de berekening van NMR-verschuivingen kan worden toegepast.
Omdat het voor de beschrijving van magnetische eigenschappen in DFT noodzake-
lijk is om niet alleen de elektronendichtheid als onderliggende variabele te gebruiken,
maar ook de stroomdichtheid, moet het FDE-formalisme hiervoor gegeneraliseerd
worden. Zo'n generalisatie wordt gevonden door uit te gaan van niet-relativistische
(stroom-)dichtheidsfunktionaaltheorie en vervolgens niet alleen de elektronendicht-
heid, maar ook de stroomdichtheid op te delen. Verder wordt aangetoond dat in dit
gegeneraliseerde FDE-formalisme de niet-additive kinetische energie, die nodig is in
de effectieve inbeddingspotentiaal, niet alleen van de elektronendichtheden, maar ook
van de stroomdichtheden in de subsystemen afhangt.

Door de gebruikelijke benaderingen te maken en de stroomafhankelijkheid van zowel
de exchange-correlatie potentiaal als de niet-additive kinetische-energie-funktionaal te
verwaarlozen, raken de stroomdichtheden van de subsystemen, geïnduceerd door een

externe magnetische veld, ontkoppeld. Hierdoor kan de NMR-verschuiving worden berekend als de som van de bijdragen van beide subsystemen. Omdat de NMR-verschuiving slechts afhangt van de geïnduceerde stroomdichtheid in de buurt van de NMR-actieve kern, is de bijdrage van de geïnduceerde stroomdichtheid in het subsysteem dat deze kern bevat dominant. Zodoende kan de bijdrage van de geïnduceerde stroom in het bevroren subsysteem gewoonlijk worden verwaarloosd. Alles bij elkaar levert deze uitbreiding van de FDE-inbeddingsmethode een eenvoudige en efficiënte methode op voor het berekenen van NMR-verschuiving in grote systemen.

Alhoewel de FDE-inbeddingsmethode in principe exact is, bevat de effectieve inbeddingspotentiaal een kinetisch-energie component v_T, die door de functionele afgeleide van de niet-additive kinetisch-energie-funktionaal wordt gegeven. Om deze v_T te berekenen, is een benaderde kinetisch-energie-funktionaal nodig, waardoor de toepasbaarheid van de FDE-inbeddingsmethode wordt beperkt door de nauwkeurigheid van de beschikbare benaderingen. Hoofdstuk 5 is daarom gewijd aan het verbeteren van de beschikbare benaderingen voor de kinetisch-energie-component v_T van de effectieve inbeddingspotentiaal.

Eén mogelijke strategie voor het ontwikkelen van benaderde funktionalen is het onderzoeken van limietgevallen, waarin het gedrag van deze funktionalen exact bekend is. In dit hoofdstuk wordt de vorm van v_T onderzocht in het geval van een zeer grote afstand tussen de twee subsystemen. Men kan voor deze limiet aantonen dat de beschikbare benaderde kinetisch-energie-funktionalen v_T een verkeerd gedrag vertonen in de gebieden van het bevroren subsysteem. De kinetisch-energie-component v_T zou tegen de elektrostatische en de exchange-correlatie componenten weg moeten vallen, maar de beschikbare benaderde kinetisch-energie-funktionalen kunnen helaas niet de grote aantrekkingskracht van de kernen compenseren.

Voor twee testsystemen, een $H_2O \cdots Li^+$ complex en een organisch kleurstofmolecuul dat door 30 watermoleculen is omgeven, wordt aangetoond dat dit verkeerde gedrag van v_T tot te lage energieën van virtuele orbitalen leidt. Dit zou tot ernstige problemen kunnen leiden door ofwel convergentieproblemen te veroorzaken of door verkeerde excitaties in berekeningen van respons-eigenschappen te introduceren. Gebaseerd op de kennis van de exacte vorm van v_T in de limiet van lange afstanden tussen de subsystemen, kan een correctie worden opgesteld die in dit geval de juiste vorm afdwingt en zo de waargenomen problemen oplost.

In deel III van dit proefschrift (hoofdstukken 6 en 7) wordt een implementatie van de FDE-inbeddingsmethode beschreven. In deze flexibele implementatie bestaat het totale systeem uit een willekeurig aantal fragmenten (subsystemen). Voor elk bevroren fragment kan worden gekozen of zijn dichtheid volledig bevroren zal worden gehouden of dat het in "freeze-and-thaw"-iteraties ("bevriezen-en-ontdooien"-iteraties) zal worden bijgewerkt. Dit maakt verschillende beschrijvingen van het totale systeem

mogelijk. Zo is het mogelijk om door meerdere bevroren fragmenten te gebruiken een benaderde omgevingsdichtheid te verkrijgen die de som is van de dichtheden van geïsoleerde moleculen. Ook is het mogelijk om de dichtheid van alle fragmenten in "freeze-and-thaw"-iteraties bij te werken, wat een efficiënt alternatief voor conventionele DFT-berekeningen kan zijn. Bovendien kan een combinatie van beide technieken gebruikt worden, dan worden slechts de dichtheden van een paar bevroren fragmenten bijgewerkt met "freeze-and-thaw"-iteraties. Dit maakt het mogelijk om de polarisatie van de omgeving als gevolg van het actieve subsysteem te beschrijven.

De implementatie maakt gebruik van een efficiënte methode voor numerieke integratie met een integratierooster dat voornamelijk gecentreerd is op het niet-bevroren subsysteem en bovendien gebruik maakt van "lineaire schalings"-technieken voor de evaluatie van de elektrostatische potentiaal en de elektronendichtheden van de bevroren subsystemen. Doordat voor voldoend grote omgevingen de grootte van het integratierooster niet toeneemt is de vereiste computertijd bijna constant met de grootte van de omgeving. Dit maakt het mogelijk om zeer grote omgevingen, in bijvoorbeeld in studies van oplosmiddeleffecten, te gebruiken en heeft al geleid tot een aantal toepassingen.

Deel IV van dit proefschrift behandelt twee toepassingen van de FDE-inbeddingsmethode. In hoofdstuk 8 wordt de nauwkeurigheid van de FDE-methode onderzocht voor zwak-wisselwerkende $CO_2 \cdot X$ (X = He, Ne, Ar, Kr, Xe, Hg) van-der-Waals-complexen. Door de resultaten van "freeze-and-thaw"-FDE berekeningen waarin de dichtheden van beide subsystemen geoptimaliseerd zijn te vergelijken met conventionele DFT-berekeningen voor het totale systeem, is het mogelijk om problemen te onderzoeken in de benaderde funktionalen voor de kinetisch-energie-component van het inbeddingspotentiaal. Uit deze vergelijking blijkt dat de berekeningen waarin de basisfuncties van de bevroren subsysteem niet worden gebruikt goed met elkaar overeenkomen. Zodra deze basisfuncties echter worden meegenomen, treden problemen op. Dit wordt toegeschreven aan de problemen in de beschikbare benaderde kinetisch-energie-funktionalen die in hoofdstuk 5 werden onderzocht.

Als tweede resultaat toont hoofdstuk 8 hoe de FDE-inbeddingsmethode kan worden gebruikt om verschillende benaderingen voor de exchange-correlatie potentiaal in verschillende gebieden te gebruiken. Voor de onderzochte $CO_2 \cdot X$ complexen leiden de gebruikelijke exchange-correlatie benaderingen niet tot een goede overeenstemming van de geïnduceerde dipoolmomenten uit de standaard DFT-berekeningen met de experimentele waarden. Het geïnduceerde dipoolmoment is hoofdzakelijk toe te schrijven aan de polarisatie van het edelgasatoom door het quadrupoolmoment van de CO_2-molecuul. Het blijkt dat geen van de benaderingen zowel de polariseerbaarheid van het edelgasatoom als het quadrupoolmoment van CO_2 correct kan beschrijven. Terwijl een conventionele GGA funktionaal zoals PW91 een nauwkeurig quadrupool-moment voor CO_2 oplevert, overschat zo'n funktionaal door zijn verkeerde asympto-

tisch gedrag de polariseerbaarheid van het edelgasatoom. Van de andere kant, voor een asymptotisch correcte potentiaal zoals SAOP komen de polariseerbaarheden goed overeen met het experiment, maar zij geven een onnauwkeurig quadrupoolemoment voor CO_2. De FDE-inbeddingsmethode is een manier om deze problemen te omzeilen door de PW91 funktionaal voor CO_2 en SAOP voor het edelgasatoom te gebruiken. Deze combinatie leidt tot geïnduceerde dipoolmomenten die in goede overeenstemming met het experiment zijn.

Een belangrijk toepassingsgebied van de FDE-inbeddingsmethode is de beschrijving van oplosmiddeleffecten op moleculaire eigenschappen. Voor een realistische beschrijving van de invloed van een oplosmiddel moet een groot aantal oplosmiddel-moleculen meegenomen worden evenals een groot aantal van structuren om de dynamica van het oplosmiddel goed te beschrijven. Daarom is voor de berekening van de moleculaire eigenschappen een efficiënte methode zoals FDE nodig.

In hoofdstuk 9 wordt een vergelijking gemaakt tussen FDE met een ander model voor de berekening oplosmiddeleffecten, het "discrete reaction field" (DRF) model. Dit is een QM/MM methode die een polariseerbaar krachtveld gebruikt. De resultaten van FDE en DRF modellen worden vergeleken voor dipool- en quadrupoolmomenten, excitatieenergiën en polariseerbaarheden. Als testsysteem wordt een watermolecuul gebruikt, die door 127 watermoleculen omringd wordt, en er wordt slechts één representatieve structuur gebruikt.

Voor eigenschappen van de grondtoestand (dipool- en quadrupolemomenten) stemmen de twee modellen goed overeen. Dit toont aan dat de elektronendichtheid en de bezette orbitalen, die met FDE en DRF worden berekend, zeer vergelijkbaar zijn. Er zijn echter significante verschillen voor de respons-eigenschappen (excitatieenergiën en polariseerbaarheden). De analyse toont aan hiervoor twee belangrijke oorzaken zijn. Ten eerste verschillen in de twee modellen de beschrijvingen van de virtuële orbitalen. De kinetisch-energie-component van het FDE-inbeddingspotentiaal geeft een nauwkeuriger beschrijving van de Pauli-repulsie dan het uitsluitend elektrostatische model in DRF. Ten tweede, omvat het DRF-model de respons van de omgeving, terwijl deze bijdrage in FDE mist. Deze omgevings-respons is verwaarloosbaar voor excitatieenergiën, maar belangrijk voor polariseerbaarheden.

Er lopen reeds verscheidene projecten die voortbouwen op de resultaten van dit proefschrift. De uitbreiding van FDE voor de berekening van NMR-verschuivingen wordt momenteel toegepast in de berekening van de invloed van verschillende oplosmiddelen op de N-verschuiving van acetonitrile.[a] Verder wordt momenteel de FDE-inbeddingsmethode uitgebreid voor de berekening van andere magnetische eigenschappen, zoals spin-spin-koppelingen.

---

[a] R. E. Bulo, Ch. R. Jacob, and L. Visscher, "NMR Solvent Shifts of Acetonitrile from Frozen-Density Embedding Calculations", to be submitted (2007).

Een zeer veelbelovende uitbreiding van FDE is om door middel van de FDE-in-beddingspotentiaal golffunctie gebaseerde *ab initio* methodes (wave-function theory, WFT) aan DFT te koppelen. Momenteel werken wij aan de toepassing van een dergelijke WFT-in-DFT-inbeddingsmethode om elektronische excitatieenergiën van moleculen in een oplosmiddel te berekenen.[b]

Een van de belangrijkste uitdagingen blijft het vinden van een uitbreiding van de FDE-inbeddingsmethode zodat deze toe te passen zal zijn op systemen waarin het actieve subsysteem covalente bindingen heeft met de bevroren omgeving. Dit zal de ontwikkeling van betere benaderde kinetisch-energie-funktionalen vereisen. Een veelbelovende aanpak zou de toepassing van de ideeën van hoofdstuk 5 op de berekening van de exacte inbeddingspotentiaal kunnen zijn.[c]

---

[b]A. Severo Pereira Gomes, Ch. R. Jacob, and L. Visscher, in preparation (2007).
[c]Ch. R. Jacob and L. Visscher, in preparation (2007).

Samenvatting

Zusammenfassung

Das "gefrorene Dichte"-Einbettungsverfahren

Das "gefrorene Dichte"-Einbettungsverfahren (frozen-density embedding, FDE), welches auf der Dichtefunktionaltheorie (DFT) basiert, ist ein sehr leistungsfähiges Werkzeug für die quantenchemische Beschreibung großer Systeme. Es basiert auf einer Unterteilung der Elektronendichte des Gesamtsystems in die Elekronendichten eines aktiven Subsystems und einer gefrorenen Umgebung. In der Berechnung der Elektronendichte des aktiven Subsystems wird der Effekt dieser gefrorenen Umgebung durch ein effektives Einbettungspotential repräsentiert, welches das elektrostatische Potential der Umgebung, einen Beitrag des Austausch-Korrelations-Potentials sowie eine kinetische Energie-Komponente enthält. Im Gegensatz zu den meisten anderen Einbettungsverfahren, die in der theoretischen Chemie verwendet werden, ist das FDE-Einbettungsverfahren im Prinzip exakt.

Diese Doktorarbeit behandelt verschiedene Aspekte des FDE-Einbettungsverfahrens. Eine Einführung in die Methoden der theoretischen Chemie, insbesondere DFT, sowie des FDE-Einbettungsverfahrens wird in Teil I dieser Arbeit gegeben.

In Teil II dieser Arbeit werden verschiedene theoretische Erweiterungen und Verbesserungen des FDE-Einbettungsverfahrens vorgestellt. In Kapitel 4 wird gezeigt, wie sich FDE für die Berechnung von NMR-Verschiebungen anwenden lässt. Da es für die Behandlung solcher magnetischer Eigenschaften in DFT notwendig ist, nicht nur die Elektronendichte sondern auch die Stromdichte als grundlegende Variablen zu verwenden, ist es hierfür nötig den FDE-Formalismus zu verallgemeinern. Ausgehend von nicht-relativistischer (Strom-)Dichtefunktionaltheorie und einer Partitionierung sowohl der Elektronendichte als auch der Stromdichte wird eine solche verallgemeinerte Formulierung präsentiert. Es wird weiter gezeigt, dass in einer solchen verallgemeinerten Formulierung die nicht-additive kinetische Energie, welche im effektiven Einbettungspotential benötigt wird, nicht nur von den Elektronendichten der Subsysteme abhängt, sondern auch von den Stromdichten in den Subsystemen.

Wenn die üblichen Näherungen eingeführt und die Abhängigkeit des Austausch-Korrelations-Potentials sowie des Funktionals der nicht-additiven kinetischen Energie von der Stromdichte vernachlässigt werden, erhält man eine Formulierung in welcher

die Stromdichten in den beiden Subsystemen, die durch ein externes magnetisches Feld induziert werden, nicht gekoppelt sind. Dadurch kann die NMR-Verschiebung als Summe von Beiträgen der beiden Subsysteme berechnet werden. Da die NMR-Verschiebung nur von der induzierten Stromdichte in unmittelbarer Nähe des NMR-aktiven Atomkerns abhängt, dominiert hierbei der Beitrag des Subsystems, welches diesen Atomkern enthält und der Beitrag des gefrorenen Subsystems kann in der Regel vernachlässigt werden. Die vorgestellte Verallgemeinerung des FDE-Einbettungsverfahrens führt hierdurch zu einem einfachen und effizienten Verfahren für die Berechnung von NMR-Verschiebungen in großen Systemen.

Auch wenn das FDE-Einbettungsverfahren im Prinzip exakt ist, enthält das effektive Einbettungspotential einen Beitrag v_T der kinetischen Energie, welcher durch die Funktionalableitung der nicht-additiven kinetischen Energie gegeben ist. Um diesen Beitrag v_T zu berechnen wird ein genähertes Funktional benötigt und die Anwendbarkeit des FDE-Verfahrens ist durch die Genauigkeit dieses genäherten Funktionals begrenzt. Kapitel 5 ist der Verbesserung der Näherungen für diesen Beitrag v_T gewidmet.

Eine mögliche Strategie für die Entwicklung genäherter Funktionale ist es, Grenzfälle zu untersuchen, für die das exakte Verhalten dieser Funktionale bekannt ist. Im vorliegenden Fall wird die Form von v_T für den Grenzfall eines sehr großen Abstandes zwischen den beiden Subsystemen untersucht. Es wird gezeigt, dass die zur Verfügung stehenden genäherten Funktionale der kinetischen Energie zu einer falschen Form von v_T am gefrorenen Subsystem führen. Dort sollte der Beitrag der kinetischen Energie den elektrostatischen sowie den Austausch-Korrelations-Beitrag aufheben, aber die genäherten Funktionale können die starke Anziehung der Atomkerne nicht kompensieren.

Für zwei Testsysteme, einen $H_2O \cdots Li^+$–Komplex und ein organisches Farbstoffmolekül umgeben von 30 Wassermolekülen, wird gezeigt, dass dieses falsche Verhalten von v_T zu zu niedrigen Energien virtueller Orbitale führt, was zu Konvergenzproblemen und einer falsche Beschreibung von Anregungsenergien und anderen Response-Eigenschaften führen kann. Basierend auf der exakten Form von v_T im Grenzfall langer Abstände zwischen den beiden Subsystemen wird eine Korrektur vorgeschlagen, welche die korrekte Form von v_T in diesem Grenzfall sicherstellt und dadurch die beobachteten Probleme behebt.

In Teil III dieser Doktorarbeit (Kapitel 6 und 7) wird eine Implementierung des FDE-Einbettungsverfahrens beschrieben. In dieser flexiblen Implementierung wird das Gesamtsystem aus einer beliebigen Anzahl von Fragmenten (Subsystemen) aufgebaut. Für jedes gefrorene Fragment kann gewählt werden, ob die Elektronendichte dieses Fragmentes komplett gefroren ist, oder ob es in "freeze-and-thaw"-Iterationen ("Einfrieren und Auftauen"-Iterationen) aktualisiert wird. Dies ermöglicht verschiedene

Beschreibungen des Gesamtsystems. Indem mehrere gefrorene Fragmente verwendet werden ist es möglich eine genäherte gefrorene Dichte für die Umgebung zu verwenden, die als Summe der Dichten der einzelnen Fragmente erhalten wird. Des weiteren ist es möglich, die Dichten aller Fragmente in "freeze-and-thaw"-Iterationen zu berechnen, was eine effiziente Alternative zu gewöhnlichen DFT-Rechnungen liefert. Außerdem sind gemischte Varianten möglich, in denen nur die Dichten einiger weniger gefrorener Fragmente in "freeze-and-thaw"-Iterationen aktualisiert werden. Dies macht es möglich, die Polarisierung der Umgebung durch das aktive System zu beschreiben.

Die Implementierung verwendet ein effizientes numerisches Integrationsverfahren mit einem Integrationsgitter das hauptsächlich auf dem nicht-gefrorenen Subsystem lokalisiert ist. Des weiteren werden für die Berechnung der Elektronendichte und des elektrostatischen Potentials der gefrorenen Subsysteme effiziente "linear scaling"-Techniken verwendet. Für große Umgebungen ist die Größe des benötigten Integrationsgitters nahezu konstant, was dazu führt dass die benötigte Rechenzeit ebenfalls konstant ist und nicht mit der Größe der gefrorenen Umgebung ansteigt. Das ermöglicht Berechnungen mit sehr großen gefrorenen Umgebungen, zum Beispiel zur Beschreibung von Lösungsmitteleffekten. Die beschriebene effiziente Implementierung wurde bereits in mehreren solchen Untersuchungen angewendet.

Teil IV dieser Doktorarbeit enthält zwei Anwendungen des FDE-Einbettungsverfahrens. In Kapitel 8 wird die Genauigkeit des FDE-Verfahrens für schwach wechselwirkende $CO_2 \cdots X$ (X = He, Ne, Ar, Kr, Xe, Hg) van-der-Waals-Komplexe untersucht. Durch Vergleich der Ergebnisse von komplett konvergierten "freeze-and-thaw"-FDE-Berechnungen, in denen die Elektronendichten beider Subsysteme optimiert werden, mit gewöhnlichen DFT-Rechnungen am Supermolekül ist es möglich, Probleme der verwendeten genäherten Funktionale der kinetischen Energie zu untersuchen. Dabei zeigt sich, dass für den Fall, dass die Basisfunktionen des gefrorenen Subsystems nicht in der Berechnung des aktiven Subsystems verwendet werden, gute Ergebnisse erzielt werden, während Probleme auftreten, wenn diese Basisfunktionen berücksichtigt werden. Dies wird auf Probleme des verwendeten Funktionals der kinetischen Energie zurückgeführt, die in Kapitel 5 eingehender untersucht wurden.

Als ein weiteres Ergebnis zeigt Kapitel 8, dass das FDE-Einbettungsverfahren angewendet werden kann, um verschiedene Näherungen für das Austausch-Korrelations-Potential für verschiedene Regionen zu verwenden. Im Fall der untersuchten $CO_2 \cdots X$-Komplexe liefert keine der verfügbaren Näherungen für das Austausch-Korrelations-Potential eine gute Übereinstimmung der in den supermolekularen DFT-Rechnungen erhaltenen induzierten Dipolmomente mit den experimentellen Daten. Dieses induzierte Dipolmoment kommt durch die Polarisierung des Edelgasatoms durch das Quadrupolmoment des CO_2-Moleküls zustande. Es zeigt sich, dass keines der genäherten Austausch-Korrelations-Potentiale sowohl die Polarisierbarkeit des Edelgasatoms als auch das Quadrupolmoment des CO_2-Moleküls korrekt beschreibt.

Zusammenfassung

Während Standard-GGA-Funktionale wie zum Beispiel PW91 das Quadrupolmoment von CO_2 korrekt beschreiben, überschätzen diese Funktionale durch ihr falsches asymptotisches Verhalten die Polarisierbarkeit der Edelgasatome. Andererseits liefert das asymptotisch korrekte SAOP-Potential Polarisierbarkeiten, die gut mit den experimentellen Daten übereinstimmen, dieses führt aber gleichzeitig zu einer ungenauen Beschreibung des Quadrupolmoments von CO_2. Das FDE-Einbettungsverfahren ermöglicht es, diese Probleme durch eine Kombination von PW91 für CO_2 mit der Verwendung von SAOP für das Edelgasatom zu umgehen. Hierdurch ist es möglich, induzierte Dipolmomente zu erhalten, die gut mit den experimentellen Daten übereinstimmen.

Ein wichtiges Anwendungsgebiet des FDE-Einbettungsverfahrens ist die Beschreibung von Lösungsmitteleffekten auf molekulare Eigenschaften. Für eine realistische Beschreibung solcher Lösungsmitteleffekte ist es notwendig, sowohl ein große Anzahl von Molekülen des Lösungsmittels zu berücksichtigen als auch eine Vielzahl von Lösungsmittelstrukturen zu betrachten, um so die Dynamik der Moleküle in Lösung angemessen beschreiben zu können. Aus diesen Gründen wird für die Berechnung der molekularen Eigenschaften eine sehr effiziente Methode wie FDE benötigt.

In Kapitel 9 wird ein Vergleich des FDE-Einbettungsverfahrens mit einem anderen Modell für Lösungsmitteleffekte, dem "discrete reaction field"-Modell (DRF-Modell), einem QM/MM-Verfahren welches ein polarisierbares Kraftfeld verwendet, präsentiert. Dieser Vergleich wird für Dipol- und Quadrupolmomente, Anregungsenergien sowie für Polarisierbarkeiten durchgeführt. Dabei wird ein Wassermolekül umgeben von einer Lösungsmittelhülle aus 127 Wassermolekülen verwendet, wobei nur eine einzige repräsentative Struktur verwendet wird.

Es zeigt sich, dass für Grundzustandseigenschaften (Dipol- und Quadrupolmomente) die beiden Methoden gut übereinstimmen. Das zeigt dass die Elektronendichte und die besetzen Orbitale mit FDE und DRF sehr ähnlich sind. Für Response-Eigenschaften (Anregungsenergien und Polarisierbarkeiten) werden allerdings deutliche Unterschiede beobachtet. Die durchgeführten Analysen führen diese Unterschiede auf zwei Ursachen zurück. Erstens unterscheidet sich die Beschreibung der virtuellen Orbitale zwischen den beiden Methoden. In den FDE-Rechnungen führt der Beitrag der kinetischen Energie zum Einbettungspotential zu einer genaueren Beschreibung der Pauli-Abstoßung der Umgebung als das rein elektrostatische Einbettungspotential, das im DRF-Modell verwendet wird. Zweitens berücksichtigt DRF den Response der Umgebung, während dieser Beitrag in den FDE-Rechnungen fehlt. Es zeigt sich dass dieser Beitrag für Anregungsenergien vernachlässigt werden kann, aber für die Berechnung von Polarisierbarkeiten berücksichtigt werden muss.

Mehrere laufende Projekte bauen auf die Ergebnisse dieser Doktorarbeit auf. Die Erweiterung des FDE-Einbettungsverfahrens auf die Berechnung von NMR-Verschieb-

ungen wird zur Zeit angewendet, um den Effekt verschiedener Lösungsmittel auf die N-Verschiebung in Acetonitril zu beschreiben.[a] Des weiteren wird an der Erweiterung des FDE-Verfahrens auf weitere magnetische Eigenschaften, z.B. Spin-Spin-Kopplungskonstanten, gearbeitet.

Eine weitere viel versprechende Verallgemeinerung des FDE-Einbettungsverfahrens ist die Anwendung des FDE-Einbettungspotentials um *ab initio* Methoden, die auf der Berechnung der Wellenfunktion basieren (wave function theory, WFT), mit DFT zu koppeln. Zur Zeit arbeiten wir an der Anwendung eines solchen "WFT-in-DFT"-Einbettungsverfahrens zur Berechnung von elektronischen Anregungsenergien von Molekülen in Lösung.[b]

Eine der größten Herausforderungen bleibt die Erweiterung der Anwendbarkeit des FDE-Verfahrens auf Systeme mit kovalenten Bindungen zwischen dem aktiven Subsystem und der gefrorenen Umgebung. Hierfür werden verbesserte Funktionale der kinetischen Energie benötigt. Ein viel versprechender Ansatz hierfür könnte die Anwendung der in Kapitel 5 vorgestellten Ideen zur Berechnung des exakten Einbettungspotentials sein.[c]

[a]R. E. Bulo, Ch. R. Jacob und L. Visscher, "NMR Solvent Shifts of Acetonitrile from Frozen-Density Embedding Calculations", to be submitted (2007).
[b]A. Severo Pereira Gomes, Ch. R. Jacob und L. Visscher, in preparation (2007).
[c]Ch. R. Jacob und L. Visscher, in preparation (2007).

Zusammenfassung

Appendix

A. ADF NewFDE User's Guide

this is an extended version of the

FDE User's Guide contained in the ADF manual

(http://www.scm.com)

A.1. Introduction

In the orbital-free frozen-density embedding (FDE) formalism,[8] the environment of an embedded subsystems is accounted for by means of the embedding potential depending explicitly on electron densities corresponding to the embedded subsystem (e.g., a solvated molecule) and its environment (e.g., solvent). For a detailed review, see Ref. 48. The ADF implementation of the method is described in detail in Refs. CJ4, CJ9. The implementation of FDE in ADF2007 has been completely revised and improved. Therefore, the input format has been changed with respect to ADF2006.

A time-dependent linear-response generalization of this embedding scheme was derived in Ref. 59. Its implementation in an approximate form, which assumes a localized response of the embedded system only, is described in the supplementary material to Ref. 60. For possible drawbacks and pitfalls in connection with this approximation, see Refs. CJ4, CJ5, 83.

A generalization of the FDE scheme to the calculation of NMR shieldings has been given in Ref. CJ6, where also the approximations involved and possible problems are discussed.

The current implementation in ADF allows the calculation of molecular properties that only depend on the electron density and of response properties using TDDFT. For an application to the calculation of several molecular properties in solution and a comparison to the DRF model also available in ADF, see Ref. CJ5. For further applications of the ADF implementation, see Ref. CJ3 (weakly interacting complexes) and Refs. CJ4, CJ5, 50, 76 (solvent effects) and[83,88,89] (other environment effects).

In the Examples section at the end of this User's Guide, several examples of different

FDE calculations can be found.

A.2. FDE Input

To invoke a frozen-density embedding calculation, two additional specifications in the input are required. First, one or more frozen fragments have to be included in the `FRAGMENTS` block, and second, the block key `FDE` has to be included. In the simplest case, this input should look like this:

```
FRAGMENTS
  ...
  FragType FragFile type=FDE
  ...
END

FDE
  PW91K
END
```

In the `FRAGMENTS` block, for any fragment it is possible to specify the option `type=FDE` to indicate that the density of this fragment is kept frozen. This density is imported from the file `FragFile`. The frozen fragments have to be included in addition to the usual, nonfrozen fragments. The atoms of the frozen fragments have to be included in the `ATOMS` block. As with normal fragments, the fragment found in the file will be rotated and translated to its position specified in the `ATOMS` block. For more details on specifying fragments, see the section "fragment files" of the ADF manual. In the FDE input block, the recommended PW91k functional is chosen for the nonadditive kinetic energy. For all other options the defaults will be used.

By including more than one frozen fragment, it is possible to use a frozen fragment that is a superposition of the densities of isolated molecules (this was possible in the previous version of ADF using the `DENSPREP` option). For a discussion and tests of the use of such approximate environment densities, see Ref. 76.

There is no restriction on the use of symmetry in FDE calculations, and usually the correct symmetry will be detected automatically. However, in the preparation of frozen fragments that will be rotated and/or translated in the FDE calculation, for technical reasons one has to include the keyword `NOSYMFIT`.

In the current implementation, only the electron density of the embedded (nonfrozen) system is calculated. Therefore, only properties that depend directly on the electron

density (e.g., dipole moments) are available. In particular, the calculation of interaction energies or of energy gradients is not implemented yet. All quantities given in the output refer (unless explicitly specified otherwise) to the nonfrozen system only.

The TDDFT extension of the FDE formalism allows the calculation of electronic excitation energies and polarizabilities. This extension is automatically activated if FDE is used in combination with the `EXCITATIONS` or the `RESPONSE` key.

To employ the extension of FDE to the calculation of NMR shieldings, the file TAPE10 has to be used in the FDE calculation (by including the option `SAVE TAPE10`), and subsequently the NMR shielding has to be calculated using the program NMR (not with ESR).

A.3. Fragment-specific FDE options

For each frozen fragment, several additional options can be applied. To do this, the fragment specification is used as a subblock key by appending a & sign. The subblock is terminated with `SubEnd`. This subblock key looks, in the most general form, as follow:

```
FRAGMENTS
  ...
  FragType FragFile type=FDE &
     {FDEOPTIONS [USEBASIS] [RELAX]}
     {FDEDENSTYPE [SCF | SCFexact | SCFfitted | FullSum ]}
     {RELAXCYCLES n}
     {XC [LDA | GGA ggapotx ggapotc | MODEL SAOP]}
  SubEnd
  ...
END
```

FDE options

- `FDEOPTIONS USEBASIS`
  If the `USEBASIS` option is specified, the basis functions of this frozen fragment will be included in the calculation of the nonfrozen subsystem. This allows it to apply the so-called "supermolecular basis set expansion", also referred to as FDE(s) calculations, which are often useful for benchmarking.

- `FDEOPTIONS RELAX`
  If the `RELAX` option is specified, the density of this frozen fragment will be

relaxed in freeze-and-thaw cycles, i.e., the active subsystem is frozen, while this fragment is thawed. This is repeated, until convergence is reached or until the maximum number of iterations has been performed. By relaxing frozen fragments, it is possible to improve a given approximate environment density by including the polarization of the environment due to the embedded system.

- **FDEOPTIONS USEBASIS RELAX**
  It is further possible to combine `USEBASIS` and `RELAX`. In this case, the basis functions of the nonfrozen fragment will be included when the density of the fragment is relaxed. This allows fully relaxed FDE(s) calculations.

DENSTYPE

The `FDEDENSTYPE` option can be used to specify which density is read from the fragment file. The possible options are:

- **FDEDENSTYPE SCF** (or `FDEDENSTYPE SCFexact`)
  The exact density (not calculated using the fit functions) is used. This is the default.

- **FDEDENSTYPE SCFfitted**
  The fitted density is used. This is in general more efficient, but can lead to less accurate results.

- **FDEDENSTYPE FullSum**
  The superposition of the densities of the initial fragments is used. This option is only included for compatibility with the `DENSPREP` option included in the previous version of ADF.

Options for relaxing

The remaining options can be used for fragments that are relaxed.

- **RELAXCYCLES n**
  This gives the maximum number of freeze-and-thaw cycles that are performed for this fragment. If the maximum number given in the FDE block is smaller, or if convergence is reached earlier, then less cycles are performed.

- **XC**
  The XC option can be used to select the exchange-correlation potential that is used for this fragment when it is relaxed. By default, the same potential as for the nonfrozen system is used, but in some cases it might be preferable to use another approximation for certain fragments.

— `XC LDA`
This option selects LDA as exchange-correlation potential for relaxing this fragment.

— `XC GGA ggapotx ggapotc`
This selects a GGA potential for relaxing this fragment. The GGA potential is specified by giving the name of the exchange potential, followed by the name of the correlation potential. The available potentials are listed in the documentation for the XC key.

— `XC MODEL SAOP`
This selects the model potential SAOP for relaxing this fragment.

A.4. General FDE options

In addition to the fragment-specific options, there are also a number of options available in FDE calculations that will be described in the following.

```
FDE
  {kinetic energy functional}
  {CJCORR}
  {GGAPOTXFD exchange functional}
  {GGAPOTCFD correlation functional}
  {FULLGRID}
  {RELAXCYCLES n}
end
```

kinetic energy functional

There are several approximate kinetic energy functionals available, that can be used for the nonadditive kinetic energy in the effective embedding potential. If no kinetic energy functional is specified, by default the local-density approximation (Thomas-Fermi functional) is used. For an assessment of functionals for weakly interacting systems see Ref. 40. Based on this study, the use of PW91k is recommended.

- `THOMASFERMI` (default)
  Thomas-Fermi LDA functional[34,35]

- `WEIZ`
  gradient-dependent von Weizsäcker functional[36] (no LDA part included)

- `TF9W`
  Thomas-Fermi functional + 1/9 von Weizsäcker functional

- `PW91k` (recommended functional)
  GGA functional based on PW91 exchange functional, reparametrized for the kinetic energy by Lembarki and Chermette[58]

- `LLP91`
  GGA functional based on Becke88 exchange functional, reparametrized for the kinetic energy by Lee, Lee, and Parr[55]

- `PW86k`
  GGA functional based on PW86 exchange functional[235]

- `OL91A, OL91B`
  gradient-dependent functionals OL1 and OL2 by Ou-Yang and Levy[236]

- `THAKKAR92`
  gradient-dependent functional by Thakkar[237]

- `COULOMB`
  This option does not stand for a kinetic energy functional, but it disables the nonadditive kinetic energy part and the exchange-correlation part in the embedding potential. The remaining embedding potential will only contain the Coulomb interaction with the frozen density. Note that the use of this option is not recommended, it is useful for analysis purposes only.

long-distance correction

As was shown in Ref. CJ7, with the available approximate kinetic-energy functionals, the embedding potential has the wrong form in the limit of a large separation of the subsystems. In particular, it was shown that this can have serious consequences in the case of FDE(s) calculations (`USEBASIS` option). In Ref. CJ7, a correction is proposed that enforces the correct long-distance limit (See also Ref. CJ7 for limitations of this correction).

- `CJCORR` [rho_cutoff]
  This option switches on the long-distance correction. This option has to be used in combination with one of the above kinetic-energy functionals. By default, a density cut-off of 0.1 is employed.

nonadditive exchange-correlation functional

By default, in the construction of the effective embedding potential the exchange-correlation functional that was specified in the `XC` block is used. It is possible to specify a different functional with the `GGAPOTXFD` and `GGAPOTCFD` options. This is particularly useful in combination with the use of model potentials like SAOP, that

can not be used in the embedding potential because of their orbital dependence (for a discussion, see Ref. CJ3).

- **GGAPOTXFD exchange functional**
  The exchange functional is used in the construction of the embedding potential. The same exchange functionals as in the XC key are available.

- **GGAPOTCFD correlation functional**
  The correlation functional is used in the construction of the embedding potential. The same correlation functionals as in the XC key are available.

integration grid

- **FULLGRID**

  By default, **FULLGRID** is not used, and in FDE calculations the integration grid is generated as described in Ref. CJ4 by including only atoms of the frozen system that are close to the nonfrozen system in the generation of the integration grid. The distance cutoff used is chosen automatically based on the extend of the basis functions of the nonfrozen system. (It can also be chosen manually, see the option qpnear in the **INTEGRATION** key.) This scheme results in a efficient and accurate integration grid. However, it is possible that the default integration scheme is not accurate enough. This can be the case for weakly interacting systems and when the distance between the frozen and the nonfrozen system is large. It is therefore recommended to check the quality of the default integration grid by comparing to results obtained using the full supermolecular grid (**FULLGRID** option).

  If the subkey **FULLGRID** is included all atoms of the frozen system are included in the generation of the integration grid. This results in the same grid that would be used in a supermolecular calculation of the combined frozen and nonfrozen system. The integration grid generated by this option might be much larger than the default grid. This option should be used to check the quality of the default integration grid.

freeze-and-thaw iterations

- **RELAXCYCLES n**
  Specifies the maximum number n of freeze-and-thaw iterations that are performed (for frozen fragments with the **RELAX**) option. If a smaller number of iterations is specified as a fragment-specific option, for this fragment this smaller number is used. Furthermore, if convergence is reached earlier, no more iterations will be performed.

- `RELAXPOSTSCF`
  If this option is included, several post-SCF properties will be calculated after each freeze-and-thaw cycle. These are otherwise only calculated in the last cycle.

A.5. Subfragments and superfragments

It is possible to apply the results of an FDE calculation as a fragments in another calculation. In this case, the frozen fragments and the active subsystem of the FDE calculation can be used separately. This might be useful for performing freeze-and-thaw cycles manually. However, this is an option for expert users only. In most common cases, it should be sufficient to apply the `RELAX` option and suitable fragment-specific options.

Suppose in the FDE calculation, two frozen fragments frozen1 and frozen2 have been used. If the results of this calculation are used in another calculation, three fragments are available: the active (nonfrozen) subsystem from the FDE calculation, and the two frozen fragments. These can be used as follows:

```
FRAGMENTS
  ...
  FragType1 FragFile [superfrag=FragType] subfrag=active
  FragType2 FragFile [superfrag=FragType] subfrag=frozen1
  FragType3 FragFile [superfrag=FragType} subfrag=frozen2
  ...
END
```

For all three fragments, the same fragment file (from the previous FDE calculation) has been used, and the subfrag option has been used to specify which fragment from this previous calculation should be used. The subfragment "active" refers to the active (nonfrozen) subsystem of the previous calculation. However, this active fragments can be composed of several nonfrozen fragments in this previous calculation. The subfragments "frozen1" and "frozen2" refer to frozen fragments with these names in the previous FDE calculations. In addition, it is of course possible to specify `type=FDE` for any of these three fragements, possibly also in combination with additional fragment-specific options.

If the same fragment file is used multiple times, the option superfrag can be used to specify which subfragments belong together. The subfragments that belong together will be rotated and translated as one fragment, i.e., the geometry of the total system from the previous calculation must not be changed. Therefore, also all parts of

this total system (the active subsystem and all frozen fragments) have to be used, otherwise this will result in an error.

If only some fragments of the previous FDE calculation (e.g., only the active subsystem) should be used, one has to include the key `ALLOW PARTIALSUPERFRAGS` in the input. However, in this case it could be that the rotation and translation is not unique, so that it is up to the user to ensure that the fragment has been handled correctly.

If in a previous FDE calculation a single frozen fragment `frozen` has been used, a manual freeze-and-thaw cycle can be performed using a `FRAGMENTS` block similar to the following:

```
FRAGMENTS
  frozen   FragFile subfrag=active type=FDE
  frag_bla FragFile subfrag=frozen
END
```

This means that the active fragment of the previous calculation (now called `frozen`) is used as a frozen fragment, while the previously frozen fragment (now called `frag_bla`) is used as nonfrozen fragment.

A.6. Restrictions and pitfalls

In the current implementation, only the electron density of the embedded system is calculated. Therefore, only properties that depend directly on the electron density (e.g., dipole moments) are available. In addition, the TDDFT extension allows the calculation of electronic excitation energies and polarizabilities, and NMR shieldings can be calculated.

Everything else is not yet implemented. In particular, interaction energies and energy gradients are not yet available.

Kinetic energy functional

Although the effective embedding potential is derived from first principles using universal density functionals, the ADF implementation relies on approximations. Currently, two implemented approximations are recommended:[40] PW91k, which uses electron densities and the corresponding gradients to express the non-additive kinetic energy component of the embedding potential, or TF (Thomas-Fermi LDA functional), which does not use gradients at all. Either approximation is applicable only

in cases where the overlap between electron densities of the corresponding interactions is small. Note: So far, no approximation has been developed for the strong-overlap case—two subsystem linked by covalent bonds for instance.

A.7. Examples

The complete input files for the examples given here can be found in the directories `examples/adf/FDE*` in the ADF distribution.

A.7.1. HeCO$_2$ freeze-and-thaw

This example demonstrates how a freeze-and-thaw FDE calculation can be performed. As test system, a He$\cdots$CO$_2$ van der Waals complex is used. It will further be shown how different exchange-correlation potential can be used for different subsystems, and how different basis set expansions can be employed. For details, see Ref. CJ3. It should be stressed that the basis set and integration grid used in this example are too small to obtain good results.

Part 1: PW91 everywhere

In the first part, the PW91 functional will be used for both the He and the CO$_2$ subsystems. In this part, the FDE(m) basis set expansion is used, i.e., basis functions of the frozen subsystem are not included in the calculation of the nonfrozen subsystem.

First, the CO$_2$ molecule is prepared. In this calculation, the C$_{2v}$ symmetry of the final complex is used, and the `NOSYMFIT` option has to be included because this molecule will be rotated as a frozen fragment.

```
$ADFBIN/adf   << eor
Title TEST 1 -- Preparation of frozen CO2

Units
 Length Bohr
end

Atoms
  C          0.000000  0.000000  0.000000
  O         -2.192000  0.000000  0.000000
  O          2.192000  0.000000  0.000000
end
```

```
Symmetry C(2V)
NOSYMFIT

Fragments
 C  t21.C
 O  t21.O
End

integration 5.0

xc
 GGA pw91
end

End Input
eor

mv TAPE21 t21.co2.0
```

Afterwards, the FDE calculation is performed. In this calculation, the He atom is the nonfrozen system, and the previously prepared CO_2 molecule is used as frozen fragment. For this frozen fragment the RELAX option is specified, so that the density of this fragment is updated in freeze-and-thaw iteration (a maximum number of three iteration is specified).

```
$ADFBIN/adf   << eor >> $SCM_TESTOUTPUT
Title TEST 1 -- Embedding calulation: He with frozen CO2 density -- freeze-and-thaw

Units
 Length Bohr
end

Atoms
 He   0.000000  0.000000  6.019000 f=He
 C    0.000000  0.000000  0.000000 f=co2
 O   -2.192000  0.000000  0.000000 f=co2
 O    2.192000  0.000000  0.000000 f=co2
end

Fragments
 He    t21.He
 co2  t21.co2.0  type=fde   &
   fdeoptions RELAX
 SubEnd
End

integration 5.0

xc
 GGA pw91
end
```

```
FDE
 PW91K
 FULLGRID
 RELAXCYCLES 3
end

End Input
eor
```

Part 2: SAOP for He; PW91 for CO_2

In this second part, the above example is modified such that PW91 is employed for the CO_2 subsystem, while the SAOP potential is used for He. This can be achieved by choosing SAOP in the `XC` key (this sets the functional that will be used for the nonfrozen subsystem). Additionally, for the frozen fragment the `XC` option is used to chose the PW91 functional for relaxing this fragment. Furthermore, the PW91 functional is chosen for the nonadditive exchange-correlation functional that is used in the embedding potential with the `GGAPOTXFD` and `GGAPOTCFD` options in the `FDE` key.

```
$ADFBIN/adf   << eor >> $SCM_TESTOUTPUT
Title TEST 2 -- Embedding calulation: He with frozen CO2 density -- freeze-and-thaw

Units
 Length Bohr
end

Atoms
 He   0.000000  0.000000  6.019000 f=He
 C    0.000000  0.000000  0.000000 f=co2
 O   -2.192000  0.000000  0.000000 f=co2
 O    2.192000  0.000000  0.000000 f=co2
end

Fragments
 He   t21.He
 co2  t21.co2.0  type=fde   &
   fdeoptions RELAX
   XC         GGA PW91
 SubEnd
End

integration 5.0

xc
 MODEL SAOP
end
```

```
FDE
 PW91K
 FULLGRID
 GGAPOTXFD PW91x
 GGAPOTCFD PW91c
 RELAXCYCLES 3
end

End Input
eor
```

Part 3: FDE(s) calculation with PW91 everywhere

In this third part, the PW91 functional is applied for both subsystems again, but in contrast to part 1, now the FDE(s) basis set expansion is used, i.e., the basis functions of the frozen subsystem are included in the calculation of the nonfrozen subsystem. This can be achieved by employing the USEBASIS option. This option can be combined with the RELAX option.

```
$ADFBIN/adf   << eor >> $SCM_TESTOUTPUT
Title TEST 3 -- Embedding calulation: He with frozen CO2 density -- freeze-and-thaw

Units
 Length Bohr
end

Atoms
 He    0.000000  0.000000  6.019000 f=He
 C     0.000000  0.000000  0.000000 f=co2
 O    -2.192000  0.000000  0.000000 f=co2
 O     2.192000  0.000000  0.000000 f=co2
end

Fragments
 He    t21.He
 co2   t21.co2.0  type=fde   &
   fdeoptions RELAX USEBASIS
 SubEnd
End

integration 5.0

xc
 GGA pw91
end

FDE
```

```
 PW91K
 FULLGRID
 RELAXCYCLES 3
end

End Input
eor
```

A.7.2. Excitation energies for H_2O surrounded by 127 H_2O

This example demonstrates how to use FDE in combination with a large environment, that is modeled as a superposition of the densities of isolated molecules. Here, the excitation energies of a water molecule surrounded by an environment of 127 water molecules. For details, see Ref. CJ5.

First, a prototype water molecule is calculated. The density of this isolated water molecules will afterwards be used to model the environment. Since this molecule will be used as a frozen fragment that is rotated and translated, the option NOSYMFIT has to be included.

```
$ADFBIN/adf << eor
Title Input generated by modco

UNITS
  length bohr
END

XC
  LDA
END

INTEGRATION 5.0 5.0

FRAGMENTS
  O  t21.DZP.O
  H  t21.DZP.H
END

ATOMS
 O     -11.38048700000000    -11.81055300000000    -4.51522600000000
 H     -13.10476265095705    -11.83766918322447    -3.96954531282721
 H     -10.51089289290947    -12.85330720999229    -3.32020577897331
END

NOSYMFIT

ENDINPUT
eor
```

```
mv TAPE21 t21.mol_1
```

Afterwards, the FDE calculation is performed. In this FDE calculation, there is one nonfrozen water molecule and the previously prepared water molecule is included as a frozen fragment that is duplicated 127 times. For this frozen fragment, the more efficient fitted density is used.

```
$ADFBIN/adf << eor

UNITS
  length bohr
END

XC
  MODEL SAOP
END

EXCITATION
  ONLYSING
  LOWEST  5
END

INTEGRATION 4.0 4.0

FRAGMENTS
  O     t21.DZP.O
  H     t21.DZP.H
  frag1  t21.mol_1 type=fde &
    fdedenstype SCFfitted
  SubEnd
END

ATOMS
  O      0.00000000000000      0.00000000000000      0.00000000000000
  H     -1.43014300000000      0.00000000000000      1.10739300000000
  H      1.43014300000000      0.00000000000000      1.10739300000000
  O    -11.38048700000000    -11.81055300000000     -4.51522600000000    f=frag1/1
  H    -13.10476265095705    -11.83766918322447     -3.96954531282721    f=frag1/1
  H    -10.51089289290947    -12.85330720999229     -3.32020577897331    f=frag1/1
  O     -1.11635000000000      9.11918600000000     -3.23094800000000    f=frag1/2
  H     -2.82271357869859      9.71703285239153     -3.18063201242303    f=frag1/2
  H     -0.12378551814273     10.53819303003839     -2.70860866559857    f=frag1/2
  O    -16.96901200000000     -3.65835300000000    -10.78571300000000    f=frag1/3
  H    -15.70823656958949     -4.23996689198245     -9.62648920152293    f=frag1/3
  H    -16.47814038897754     -4.36080868684451    -12.37857352487904    f=frag1/3
...
...
...
  O      5.96480100000000      4.51370300000000      3.70332800000000    f=frag1/127
  H      5.24291272273548      3.06620845434369      2.89384293177905    f=frag1/127
```

```
 H         4.73614594944492      5.00201400735317      4.93765482424434     f=frag1/127
END


FDE
  PW91K
END


ENDINPUT
eor
```

A.7.3. NMR shielding for acetonitrile in water

This examples demonstrates both the calculation of NMR shieldings using FDE, and how the approximate environment density can be improved by partial relaxation of individual solvent molecules. The test system is a cluster of acetonitrile and 12 solvent water molecules, of which for two the densities are relaxed, while for the remaining 10 the frozen density of the isolated water is used. For details, see Refs. CJ9, 167.

First, the isolated solvent water molecule is prepared. Again, because this will be rotated and translated afterwards, the option NOSYMFIT has to be included.

```
$ADFBIN/adf << eor

 UNITS
   Length Angstrom
 END

 ATOMS
      O       -1.46800       2.60500       1.37700
      H       -0.95200       3.29800       0.96500
      H       -1.16100       1.79900       0.96100
 END

 FRAGMENTS
   H        t21.H.DZP
   O        t21.O.DZP
 END

 XC
   LDA
 END

 INTEGRATION 4.0

end input
eor

mv TAPE21 t21.h2o
```

Afterwards, the FDE calculation is performed. In addition to the nonfrozen acetonitrile molecule, three different fragments are used for the solvent water molecules. The first two fragments `frag1` and `frag2` are relaxed (in up to two freeze-and-thaw cycles), while the third fragment is used for the remaining 10 solvent molecules. Since a calculation of the shielding is performed afterwards, the option `SAVE TAPE10` has to be included.

```
$ADFBIN/adf << eor >> $SCM_TESTOUTPUT

 UNITS
   Length Angstrom
 END

 ATOMS
      C      0.83000       0.66100      -0.44400
      N      0.00000       0.00000       0.00000
      C      1.87800       1.55900      -0.81900
      H      1.78500       2.40300      -0.13500
      H      1.76200       1.94900      -1.83000
      H      2.82900       1.12200      -0.51300
      O     -1.46800       2.60500       1.37700    f=frag1
      H     -0.95200       3.29800       0.96500    f=frag1
      H     -1.16100       1.79900       0.96100    f=frag1
      O      2.40400      -2.51000      -0.36200    f=frag2
      H      2.70000      -3.41900      -0.40900    f=frag2
      H      1.77500      -2.50000       0.35900    f=frag2
      O     -3.22800      -1.61500       1.18500    f=frag3/1
      H     -3.33300      -2.55300       1.03000    f=frag3/1
      H     -3.14200      -1.23600       0.31000    f=frag3/1
...
...
...
      O     -3.44400       2.36700       3.13700    f=frag3/10
      H     -2.70200       2.29200       2.53700    f=frag3/10
      H     -3.47300       3.29500       3.36800    f=frag3/10
 END

 FRAGMENTS
   H        t21.H.DZP
   C        t21.C.DZP
   N        t21.N.DZP
   frag1  t21.h2o   type=FDE  &
     fdeoptions RELAX
     RELAXCYCLES 2
   SubEnd
   frag2  t21.h2o   type=FDE  &
     fdeoptions RELAX
     RELAXCYCLES 2
   SubEnd
   frag3  t21.h2o   type=FDE  &
     FDEDENSTYPE SCFfitted
   SubEnd
```

```
 END

 XC
   GGA BP86
 END

 INTEGRATION 4.0

 SAVE TAPE10

 FDE
   PW91k
 END

End Input
eor
```

Finally, the calculation of the NMR shielding of the nitrogen atom is performed using the Nmr program.

```
$ADFBIN/nmr << eor >> $SCM_TESTOUTPUT
 NMR
  out tens iso
  nuc 3
 END
eor
```

B. ADF NewFDE Code Documentation

B.1. Introduction

This document gives a technical overview of the new implementation of frozen-density embedding (FDE) in the ADF program package. The new and unique features of the implementation are discussed in Ref. CJ9 and in the User's Guide (see Appendix A) and, therefore, this document will only focus on the technical aspects. It is mainly intended for those who plan to maintain, improve and extend the code in the future and those who want to make use of the flexible infrastructure it provides in other parts of ADF.

The main feature of the new FDE implementation is the flexible, fragment-based setup that allows it to employ any number of frozen fragments. This flexible setup required a large rewrite of the way in which fragments are represented in ADF. For this purpose, abstract data types (ADTs) representing these fragments have been introduced. These contain all relevant information about a fragment, such as, e.g., its geometry, the corresponding basis and fit functions, or its fit and molecular orbital coefficients. An overview of these ADTs will be given in Sec. B.2.

In Section. B.3 it is explained how the fragment ADTs are initialized and finally, in Sec. B.4, an overview of the most important subroutines of the new FDE implementation is given. Further information on the implementation described here can be found in the detailed comments contained in the code.

B.2. Abstract data types

The new implementation makes use of abstract data types (ADTs) for representing fragments. Each ADT is a Fortran type structure containing a number of related variables (attributes). This type is contained within a module, together with subroutines for manipulating it (methods). Usually, the attributes are not supposed to

be modified directly, but its methods should be used instead. These can then, for instance, ensure that all data is consistent and take care of memory management.

The central ADT of the new FDE implementation is `FragmentType`, which represents a fragment. It relies on a number of other ADTs, which are used for storing the different data that is required for a fragments (such as, e.g., its geometry, its basis and fit functions, or its MOs). The ADT `FragmentsArrayType` is used to store instances of `FragmentType`, that represent all the required fragments. Figure B.1 gives a schematic overview of the most important attributes of `FragmentsArrayType`, of `FragmentType`, and of the ADTs they rely on. Even though the ADTs described here have been introduced to make the new FDE implementation possible, their use is not limited to FDE calculations. They are already now used in all kinds of ADF calculations, and they can be employed in the future to rewrite other parts of ADF in a more modular way.

All ADTs described below contain an attribute `id`, which is used as an identifier in ADF's memory management (in particular in `chckmem`). For the attributes, it has been tried to use names that are as descriptive as possible. However, for variables that are also present as global variables in other places, the same names as for these global variables have been used. In most ADTs, some attributes have been marked as *"Extras"*. These attributes contain information that can be calculated in a simple way from the other attributes. These are updated whenever the variables they depend on are changed using a special method (usually `initExtras`).

All ADTs come with a `new` method, a `newCopy` method, and a `delete` method[a], which are used as constructor, copy constructor, and destructor, respectively, and an assignment operator (=) has been defined for them. For most ADTs, the methods `saveBla` and `readBla` are defined, which can be used to save the data contained in the ADT to file (TAPE21) and to read it in from file, respectively.

FragmentsArrayType

An instance of `FragmentsArrayType` is used to store all fragments that are required during an ADF calculation.

The list of the initial fragments is stored in the array `fragments`, with each initial fragment represented by a `FragmentType`. The method `getFragmentByIndex` can be used to obtain a pointer to a fragment by giving its index. Similarly, `getFragmentByName` can be used to obtain a pointer to a fragment by giving its fragment type. To loop over all initial fragments, a construction similar to the following can be used:

---

[a]The names of these methods might be changed in the future, in order to be consistent with ADF's new programming rules.

Figure B.1.: Schematic overview of the most important attributes of `FragmentsArrayType`, `FragmentType`, and the ADTs they rely on.
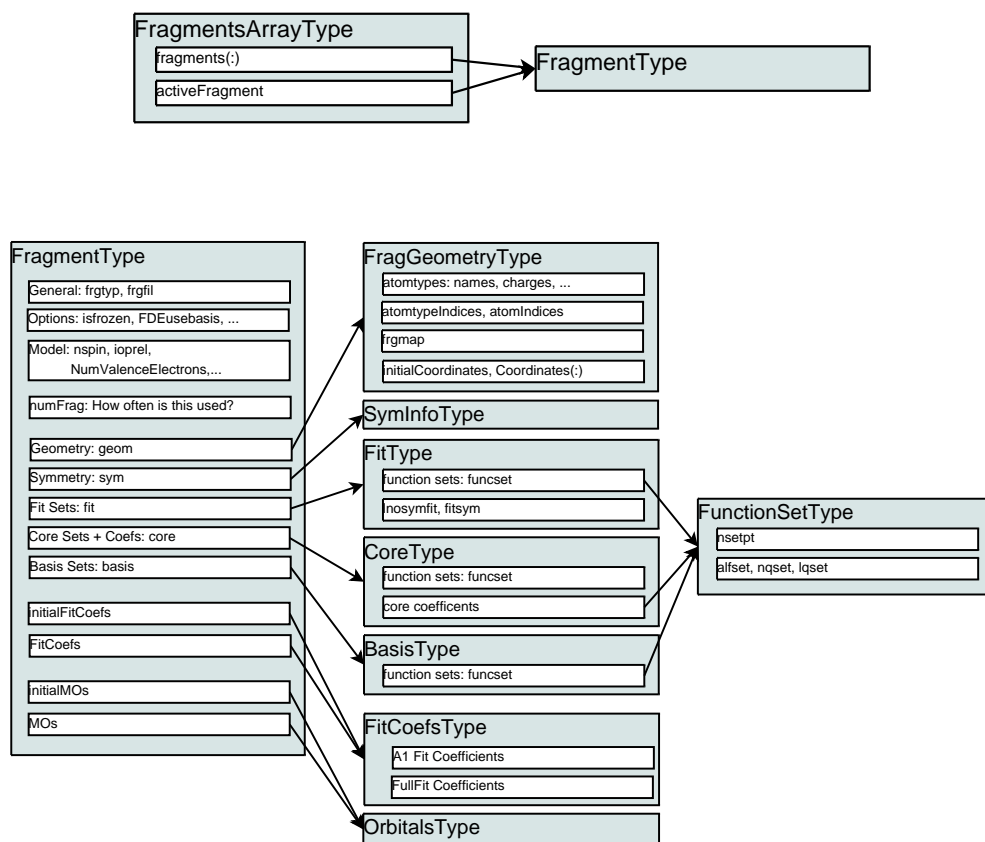
```
type(FragmentType), pointer :: frag
...
do iftyp = 1, fragarray%nftyp
   frag => getFragmentByIndex(fragarray, iftyp)
   if (frag%isInactive) cycle

   [do something with frag]

end do
```

In addition to the list of the initial fragments, the *"active fragment"* is stored in `activeFragment`. This active fragment represents the system on which the actual calculation is performed. It is composed of all nonfrozen initial fragments. The active fragment stores information that is similar to that previously (or still) stored in global variables. As far as they are still present, these global variables now duplicate information that is also present in the active fragment (see also Section B.3.4).

Further important methods are:

- `addFragment`:
  inserts a new initial fragment into the array `fragments`

- `readFragments`, `readFragmentsCreateMode`:
  reads the information about the initial fragments from the fragment file (or in CREATE mode, from the atomic data file). See Section B.3.1.

- `initFragmentGeometries`, `initAtomtypeIndices`:
  initialization of the geometries of the initial fragments, see Sections B.3.1 and B.3.2.

- `initActiveFragment`, `initActiveFragmentSymmetry`, `initActiveFragmentA1Fit`, `initActiveFragmentOrbitals`:
  initialization of the active fragment, see Section B.3.3.

FragmentsType

A fragment is represented by an instance of `FragmentType`, which stores all information needed for a fragment during an ADF calculation. A fragment is identified by its type, stored in `frgtyp`, and is usually associated with a fragment file, given in `frgfil`.

One instance of `FragmentType` represents one *initial* fragment, which can be used multiple times in the overall molecule. In this case, the initial geometry of the frag-

ment is mapped onto the geometries of the different appearances of the fragment in the overall molecule by suitable translations and rotations (compare also the general documentation of ADF). The attribute `numFrag` gives the number of copies of the initial fragment that are used in the overall molecule. `FragmentType` stores both information on the initial fragment and on the rotated copies of it (this mainly concerns the atomic coordinates and the fit and MO coefficients).

The number of valence electrons in the fragment is given by `numValenceElectrons` (and separately for alpha and beta spin in `numValenceElectronsPerSpin`), and the charge of the fragment is given by `charge`. Further attributes contain general options relevant for the electronic structure of the fragment, such as `nspin`, `lzora`, and `lspinorbit`.

The option `isInactive` is true if the fragment is *inactive*, which means that it will be ignored when setting up the active fragment (see also Section B.4.5). Whether the fragment is a frozen FDE fragment is specified by the attribute `isFrozen`. Further attributes with names starting with `FDE` contain additional FDE-related options.

Further attributes of `FragmentType` are:

- `geom`:
  fragment geometry (using `FragGeometryType`)

- `sym`:
  symmetry information (using `SymInfoType`)

- `basis`:
  basis functions (using `BasisType`)

- `fit`:
  fit functions and A1 fit combinations (using `FitType`)

- `core`:
  frozen core functions and coefficients (using `CoreType`)

- `initialFitCoefs`:
  fit coefficients of the initial fragment (using `FitCoefsType`)

- `FitCoefs`:
  fit coefficients of the rotated fragments (using `FitCoefsType`)

- `initialMOs`:
  MO coefficients of the initial fragment (using `OrbitalsType`)

- `MOs`:
  MO coefficients of the rotated fragments (using `OrbitalsType`)

FragGeometryType

`FragGeometryType` stores the data related to the geometry of a fragment. This includes the information on the atom types, such as their names (in `atmtyp`), their charges (total charge in `atomtypeTotalCharge`, and effective charge in `atomtypeEffectiveCharge`), and their masses (in `atmmass`)

The atomic coordinates of the initial fragment are store in `initialCoordinates`, and those of the rotated fragments in `Coordinates`. The affine transformations relating the coordinates of the initial fragment to those of the rotated fragments are kept in `frgmap`.

Furthermore, the arrays `atomtypeIndices` and `atomIndices` give the mapping between the atom types and the atoms in this fragment and those in the overall geometry, respectively (see also Sections B.3.1 and B.3.2).

SymInfoType

`SymInfoType` keeps the information related to the symmetry of a fragment. In particular, the Schönfliess symbol of the point group is given in `grouplabel`, and the labels of its irreducible representations in the array `bb`. Furthermore, information on the symmetry-equivalent atoms is kept in the attributes `nsetat`, `nratst`, `noat`, and `notyps`.

BasisType

`BasisType` stores the information on the basis set of a fragment. It uses an instance of `FunctionSetType` in `funcset` to store the basis functions. Furthermore, the attributes `bradtypint` and `bradint` contain the "radii" of the basis functions, which are used to achieve linear scaling.

FitType

`FitType` stores the fit functions as well as the A1 fit combinations of a fragment. It uses an instance of `FunctionSetType` in `funcset` to store the fit functions. As for the basis set, the attributes `fradtypint` and `fradint` contain the "radii" of the fit functions, which are used to achieve linear scaling.

A number of additional attributes is used to keep the A1 fit combinations. Information

on the meaning of these variables can be found in the comments in the subroutine `symfit` and in the general documentation of ADF.

In the attribute `sym` an instance of `SymInfoType` is used to store the symmetry that has been used for generating the A1 fit combinations. This is not always the same as the symmetry of the fragment because in a number of cases symmetry can not be used in the fit (e.g., in TD-DFT calculations).

CoreType

`CoreType` contains the information on the frozen cores of a fragment. It uses an instance of `FunctionSetType` in `funcset` to store the core functions, and the array `ccor` contains the corresponding core coefficients.

FunctionSetType

`FunctionSetType` stores information on a set of Slater-type atomic orbitals (these can be used as basis functions, core functions, or fit functions). The index array `nsetpt` identifies which functions in this set belong to which atom type, and `nqset`, `lqset`, and `alfset` store for each function the n and l quantum numbers and the exponent α, respectively.

Several attributes, which can be calculated from the above refer to a different representation of the set of functions, in which each Cartesian component is listed separately (`nsptr`, `kx`, `ky`, `kz`). In addition, the normalization constants (in `setnrm`) and the integrals of the functions (in `Integral`) are stored.

FitCoefsType

`FitCoefsType` is used for storing the fit coefficients, both of the full Cartesian fit functions (in `fullfit`) and of the A1 fit combinations (in `fita1`). It provides methods for reading in these coefficients and takes care of the conversion between these two representations (using the methods `ConvertFullfitToA1fit` and `ConvertA1fitToFullfit`).

`OrbitalsType` and related ADTs

`OrbitalsType` is used for storing MO coefficients. In `irreps` it keeps for each irreducible representation (irrep) of the point group of the molecule the coefficients of the corresponding MOs using `IrrepOrbitalsType`.

`IrrepOrbitalsType` stores the coefficients of the MOs in one irrep. In `bb`, the symmetry label of the irrep in question is stored and the array `npart` keeps a list of the basis functions that participate in the MOs of this irrep (the coefficients are kept only for these functions). In `sp`, the MO coefficients are kept using `SpinOrbitalsType`. For spin-unrestricted calculations, two instance of `SpinOrbitalsType` are used to keep the MO coefficients for alpha and beta spin.

`SpinOrbitalsType` finally stores the MO coefficients in the array `eigbas`, the orbital energies in `eps`, and the occupations numbers in `froc`.

In calculations that include spin-orbit coupling, the situation is complicated by the use of double group symmetry. In this case, the MO coefficients for one irrep are not stored in the attribute `sp` of `IrrepsOrbitalsType`, but instead the array `relorbs` keeps a list of `RelSpinOrbitalsType` for each relativistic symmetry and for each spin.

`RelSpinOrbitalsType` stores the real and imaginary MO coefficients in calculations including spin-orbit coupling in `eigbasr` and `eigbasi`, respectively. In addition, the orbital energies are kept in `epsr`, and the occupation numbers in `frocr`.

B.3. Initialization of fragments

In the main program of ADF (source code file `adf.d`), an instance of `FragmentsArrayType` is created, which is passed as an argument to all relevant subroutines of ADF. This FragmentsArray contains both the list of the initial fragments in the array `fragments`, and the active fragment, which is the system that is used in the actual calculation (i.e., the nonfrozen subsystem composed of all nonfrozen fragments), in `activeFragment`.

In the following, the several steps in the initialization of the initial fragments in `fragments` and of the active fragment in `activeFragment` are explained. An overview of these steps and of the relevant subroutines is given in Table B.1.

Table B.1.: Overview of the steps and the relevant subroutines in the initialization of the global FragmentsArray

initialization of	called from	relevant subroutine(s)
global instance of FragmentsArrayType	main program (adf.d)	newFragmentsArray
initial fragments (number, types, ...)	geoinp	ftypes initAtomtypeIndices frgfls rqfrag
initial fragments (data from fragment files)	geoinp	readFragments readFragmentsCreateMode
rotated initial fragments	geofrg, DoSinglePoint	initFragmentGeometries rotateFitCoefs rotateMOs
active fragment (geometry, basis, fit, ...)	geofrg, fragm, DoSinglePoint	initActiveFragment
active fragment (electronic configuration)	DoSinglePoint	initElectronicConfiguration
active fragment (symmetry, A1 fit, MOs)	DoSCFPreps	initActiveFragmentSymmetry initActiveFragmentA1Fit initActiveFragmentOrbitals
global variables	fragm	inputf

B.3.1. Initialization of the initial fragments

The initialization of the initial fragments is called from the subroutine `geoinp`, where the geometry and related information are read from the input file. First, the subroutine `ftypes` determines the number of fragments that are present and their types from the `ATOMS` input key and initializes the `FragmentType`s in the list of initial fragments (the array `fragments`). Next, the subroutines `frgfls` and `rqfrag` read the `FRAGMENTS` input key and initialize the names of the corresponding fragment files as well as the other fragment settings specified there. In particular, the fragment-specific FDE options are read in `rqfrag` and the corresponding attributes of the initial fragments are initialized accordingly.

In the following step, for all initial fragments the `atomtypeIndices` and `atomIndices` (of the fragment geometry `geom`) are set up in the subroutine `initAtomtypeIndices`. This subroutine employs the information read from the `ATOMS` block earlier to save for each atom type and for each atom of the initial fragments the number of the corresponding atom / atom type in the overall geometry (as it is stored in an instance of `GeometryType`).

Finally, the subroutine `readFragments` is used to read the information on the initial fragments from the fragment files. This includes the geometry of the fragment (atomic charges, and masses, and atomic coordinates of the initial fragment), the basis functions, core functions and coefficients, fit functions, as well as the fit coefficients and MOs of the initial fragment. For reading this data, the `readBla` methods of the corresponding ADTs are used.

In CREATE mode (when an initial atomic fragment is created), `ReadFragments-CreateMode` is used instead, which relies on the `readBlaCreateMode` methods of the corresponding ADTs. Instead of reading the data from a fragment files, this will read the required information from the CREATE atomic data file.

B.3.2. Initialization of the fragment geometries

After the atomic coordinates of the fragments, as they were initially oriented during their creation, have been read in from the corresponding fragment file (to `geom%initialCoordinates`), and the indices of the corresponding atom types and atoms in the overall geometry (`geom%atomTypeIndices` and `geom%atomIndices`) have been initialized, the subroutine `initFragmentGeometries` is used to initialize the coordinates of the fragments as they are oriented in the overall geometry (`geom%Coordinates`).

The subroutine `initFragmentGeometries` takes as arguments the `FragmentsArray-`

`Type` containing the list of initial fragments and the `GeometryType` giving the overall geometry. For each fragment, it then initializes the coordinates of the atoms in the rotated fragments (`geom%Coordinates`) to those of the corresponding atoms in the overall geometry. By comparing the initial coordinates of the fragment (`geom%initial-Coordinates`) to those of the rotated copies of the fragment (`geom%Coordinates`), the affine transformations (rotation matrices and translation vectors) in `frgmap` are set up. Note that one initial fragment, represented by one `FragmentType`, can be used multiple times (see the attribute `NumFrag`), i.e., there can be more than one affine transformation per initial fragment.

Using `frgmap`, the initial fit coefficients (`initialFitCoefs`) are then rotated to those of the rotated fragments (`FitCoefs`) by the subroutine `rotateFitCoefs`. Similarly, the subroutine `rotateMOs` is used to rotate the initial MO coefficients `initialMOs` to those of the rotated fragments (`MOs`).

B.3.3. Initialization of the active fragment

After the initial fragments (in the array `fragments`) have been initialized, the subroutine `initActiveFragment` is used to initialize the active fragment (in `activeFragment`). The active fragment is assembled by adding all nonfrozen fragments, i.e., the active fragment is a single fragment containing all nonfrozen fragments.

The geometry, basis functions, fit functions, core functions and core coefficients, as well as the initial fit coefficients are obtained by adding those of the nonfrozen initial fragments. This is done by employing the `addBla` methods of the corresponding ADTs. For frozen fragments for which the `USEBASIS` option has been specified, the basis functions and fit functions are also included in the active fragment, but the electrons and the nuclear charges of the frozen fragments are not included.

However, not all information on the active fragment can be obtained by a simple "addition" of the initial fragments. In particular everything that is related to the symmetry of the active fragment (symmetry information, A1 fit combinations, MO information) has to be initialized considering the full active fragment. Since the symmetry handling of ADF is currently very cumbersome, these steps have not been rewritten to use the newly introduced ADTs. Instead, these subroutines still operate on global variables and the corresponding parts of the active fragment are initialized by copying the needed information from the global variables initialized by these subroutines.

Therefore, after `initActiveFragment` has initialized the active fragment, some other subroutines have to be called to initialized the remaining parts. To initialize the electronic configuration of the active fragment (in particular the number of alpha

and beta electrons in spin-unrestricted calculations), `initElectronicConfiguration` has to be called. The symmetry information of the active fragment (in `sym`) can be initialized using `initActiveFragmentSymmetry` after the symmetry information in the global variables has been set up by `maisya`. The A1 fit combinations (a part of `fit`) are set up by `initActiveFragmentA1Fit` after the A1 fit combinations have been obtained by `symfit`, and the MOs of the active fragment (in `initialMOs` and `MOs`) are initialized by `initActiveFragmentOrbitals`, after the symmetrized MO combinations have been obtained by `symorb`.

B.3.4. Initialization of global variables

Even though this would be desirable, the newly introduced ADTs are currently not used in all parts of ADF, and a large number of subroutines still relies on data in global variables instead. These global variables are initialized by the subroutine `inputf`, which uses the data stored in the active fragment for this purpose. This way, it is ensured that both the active fragment and the global variables contain the same information and can be used alongside.

In this step, care has to be taken in the conversion between variables in the active fragment ADT and those in global variables. The latter always contain all atoms and atom types that are present in the overall geometry, while the active fragment only contains atoms and atom types of the nonfrozen fragment. Therefore, different numberings are used for the atoms and atom types, and the mapping between them is given by `geom%atomIndices` and `geom%atomtypeIndices`, respectively. In `inputf` and also in `initActiveFragmentSymmetry`, `initActiveFragmentA1Fit`, and `initActiveFragmentOrbitals` these different numberings are considered. Details can be found in the comments in the code.

B.3.5. Initialization passes

The initialization of the fragments described above is performed in several passes. An overview of the different steps in this process is given in Table B.2.

The first stage of the initialization is performed only once at the beginning of ADF. In this step, the initial fragments are read in, their geometries are initialized, and the active fragment is set up for the first time (except for the parts that depend on the symmetry information).

Each time, the initial fragments change (e.g., when performing freeze-and-thaw iterations in an FDE calculation), `DoInits` must be called. This will re-initializes the

Table B.2.: Summary of the different initialization passes that are used to set up the global FragmentsArray

initialization stage	called from	initialized parts
once at the start	`geomet` (`geoinp, geofrg`)	initial fragments (including rotated initial fragments) active fragment (except for symmetry, A1 fit, MOs)
each time the fragments changed	`DoInits` (`fragm`)	active fragment (except for symmetry, A1 fit, MOs) global variables
each time the geometry changed	`DoSinglePoint`	rotated initial fragments active fragment (except for symmetry, A1 fit, MOs)
before the SCF procedure	`DoSCFPreps`	active fragment (symmetry, A1 fit, MOs)

active fragment by calling `initActiveFragment`, and the global variables are initialized again using `inputf` using the new active fragment.

Each time the overall geometry changes (e.g., in a geometry optimization), the geometries of the rotated initial fragments are re-initialized by calling `initFragmentGeometries`, and subsequently, the active fragment is initialized again using `initActiveFragment` to update its geometry. These initialization steps are invoked at the beginning of `DoSinglePoint`.

Finally, in the preparation for the SCF procedure, `DoSCFPreps` invokes the initialization of the parts of the active fragment that rely on data in global variables (i.e., the symmetry information, the A1 fit combinations, and the MOs).

B.4. Important FDE subroutines

In this section, a brief overview of the most important subroutines of the FDE implementation is given, and it is briefly explained how these subroutines work and how they can be used in future developments. Most of the subroutines mentioned below rely on other subroutines, details can be found in the code itself and in the comments contained within the code.

In particular, the input reading and initialization of the global FDE options will be discussed, followed by a description of the subroutine relevant for the construction of the integration grid in FDE calculations. Furthermore, the construction of the frozen density and of the individual terms of the embedding potential will be explained. Finally, the subroutine responsible for performing freeze-and-thaw iterations (`RELAX` option) is briefly discussed. An overview of the subroutines described here is given in Table B.3.

B.4.1. Input reading and initialization

All general initialization that is specific to FDE calculations is performed in the `FrozenDensity` module. This module also contains the global variables which store general setting related to FDE (such as the kinetic-energy functional used, and other options chosen in the `FDE` input key).

The subroutine `InitFrozen` initializes these variables to default values. It should be called in all calculations and from all programs using libtc. The initializations specific to FDE calculations are invoked from the subroutine `InputFrozen`, which is called by ADF at the very beginning of all calculations when the input file is processed.

Table B.3.: Overview of the important subroutines of the FDE implementation

task	subroutine	relies on
initialization	InitFrozen	
	InputFrozen	ReadFrozenKey
		PrintFrozenInfo
grid generation	genptFD	genpt
construction of frozen density	GetFrozenDensity	GetFittedFragmentDensity
		GetExactFragmentDensity
evaluation of constant parts of embedding potential	CalcConstantPotentials	CalcNuclearPotential
		CalcCorePotential
		CalcFrozenElectronPotential
evaluation of ρ_I-dependent parts of embedding potential	embinscf	CalcNonadditiveXCPotential
		CalcKineticEnergyPotential
freeze-and-thaw iterations	DoEmbeddingSCF	DoInits, DoSCF

It checks for the `FDE` input key and in case this is present, calls `ReadFrozenKey` for processing it. Any new FDE input options should be added in this subroutine. The FDE header and related output are printed by the subroutine `PrintFrozenInfo`.

The FDE-related processing of other part of the input file (in particular of the `FRAGMENTS` input key) as well as the initialization of the fragment ADTs is explained in the previous section.

B.4.2. Generation of the integration grid

The generation of the integration grid in FDE calculations relies on the subroutine `genpt`, which is also employed in standard ADF calculations. This subroutine takes a arguments a `FragmentType` specifying the active fragment, for which the integrations grid is constructed (only the geometry and basis and fit function information will be used). In addition, a list of point charges can be given, which will also be considered in the construction of the integration grid. However, for point charges, additional integration points will only be generated when they are not too far away (the cut-off depends of the most diffuse basis function used) from the atoms in the active fragment.

In FDE calculations, the wrapper routine `genptFD` is used to control the generation of the integration grid. This subroutines calls `genpt` which a suitable active fragment and point charges.

In the case the option `ONEGRID` is used, only the nonfrozen subsystem will be used as active fragment for the generation of the integration points, resulting in an integration grid that is centered on the nonfrozen subsystem only. However, this is usually not sufficient to integration the nuclear attraction part of the embedding potential accurately.

If the option `FULLGRID` is used, all fragments (frozen and nonfrozen) are added to a temporary "total fragment" which is then used as the active fragment in the generation of the integration grid. This results in an integration grid that extends over both the nonfrozen and the frozen fragments and that is identical to the grid that would be employed in a supermolecular calculation. However, while this can be useful for benchmarking, such an integration grid is usually too large.

For the generation of the default grid for FDE calculation,[CJ4] the nonfrozen subsystem only is used as the active fragment in the generation of the integration points. In addition, point charges corresponding to all atoms in the frozen fragments will be added to the list which is passed to `genpt`. This will result in the use of the defaults for point charges for the frozen fragments, leading to an integration grid centered on the nonfrozen system, which included additional integration points only for atoms of

the frozen environment which are close to the nonfrozen subsystem.

In the case that freeze-and-thaw cycles are performed (i.e., the `RELAX` option is used for one ore more fragments), a new integration grid will be generated before each freeze-and-thaw cycles, i.e., each time another nonfrozen subsystem is used.

B.4.3. Construction of the frozen density

The frozen density, which is needed for the evaluation of the nonadditive kinetic-energy component and of the nonadditive exchange-correlation component of the embedding potential, is constructed using the subroutine `GetFrozenDensity`.

This subroutine calculates the frozen density, and—if requested—its first and second derivatives, in a block of integration points. It loops over all frozen fragments and calculates (depending on the `FDEdenstype` attribute of the fragments) either the exact or the fitted density of each fragment using `GetExactFragmentDensity` or `GetFittedFragmentDensity`, respectively. The densities of these individual fragments are then added.

Both `GetExactFragmentDensity` and `GetFittedFragmentDensity` employ distance cut-off to achieve linear-scaling of the construction of the fragment densities,[CJ4,125] and fragments that are too far away from the current block of integration points are skipped completely. Usually, the construction of the fitted density is faster than the construction of the exact density (roughly by a factor of 2).

Depending on the argument `nspin`, either an unrestricted or a restricted frozen density is constructed. In case a spin-unrestricted fragment is used in the construction of a spin-restricted frozen density, the spin densities are added. Similarly, in the case of a spin-restricted calculation in the construction of a spin-unrestricted frozen density calculation, the fragment density is distributed equally over both spins.

Finally, to avoid problems with inaccurate fit densities, it is ensured that the resulting frozen density is non-negative in all grid points.

B.4.4. Construction of the embedding potential

The FDE embedding potential for the (nonfrozen) subsystem i due to all other (frozen) subsystems $j \neq i$ is given by,

$$
\begin{aligned}
v_{\text{emb}}^{(i)}[\rho_1, \ldots, \rho_N] = &\sum_{j \neq i} v_j^{\text{nuc}}(\boldsymbol{r}) + \sum_{j \neq i} \int \frac{\rho_j(\boldsymbol{r}')}{|\boldsymbol{r} - \boldsymbol{r}'|} d\boldsymbol{r}' \\
&+ \left. \frac{\delta E_{\text{xc}}[\rho]}{\delta \rho} \right|_{\rho = \rho_{\text{tot}}(\boldsymbol{r})} - \left. \frac{\delta E_{\text{xc}}[\rho]}{\delta \rho} \right|_{\rho = \rho_i(\boldsymbol{r})} \\
&+ \left. \frac{\delta T_s[\rho]}{\delta \rho} \right|_{\rho = \rho_{\text{tot}}(\boldsymbol{r})} - \left. \frac{\delta T_s[\rho]}{\delta \rho} \right|_{\rho = \rho_i(\boldsymbol{r})},
\end{aligned}
\tag{B.1}
$$

where $\rho_{\text{tot}} = \sum_i \rho_i$. It consists of the potential of the nuclei in the frozen subsystems, the Coulomb potential of the electron densities of the frozen subsystems, a nonadditive exchange-correlation component and a nonadditive kinetic-energy component. The first two parts (i.e., the nuclear and the electric Coulomb potentials) are constant during the SCF procedure for the nonfrozen subsystem and thus only have to be determined once. However, the exchange-correlation and the kinetic-energy component depend on the electron density of the nonfrozen subsystem and, therefore, have to be evaluated in each SCF cycle.

The constant parts of the embedding potential are evaluated together with the other constant parts of the total potential (nuclear potential of the nonfrozen subsystem, potential due to point charges and electric field) in the subroutine `CalcConstantPotentials`. This makes use of the subroutines `CalcNuclearPotential` and `CalcCorePotential`, which evaluate the nuclear and frozen core potential, respectively, of the atoms in a specific fragment in a block of integration points.

The Coulomb potential of the electrons of the frozen subsystems is evaluated using the subroutine `CalcFrozenElectronPotential`. This performs a loop over all frozen fragments and adds the Coulomb potentials of the electrons in these fragments. The Coulomb potential is evaluated using the fitted density,[CJ4] and distance cut-offs are used to achieve linear scaling.

The remaining parts of the embedding potential that depends on the density of the nonfrozen subsystem is evaluated by the subroutine `embinscf`, which is called in each SCF cycle by `focky`, which builds the Fock matrix. The subroutine `embinscf` provides the exchange-correlation and kinetic energy components of the embedding potential in a block of integration points. In the first SCF iteration, it obtains the frozen electron density using `GetFrozenDensity`, which is stored on file for use in the following iterations. The exchange-correlation component is then evaluated using `CalcNonadditiveXCPotential`, and the kinetic-energy component is evaluated using `CalcKineticEnergyPotential`.

B.4.5. Freeze-and-thaw iterations

If the `RELAX` option is used for one or more frozen fragments, it is necessary to per-
form freeze-and-thaw iterations, in which these frozen fragments are thawed. These
freeze-and-thaw iterations are taken care of by the subroutine `DoEmbeddingSCF`, which
replaces the standard subroutine `DoSCF` in FDE calculations.

First, `DoSCF` is called to perform an initial calculation on the nonfrozen subsystem.
The active fragment `activeFragment` obtained in this calculation is then saved in the
list of initial fragments, and the previously nonfrozen initial fragments are marked as
inactive (which means that they will be completely ignored in the following). At
this point, the list of initial fragments (`fragments`) contains the "main fragment"
(obtained from the first calculation) and the frozen fragments (and the remaining
initial fragments, which are inactive and will be ignored).

Following this initial step, the freeze-and-thaw cycles are performed. The main frag-
ment is marked as frozen, and one initially frozen fragment is marked as nonfrozen.
Using `DoInits`, the new active fragment is initialized, and a calculations on this frag-
ment is performed by calling `DoSCF`. The resulting active fragment is then used to
replace the previously frozen initial fragment. This is repeated for all frozen frag-
ments for which the `RELAX` option has been specified. When all these fragments have
been handled, the initially nonfrozen fragment (the main fragment that was save in
the first step) is marked as nonfrozen again, and another calculation on this fragment
is performed. If required, this freeze-and-thaw step is repeated until the densities of
all fragments are converged, or until the maximum number of freeze-and-thaw cycles
has been reached. A simplified flow chart of `DoEmbeddingSCF` is show in Fig. B.2.

Several additional options are taken care of during these freeze-and-thaw iterations.
If requested, the exchange-correlation potential that is used in the SCF procedure is
changed, and in case the `USEBASIS` option is specified for a frozen fragment, additional
tricks are employed. Details can be found in the code itself.

Figure B.2.: Simplified flow chart showing how freeze-and-thaw cycles are performed in the subroutine `DoEmbeddingSCF`
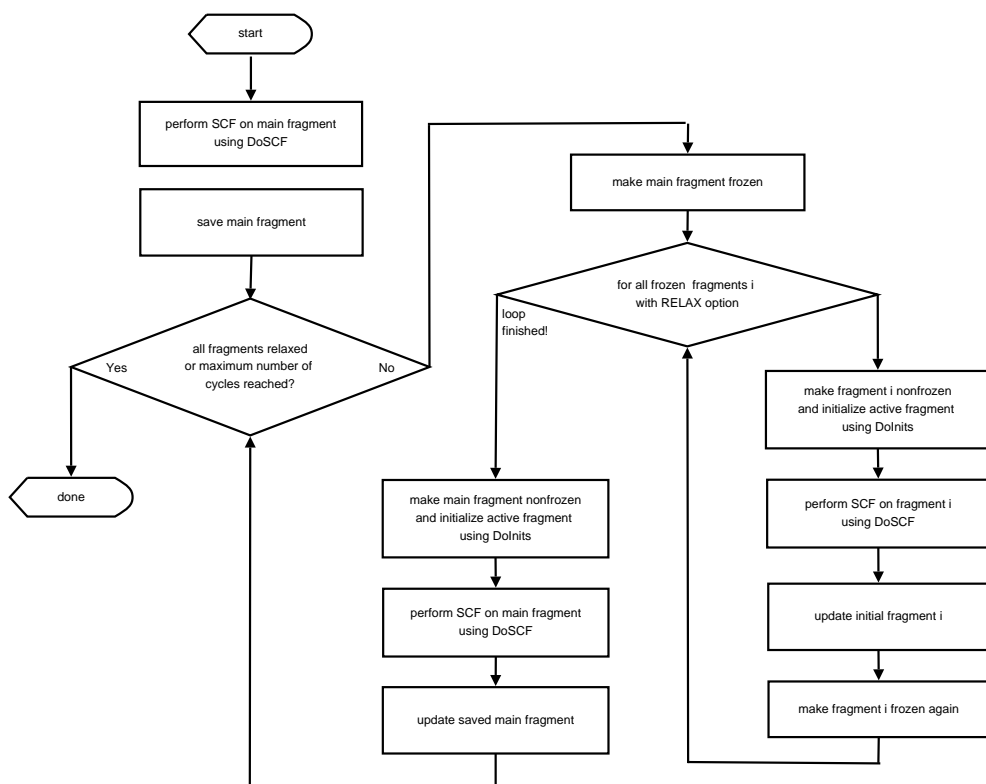
List of Publications

[CJ1] F. Furche, R. Ahlrichs, P. Weis, Ch. Jacob, S. Gilb, T. Bierweiler, and M. M. Kappes, "The structures of small gold cluster anions as determined by a combination of ion mobility measurements and density functional calculations", *J. Chem. Phys.* **117** (2002), 6982–6990.

[CJ2] P. Schwerdtfeger, R. Bast, M. C. L. Gerry, Ch. R. Jacob, M. Jansen, V. Kellö, A. V. Mudring, A. J. Sadlej, T. Saue, T. Söhnel, and F. E. Wagner, "The quadrupole moment of the $3/2^+$ nuclear ground state of ^{197}Au from electric field gradient relativistic coupled cluster and density-functional theory of small molecules and the solid state", *J. Chem. Phys* **122** (2005), 124317.

[CJ3] Ch. R. Jacob, T. A. Wesolowski, and L. Visscher, "Orbital-free embedding applied to the calculation of induced dipole moments in $CO_2 \cdots X$ (X=He, Ne, Ar, Kr, Xe, Hg) van der Waals complexes", *J. Chem. Phys.* **123** (2005), 174104.

(Chapter 8 of this thesis)

[CJ4] J. Neugebauer, Ch. R. Jacob, T. A. Wesolowski, and E. J. Baerends, "An explicit quantum chemical method for modeling large solvation shells applied to aminocoumarin C151", *J. Phys. Chem. A* **109** (2005), 7805–7814.

(Chapter 6 of this thesis is based on a part of this paper)

[CJ5] Ch. R. Jacob, J. Neugebauer, L. Jensen, and L. Visscher, "Comparison of frozen-density embedding and discrete reaction field solvent models for molecular properties", *Phys. Chem. Chem. Phys.* **8** (2006), 2349–2359.

(Chapter 9 of this thesis)

[CJ6] Ch. R. Jacob and L. Visscher, "Calculation of nuclear magnetic resonance shieldings using frozen-density embedding", *J. Chem. Phys.* **125** (2006), 194104.

(Chapter 4 of this thesis)

[CJ7]   Ch. R. Jacob, S. M. Beyhan, and L. Visscher, "Exact functional derivative of the nonadditive kinetic-energy bifunctional in the long-distance limit", *J. Chem. Phys.* **126** (2007), 234116,

also selected for the *Virtual Journal of Biological Physics Reasearch* **14** (2007), Issue 1.

(Chapter 5 of this thesis)

[CJ8]   Ch. R. Jacob, L. Visscher, C. Thierfelder, and P. Schwerdtfeger, "Nuclear quadrupole moment of ^{139}La from relativistic electronic structure calculations of the electric field gradients in LaF, LaCl, LaBr and LaI", *J. Chem. Phys.* (2007), in press.

[CJ9]   Ch. R. Jacob, J. Neugebauer, and L. Visscher, "A flexible implementation of frozen-density embedding for use in multilevel simulations", *J. Comput. Chem.* (2007), in press.

(Chapter 7 of this thesis)

References

[1] C. J. Cramer, *Essentials of Computational Chemistry*, Wiley, New York, 2002.

[2] T. Helgaker, P. Jørgensen, and J. Olsen, *Molecular Electronic Structure Theory*, John Wiley & Sons, Chichester, 2000.

[3] W. Koch and M. C. Holthausen, *A Chemist's Guide to Density Functional Theory*, 2nd edition, Wiley-VCH, Weinheim, 2001.

[4] P. Sherwood, "Hybrid quantum mechanics/molecular mechanics approaches", in: *Modern Methods and Algorithms of Quantum Computing*, edited by J. Grotendorst, volume 1, NIC Series, John von Neumann Institute for Computing, Jülich, 2000, 257–277, URL: http://www.fz-juelich.de/nic-series.

[5] H. M. Senn and W. Thiel, "QM/MM Methods for Biological Systems", *Top. Curr. Chem.* **268** (2007), 173–290.

[6] S. Humbel, S. Sieber, and K. Morokuma, "The IMOMO method: Integration of different levels of molecular orbital approximations for geometry optimization of large systems: Test for n-butane conformation and SN_2 reaction: $RCl+Cl^-$", *J. Chem. Phys.* **105** (1996), 1959–1967.

[7] M. Svensson, S. Humbel, R. Froese, T. Matsubara, S. Sieber, and K. Morokuma, "ONIOM: A Multilayered Integrated MO + MM Method for Geometry Optimizations and Single Point Energy Predictions. A Test for Diels-Alder Reactions and $Pt(P(t-Bu)_3)_2 + H_2$ Oxidative Addition", *J. Phys. Chem.* **100** (1996), 19357–19363.

[8] T. A. Wesolowski and A. Warshel, "Frozen Density Functional Approach for ab Initio Calculations of Solvated Molecules", *J. Phys. Chem.* **97** (1993), 8050–8053.

[9] D. Bakowies and W. Thiel, "Hybrid Models for Combined Quantum Mechanical and Molecular Mechanical Approaches", *J. Phys. Chem.* **100** (1996), 10580–10594.

[10] S. Borini, D. Maynau, and S. Evangelisti, "A combined freeze-and-cut strategy for the description of large molecular systems using a localized orbitals approach", *J. Comput. Chem.* **26** (2005), 1042–1051.

[11] T. M. Henderson, "Embedding wave function theory in density functional theory", *J. Chem. Phys.* **125** (2006), 014105.

References

[12] P. Strange, *Relativistic Quantum Mechanics*, Cambridge University Press, Cambridge, 1998.

[13] K. G. Dyall and K. Fægri Jr., *Introduction to Relativistic Quantum Chemistry*, Oxford University Press, New York, 2007.

[14] C. Cohen-Tannoudji, B. Dui, and F. Laloë, *Quantenmechanik, Teil 1 und 2*, 2nd edition, Walter de Gruyter, Berlin, 1999.

[15] W. Kutzelnigg, *Einführung in die theoretische Chemie, Band 1 und 2*, Verlag Chemie, Weinheim, 1978.

[16] A. Szabo and N. S. Ostlund, *Modern Quantum Chemistry*, Dover Publications, Mineola, N.Y., 1996.

[17] R. G. Parr and W. Yang, *Density-Functional Theory of Atoms and Molecules*, Oxford University Press, Oxford, 1989.

[18] P. Hohenberg and W. Kohn, "Inhomogeneous Electron Gas", *Phys. Rev.* **136** (1964), B864–B871.

[19] W. Kohn and L. J. Sham, "Self-Consistent Equations Including Exchange and Correlation Effects", *Phys. Rev.* **140** (1965), A1133–A 1138.

[20] D. M. Ceperley and B. J. Alder, "Ground State of the Electron Gas by a Stochastic Method", *Phys. Rev. Lett.* **45** (1980), 566–569.

[21] A. D. Becke, "Density-functional exchange-energy approximation with correct asymptotic behavior", *Phys. Rev. A* **38** (1988), 3098–3100.

[22] J. P. Perdew, in: *Electronic Structure of solids*, edited by P. Ziesche and H. Eschrig, Akademie Verlag, Berlin, 1991, 11.

[23] J. P. Perdew, "Density-functional approximation for the correlation energy of the inhomogeneous electron gas", *Phys. Rev. B* **33** (1986), 8822–8824.

[24] C. Lee, W. Yang, and R. G. Parr, "Development of the Colle-Salvetti correlation-energy formula into a functional of the electron density", *Phys. Rev. B* **37** (1988), 785–789.

[25] J. Tao, J. P. Perdew, V. N. Staroverov, and G. E. Scuseria, "Climbing the Density Functional Ladder: Nonempirical Meta–Generalized Gradient Approximation Designed for Molecules and Solids", *Phys. Rev. Lett.* **91** (2003), 146401.

[26] P. R. T. Schipper, O. V. Gritsenko, S. J. A. van Gisbergen, and E. J. Baerends, "Molecular calculations of excitation energies and (hyper)polarizabilities with a statistical average of orbital model exchange-correlation potentials", *J. Chem. Phys.* **112** (2000), 1344–1352.

[27] M. Grüning, "Density functional theory with improved gradient and orbital dependent functionals", PhD thesis, Amsterdam: Vrije Universiteit Amsterdam, 2003.

[28] M. Grüning, O. V. Gritsenko, and E. J. Baerends, "Exchange-correlation energy and potential as approximate functionals of occupied and virtual Kohn–Sham orbitals: Application to dissociating H_2", *J. Phys. Chem.* **118** (2003), 7183–7192.

[29] M. Levy, "Universal variational functionals of electron densitoes, first-order density matrices, and natural spin-orbitals and the solution of the v-representability problem", *Proc. Natl. Acad. Sci. USA* **76** (1997), 6062–6065.

[30] M. Levy, "Electron densities in search of Hamiltonians", *Phys. Rev. A* **26** (1982), 1200–1208.

[31] R. van Leeuwen, "Kohn–Sham potentials in density functional theory", PhD thesis, Amsterdam: Vrije Universiteit Amsterdam, 1994.

[32] J. P. Perdew, R. G. Parr, M. Levy, and J. L. Balduz Jr, "Density-Functional Theory for Fractional Particle Number: Derivative Discontinuities of the Energy", *Phys. Rev. Lett.* **49** (1982), 1691–1694.

[33] Y. A. Wang and E. A. Carter, "Orbital-free kinetic-energy density functional theory", in: *Theoretical Methods in Condensed Phase Chemistry*, edited by S. D. Schwartz, Kluwer, Dordrecht, 2000, chapter 5, 117–184.

[34] L. Thomas, "The calculation of atomic fields", *Proc. Cambridge Philos. Soc.* **23** (1927), 542.

[35] E. Fermi, "Eine statistische Methode zur Bestimmung einiger Eigenschaften des Atoms und ihre Anwendung auf die Theorie des periodischen Systems der Elemente", *Z. Phys.* **48** (1928), 73–79.

[36] C. F. von Weizsäcker, "Zur Theorie der Kernmassen", *Z. Phys.* **96** (1935), 431–458.

[37] G. K.-L. Chan, A. J. Cohen, and N. C. Handy, "Thomas–Fermi–Dirac–von Weizsäcker models in finite systems", *J. Chem. Phys.* **114** (2001), 631–638.

[38] F. Tran and T. A. Wesolowski, "Link between the Kinetic- and Exchange-Energy Functionals in the Generalized Gradient Approximation", *Int. J. Quantum Chem.* **89** (2002), 441 –446.

[39] V. V. Karasiev, S. B. Trickey, and F. E. Harris, "Born–Oppenheimer Interatomic Forces from Simple, Local Kinetic Energy Density Functionals", *J. Comput. Aided Mater. Des.* **13** (2006), 111–129.

[40] T. A. Wesolowski, "Density functional theory with approximate kinetic energy functionals applied to hydrogen bonds", *J. Chem. Phys.* **106** (1997), 8516–8526.

[41] Y. A. Wang, N. Govind, and E. A. Carter, "Orbital-free kinetic-energy functionals for the nearly free electron gas", *Phys. Rev. B* **58** (1998), 13465–13471.

References

[42] Y. A. Wang, N. Govind, and E. A. Carter, "Orbital-free kinetic-energy density functionals with a density-dependent kernel", *Phys. Rev. B* **60** (1999), 16350–16358.

[43] B. Zhou, V. L. Ligneres, and E. A. Carter, "Improving the orbital-free density functional theory description of covalent materials", *J. Chem. Phys.* **122** (2005), 044103.

[44] N. Choly and E. Kaxiras, "Kinetic energy density functional for non-periodic systems", *Solid State Commun.* **121** (2002), 281–286.

[45] M. Fago, R. L. Hayes, E. A. Carter, and M. Ortiz, "Density-functional-theory-based local quasicontinuum method: Predition of dislocal nucleation", *Phys. Rev. B* **70** (2004), 100102.

[46] G. Ho, M. T. Ong, K. J. Caspersen, and E. A. Carter, "Energetics and kinetics of vacancy diffusion and aggregation in shocked aluminium via orbital-free density functional theory", *Phys. Chem. Chem. Phys.* **9** (2007), 4951–4966.

[47] T. J. Frankcombe, G.-J. Kroes, N. I. Choly, and E. Kaxiras, "Orbital-Free Density Functional Theory Applied to $NaAlH_4$", *J. Phys. Chem. B* **109** (2005), 16554–16562.

[48] T. A. Wesolowski, "One-electron equations for embedded electron density: challenge for theory and practical payoffs in multilevel modelling of complex polyatomic systems", in: *Computational Chemistry: Reviews of Current Trends*, edited by J. Leszczynski, volume 10, World Scientific, Singapore, 2006.

[49] T. Wesolowski and A. Warshel, "Ab Initio Free Energy Pertubation Calculations of Solvation Free Energy Using the Frozen Density Functional Approach", *J. Phys. Chem.* **98** (1994), 5183–5187.

[50] J. Neugebauer, M. J. Louwerse, P. Belanzoni, T. A. Wesolowski, and E. J. Baerends, "Modeling solvent effects on electron-spin-resonance hyperfine couplings by frozen-density embedding", *J. Chem. Phys.* **123** (2005), 114101.

[51] P. Cortona, "Self-consistently determined properties of solids without band-structure calculations", *Phys. Rev. B* **44** (1991), 8454–8458.

[52] T. A. Wesolowski and J. Weber, "Kohn-Sham equations with constrained electron density: an iterative evaluation of the ground-state electron density of interaction molecules", *Chem. Phys. Lett.* **248** (1996), 71–76.

[53] M. Iannuzzi, B. Kirchner, and J. Hutter, "Density functional embedding for molecular systems", *Chem. Phys. Lett.* **421** (2006), 16–20.

[54] F. Shimojo, R. K. Kalia, A. Nakano, and P. Vashishta, "Embedded divide-and-conquer algorithm on hierarchical real-space grids: parallel molecular dynamics simulation based on linear-scaling density functional theory", *Comput. Phys. Commun.* **167** (2005), 151–164.

[55] H. Lee, C. Lee, and R. G. Parr, "Conjoint gradient correction to the Hartree-Fock kinetic- and exchange-energy density functionals", *Phys. Rev. A* **44** (1991), 768–771.

[56] T. A. Wesolowski, H. Chermette, and J. Weber, "Accuracy of approximate kinetic energy functionals in the model of Kohn-Sham equations with constrained electron density: The FH···NCH complex as a test case", *J. Chem. Phys.* **105** (1996), 9182–9190.

[57] T. A. Wesolowski and J. Weber, "Kohn-Sham Equations with Constrained Electron Density: The Effect of Various Kinetic Energy Functiona Parametrizations on the Ground-State Molecular Properties", *Int. J. Quantum Chem.* **61** (1997), 303–311.

[58] A. Lembarki and H. Chermette, "Obtaining a gradient-corrected kinetic-energy functional from the Perdew-Wang exchange functional", *Phys. Rev. A* **50** (1994), 5328–5331.

[59] M. E. Casida and T. A. Wesolowski, "Generalization of the Kohn-Sham Equations with Conatrained Electron Density Formalism and Its Time-Dependent Response Theory Formulation", *Int. J. Quantum Chem.* **96** (2004), 577–588.

[60] T. A. Wesolowski, "Hydrogen-Bonding-induced Shifts of the Excitaion Energies in Nucleic Acid Bases: An Interplay between Electrostatic and Electron Density Overlap Effects", *J. Am. Chem. Soc.* **126** (2004), 11444–11445.

[61] J. Neugebauer, "Couplings between electronic transitions in a subsystem formulation of time-dependent density functional theory", *J. Chem. Phys.* **126** (2007), 134116.

[62] N. Govind, Y. A. Wang, A. J. R. da Silva, and E. A. Carter, "Accurate ab initio energetics of extended systems via explicit correlation embedded ia a density functional environment", *Chem. Phys. Lett.* **295** (1998), 129–134.

[63] N. Govind, Y. A. Wang, and E. A. Carter, "Electronic-structure calculations by first-principles density-based embedding of explicitly correlated systems", *J. Chem. Phys.* **110** (1999), 7677–7688.

[64] P. Huang and E. A. Carter, "Self-consistent embedding theory for locally correlated configuration interaction wave functions in condensed matter", *J. Chem. Phys.* **125** (2006), 084102.

[65] D. Lahav and T. Klüner, "A self-consistent density based embedding scheme applied to the adsorption of CO on Pd(111)", *J. Phys.: Condens. Matter* **19** (2007), 226001.

[66] A. Severo Pereira Gomes, Ch. R. Jacob, and L. Visscher, in preparation (2007).

[67] T. Klüner, N. Govind, Y. A. Wang, and E. A. Carter, "Prediction of Electronic Excited States of Adsorbates on Metal Surfaces from First Principles", *Phys. Rev. Lett.* **86** (2001), 5954–5957.

References

[68] T. Klüner, N. Govind, Y. A. Wang, and E. A. Carter, "Periodic density functional embedding theory for complete active space self-consistent field and configuration interaction calculations: Ground and excited state", *J. Chem. Phys.* **116** (2002), 42–54.

[69] R. Kevorkyants, M. Dulak, and T. A. Wesolowski, "Interaction energies in hydrogen-bonded systems: A testing ground for subsystem formulation of density-functional theory", *J. Chem. Phys.* **124** (2006), 024104.

[70] M. Dułak, J. W. Kamiński, and T. A. Wesołowski, "Equilibrium Geometries of Noncovalently Bound Intermolecular Complexes Derived from Subsystem Formulation of Density Functional Theory", *J. Chem. Theory Comput.* (2007).

[71] T. A. Wesolowski, Y. Ellinger, and J. Weber, "Density functional theory with an approximate kinetic energy functional applied to study structure and stability of weak van der Waals complexes", *J. Chem. Phys.* **108** (1998), 6078–6083.

[72] T. A. Wesolowski, P.-Y. Morgantini, and J. Weber, "Intermolecular interaction energies from the total energy bifunctional: A case study of carbazole complexes", *J. Chem. Phys.* **116** (2002), 6411–6421.

[73] T. A. Wesolowski and F. Tran, "Gradient-free and gradient-dependent approximations in the total energy bifunctional for weakly overlapping electron densities", *J. Chem. Phys.* **118** (2003), 2072–2080.

[74] M. Dułak and T. A. Wesołowski, "On the electron leak problem in orbital-free embedding calculations", *J. Chem. Phys.* **124** (2006), 164101.

[75] T. A. Wesolowski, "Application of the DFT-based embedding scheme using an explicit functional of the kinetic energy to determine the spin density of Mg^+ embedded in Ne and ar matrices", *Chem. Phys. Lett.* **311** (1999), 87–92.

[76] J. Neugebauer, M. J. Louwerse, E. J. Baerends, and T. A. Wesolowski, "The merits of the frozen-density embedding scheme to model solvatochromic shifts", *J. Chem. Phys.* **122** (2005), 094115.

[77] T. Wesolowski, R. P. Muller, and A. Warshel, "Ab Initio Frozen Density Calculations of Proton Trasfer Reactions in Solution", *J. Phys. Chem.* **100** (1996), 15444–15449.

[78] M. Štrajbl, G. Hong, and A. Warshel, "Ab Initio QM/MM Simulation with Proper Sampling: "First Principle" Calculations of the Free Energy of the Autodissociation of Water in Aqueous Solution", *J. Phys. Chem. B* **106** (2002), 13333–13343.

[79] G. Hong, M. Strajbl, T. A. Wesolowski, and A. Warshel, "Constraining the Electron Densities in DFT Method as an Effective Way for it Ab Initio Studies of Metal-Caltalyzed Reactions", *J. Comput. Chem.* **21** (2000), 1554–1561.

[80] M. H. M. Olsson, G. Hong, and A. Warshel, "Frozen Density Functional Free Energy Simulations of Redox Proteins: Computational Studies of the Reduction Potential of Plastocyanin and Rusticyanin", *J. Am. Chem. Soc.* **125** (2003), 5025–5039.

[81] T. A. Wesolowski, A. Goursot, and J. Weber, "Properties of CO absorbed in ZSM5 zeolite: Density functional theory study using the embedding scheme based on electron density partitioning", *J. Chem. Phys.* **115** (2001), 4791–4797.

[82] M. Leopoldini, N. Russo, M. Toscano, M. Dulak, and T. A. Wesolowski, "Mechanism of Nitrate Reduction by Desulfovibrio desulfuricans Nitrate Reductase - A Theoretical Investigation", *Chem. Eur. J.* **12** (2006), 2532–2541.

[83] J. Neugebauer and E. J. Baerends, "Exploring the Ability of Frozen-Density Embedding to Model Induced Circular Dichroism", *J. Phys. Chem. A* **110** (2006), 8786–8796.

[84] E. V. Stefanovich and T. N. Truong, "Embedded density functional approach for calculations of adsorption on ionic crystals", *J. Chem. Phys.* **104** (1995), 2946–2955.

[85] J. R. Trail and D. M. Bird, "Density-functional embedding using a plane-wave basis", *Phys. Rev. B* **62** (2000), 16402–16411.

[86] N. Choly, G. Lu, Weinan E, and E. Kaxiras, "Multiscale simulations in simple metals: A density-functional-based methodology", *Phys. Rev. B* **71** (2005), 094101.

[87] J. M. García-Lastra, T. Wesolowski, M. T. Barriuso, J. A. Aramburu, and M. Moreno, "Optical and vibrational properties of MnF_6^{4-} complexes in cubic fluoroperovskites: insight through embedding calculations using Kohn–Sham equations with constrained electron density", *J. Phys.: Condens. Matter* **18** (2006), 1519–1534.

[88] M. Zbiri, M. Atanasov, C. Daul, J. M. Garcia-Lastra, and T. A. Wesolowski, "Application of the density functional theory derived orbital-free embedding potential to calculate the splitting energies of lanthanide cations in chloroelpasolite crystals", *Chem. Phys. Lett.* **397** (2004), 441–446.

[89] M. Zbiri, C. A. Daul, and T. A. Wesolowski, "Effect of the f-Orbital Delocalization on the Ligand-Field Splitting Energies in Lanthanide-Containing Elpasolites", *J. Chem. Theory Comput.* **2** (2006), 1106–1111.

[90] P. Cortona, "Direct determination of self-consistent total energies and charge densities of solids: A study of the cohesive properties of the alkali halides", *Phys. Rev. B* **46** (1992), 2008–2014.

[91] P. Cortona and A. Villafiorita Monteleone, "Self-consistent calculations of total energies and charge densities of solids without solving the band-structure problem", *Int. J. Quantum Chem.* **52** (1994), 987–992.

[92]   P. Cortona, A. Villafiorita Monteleone, and P. Becker, "Direct calculations of charge densities of solids: Applications to the alkali-earth sulfides", *Int. J. Quantum Chem.* **56** (1995), 831–837.

[93]   P. Cortona and A. Villafiorita Monteleone, "Ab initio calculations of cohesive and structural properties of the alkali-earth oxides", *J. Phys.: Condens. Matter* **8** (1996), 8983–8994.

[94]   P. Cortona and P. Masri, "Cohesive properties and behaviour under pressure of CaS, CaSe, and CaTe: results of ab initio calculations", *J. Phys.: Condens. Matter* **10** (1998), 8947–8955.

[95]   J.-M. Gillet and P. Cortona, "Analysis of the MgO structure factors", *Phys. Rev. B* **60** (1999), 8569–8574.

[96]   P. Cortona, "Ab-Initio Study of the Structural Phase Transition of SrSe and SrTe Under Pressure", *Int. J. Quantum Chem.* **99** (2004), 828–832.

[97]   L. L. Boyer and M. J. Mehl, "A self consistent atomic deformation model for total energy calculations: Application to ferroelectrics", *Ferroelectrics* **150** (1993), 13–24.

[98]   W. N. Mei, L. L. Boyer, M. J. Mehl, M. M. Ossowski, and H. T. Stokes, "Calculation of electronic, structural, and vibrational properties in alkali halides using a density-functional method with localized densities", *Phys. Rev. B* **61** (2000), 11425–11431.

[99]   M. M. Ossowski, L. L. Boyer, M. J. Mehl, and H. T. Stokes, "Lattice dynamics and elastic properties of corundum by the self-consistent atomic deformation method", *Phys. Rev. B* **66** (2002), 224302.

[100] CP2K, The CP2K developers group, URL: http://cp2k.berlios.de.

[101] J. VandeVondele, M. Krack, F. Mohamed, M. Parrinello, T. Chassaing, and J. Hutter, "QUICKSTEP: Fast and accurate density functional calculations using a mixed Gaussian and plane waves approach", *Comp. Phys. Comm.* **167** (2005), 103–128.

[102] P. Vashishta, R. Kalia, and A. Nakano, "Multimillion Atom Simulations of Dynamics of Oxidation of an Aluminum Nanoparticle and Nanoindentation on Ceramics", *J. Phys. Chem. B* **110** (2006), 3727–3733.

[103] *Calculation of NMR and EPR Parameters. Theory and Applications*, edited by Martin Kaupp, Michael Bühl, and Vladimir G. Malkin, Wiley-VCH, Weinheim, 2004.

[104] T. Helgaker, M. Jaszuński, and K. Ruud, "Ab Initio Methods for the Calculation of NMR Shieldings and Indirect Spin–Spin Coupling Constants", *Chem. Rev.* **99** (1999), 293–352.

[105] M. Swart, C. Fonseca Guerra, and F. M. Bickelhaupt, "Hydrogen Bonds of RNA Are Stronger than Those of DNA, but NMR Monitors Only Presence of Methyl Substituent in Uracil/Tymine", *J. Am. Chem. Soc.* **126** (2004), 16718–16719.

[106] J. Vollet, J. R. Hartig, and H. Schnöckel, "$Al_{50}C_{120}H_{180}$: A Pseudofullerene Shell of 60 Carbon Atoms and 60 Methyl Groups Protecting a Cluster Core of 50 Aluminum Atoms", *Angew. Chem. Int. Ed.* **43** (2004), 3186–3189.

[107] J. Gracia, J. M. Poblet, J. Autschbach, and L. P. Kazansky, "Density-Functional Calculation of the ^{183}W and ^{17}O NMR Chemical Shifts for Large Polyoxotungstates", *Eur. J. Inorg. Chem.* **2006** (2006), 1139–1148.

[108] M. Bühl, F. T. Mauschick, F. Terstegen, and B. Wrackmeyer, "Remarkably Large Geometry Dependence of ^{57}Fe NMR Chemical Shifts", *Angew. Chem. Int. Ed.* **41** (2002), 2312–2315.

[109] M. Profeta, F. Mauri, and C. J. Pickard, "Accurate First Principles Prediction of ^{17}O NMR Parameters in SiO_2: Assignment of the Zeolite Ferrierite Spectrum", *J. Am. Chem. Soc.* **125** (2003), 541–548.

[110] C. Ochsenfeld, J. Kussmann, and F. Koziol, "Ab initio NMR spectra for molecular systems with a thousand and more atoms: A linear scaling method", *Angew. Chem. Int. Ed.* **43** (2004), 4485–4489.

[111] M. A. Watson, P. Sałek, P. Macak, M. Jaszuński, and T. Helgaker, "The Calculation of Indirect Nuclear Spin-Spin Coupling Constants in Large Molecules", *Chem. Eur. J.* **10** (2004), 4627–4639.

[112] Q. Cui and M. Karplus, "Molecular Properties from Combined QM/MM Methods. 2. Chemical Shifts in Large Molecules", *J. Phys. Chem. B* **104** (2000), 3721–3743.

[113] J. Tomasi, B. Mennucci, and R. Cammi, "Quantum Mechanical Continuum Solvation Models", *Chem. Rev.* **105** (2005), 2999–3094.

[114] P.-O. Åstrand, K. V. Mikkelsen, P. Jørgensen, K. Ruud, and T. Helgaker, "Solvent effects on nuclear shieldings and spin–spin couplings of hydrogen selenide", *J. Chem. Phys.* **108** (1998), 2528–2537.

[115] R. Cammi, "The Hartee–Fock calculation of the magnetic properties of molecular solutes", *J. Chem. Phys.* **109** (1998), 3185–3196.

[116] B. Mennucci, J. M. Martínez, and J. Tomasi, "Solvent Effects on Nuclear Shieldings: Continuum or Discrete Solvation Models To Treat Hydrogen Bond and Polarity Effects?", *J. Phys. Chem. A* **105** (2001), 7287–7296.

[117] B. Mennucci, "Hydrogen Bond versus Polar Effects: An Ab Initio Analysis on n -¿ pi* Absorption Spectra and N Nuclear Shieldings of Diazines in Solution", *J. Am. Chem. Soc.* **124** (2002), 1506–1515.

References

[118] M. Cossi and O. Crescenzi, "Different models for the calculation of solvent effects on ^{17}O nuclear magnetic shielding", *J. Chem. Phys.* **118** (2003), 8863–8872.

[119] G. Vignale and M. Rasolt, "Density-Functional Theory in Strong Magnetic Fields", *Phys. Rev. Lett.* **59** (1987), 2360–2363.

[120] E. Engel, "Relativistic Density Functional Theory: Foundations and Basic Formalism", in: *Relativistic Electron Structure Theory, Part 1: Fundamentals*, edited by P. Schwerdtfeger, Elsevier Science, Amsterdam, 2002, chapter 10, 523–621.

[121] C. van Wüllen, "Chemical Shifts with Hartree–Fock and Density Functional Methods", in: *Calculation of NMR and EPR Parameters. Theory and Applications*, edited by Martin Kaupp, Michael Bühl, and Vladimir G. Malkin, Wiley-VCH, Weinheim, 2004, 85–100.

[122] W. Kutzelnigg, "Fundamentals of Nonrelativistic and Relativistic Theory of NMR and EPR Parameters", in: *Calculation of NMR and EPR Parameters. Theory and Applications*, edited by Martin Kaupp, Michael Bühl, and Vladimir G. Malkin, Wiley-VCH, Weinheim, 2004, 43–82.

[123] R. Ditchfield, "Self-consistent perturbation theory of diamagnetism; I. A gauge-invariant LCAO method for N.M.R. chemical shifts", *Mol. Phys.* **27** (1974), 789–807.

[124] ADF, *Amsterdam density functional program*, Theoretical Chemistry, Vrije Universiteit Amsterdam, URL: http://www.scm.com.

[125] G. te Velde, F. M. Bickelhaupt, E. J. Baerends, C. Fonseca Guerra, S. J. A. van Gisbergen, J. G. Snijders, and T. Ziegler, "Chemistry with ADF", *J. Comput. Chem.* **22** (2001), 931–967.

[126] G. Schreckenbach and T. Ziegler, "Calculation of NMR Shielding Tensors Using Gauge-Including Atomic Orbitals and Modern Density Functional Theory", *J. Phys. Chem.* **99** (1995), 606–611.

[127] O. V. Gritsenko, P. R. T. Schipper, and E. J. Baerends, "Approximation of the exchange-correlation Kohn-Sham potential with a statistical average of different orbital model potentials", *Chem. Phys. Lett.* **302** (1999), 199–207.

[128] O. V. Gritsenko, P. R. T. Schipper, and E. J. Baerends, "Ensuring proper short-range and asymptotic behavior of the exchange-correlation Kohn-Sham potential by modeling with a statistical average of different orbital model potentials", *Int. J. Quantum Chem.* **76** (2000), 407–419.

[129] J. Poater, E. van Lenthe, and E. J. Baerends, "Nuclear magnetic resonance chemical shifts with the statistical average of orbital-dependent model potentials in Kohn–Sham density functional theory", *J. Chem. Phys.* **118** (2003), 8584–8593.

[130] J. P. Perdew, J. A. Chevary, S. H. Vosko, K. A. Jackson, M. R. Pederson, D. J. Singh, and C. Fiolhais, "Atoms, molecules, solids, and surfaces: Applications of the generalized gradient approximation for exchange and correlation", *Phys. Rev. B* **46** (1992), 6671–6687.

[131] R. Cammi, B. Mennucci, and J. Tomasi, "Nuclear magnetic shieldings in solution: Gauge invariant atomic orbital calculation using the polarizable continuum model", *J. Chem. Phys.* **110** (1999), 7627–7638.

[132] G. Merino, T. Heine, and G. Seifert, "The Induced Magnetic Field in Cyclic Molecules", *Chem. Eur. J.* **10** (2004), 4367–4371.

[133] T. Heine, C. Corminboeuf, and G. Seifert, "The Magnetic Shielding Function of Molecules and Pi-Electron Delocalization", *Chem. Rev.* **105** (2005), 3889–3910.

[134] C. Reichardt, *Solvents and Solvent Effects in Organic Chemistry*, 3rd edition, Wiley-VCH, Weinheim, 2003.

[135] J. P. Perdew, K. Burke, and M. Ernzerhof, "Generalized Gradient Approximation Made Simple", *Phys. Rev. Lett.* **77** (1996), 3865–3868.

[136] R. van Leeuwen and E. J. Baerends, "Exchange-correlation potential with correct asymptotic behavior", *Phys. Rev. A* **49** (1994), 2421–2431.

[137] J. D. Talman and W. F. Shadwick, "Optimized effective atomic central potential", *Phys. Rev. A* **14** (1976), 36–40.

[138] Q. Zhao, R. C. Morrison, and R. G. Parr, "From electron densities to Kohn-Sham kinetic energies, orbital energies, exchange-correlation potentials, and exchange-correlation energies", *Phys. Rev. A* **50** (1994), 2138–2142.

[139] Y. Wang and R. G. Parr, "Construction of exact Kohn-Sham orbitals from a given electron density", *Phys. Rev. A* **47** (1993), R1591–R1593.

[140] M. Dulak and T. Welosowski, private communication (2006).

[141] ADF-GUI, Scientific Computing and Modeling, Amsterdam, URL: https://www.scm.com.

[142] A. Laio, J. VandeVondele, and U. Rothlisberger, "A Hamiltonian electrostatic coupling scheme for hybrid Car–Parrinello molecular dynamics simulations", *J. Chem. Phys.* **116** (2002), 6941–6947.

[143] R. Poteau, I. Ortega, F. Alary, A. Solis, J.-C. Barthelat, and J.-P. Daudey, "Effective Group Potentials. 1. Method", *J. Phys. Chem. A* **105** (2001), 198–205.

[144] R. Poteau, F. Alary, H. Abou El Makarim, J.-L. Heully, J.-C. Barthelat, and J.-P. Daudey, "Effective Group Potentials. 2. Extraction and Transferability for Chemical Groups Involved in Covalent or Donor-Acceptor Bonds", *J. Phys. Chem. A* **105** (2001), 206–214.

References

[145] W. Humphrey, A. Dalke, and K. Schulten, "VMD -Visual Molecular Dynamics", *J. Mol. Graphics* **14** (1996), 33–38.

[146] O. Gritsenko and E. J. Baerends, "Asymptotic correction of the exchange–correlation kernel of time-dependent density functional theory for long-range charge-transfer excitations", *J. Chem. Phys.* **121** (2004), 655–660.

[147] J. Neugebauer, O. Gritsenko, and E. J. Baerends, "Assessment of a simple correction for the long-range charge-transfer problem in time-dependent density-functional theory", *J. Chem. Phys.* **124** (2006), 214102.

[148] M. E. Casida, in: *Recent Advances in Density-Functional Methods*, edited by D. P. Chong, World Scientific, Singapore, 1995, 155–192.

[149] S. J. A. van Gisbergen, J. G. Snijders, and E. J. Baerends, "Implementation of time-dependent density functional response equations", *Comput. Phys. Commun.* **118** (1999), 119–138.

[150] J. Autschbach and T. Ziegler, *Coord. Chem. Rev.* **238/239** (2003), 83–126.

[151] G. te Velde and E. J. Baerends, "Numerical Integration for Polyatomic Systems", *J. Comp. Phys.* **99** (1992), 84–98.

[152] C. Fonseca Guerra, J. G. Snijders, G. te Velde, and E. J. Baerends, *Theor. Chem. Acc.* **99** (1998), 391.

[153] J. C. Schöneboom, F. Neese, and W. Thiel, "Toward Identification of the Compound I Reactive Intermediate in Cytochrome P450 Chemistry: A QM/MM Study of Its EPR and Mössbauer Parameters", *J. Am. Chem. Soc.* **127** (2005), 5840–5853.

[154] E. J. M. Leenders, L. Guidoni, U. Röthlisberger, J. Vreede, P. G. Bolhuis, and E. J. Meijer, "Protonation of the Chromophore in the Photoactive Yellow Protein", *J. Phys. Chem. B* **111** (2007), 3765–3773.

[155] R. Prabhakar, T. Vreven, M. J. Frisch, K. Morokuma, and D. G. Musaev, "Is the Protein Surrounding the Active Site Critical for Hydrogen Peroxide Reduction by Selenoprotein Glutathione Peroxidase? An ONIOM Study", *J. Phys. Chem. B* **110** (2006), 13608–13613.

[156] A. Warshel and M. Levitt, "Theoretical studies of enzymic reactions: Dielectric, electrostatic and steric stabilization of the carbonium ion in the reaction of lysozyme", *J. Mol. Biol.* **103** (1976), 227–249.

[157] J. Gao, "Methods and applications of combined quantum mechanical and molecular mechanics potentials", in: *Reviews in Computational Chemistry*, edited by K. B. Lipkowitz and D. B. Boyd, volume 7, VCH, New York, 1995, 119–185.

[158] T. Vreven and K. Morokuma, "On the Application of the IMOMO (integrated Molecular Orbital + Molecular Orbital) Method", *J. Comput. Chem.* **21** (2000), 1419–1432.

[159]   M. Swart and F. M. Bickelhaupt, "QUILD: QUantum-regions Interconnected by Local Descriptions", *J. Comput. Chem.* (2007), in press, URL: http://dx.doi.org/10.1002/jcc.20834.

[160]   J. Kongsted, A. Osted, K. V. Mikkelsen, and O. Christiansen, "Molecular electric properties of liquid water calculated using the combined coupled cluster/molecular mechanics method", *J. Mol. Struct.: THEOCHEM* **632** (2003), 207–225.

[161]   L. Jensen, P. Th. van Duijnen, and J. G. Snijders, "A discrete solvent reaction field model within density functional theory", *J. Chem. Phys.* **118** (2003), 514–521.

[162]   L. Jensen, P. Th. van Duijnen, and J. G. Snijders, "A discrete solvent reaction field model for calculating molecular linear response properties in solution", *J. Chem. Phys.* **119** (2003), 3800–3809.

[163]   A. M. Köster, P. Calaminici, M. E. Casida, R. Flores-Moreno, G. Geudtner, A. Goursot, T. Heine, A. Ipatov, F. Janetzko, J. M. del Campo, S. Patchkovskii, J. U. Reveles, D. R. Salahub, and A. Vela, DEMON2K, URL: http://www.demon-software.com, 2006.

[164]   M. Dulak and T. A. Wesolowski, "The basis set effect on the results of the minimization of the total energy bifunctional E[rhoA,rhoB]", *Int. J. Quantum Chem.* **101** (2004), 543–549.

[165]   M. Dułak, J. W. Kamiński, and T. A. Wesołowski, "Equilibrium Geometries of Noncovalently Bound Intermolecular Complexes Derived from Subsystem Formulation of Density Functional Theory", *J. Chem. Theory Comput.* **3** (2007), 735–745.

[166]   F. M. Bickelhaupt and E. J. Baerends, "Kohn-Sham Density Functional Theory: Predicting and Understanding Chemistry", in: *Reviews in Computational Chemistry*, edited by Kenny B. Lipkowitz and Donald B. Boyd, volume 15, Wiley-VCH, New York, 2000, 1–86.

[167]   R. E. Bulo, Ch. R. Jacob, and L. Visscher, "NMR Solvent Shifts of Acetonitrile from Frozen-Density Embedding Calculations", to be submitted (2007).

[168]   L. Kalé, R. Skeel, M. Bhandarkar, R. Brunner, A. Gursoy, N. Krawetz, J. Phillips, A. Shinozaki, K. Varadarajan, and K. Schulten, "NAMD2: Greater Scalability for Parallel Molecular Dynamics", *J. Comput. Phys.* **151** (1999), 283–312.

[169]   A. D. MacKerell Jr., B. Brooks, C. L. Brooks III, L. Nilsson, B. Roux, Y. Won, and M. Karplus, "CHARMM: The Energy Function and Its Parameterization", in: *The Encyclopedia of Computational Chemistry*, edited by Paul von Ragué Schleyer, volume 1, John Wiley & Sons, Chichester, 1998, 271–277.

References

[170] W. L. Jorgensen, J. Chandrasekhar, J. D. Madura, R. W. Impey, and M. L. Klein, "Comparison of simple potential functions for simulating liquid water", *J. Chem. Phys.* **79** (1983), 926–935.

[171] M. J. Weida, J. M. Sperhac, D. J. Nesbitt, and J. M. Hutson, "Signatures of large amplitude motion in a weakly bound complex: High-resolution IR spectroscopy and quantum calculations for $HeCO_2$", *J. Chem. Phys.* **101** (1994), 8351–8363.

[172] G. T. Fraser, A. S. Pine, and R. D. Suenram, "Optothermal-infrared and pulsed-nozzle Fourier-transform microwave spectroscopy of rare gas-CO_2 complexes", *J. Chem. Phys.* **88** (1988), 6157–6167.

[173] Y. Xu and W. Jäger, "Fourier transform microwave spectra of the very weakly bound He-CO_2 dimer", *J. Mol. Struct.* **599** (2001), 211–217.

[174] J. M. Steed, T. A. Dixon, and W. Klemperer, "Determination of the structure of $ArCO_2$ by radio frequency and microwave spectroscopy", *J. Chem. Phys.* **70** (1979), 4095–4100.

[175] M. Iida, Y. Oshshima, and Y. Endo, "Induced Dipole Moments and Intermolecular Force Fields of Rare Gas - CO_2 Complexes Studied by Fourier-Transform Microwave Spectroscopy", *J. Phys. Chem.* **97** (1993), 357–362.

[176] M. Iida, Y. Oshshima, and Y. Endo, "Fourier transform microwave spectroscopy of Hg-CO_2", *J. Chem. Phys.* **95** (1991), 4772–4777.

[177] G. Yan, M. Yang, and D. Xie, "Ab initio potential energy surface and rovibrational spectra of He-CO_2", *J. Chem. Phys.* **109** (1998), 10284–10292.

[178] F. Negri, F. Ancilotto, G. Mistura, and F. Toigo, "Ab initio potential energy surfaces of He-CO_2 and Ne-CO_2 van der Waals complexes", *J. Chem. Phys.* **111** (1999), 6439–6445.

[179] P. J. Marshall, M. M. Szczęśniak, J. Sadlej, G. Chałasiński, M. A. ter Horst, and C. J. Jameson, "Ab initio study of van der Waals interaction of CO_2 with Ar", *J. Chem. Phys.* **104** (1996), 6569–6576.

[180] A. J. Misquitta, R. Bukowski, and K. Szalewicz, "Spectra of Ar-CO_2 from ab initio potential energy surfaces", *J. Chem. Phys.* **112** (2000), 5308–5319.

[181] G. Maroulis and A. Haskopoulos, "Interaction induced dipole moments and polarizability in $CO_2 \cdots$ Rg, Rg = He, Ne, Ar, Kr and Xe", *Chem. Phys. Lett.* **349** (2001), 335–341.

[182] E. van Lenthe, E. J. Baerends, and J. G. Snijders, "Relativistic regular two-component Hamiltonians", *J. Chem. Phys.* **99** (1993), 4597–4610.

[183] E. van Lenthe, E. J. Baerends, and J. G. Snijders, "Relativistic total energy using regular approximations", *J. Chem. Phys.* **101** (1994), 9783–9792.

[184] E. van Lenthe, J. G. Snijders, and E. J. Baerends, "The zero-order regular approximation for relativistic effects: The effect of spin-orbit coupling in closed shell molecules", *J. Chem. Phys.* **105** (1996), 6505–6516.

[185] S. J. A. van Gisbergen, J. G. Snijders, and E. J. Baerends, "A density functional theory study of frequency-dependent polarizabilities and Van der Waals dispersion coefficients for polyatomic molecules", *J. Chem. Phys.* **103** (1995), 9347–9354.

[186] D. P. Chong, E. van Lenthe, S. van Gisbergen, and E. J. Baerends, "Even-tempered slater-type orbitals revisited: From hydrogen to krypton", *J. Comput. Chem.* **25** (2004), 1030.

[187] D. P. Chong, M. Grüning, and E. J. Baerends, "STO and GTO Field-Induced Polarization Functions for H to Kr", *J. Comput. Chem.* **24** (2003), 1582–1591.

[188] D. P. Chong, "Augmenting basis sets for time-dependent density functional theory calculation of exitation energies: Slater-type orbitals for hydrogen to krypton", *Mol. Phys.* **103** (2005), 749–761.

[189] G. Graner, C. Rossetti, and D. Bailly, "The carbon dioxide molecule: A test case for the r_0, r_e and r_m structures", *Mol. Phys.* **58** (1986), 627.

[190] *CRC Handbook of Chemistry and Physics*, edited by David R. Lide, 78th edition, CRC, Boca Raton, FL, 1998.

[191] D. Goebel and U. Hohm, "Dipole Polarizability, Cauchy Moments, and Related Properties of Hg", *J. Phys. Chem.* **100** (1996), 7710–7712.

[192] J. N. Watson, I. E. Craven, and G. L. D. Ritchie, "Temperature dependence of electric field-gradient induced birefringence in carbon dioxide and carbon disulfide", *Chem. Phys. Lett.* **274** (1997), 1.

[193] C. J. Cramer and D. G. Truhlar, "Implicit Solvation Models: Equilibria, Structure, Spectra, and Dynamics", *Chem. Rev.* **99** (1999), 2161–2200.

[194] M. Orozco and F. J. Luque, "Theoretical Methods for the Description of the Solvent Effect in Biomolecular Systems", *Chem. Rev.* **100** (2000), 4187–4226.

[195] J. Tomasi, "Thirty years of continuum solvation chemistry: a review, and prospects for the near future", *Theor. Chem. Acc.* **112** (2004), 184–203.

[196] J. Tomasi, R. Cammi, B. Mennucci, C. Cappelli, and S. Corni, "Molecular properties in solution described with a continuum solvation model", *Phys. Chem. Chem. Phys.* **4** (2002), 5697–5712.

[197] T. D. Poulsen, P. R. Ogilby, and K. V. Mikkelsen, "Linear response properties for solvated molecules described by a combined multiconfigurational self-consistent-field/molecular mechanics model", *J. Chem. Phys.* **116** (2002), 3730–3738.

References

[198] J. Zeng, N. S. Hush, and J. R. Reimers, "Solvent effects on molecular spectra. III. Absorption to and emission from the lowest singlet (n,pi*) state of dilute pyrimidine in water", *J. Chem. Phys.* **99** (1993), 1508–1521.

[199] K. Coutinho, S. Canuto, and M. C. Zerner, "Calculation of the absorption spectrum of benzene in condensed phase. A study of the solvent effects", *Int. J. Quantum Chem.* **65** (1997), 885–891.

[200] T. Malaspina, K. Coutinho, and S. Canuto, "Ab initio calculation of hydrogen bonds in liquids: A sequential Monte Carlo quantum mechanics study of pyridine in water", *J. Chem. Phys.* **117** (2002), 1692–1699.

[201] N. A. Besley, M. T. Oakley, A. J. Cowan, and J. D. Hirst, "A Sequential Molecular Mechanics/Quantum Mechanics Study of the Electronic Spectra of Amides", *J. Am. Chem. Soc.* **126** (2004), 13502–13511.

[202] U. F. Röhrig, I. Frank, J. Hutter, A. Laio, J. VandeVondele, and U. Rothlisberger, "QM/MM Car-Parrinello Molecular Dynamics Study of the Solvent Effects on the Ground State and on the First Excited Singlet State of Acetone in Water", *ChemPhysChem* **4** (2003), 1177–1182.

[203] Y. Luo, P. Norman, and H. Ågren, "A semiclassical approximation model for properties of molecules in solution", *J. Chem. Phys.* **109** (1998), 3589–3595.

[204] P. Macak, P. Norman, Y. Luo, and H. Ågren, "Modeling of dynamic molecular solvent properties using local and cavity field approaches", *J. Chem. Phys.* **112** (2000), 1868–1875.

[205] D. Jonsson, P. Norman, H. Ågren, Y. Luo, K. O. Sylvester-Hvid, and K. V. Mikkelsen, "Excited state polarizabilities in solution obtained by cubic response theory: Calculations on para-, ortho-, and meta-nitroaniline", *J. Chem. Phys.* **109** (1998), 6351–6357.

[206] K. V. Mikkelsen, P. Jørgensen, K. Ruud, and T. Helgaker, "A multipole reaction-field model for gauge-origin independent magnetic properties of solvated molecules", *J. Chem. Phys.* **106** (1997), 1170–1180.

[207] C.-G. Zhan and D. M. Chipman, "Reaction field effects on nitrogen shielding", *J. Chem. Phys.* **110** (1999), 1611–1622.

[208] J. Tomasi and M. Persico, "Molecular Interactions in Solution: An Overview of Methods Based on Continuous Distributions of the Solvent", *Chem. Rev.* **94** (1994), 2027–2094.

[209] D. Frenkel and B. Smit, *Understanding molecular simulation*, 2nd edition, Academic Press, New York, 2002.

[210] R. Car and M. Parrinello, "Unified Approach for Molecular Dynamics and Density-Functional Theory", *Phys. Rev. Lett.* **55** (1985), 2471–2474.

[211] D. Marx and J. Hutter, "Ab initio molecular dynamics: Theory and Implementation", in: *Modern Methods and Algorithms of Quantum Computing*, edited by J. Grotendorst, volume 1, NIC Series, John von Neumann Institute for Computing, Jülich, 2000, 257–277, URL: http://www.fz-juelich.de/nic-series.

[212] E. Runge and E. K. U. Gross, "Density-Functional Theory for Time-Dependent Systems", *Phys. Rev. Lett.* **52** (1984), 997–1000.

[213] E. R. Batista, S. S. Xantheas, and H. Jónsson, "Multipole moments of water molecules in clusters and ice I$_h$ from first principles calculations", *J. Chem. Phys.* **111** (1999), 6011–6015.

[214] B. T. Thole and P. Th. van Duijnen, "On the quantum mechanical treatment of solvent effects", *Theor. Chim. Acta* **55** (1980), 307–318.

[215] M. J. Field, P. A. Bash, and M. Karplus, "A combined quantum mechanical and molecular mechanical potential for molecular dynamics simulations", *J. Comput. Chem.* **11** (1990), 700–733.

[216] A. Genest, A. Woiterski, S. Krüger, A. M. Shor, and N. Rösch, "The IMOMM (Integrated Molecular Orbitals/Molecular Mechanics) Approach for Ligand-Stabilized Metal Clusters. Comparison to Full Density Functional Calculations for the Model Thiolate Cluster $Cu_{13}(SCH_2CH_3)_8$", *J. Chem. Theory Comput.* **2** (2006), 47–58.

[217] J. Kongsted, A. Osted, K. V. Mikkelsen, and O. Christiansen, "Linear response functions for coupled cluster/molecular mechanics including polarization interactions", *J. Chem. Phys.* **118** (2003), 1620–1633.

[218] L. Jensen, M. Swart, and P. Th. van Duijnen, "Microscopic and macroscopic polarization within a combined quantum mechanics and molecular mechanics model", *J. Chem. Phys.* **122** (2005), 034103.

[219] L. Jensen and P. Th. van Duijnen, "Refractive index and third-order nonlinear susceptibility of C_60 in the condensed phase calculated with the discrete solvent reaction field model", *Int. J. Quantum Chem.* **102** (2005), 612 –619.

[220] L. Jensen and P. Th. van Duijnen, "The first hyperpolarizability of p-nitroaniline in 1,4-dioxane: A quantum mechanical/molecular mechanics study", *J. Chem. Phys.* **123** (2005), 074307.

[221] J. Kongsted, A. Osted, K. V. Mikkelsen, and O. Christiansen, "Dipole and quadrupole moments of liquid water calculated within the coupled cluster/molecular mechanics method", *Chem. Phys. Lett.* **364** (2002), 379–386.

[222] L. Jensen, P.-O. Åstrand, K. O. Sylvester-Hvid, and K. V. Mikkelsen, "Frequency-Dependent Molecular Polarizability Calculated within an Interaction Model", *J. Phys. Chem. A* **104** (2000), 1563–1569.

References

[223] L. Jensen, P.-O. Åstrand, A. Osted, J. Kongsted, and K. V. Mikkelsen, "Polarizability of molecular clusters as calculated by a dipole interaction model", *J. Chem. Phys.* **116** (2002), 4001–4010.

[224] B. Thole, "Molecular polarizabilities calculated with a modified dipole interaction", *Chem. Phys.* **59** (1981), 341–350.

[225] P. Th. van Duijnen and M. Swart, "Molecular and Atomic Polarizabilities: Thole's Model Revisited", *J. Phys. Chem. A* **102** (1998), 2399–2407.

[226] M. B. Robin, *Higher excited states of polyatomic molecules*, volume I, Academic Press, New York, 1975.

[227] M. B. Robin, *Higher excited states of polyatomic molecules*, volume III, Academic Press, New York, 1985.

[228] G. D. Kerr, R. N. Hamm, M. W. Williams, R. D. Birkhoff, and L. R. Painter, "Optical and Dielectric Properties of Water in the Vacuum Ultraviolet", *Phys. Rev. A* **5** (1972), 2523–2527.

[229] O. Christiansen, T. M. Nymand, and K. V. Mikkelsen, "A theoretical study of the electronic spectrum of water", *J. Chem. Phys.* **113** (2000), 8101–8112.

[230] M. Grüning, O. V. Gritsenko, S. J. A. van Gisbergen, and E. J. Baerends, "On the required shape corrections to the local density and generalized gradient approximations to the Kohn–Sham potentials for molecular response calculations of (hyper)polarizabilities and excitation energies", *J. Chem. Phys.* **116** (2002), 9591–9601.

[231] J. Neugebauer, E. J. Baerends, and M. Nooijen, "Vibronic coupling and double excitations in linear response time-dependent density functional calculations: Dipole-allowed states of N_2", *J. Chem. Phys.* **121** (2004), 6155–6166.

[232] G. Maroulis, "Hyperpolarizabilities of H_2O revisited: accurate estimate of the basis set limit and the size of electron correlation effects", *Chem. Phys. Lett.* **289** (1998), 403–411.

[233] A. J. Russel and M. A. Spackmann, "Vibrational avaraging of electrical properties", *Mol. Phys.* **84** (1995), 1239–1255.

[234] Ch. R. Jacob and L. Visscher, in preparation (2007).

[235] J. P. Perdew and Wang Yue, "Accurate and simple density functional for the electronic exchange energy: Generalized gradient approximation", *Phys. Rev. B* **33** (1986), 8800–8802.

[236] H. Ou-Yang and M. Levy, "Approximate noninteracting kinetic energy functionals from a nonuniform scaling requirement", *Int. J. Quantum Chem.* **40** (1991), 379–388.

[237] A. J. Thakkar, "Comparison of kinetic-energy density functionals", *Phys. Rev. A* **46** (1992), 6920–6924.

Acknowledgments
Dankwoord
Danksagungen

Allereerst wil ik mijn co-promotor Luuk Visscher hartelijk bedanken. Luuk, bedankt voor de interessante project en voor de mogelijkheid een nieuw onderwerp te beginnen, dat nu in jouw groep heel groot is geworden. Ik wil je verder bedanken, dat je altijd tijd had voor vragen en discussies, dat jij altijd in mijn werk geïnteresserd was en dat jij me ook de gelegenheid hebt gegeven om mijn eigen ideeën te volgen.

Mijn promotor Evert Jan Baerends wil ik bedanken voor het kritisch doorlezen van mijn manuscript, vele goede discussies over FDE en voor zijn grote interesse in mijn onderzoek.

Johannes, vielen Dank für die gute Zusammenarbeit, unsere Diskussionen über Wissenschaft und andere Dinge, und deine zahlreichen Beiträge zu dieser Doktorarbeit. Vieles wäre ohne deine Vorarbeiten und ohne deine Ideen nicht möglich gewesen. Und auch noch einmal Danke, dass du während deiner Zeit in Amsterdam ein so perfekter Mitbewohner warst (vor allem, weil wir eigentlich beide keinen Mitbewohner wollten).

I would like to thank Tomasz Wesolowski, for the development of the orbital-free embedding scheme that is the topic of this thesis, for providing his initial implementation of this scheme in ADF and for the very fruitful collaboration on different parts of this thesis, in particular the CO_2 and the aminocoumarin papers. I would further like to thank Lasse Jensen for the collaboration on the comparison of FDE with the DRF model, and for "inventing" the acronym FDE.

I am very grateful for the support I got from SCM, especially for all the ADF-related help from Erik, Alexej, and Olivier. Furthermore, I want to thank Stan for giving me the opportunity to attend the ACS meeting in San Francisco.

Andre, thanks a lot for being such a good office mate, for all the conversations about computers, science, sports, and (Brazilian) politics, and I hope that there will be lots of results coming out of the projects we have started. Thank you also to my second office mate Jetze. Jetze, I will really miss the smell of burning rubber every morning.

seid.

Anna, die mich fast während der gesamten Zeit meiner Doktorarbeit begleitet hat, möchte ich hier noch einmal ganz besonders danken. Ohne Dich wäre diese Arbeit sicher nicht so gut geworden, und es hätte auch nur halb so viel Spaß gemacht.

Zum Schluss danke ich meinem Vater, meiner Mutter und meinem Bruder Peter für ihre Unterstützung während meines Studiums, meiner Zeit in Neuseeland und meiner Doktorarbeit.